

Influence of Reynolds Number and Blade Geometry on Low Pressure Turbine Performance

by

Mark Eric Bury

B.S. Aerospace Engineering
University of Colorado (1995)

Submitted to the Department of Aeronautics and Astronautics
in partial fulfillment of the requirements for the degree of

MASTER OF SCIENCE

at the

MASSACHUSETTS INSTITUTE OF TECHNOLOGY

June 1997

© Massachusetts Institute of Technology 1997. All rights reserved.

Author _____
Department of Aeronautics and Astronautics
May 23, 1997

Certified by _____
Dr. Choon S. Tan
Principal Research Scientist, Gas Turbine Laboratory
Thesis Supervisor

Accepted by _____
Professor Jaime Peraire
Chair, Graduate Office

MASSACHUSETTS INSTITUTE
OF TECHNOLOGY

AERO

JUN 10 1997

Influence of Reynolds Number and Blade Geometry on Low Pressure Turbine Performance

by

Mark Eric Bury

Submitted to the Department of Aeronautics and Astronautics
on May 23, 1997, in partial fulfillment of the
requirements for the degree of
Master of Science

Abstract

A first-of-a-kind computational experiment was implemented to assess the influence of Reynolds number and blade design (for identical gas flow angles) on low pressure turbine performance. The objective is to link the time-average performance of a low pressure turbine blade with the flow unsteadiness accompanying a separation of the suction side boundary layer. Specifically, this is accomplished using a time-accurate, two-dimensional, incompressible direct Navier-Stokes simulation of flow in three low pressure turbine blade designs for Reynolds numbers ranging from 20,000 to 120,000.

Comparisons of the three geometries reveal that the separated region for the aft loaded blade design is characterized by a time-average separation bubble that is shorter in length than the forward loaded blade. The difference in design translates into a “lagging” of the shear layer roll-up process on the suction side for the forward loaded blade as compared to the aft loaded blade; for a given Reynolds number, the aft loaded design is closer to a point of periodic boundary layer re-attachment relative to the forward loaded design.

Forward loading produces greater profile loss due to the higher velocities in the forward half of the passage. However, the unsteady features for the aft loaded blade are very different from those seen for the forward loading case; this is reflected in the time-averaged flow, with the forward loading having a smaller trailing edge flow blockage. Thus, one can deduce that the mixed-out total pressure loss will be larger for the aft loading situation. Differences in the the time-average and unsteady flow features between the two designs are even more apparent at a Reynolds number of 120,000.

The performance of the low pressure turbine blade increases significantly when periodic re-attachment of the suction side boundary layer occurs. The total pressure loss generated in the passage drops by nearly a factor of 2 between the fully separated boundary layer and the periodically re-attaching boundary layer.

This investigation has demonstrated the feasibility of using a high-order scheme to potentially link the unsteady flow features with the time-average low pressure turbine blade performance. The ability of this high-order Navier-Stokes flow solver to compute differences in flow behavior and performance between seemingly similar blade designs for Reynolds numbers up to 120,000 highlights the usefulness of the technique as a design tool.

Thesis Supervisor: Dr. Choon S. Tan

Title: Principal Research Scientist, Gas Turbine Laboratory

Acknowledgments

First, I would like to thank Pratt and Whitney for their involvement in this research. I appreciate the input and direction provided by Dr. Om Sharma, Brent Staubach, and Gary Stetson.

I would also like to thank NASA Lewis Research Center for the use of their computational facilities. Specifically, the time and effort put forth by Dr. David Ashpis in answering my questions and helping me to produce the videos of the calculations was of great help to this investigation.

Thanks to Choon for taking me on as a student, and doing everything possible to help me from the first day we met.

Thanks to my friends who made working (and almost living) in the GTL an enjoyable experience.

Finally, I can not express enough appreciation towards my parents, whose love and support gave me the opportunity to earn this degree. Thanks.

Contents

1	Introduction	17
1.1	Technical Background	18
1.1.1	Effect of Reynolds Number on Engine Performance	18
1.1.2	Consequences of Flow Separation	19
1.2	Motivation	26
1.3	Technical Objective	28
1.4	Summary of Contributions	28
1.5	Thesis Overview	29
2	Method	30
2.1	Numerical Scheme	30
2.2	Blade Geometries	32
2.3	Computational Method	34
2.3.1	Grid Generation	34
2.3.2	Determination of Time for Solution to Reach Periodicity	36
2.3.3	Time-Averages	39
2.3.4	Total Pressure Loss Calculations	41
2.3.5	Conventions	45
3	Presentation of Computed Results	47
3.1	Chapter Overview	47
3.1.1	Postprocessing of Results	49
3.2	Low Reynolds Number Solutions	50
3.2.1	Time-Average Solutions at $Re = 20,000$	50
3.2.2	Total Velocity and Static Pressure Contours at $Re = 20,000$	50

3.2.3	Surface Static Pressure Coefficient and Skin Friction at Re = 20,000	53
3.2.4	Total Pressure Loss at Re = 20,000	57
3.2.5	Summary of Time-Averaged Results at Re = 20,000	64
3.2.6	Unsteady Flow Features at Re = 20,000	65
3.2.7	Total Pressure Variation in the Wake at Re = 20,000	66
3.2.8	Shear Layer Behavior at Re = 20,000	69
3.2.9	Location of Separation Point in Steady versus Unsteady Flow	74
3.2.10	Static Pressure Deviations Due to Unsteadiness at Re = 20,000	76
3.2.11	Dissipation Coefficient at Re = 20,000	78
3.2.12	Summary of Observed Unsteady Features at Re = 20,000	79
3.2.13	Time-Average Solutions at Re = 30,000	80
3.2.14	Total Velocity and Static Pressure Contours at Re = 30,000	80
3.2.15	Surface Static Pressure Coefficient and Skin Friction at Re = 30,000	81
3.2.16	Total Pressure Loss at Re = 30,000	85
3.2.17	Summary of Time-Averaged Results at Re = 30,000	86
3.2.18	Unsteady Features at Re = 30,000	87
3.2.19	Total Pressure Variation in the Wake at Re of 30,000	87
3.2.20	Shear Layer Behavior at Re = 30,000	87
3.2.21	Static Pressure Deviations Due to Unsteadiness at Re = 30,000	95
3.2.22	Dissipation Coefficient at Re = 30,000	97
3.2.23	Summary of Observed Unsteady Features at Re = 30,000	98
3.3	High Reynolds Number Solutions	99
3.3.1	Time-Average Solutions at Re = 60,000	99
3.3.2	Total Velocity and Static Pressure Contours at Re = 60,000	99
3.3.3	Surface Static Pressure Coefficient and Skin Friction at Re = 60,000	101
3.3.4	Total Pressure Loss at Re = 60,000	101
3.3.5	Summary of Time-Averaged Results at Re = 60,000	104
3.3.6	Unsteady Features at Re = 60,000	105
3.3.7	Total Pressure Variation in the Wake at Re = 60,000	105

3.3.8	Shear Layer Behavior at $Re = 60,000$	108
3.3.9	Static Pressure Deviations Due to Unsteadiness at $Re = 60,000$. . .	110
3.3.10	Dissipation Coefficients at $Re = 60,000$	112
3.3.11	Summary of Observed Unsteady Features at $Re = 60,000$	113
3.3.12	Time-Average Solutions at $Re = 90,000$ and $120,000$	113
3.3.13	Total Velocity and Static Pressure Contours at $Re = 90,000$ and $120,000$	113
3.3.14	Surface Static Pressure Coefficient and Skin Friction at $Re = 90,000$ and $120,000$	114
3.3.15	Total Pressure Loss at $Re = 90,000$ and $120,000$	114
3.3.16	Summary of Time-Averaged Results at $Re = 90,000$ and $120,000$. .	122
3.3.17	Unsteady Features at $Re = 90,000$ and $120,000$	122
3.3.18	Total Pressure Variation in the Wake at $Re = 90,000$ and $120,000$.	122
3.3.19	Shear Layer Behavior at $Re = 90,000$ and $120,000$	123
3.3.20	Static Pressure Deviations Due to Unsteadiness at $Re = 90,000$ and $120,000$	126
3.3.21	Dissipation Coefficients at $Re = 90,000$ and $120,000$	130
3.3.22	Summary of Observed Unsteady Features at $Re = 90,000$ and $120,000$	130
3.3.23	Summary of Key Results Presented	130
4	Implications on LPT Design and Issues of Fluid Dynamical Interest	134
4.1	Implications on LPT Blade Design	135
4.2	Implications on Fluid Dynamic Issues	136
4.2.1	Determination of Shedding Frequency	136
4.2.2	Estimation of Point of Vortex Formation	138
4.2.3	Variation in Profile and Mixed-Out Losses with Reynolds Number .	140
4.2.4	Effects of Blade Loading on Shear Layer Development	145
4.2.5	Profile and Mixing Loss Tradeoffs Associated with Choice of Blade Geometry	147
5	Summary and Conclusions	149
5.1	Summary and Conclusion	149

5.2	Future Work	150
A	Effects of Inflow and Outflow Boundary Placement on Solution	151
A.1	Results	153
A.2	Explanation of Results	158
A.3	Implications	159
B	Loss Calculation Procedures	162
B.1	Loss Calculations	162
B.2	Loss Calculation for a Blasius Profile	164
C	Grid Effects and	
	Computational Effort	168
C.1	Effect of Gridding on Solution Stability	168
C.2	Computational Effort	171

List of Figures

1-1	Effect of altitude increase from sea level take-off to cruise on the chord based Reynolds number for a mid-size engine [8]	19
1-2	Loss breakdown for a turbine cascade [4]	20
1-3	Range of regimes encountered in LPT operation [8]	21
1-4	Effect of acceleration on the transition to turbulence [8]	22
1-5	Inviscid instability of a vortex sheet	23
1-6	Laminar Separation followed by turbulent reattachment, after Horton [7] . .	25
1-7	Constant Strouhal number, based on boundary layer thickness and local freestream velocity, infers an earlier shear layer roll up as the Reynolds number increases, for constant freestream velocity	25
2-1	Breakup of domain into spectral elements	31
2-2	Spectral element, and collocation points	32
2-3	Blade geometries used in calculations	33
2-4	Nomenclature	34
2-5	Inviscid static pressure coefficient on blade surface, blade 1, 2, 3, and comparison	35
2-6	Inviscid loading (pressure difference over blade), blade 1, 2, 3	35
2-7	Typical high Reynolds number grid	36
2-8	Flow field in initial phases of the solution consisting of a starting vortex shed from each blade, with a large influence on the overall flow field	37
2-9	Area-averaging plane used to determine convergence	39
2-10	Top plot : velocity residual; Bottom plot : area-average versus convective time unit for a typical case, and the running average used for determination of convergence	40

2-11	Effect of numerical noise on the total pressure coefficient, leading to the convection downstream of the total pressure deficit associated with the noise, Blade 1, $Re = 120,000$	42
2-12	Nomenclature used for boundary layer parameters	43
3-1	Time-averaged total velocity and static pressure coefficient contours for all blades at $Re = 20,000$, illustrating suction side flow separation and a separation bubble on pressure side	52
3-2	<i>Blade 1</i> , $Re = 20,000$, time-averaged velocity vectors indicating presence of a vortex at the trailing edge region	53
3-3	<i>Blade 3</i> , $Re = 20,000$, time-averaged velocity vectors indicating presence of a vortex at the trailing edge region	54
3-4	Nomenclature for separated region used in calculating the percentage of blockage, w/S	54
3-5	Time-averaged static pressure on the blade surface for $Re = 20,000$	55
3-6	Time-averaged skin friction on blade surface for $Re = 20,000$	56
3-7	Comparison of leading edge geometry for the pressure side, showing the smaller radius of curvature for <i>blade 3</i> than for <i>blade 1</i>	56
3-8	Variation of the dissipation coefficient with momentum thickness Reynolds number, laminar and turbulent, after [4]	59
3-9	Freestream velocity versus axial position, comparison for the three geometries at exit Reynolds number of 20,000	60
3-10	Mass-averaged total pressure loss, dimensionalized by exit dynamic head, for the suction and pressure sides at a Reynolds number of 20,000; majority of the loss occurs on the suction side, and <i>blade 3</i> has a higher loss value just until the trailing edge region	61
3-11	Loss for all three geometries, calculated using enstrophy at $Re = 20,000$	62
3-12	Variation in the static pressure across the blade passage at the trailing edge plane for blade 1, $Re = 20,000$, showing the that the pressure is not constant within the separated region	63
3-13	Nomenclature used for an approximate calculation of the mixing loss due to a separated boundary layer	65

3-14	Variation of area-averaged total pressure in the wake as a function of time showing the differences in the wake structure for each blade, $Re = 20,000$	67
3-15	Variation in total pressure with time for an averaging plane moving through a line of vortices	68
3-16	Power spectral density of time traces given in figure (3-14), variation in shedding frequencies for the three blades, $Re = 20,000$	70
3-17	Instantaneous vorticity field for <i>blade 1</i> , $Re = 20,000$	71
3-18	Instantaneous vorticity field for <i>blade 3</i> , $Re = 20,000$	71
3-19	Shear layer roll-up and the time-averaged flow corresponding for this situation	73
3-20	Instantaneous skin friction on suction surface, and instantaneous total velocity contours for the same time, <i>blade 1</i> , $Re = 20,000$, showing that the point of zero skin friction does not correspond to the point of separation in unsteady flow	75
3-21	Static pressure envelopes over the blade surface and standard deviation of the fluctuations for blades 1, 2, 3, at $Re = 20,000$	77
3-22	Laminar and unsteady dissipation coefficients on the suction side for all three geometries at $Re = 20,000$, plotted along the blade surface	79
3-23	Ratio of the unsteady to laminar dissipation coefficients on the suction side, $Re = 20,000$, plotted along the blade surface	80
3-24	Time-averaged total velocity and static pressure coefficient contours, blades 1, 2, 3, $Re = 30,000$	82
3-25	<i>Blade 1</i> , $Re = 30,000$, time-averaged velocity vectors indicating presence of a vortex at the trailing edge region	83
3-26	<i>Blade 3</i> , $Re = 30,000$, time-averaged velocity vectors indicating presence of a vortex at the trailing edge region	83
3-27	Time-averaged static pressure on the blade surface for $Re = 30,000$	84
3-28	Time-averaged skin friction on blade surface for $Re = 30,000$	84
3-29	Mass-averaged total pressure loss, made non-dimensional by exit dynamic head, for the suction and pressure sides at a Reynolds number of 30,000	85
3-30	Loss for all three geometries, calculated using enstrophy at $Re = 30,000$	86

3-31	Variation of area-averaged total pressure in the wake as a function of time showing the differences in the wake structure for each blade, $Re = 30,000$ (the break in the curve for <i>blade 3</i> is due to a loss of data)	88
3-32	Power spectral density of time traces given in figure 3-31, variation in shedding frequencies for the three blades, $Re = 30,000$	89
3-33	Instantaneous vorticity field for <i>blade 1</i> , $Re = 30,000$, $T = 0.00$ ctu	91
3-34	Instantaneous vorticity field for <i>blade 1</i> , $Re = 30,000$, $T = 0.09$ ctu	91
3-35	Instantaneous vorticity field for <i>blade 1</i> , $Re = 30,000$, $T = 0.18$ ctu	92
3-36	Instantaneous vorticity field for <i>blade 1</i> , $Re = 30,000$, $T = 0.27$ ctu	92
3-37	Instantaneous vorticity field for <i>blade 1</i> , $Re = 30,000$, $T = 0.36$ ctu	93
3-38	Instantaneous vorticity field for <i>blade 1</i> , $Re = 30,000$, $T = 0.45$ ctu	93
3-39	Instantaneous vorticity field for <i>blade 1</i> , $Re = 30,000$, $T = 0.54$ ctu	94
3-40	Instantaneous vorticity field for <i>blade 1</i> , $Re = 30,000$, $T = 0.63$ ctu	94
3-41	Instantaneous vorticity field for <i>blade 3</i> , $Re = 30,000$	95
3-42	Static pressure envelopes over the blade surface and standard deviation of the fluctuations for blades 1, 2, 3, at $Re = 30,000$	96
3-43	Laminar dissipation coefficient and dissipation coefficient associated with unsteadiness on the suction side for all three geometries at $Re = 30,000$, plotted along the blade surface	97
3-44	Ratio of the unsteady to laminar dissipation coefficients on the suction side, $Re = 30,000$, plotted along the blade surface	98
3-45	Time-averaged total velocity and static pressure coefficient contours, blades 1, 3, $Re = 60,000$	100
3-46	Time-averaged static pressure and skin friction on blade surface for $Re = 60,000$, blades 1 and 3	102
3-47	Mass-averaged total pressure loss, dimensionalized by exit dynamic head, for the suction and pressure sides at a Reynolds number of 60,000	103
3-48	Loss calculated using enstrophy, $Re = 60,000$	104
3-49	Variation of area-averaged total pressure in the wake as a function of time showing the differences in the wake structure for each blade, $Re = 60,000$.	106
3-50	Power spectral density of time traces given in figure 3-49, variation in shedding frequencies for the three blades, $Re = 60,000$	107

3-51	Instantaneous vorticity field for <i>blade 1</i> , Re = 60,000	109
3-52	Instantaneous vorticity field for <i>blade 3</i> , Re = 60,000	109
3-53	Static pressure envelopes over the blade surface and standard deviation of the fluctuations for blades 1, 3, at Re = 60,000	111
3-54	Laminar and unsteady dissipation coefficients on the suction side for all three geometries at Re = 60,000, plotted along the blade surface	112
3-55	Ratio of the unsteady to laminar dissipation coefficients on the suction side, Re = 60,000, plotted along the blade surface	113
3-56	Time-averaged total velocity and static pressure coefficient contours, Re = 90,000 blade 1, Re = 120,000 blades 1 and 3	115
3-57	<i>Blade 1</i> , Re = 90,000, time-averaged velocity vectors indicating presence of a vortex at the trailing edge region	116
3-58	<i>Blade 1</i> , Re = 120,000, time-averaged velocity vectors indicating presence of a vortex at the trailing edge region	116
3-59	<i>Blade 3</i> , Re = 120,000, time-averaged velocity vectors indicating presence of a vortex at the trailing edge region	117
3-60	Time-averaged static pressure and skin friction on blade surface for <i>blade 1</i> at Re = 90,000, 120,000	117
3-61	Time-averaged static pressure and skin friction on blade surface for Re = 120,000, blades 1 and 3	118
3-62	Mass-averaged total pressure loss, dimensionalized by exit dynamic head, for the suction and pressure sides at a Reynolds number of 90,000 and 120,000	119
3-63	Mass-averaged total pressure loss, dimensionalized by exit dynamic head, for the suction and pressure sides at a Reynolds number of 120,000 for <i>blade 1</i> and <i>blade 3</i>	120
3-64	Loss calculated using enstrophy, Re = 90,000 and 120,000	121
3-65	Loss calculated using enstrophy, Re = 120,000, <i>blade 1</i> and <i>blade 3</i>	121
3-66	Variation of area-averaged total pressure in the wake as a function of time showing the wake structure for <i>blade 1</i> , Re = 90,000	123
3-67	Variation of area-averaged total pressure in the wake as a function of time showing the wake structure for <i>blade 1</i> , Re = 120,000	124

3-68	Variation of area-averaged total pressure in the wake as a function of time showing the wake structure for <i>blade 3</i> , $Re = 120,000$	124
3-69	Power spectral density of time trace given in figure (3-66), <i>blade 1</i> , $Re = 90,000$	125
3-70	Power spectral density of time trace given in figure (3-67), <i>blade 1</i> , $Re = 120,000$	125
3-71	Power spectral density of time trace given in figure (3-68), <i>blade 3</i> , $Re = 120,000$	126
3-72	Instantaneous vorticity field for <i>blade 1</i> , $Re = 90,000$, $T = 0.00$ ctu	127
3-73	Instantaneous vorticity field for <i>blade 1</i> , $Re = 90,000$, $T = 0.09$ ctu	127
3-74	Instantaneous vorticity field for <i>blade 1</i> , $Re = 90,000$, $T = 0.18$ ctu	128
3-75	Instantaneous vorticity field for <i>blade 1</i> , $Re = 90,000$, $T = 0.27$ ctu	128
3-76	Static pressure envelopes over the blade surface and standard deviation of the fluctuations for blade 1, at $Re = 90,000$ and $120,000$	129
3-77	Laminar and unsteady dissipation coefficients on the suction side for <i>blade 1</i> at $Re = 90,000$ and $120,000$, plotted along the blade surface	131
3-78	Ratio of the unsteady to laminar dissipation coefficients on the suction side, $Re = 90,000$ and $120,000$, plotted along the blade surface	131
3-79	Laminar and unsteady dissipation coefficients on the suction side for <i>blade 3</i> at $Re = 120,000$, plotted along the blade surface	132
3-80	Ratio of the unsteady to laminar dissipation coefficients on the suction side for <i>blade 1</i> at $Re = 120,000$, plotted along the blade surface	132
4-1	Mass-averaged total pressure loss for the three geometries at $Re = 20,000$ and $30,000$	141
4-2	Mass-averaged total pressure loss for <i>blade 1</i> and <i>blade 3</i> at $Re = 60,000$. .	142
4-3	Mass-averaged total pressure loss for <i>blade 1</i> and <i>blade 3</i> at $Re = 120,000$.	142
4-4	Mass-averaged total pressure loss for <i>blade 1</i> , at all Reynolds numbers used in the investigation	143
4-5	Total pressure loss calculated using enstrophy for calculations	144
4-6	Loss vs. Reynolds number, using mass-average	144
4-7	Loss vs. Reynolds number, using enstrophy	145

4-8	Nomenclature for determining the angle the shear layer makes with the wall at the separation point	147
A-1	Grid used for the cases shown in table (3.1), “normal” grid	152
A-2	Grid used the “large” grid cases	152
A-3	Grid used the “inflow” grid cases	153
A-4	Static pressure comparison for <i>blade 1</i> at $Re = 30,000$ between the three different boundary placements used, “normal”, “large”, and the “inflow” cases	154
A-5	Static pressure envelope and standard deviation of the pressure from the mean for <i>blade 1</i> at $Re = 30,000$, “normal” case	154
A-6	Static pressure envelope and standard deviation of the pressure from the mean for <i>blade 1</i> at $Re = 30,000$, “large” case	155
A-7	Static pressure comparison for <i>blade 3</i> at $Re = 30,000$ between the two different boundary placements used, “normal”, “large” cases	156
A-8	Static pressure envelope and standard deviation of the pressure from the mean for <i>blade 3</i> at $Re = 30,000$, “normal” case	156
A-9	Static pressure envelope and standard deviation of the pressure from the mean for <i>blade 3</i> at $Re = 30,000$, “large” case	157
A-10	Static pressure envelope and standard deviation of the pressure from the mean for <i>blade 1</i> at $Re = 30,000$, “inflow” case	157
A-11	Total pressure variation at the inflow plane for <i>blade 1</i> and <i>blade 3</i> for the three various boundary placements	158
A-12	Total pressure variation at the leading edge plane, $x/c = 0$, for <i>blade 1</i> and <i>blade 3</i> for the three various boundary placements	159
A-13	Total pressure variation at a plane $x/c = 0.75$ for <i>blade 1</i> and <i>blade 3</i> for the three various boundary placements	160
A-14	Total pressure variation at the inflow plane for all the “normal” grid solutions	161
B-1	Typical vorticity profile across the passage, used for the determination of boundary layer thicknesses	163
B-2	Nomenclature to be used for calculating the loss associated with a Blasius boundary layer	165
B-3	Boundary layer profiles at edges of control volume, for $\mu = 1/20000$	167

C-1 Typical skewing of spectral elements in center of the passage, trailing edge region	169
C-2 Important to have nearly equal element widths on either side of the grid sections	170

List of Tables

3.1	Matrix of solutions obtained for the three geometries for the range of exit Reynolds numbers from 20,000 to 120,000	48
3.2	Values used for calculation of ω^* , Re = 20,000	73
3.3	Values used for calculation of ω^* , Re = 30,000	95
3.4	Values used for calculation of ω^* , Re = 60,000	110
4.1	Values used for determination of Strouhal number at point of separation . .	137
4.2	Values used for calculation of ω^*	138
4.3	Values used for calculation of ω^*	146
4.4	Calculation of angle shear layer makes with solid surface at point of separation	148
B.1	Comparison of mass-averaged total pressure loss and loss calculated using entstrophy for a Blasius boundary layer	166
C.1	Typical solver sizes and time-steps for the various grids used	171

Chapter 1

Introduction

The development of modern gas turbines has reached a point where major efficiency increases will only be realized if a breakthrough in materials used in blade technology occurs, allowing higher turbine inlet temperatures, or if strides towards decreasing the surge margin are successful. Without any of these advances, an engineer must rely on a better understanding of the physical processes found in the engine to achieve performance increases. It is no longer sufficient in a competitive market to use only experience and correlations to design an engine. The development of improved methods in which to investigate new design concepts based on first principles rather than correlations is a key to further advances in performance.

A component of the engine that could be overlooked when efficiency gains are needed is the low pressure turbine (LPT). The favorable pressure gradient and less hostile environment, as compared to the high pressure turbine, provide a more forgiving design to flaws, as opposed to compressor blading where an error could mean stability reductions and performance degradation. Therefore, advances in the low pressure turbine may occur through subtleties in blade design that are brought about by new understandings of the fluid dynamics that lead to the potential reduction in loss.

This thesis examines unsteady two-dimensional flow in a low pressure turbine blade row, with a focus on the dynamics that occur in the separated flow regions and their relation to blade performance. It does not constitute a study of the transitional behavior of the flow to turbulence, but rather an examination of the role flow unsteadiness has on LPT performance. The following thesis is meant to serve as a starting point, showing

the usefulness of highly accurate numerical simulations, and to give a designer a way to differentiate between seemingly similar blades.

In the next section, we describe the technical background that motivates the present investigation; the issues of engineering interest pertaining to LPT operation are delineated. This is followed by an explanation of the thought process behind the formulation of the present research investigation. The overall goal and the specific technical objectives are then stated. Finally, the contributions from the present effort are summarized.

1.1 Technical Background

1.1.1 Effect of Reynolds Number on Engine Performance

The effect of Reynolds number on the boundary layer is most pronounced in the low pressure turbine. In a compressor, the efficiency depends on mass flow and rotational speed. The turbine on the other hand, has a much smaller variation in efficiency with these parameters, however an increase of altitude from takeoff to cruise causes a noticeable change in performance due to the lower Reynolds numbers encountered in the LPT (figure 1-1). The change in altitude can place the LPT in a Reynolds number regime where laminar boundary layers may exist. A change in the boundary layer state from turbulent to laminar is accompanied by the added tendency for the boundary layer to separate from the blade surface. This is due to the ability of the turbulent boundary layer to resist greater adverse pressure gradients than a laminar boundary layer. Mayle [8] points out that, as the engine is brought to altitude, the turbine inlet Reynolds number decreases on the order of one half of the value at sea level take off. The same change in the magnitude of Reynolds number is found in the rest of the engine, but because the Reynolds number in the LPT is low to begin with, the effects of this change are more pronounced.

The measured and predicted values of loss coefficient for a turbine cascade shown in figure (1-2) indicate that the blade suction side boundary layer constitutes a major part of the entropy produced. For a given blade, the state of the boundary layer, laminar or turbulent, is a function of Reynolds number, thus changes in performance with altitude can be attributed to changes in profile loss. Other factors such as the pressure gradients and geometry do not change significantly or at all with the increase in altitude. Thus, a knowledge of the variation in profile loss throughout the engine operating range, from high

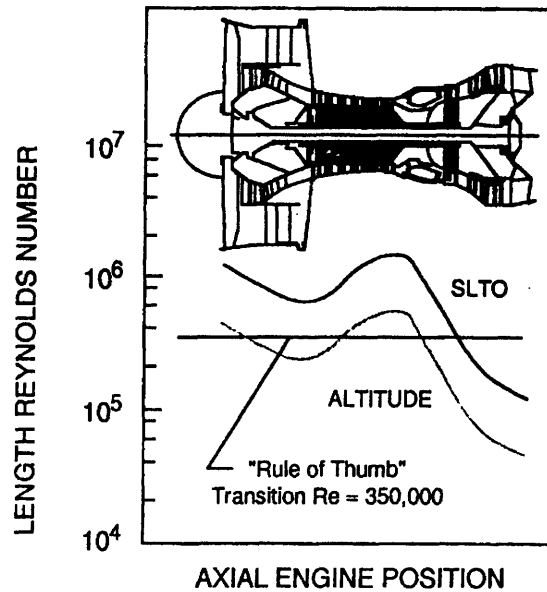


Figure 1-1: Effect of altitude increase from sea level take-off to cruise on the chord based Reynolds number for a mid-size engine [8]

to low Reynolds numbers, is essential for a successful LPT blade design.

1.1.2 Consequences of Flow Separation

Blade surface boundary layer separation can lead to deterioration in the performance of a blade row. This performance deterioration is a result of

1. an increase in the mixed out loss due to greater momentum thickness
2. additional deviations in the exit gas angles from the design values
3. aeromechanical response associated with the unsteady blade loading at frequencies corresponding to the natural blade frequency

Thus, circumstances leading to a fully separated region in the LPT should ideally be avoided at all engine operating conditions.

On the other hand, a separated region that re-attaches prior to the trailing edge gives only a slight rise in loss corresponding to an increase in shape factor [8]. It is customary to neglect this loss except for the fact that these bubbles are usually associated with a transition of the flow leading to higher losses [4].

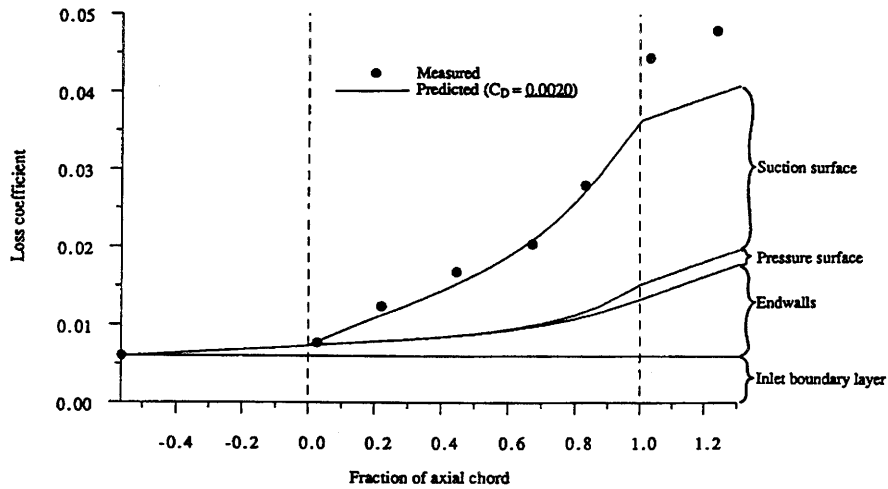


Figure 1-2: Loss breakdown for a turbine cascade [4]

Therefore, an understanding of the processes leading to boundary layer re-attachment are of interest in the design of LPT blading. A major issue is the ability to predict the location on the blade where transition of the boundary layer from laminar to turbulent flow takes place. Although turbulent boundary layers produce higher losses, they are much less prone to separation in regions of adverse pressure gradients. Therefore, an ability to predict boundary layer transition allows the designer to better tailor a blade pressure distribution in hope of optimizing the blade performance throughout the operating range.

The following gives a brief review of the present understanding of the types of transition occurring in turbomachinery flow situations, with emphasis on those relevant to low pressure turbines. Factors affecting the stability of a separated shear layer will also be reviewed.

Transition Modes

The transition of a laminar boundary layer over a solid wall can occur via various means. The modes are natural, bypass, and separated flow transition. Each mode may occur on any given blade at the same time, posing significant difficulties in developing models and techniques for the prediction of transition locations over a LPT blade.

Natural transition is best illustrated by looking at the development of the flow over a flat plate with zero pressure gradient. Upstream disturbances in the form of Tollmien-Schlichting (T-S) waves are amplified by the three-dimensional stretching of the vortex lines, leading to

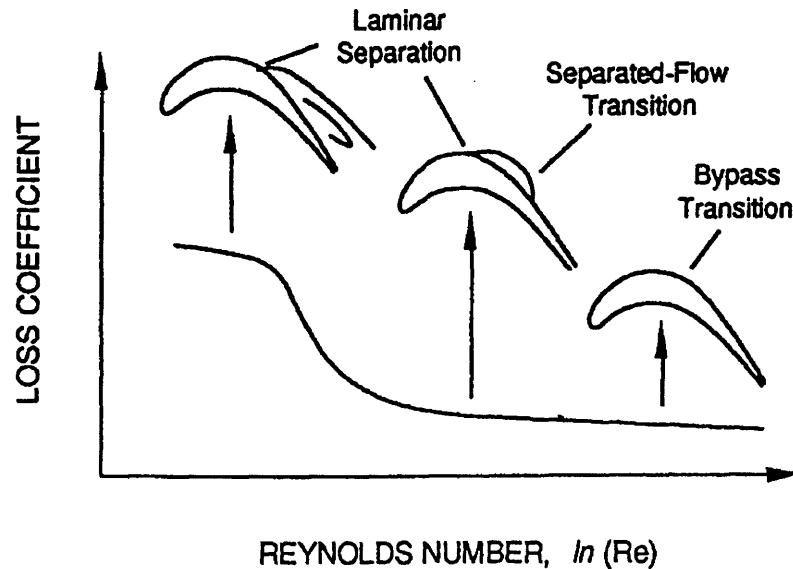


Figure 1-3: Range of regimes encountered in LPT operation [8]

turbulent spot development. These spots spread downstream, leading to a fully turbulent boundary layer. Whether or not a perturbation will cause transition is a function of the frequency of the disturbance and the Reynolds number based on local momentum thickness [2].

Bypass transition is characterized by the production of a turbulent region without the need for the development of T-S waves to precede it. The freestream turbulence drives the formation of turbulent spots, bypassing the normal modes of transition found in linear stability theory.

The third mode of transition is found in a separated boundary layer. Once separation occurs, the free shear layer is much more unstable to disturbances due to the lack of a laminar sublayer found in wall bounded flows. Thus, transition occurs at earlier Reynolds numbers based on boundary layer thickness. Instabilities in the form of T-S waves or the existence of free-stream turbulence can trigger transition.

All of the above transition modes are found in turbomachinery, with bypass transition being the most common mechanism due to the high turbulence levels found throughout the engine. Separation transition is a factor when dealing with high loading situations in the compressor and low turbine. A detailed look at the three modes and the factors governing

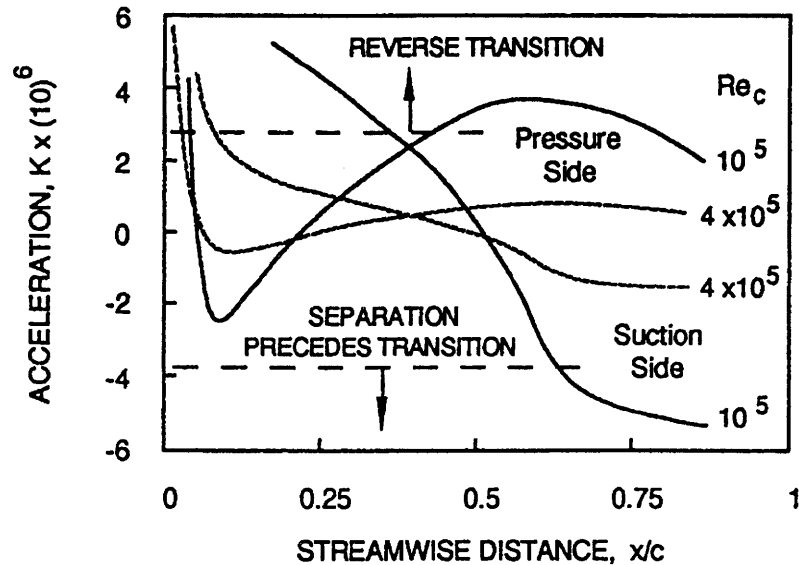


Figure 1-4: Effect of acceleration on the transition to turbulence [8]

each can be found in Mayle [8].

The bypass and separated transition modes are of most importance in the LPT. As the engine moves from the takeoff conditions towards cruise, the LPT undergoes a range of Reynolds numbers in which the suction side boundary layer can be fully turbulent, to laminar separation followed by turbulent re-attachment, and finally to a regime where full laminar separation occurs (figure 1-3). Figure (1-4) indicates the effect of pressure gradient upon transition, where the acceleration parameter, K , is defined as $K = \frac{\nu(\frac{dU}{dx})}{U_e^2}$. This parameter is associated with the acceleration or the deceleration of the freestream flow. For strong enough adverse pressure gradients, separation may occur on the suction side before the boundary layer transitions to turbulent flow. This is precisely the situation that may be encountered in the LPT during operation at cruise altitude [8]. The laminar separation causes an abrupt increase in loss as indicated in figure (1-3).

Effects of Reynolds Number and Pressure Gradient on Separation Bubbles

A topic of interest for the design of LPT blades is the development of a shear layer once it separates. A shear layer is inherently unstable to disturbances, rolling up into discrete vortices when subjected to any infinitesimal disturbance (figure 1-5). The influence of

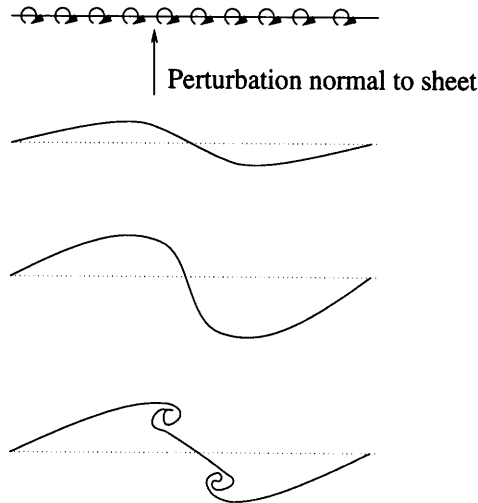


Figure 1-5: Inviscid instability of a vortex sheet

Reynolds number and pressure gradient upon the development of the shear layer in the vicinity of a solid surface is a prime concern for a LPT blade; a drastic decrease in loss from a fully separated boundary layer to one that re-attaches upstream of the trailing edge can be expected. On an appropriate time-averaged basis, the formation of a separation bubble can be associated with the vortex roll up and shedding over a surface at high enough Reynolds numbers (figure 1-6). These bubbles are characterized by a “dead air” region directly behind the point of the boundary layer separation, with a downstream vortex serving as the mechanism that drives the recirculation of the low momentum fluid. The flow field associated with this vortex carries the shear layer vortical fluid back to the solid surface, creating a strong pressure gradient at the point where re-attachment occurs [7]. The following gives a review of how the Reynolds number and pressure gradient effect the bubble dimensions, and thus whether or not the time-averaged flow will be re-attached upstream of trailing edge.

Computations as well as experiments have been implemented to detail the effects of an adverse pressure gradient and of Reynolds number on a separated shear layer. It was concluded in a paper by Pauley [11] that the Strouhal number based on local freestream velocity and boundary layer thickness was independent of the Reynolds number as well as the pressure gradient. Thus a computation of a shedding frequency for the shear layer can be performed once the boundary layer characteristics at separation are known. The computational experiment involved solving the unsteady, incompressible, laminar Navier-Stokes equations for the flow through a channel, with an adverse pressure gradient established us-

ing suction through the top surface of the passage. Investigations were made for gradients small enough to cause a steady separation bubble, up to regimes where unsteady vortex shedding occurred. The position of shear layer roll-up was found to correspond to the point predicted by an inviscid linear stability analysis. The non-dimensionalized shedding frequency, using a type of boundary layer thickness and the velocity ratio across the shear layer, matched the most amplified frequency predicted by a numerical analysis done by Michalke [9]. Such information is useful from the designers point of view because the point of the shear layer roll up corresponds to the location of the time-averaged vortex found in the separation bubble, and thus with the point of re-attachment.

If the Strouhal number is invariant as the Reynolds number changes, some predictions as to where the shear layer may form into a vortex can be made. Pauley demonstrates [11] the trend of increased shedding frequency as the Reynolds number increases. To take this idea further and explain why this is so, the relation of Reynolds number with boundary layer thickness is used. As the Reynolds number increases, the boundary layer thickness will correspondingly decrease. The Strouhal number used in the referenced computational experiment [11] was determined using the momentum thickness at separation, θ , as the length scale, and the local freestream velocity, u_e , as the reference velocity, i.e. :

$$S_t = \frac{f_{shed}\theta}{u_e} \quad (1.1)$$

So a decrease in momentum thickness with increasing Reynolds number should cause the vortex shedding frequency, f_{shed} , to increase. If the freestream velocity is assumed to remain constant, this increase in the shedding frequency translates to a vortex roll up further forward on the blade (figure 1-7). This statement is made because, the constant velocity, u_e , will carry the shed vortices downstream, and if the frequency of shedding is increased, a smaller distance between vortices should be observed. This decrease in the wavelength translates to an earlier roll-up along the blade surface, and hence a smaller separation bubble.

The time-averaged separation bubbles observed in the referenced computational experiment [11] have the same characteristics as laminar bubbles produced in experiments in terms of how the bubble length changes with pressure gradient. It was found that the stronger the adverse pressure gradient, the shorter the length of the time-averaged separation region.

The explanation for this result relates to how the pressure gradient effects the position of shear layer roll-up. The distance from the separation point to the point at which a vortex forms decreases as the adverse pressure gradient increases. Thus, on the time-average, the expanse of the separation bubble from separation to re-attachment will be smaller as one increases the adverse gradient. This result was also found experimentally [14], with the explanation being that the stronger the adverse gradient, the quicker the laminar shear layer tends to transition to turbulence.

For a two-dimensional flow, an increase in the pressure gradient leads to the development of unsteady vortex shedding, as compared to a smaller gradient resulting in a steady bubble. The shedding was shown in [11] to dramatically reduce the time-average separation bubble length. The momentum transfer accompanying the unsteady flow is the primary driver of this effect.

The formation of vortices in a shear layer is the prime factor in determining the time-average separation bubble characteristics over a blade surface. These findings suggest that an increase in Reynolds number and an increase in the adverse pressure gradient both lead to an earlier point of shear layer instability, and vortex roll-up. Thus, the ability to determine the point a shear layer becomes unstable is critical in the understanding of the separation dynamics associated with low Reynolds number LPT operation.

From the above background information, it is inferred that the magnitude of the adverse pressure gradient can have an impact upon LPT blade performance. Also, some clues towards an understanding of the processes influencing the roll-up of a separated shear layer were discussed. These findings are of interest to the design of a LPT blade that may be subjected to separated flow in a segment of its operating range.

1.2 Motivation

As the blade geometry essentially sets the flow, it is appropriate to assess if small design changes in blade profile can be used to create an impact on blade performance. If it is possible to perform such a change, the unsteady, dynamical structure would provide clues on design parameters that may effect loss. Thus, the premise is made that in order to gain additional points of efficiency, the fluid mechanical processes that result in performance degradation must be accurately represented and quantitatively understood. Not only must

this be done spatially, but the temporal variations must be correct in order to obtain information on the sequence of events for the various processes.

An ideal calculation would incorporate all three space dimensions, as well as be time accurate. Also, no turbulence modeling should be used in such a calculation due to the associated uncertainties. Even if all of these conditions were met, the scheme used for this calculation would have to have high accuracy to keep numerical errors from corrupting the solution. Such a calculation can certainly not be done with the current level of technology, so some aspects must be relaxed. The determination of what is important or not for the solution is a function of what problem the research is focused upon.

One of the goals for the design of a three-dimensional LPT blade is to produce, as much as possible, a nearly two-dimensional flow over the majority of the blade span. Thus, a starting point for determining the major flow features that lead to loss would be to perform two-dimensional calculations. Since this investigation is driven towards understanding the flow mechanisms involved, it can be argued that the abandoning of the third space dimension in favor of a time accurate calculation is a reasonable approximation.

Next, for the computational accuracy required, a high order spectral code is used. The spectral formulation is minimally dissipative and dispersive. Details of the numerical scheme will be described in chapter (2).

Another assumption made using the current code, is that the flow is incompressible. Mach numbers in the LPT are on the order of 0.3 to 0.6, therefore some variances from a truly physical solution are encountered, but since the overall flow features are what is desired, this does not seem to be of great importance at this stage of the investigation. Also, the blade geometries used for the present investigation have been scaled from the compressible profiles to ones corresponding to a low-speed, incompressible flow.

Due to the computational resources required for these direct simulations, the flow through a single passage is computed, with periodic flow conditions implemented at the solution boundaries, as opposed to computing the flow in a multi-blade situation.

Lastly, the problems associated with using turbulence modeling will be addressed by not using any at all. Performing such a direct simulation requires a large degree of freedom to accurately resolve the gradients associated with the flow.

These two-dimensional, direct calculations are motivated by the need to demonstrate if modern CFD tools can be used to resolve the vortex dynamics associated with the sepa-

rated flows encountered in the low Reynolds number regimes of a LPT. To gain a better understanding of these flow fields, they must be resolved sufficiently, thus justifying the use of a spectral scheme.

1.3 Technical Objective

The overall objective of this thesis is to examine the performance characteristics for three LPT blade profiles at a range of exit Reynolds numbers from 20,000 to 120,000. This range covers the region where the blades are totally separated up to the Reynolds numbers where periodic re-attachment of the suction side shear layer occurs (figure 1-3). Not only were the total pressure losses of interest, but more importantly, descriptions of the observed dynamics were desired. This objective relies on the fact that the scheme used can capture changes in the flow field associated with slight differences in geometry, as well as be effective at performing direct computations at Reynolds numbers on the order of 100,000.

Thus, these calculations are a preliminary step in determining the usefulness of direct calculations in LPT blade design. The questions not answered here are, one, how well the solutions correspond to reality, and two, if a LPT blade is designed to have the lowest loss out of a series of geometries based upon two-dimensional calculations, does this blade translate to a well designed three-dimensional blade [13]?

1.4 Summary of Contributions

This investigation adds three contributions to the present state of knowledge. Two are related to the confirmation and understanding of the flow physics, and the other stems from the use of this high order code.

First, a follow up on the observations by Pauley [11] were made regarding the point at which a separated shear layer tends to become unstable. It has been shown that the instability that causes vortex formation is inviscid in nature, and the use of inviscid linear stability theory allows one to predict the non-dimensional frequency that will be most amplified [9]. Computations of these non-dimensional frequencies for the solutions obtained in this investigation correspond to this most amplified frequency. Therefore, this process confirms the results set forth by Pauley [11].

Second, the calculation of the Strouhal number (based upon momentum thickness) at

the point of separation shows that it is dependent upon the shedding dynamics. Once the formation of suction side vortices occurs upstream of the trailing edge, a change in the Strouhal number is noticed. A knowledge of this behavior, as well as the use of the linear stability theory allow one to calculate the approximate location of shear layer instability.

Finally, and most importantly, this research has proven the abilities of this high order scheme to capture slight geometry changes, as well as being able to resolve the changing fluid dynamics that occur as the Reynolds number is increased. The resolution of individual vortices, and the ability to accurately compute the separation dynamics, are qualities not found for current finite volume or finite element schemes.

These calculations are the first direct, two-dimensional simulations run using this spectral code in a Reynolds number range of 100,000. Thus, the ability to compute solutions in this range demonstrates that the limit on the type of two-dimensional simulation that can be run is not set by a ceiling on the magnitude of the Reynolds number, but instead the limit is set by the availability of computational resources.

1.5 Thesis Overview

This thesis is organized as follows. The next chapter presents the technical approach, including the computational scheme and grid generation used to simulate LPT flows, as well as the process used to postprocess the computed results. This is followed by a chapter describing the results for the three blades at the Reynolds numbers ranging from 20,000 to 120,000. The unsteady results are examined to determine the influence of blade geometry and Reynolds number on performance. The implications of these results will be discussed in chapter (4). Particularly, the effect of blade pressure distribution will be looked at, with emphasis on how changing the blade geometry can effect the separation process. Appendices will detail the effect of inflow and outflow boundary placement on solutions, solution stability as determined by grid quality, the computational effort involved, and the differences in various loss calculation techniques.

Chapter 2

Method

2.1 Numerical Scheme

As stated previously, it is desired to obtain the solution of the two-dimensional Navier-Stokes equations for a LPT cascade. An incompressible, three-dimensional spectral solver, developed at the M.I.T. Gas Turbine Laboratory was used, with the direct two-dimensional solution being a special case of this code. The scheme used will only be described briefly, as it is thoroughly dealt with in the doctoral thesis by T. Valkov [15].

The two-dimensional Navier-Stokes equations, without turbulence modeling, and the boundary conditions used are :

$$\frac{\partial \mathbf{u}}{\partial t} = \mathbf{u} \times \boldsymbol{\omega} - \nabla p_t + \frac{1}{Re} \nabla^2 \mathbf{u} \quad (2.1)$$

$$\nabla \cdot \mathbf{u} = 0$$

$$\textit{solid boundary} : \quad \mathbf{u} = 0 \quad \nabla p \cdot \mathbf{n} = 0$$

$$\textit{inlet boundary} : \quad \mathbf{u} = \mathbf{u}_{\text{inlet}} \quad \nabla p \cdot \mathbf{n} = 0$$

$$\textit{exit boundary} : \quad \nabla p \cdot \mathbf{n} = 0$$

$$\textit{periodic boundary} : \quad \mathbf{u}(x, y + S, t) = \mathbf{u}(x, y, t) \quad p_t(x, y + S, t) = p_t(x, y, t)$$

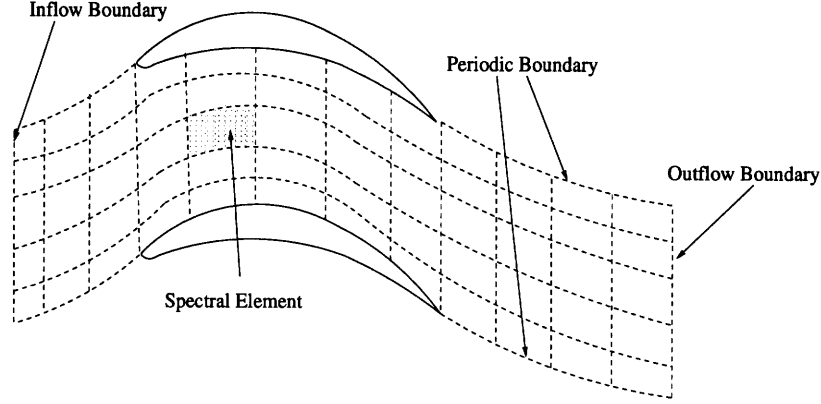


Figure 2-1: Breakup of domain into spectral elements

The time-stepping scheme is a fractional time-splitting method consisting of convective, pressure, and viscous steps [10]. The solution begins with an approximate velocity field, and then the flow is stepped through the following procedure to the next time step.

$$\mathbf{u}^* = \mathbf{u}^n + \int_t^{t+\Delta t} \mathbf{u} \times \boldsymbol{\omega} dt \quad (2.2)$$

$$\mathbf{u}^{**} = \mathbf{u}^* - \int_t^{t+\Delta t} \nabla p dt \quad (2.3)$$

$$\mathbf{u}^{n+1} = \mathbf{u}^{**} + \frac{1}{Re} \int_t^{t+\Delta t} \nabla^2 \mathbf{u} dt \quad (2.4)$$

The convective step is implemented through a fourth-order Runge-Kutta integration scheme, the pressure step is achieved using a backward Euler scheme, and the viscous step uses a semi-implicit Crank-Nicholson scheme. The pressure step requires the computation of the pressure field implicitly, while satisfying continuity : $\nabla \cdot \mathbf{u}^{**} = 0$

The spatial discretization is based on dividing the computational domain into a number of spectral elements, with each element consisting of an $N \times N$ array of collocation points (figure 2-1). The collocation points are placed following a Gaussian distribution, allowing Chebycheff polynomials to be used as the interpolants representing the flow variables over each element (figure 2-2). The optimal scheme uses $N = 7$.

$$\begin{pmatrix} \mathbf{u}(\zeta, \eta) \\ p_t(\zeta, \eta) \end{pmatrix} = \sum_{j=1}^7 \sum_{k=1}^7 \mathbf{u}_{jk} h_j(\zeta) h_k(\eta)$$

where :

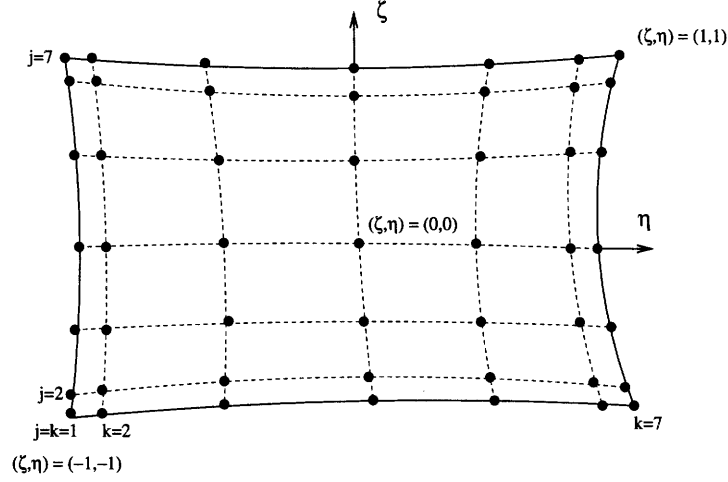


Figure 2-2: Spectral element, and collocation points

$$h_m(\zeta) = \sum_{n=1} t_{mn} T_{n-1}(\zeta) \text{ where } t_{mn} = \frac{2}{(N-1)C_m C_n} T_{n-1}(\zeta_m)$$

$$C_i = \begin{cases} 1 & m \neq 1, N \\ 2 & m = 1, N \end{cases}$$

The Gaussian distribution of collocation points results in the following :

$$h_m(\zeta_n) = h_m(\eta_n) = \delta_{mn} \text{ where } \rightarrow \delta_{ij} = 1 \text{ if } i = j \text{ or } \delta_{ij} = 0 \text{ if } i \neq j$$

Therefore, no transformation from real space to modal space is needed because :

$$\mathbf{u}_{jk} = \mathbf{u}(\zeta_j, \eta_k)$$

The set of equations is re-arranged using static condensation to allow for the solution of only the points on the element boundaries, termed global points. Then the solution is completed by using this result and interpolating the solution for the nodes internal to each element. This process is used both in the pressure and viscous steps. Again, a detailed explanation of this scheme can be found in [15].

2.2 Blade Geometries

Three geometries representative of LPT two-dimensional profiles were used for the investigation. The blades (figure 2-3) were designed to produce identical gas angles, and thus

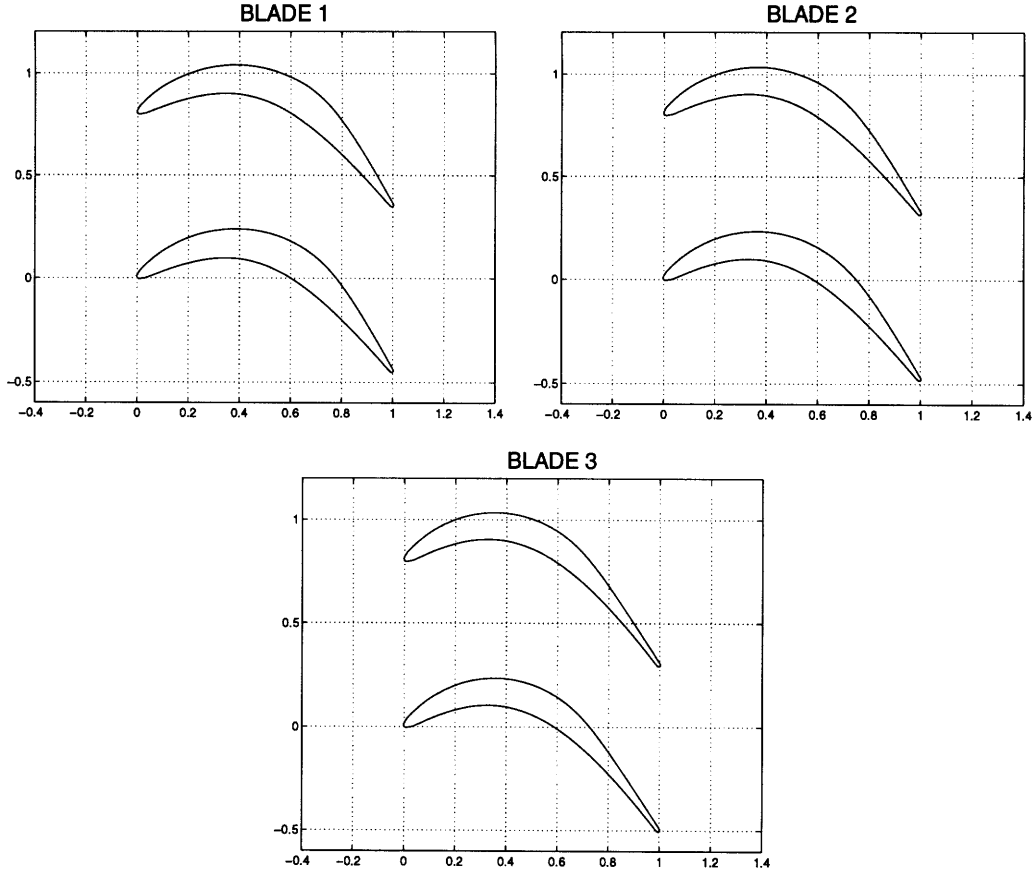


Figure 2-3: Blade geometries used in calculations

reasonable blade-to-blade comparisons can be made between the effectiveness of each design. The inlet gas angle used in all computations was $\alpha_1 = 37^\circ$, and with an exit gas angle of nearly $\alpha_2 = 58^\circ$, the resulting total velocity ratio is $\frac{V_{T_{exit}}}{V_{T_{inlet}}} \approx 1.5$. The solidity based on axial chord used for all calculations is, $\sigma = \frac{\text{axial chord}}{\text{blade spacing}} = \frac{c}{S} = 0.8$. This was the solidity provided with the blade geometries (figure 2-4). All geometries used rounded trailing edges as opposed to a sharp or squared trailing edge.

The pressure distributions, calculated using an Euler code [16], indicate that *blade 1* has the most aft loading, whereas *blade 2* and *blade 3* have their loading peaks further upstream, with *blade 3* the farthest forward (figure 2-5 and 2-6). The total load on each blade is the same, i.e., $C_l = \int_0^1 \Delta C_p d(\frac{x}{c})$ for the inviscid flow is the same for each geometry. Therefore, the extremes are the aft loading for *blade 1* with a sharp pressure rise in the last 3/10 axial chords, to the loading for *blade 3*, which has its minimum pressure at 0.65 axial chords with only a slight adverse pressure gradient in the last 2/10 of chord.

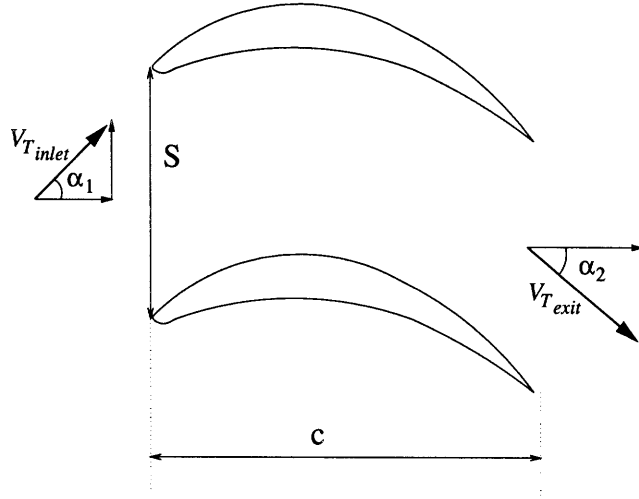


Figure 2-4: Nomenclature

2.3 Computational Method

2.3.1 Grid Generation

The spectral grids used for the computations were generated using a code written by T. Valkov. The code produces a spectral H-grid using metric-preserving Euclidean transformations. Emphasis is placed on the clustering of elements where high gradients in flow properties occur, such as near the leading and trailing edges, and in the boundary layers. A typical grid used for a high Reynolds number solution (exit $Re = 120,000$) is shown in figure (2-7). It should be remembered that each element shown contains an array of 7×7 collocation points over which the flow variables are interpolated.

For all computations, the inlet boundary was located 0.35 *axial chords* upstream of the leading edge. The downstream boundary was placed 0.7 *axial chords* from the trailing edge. It is recognized that these boundary placements are fairly close to the regions of interest, but the need to keep computational costs down drove this decision. The effects of the location of the computational boundaries are described in appendix (A), as well as the effects of element sizes on the stability of the spectral code. Again, reference should be made to T. Valkov's thesis [15] for details on the grid generation process and the solution procedure.

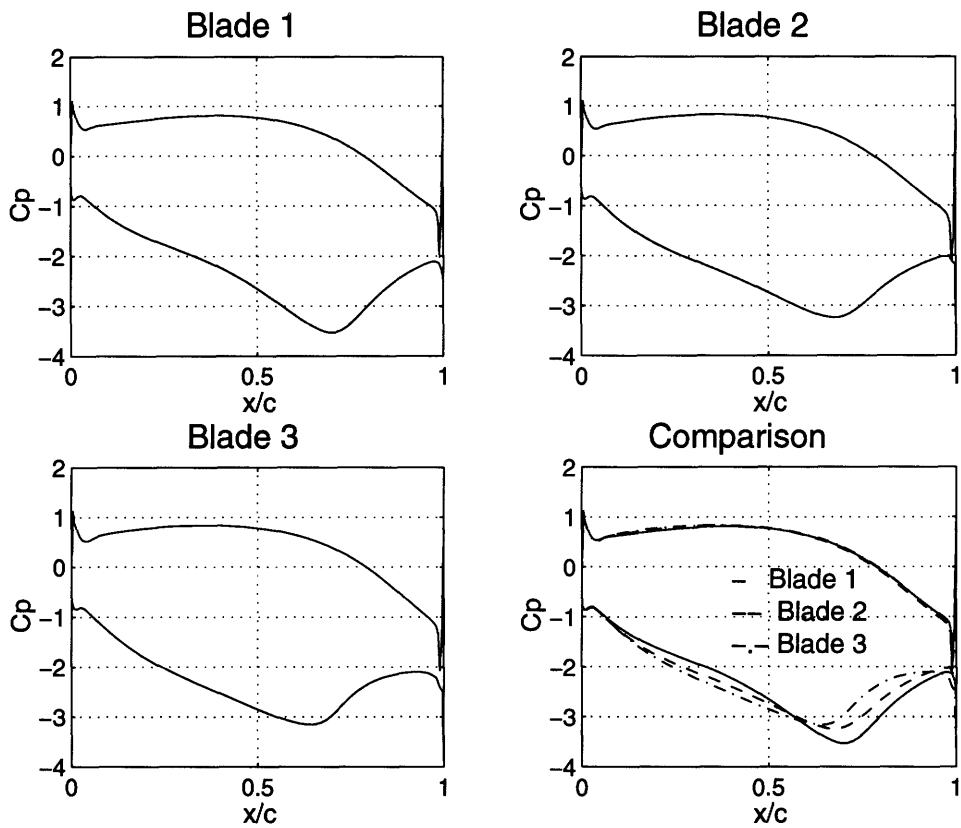


Figure 2-5: Inviscid static pressure coefficient on blade surface, blade 1, 2, 3, and comparison

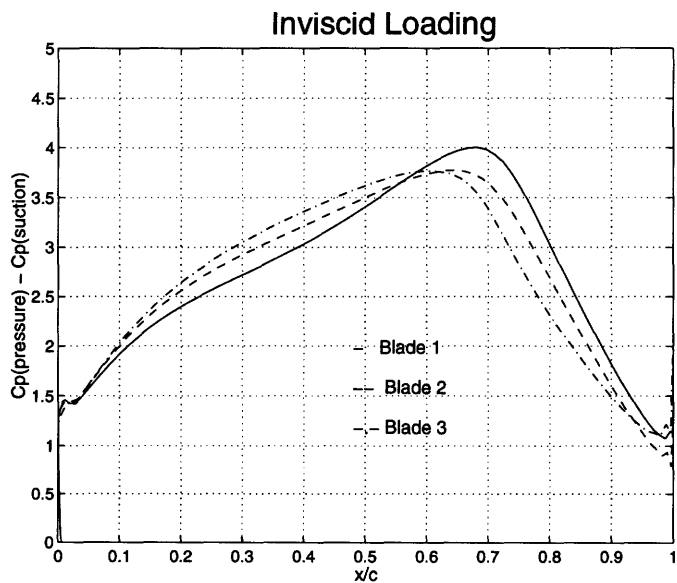


Figure 2-6: Inviscid loading (pressure difference over blade), blade 1, 2, 3

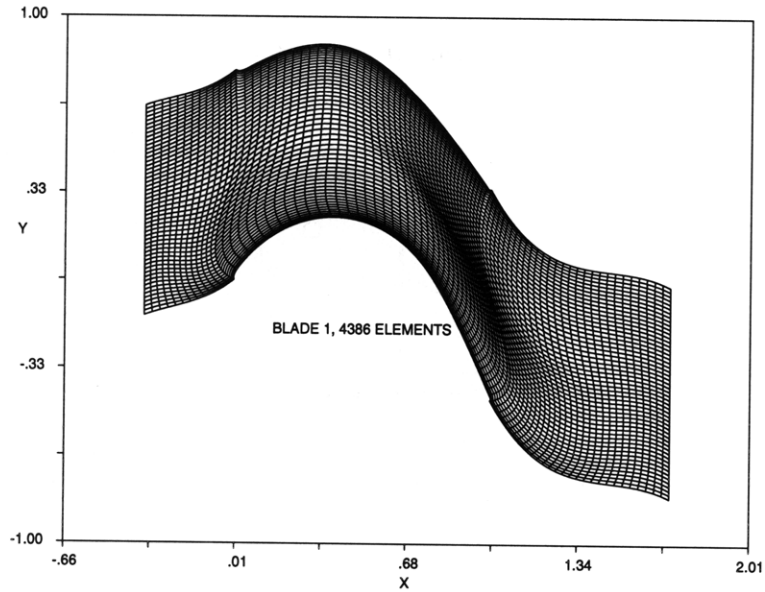


Figure 2-7: Typical high Reynolds number grid

2.3.2 Determination of Time for Solution to Reach Periodicity

The flows that are calculated in this investigation are unsteady in time, due to the dynamics associated with the separated regions. In fact, the reason for doing these calculations is to assess the impact of flow unsteadiness on blade performance. Unlike a steady code, which can be run until a convergence criterion is met, no such criterion can be set for the time varying flows of interest for these computational experiments. Therefore, some measure of the state of the flow must be made in order to :

1. determine a suitable point at which the flow quantities can begin to be averaged
2. reduce the computational time necessary to complete a useful calculation

The initial phases of the flow development consist of the shedding of a starting vortex associated with the production of circulation around the blade (figure 2-8). The starting vortices have a substantial impact on the flow field as they are convected downstream. Thus, the time it takes for the starting vortex to move far enough downstream so that it no longer effects the development of the flow around the blade is of interest. Because the outflow boundary used for all of the solutions is fairly close to the trailing edge plane (0.7 chords away), the characteristic time for the starting vortex to cease to have any influence is of the order of the axial velocity times the distance between the trailing edge and the outflow boundary. The axial velocity is dimensionalized to be $u_x = 1.0$, which corresponds

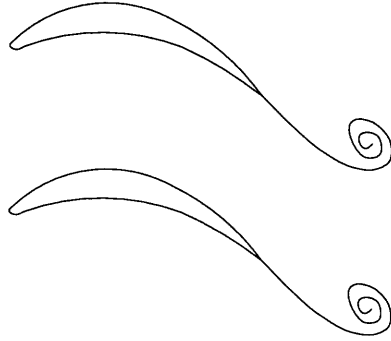


Figure 2-8: Flow field in initial phases of the solution consisting of a starting vortex shed from each blade, with a large influence on the overall flow field

to a characteristic time of $0.7 \text{ } ctu$.

Also, the time for the boundary layers to develop must be accounted for. The characteristic time period for the boundary layers to develop is governed by the time necessary for the diffusion of the vorticity from the blade surface outwards into the freestream. The final boundary layer thickness is determined by the ratio of the convection time to the diffusion time. For the Reynolds numbers of concern in this investigation, the diffusion of vorticity happens on a much slower rate than the convection time, thus the vorticity is convected downstream faster than it can be produced at the solid surface, leading to thin boundary layers.

A conservative estimate of the time needed for the full development of the boundary layers could be obtained by imagining a fluid particle traveling in the boundary layer at $1/2$ the freestream axial velocity, and moving a distance of 1 axial chord. Taking the axial velocity to be equal to 1.0, a convection time of $2 \text{ } ctu$'s is needed for the particle to convect through the passage. Therefore, following this simplistic line of reasoning, the time for the boundary layer to develop is the limiting characteristic time as compared to the time period necessary for the starting vortex to no longer influence the solution.

Two possible methods for determining the time scale for periodic convergence of the solutions were investigated. One method involved looking at the velocity residual. This is the difference between the velocity field from the previous time step from the current. The other uses a time trace of the area-averaged total pressure loss in the wake, with the averaging plane shown in figure (2-9). The area-averaged total pressure is subtracted from the total pressure found at the inflow and then dimensionalized by the inlet total pressure

to create the loss value used for the time trace.

$$\overline{p}_t^{area} = \frac{\int_y^{y+S} p_t dy}{\int_y^{y+S} dy} \quad (2.5)$$

$$Y^{area} = \frac{(\overline{p}_t^{area})_{inlet} - (\overline{p}_t^{area})_{x-station}}{(\overline{p}_t^{area})_{inlet}} \quad (2.6)$$

$$(Y^{area})^{running\ ave} = \frac{\sum_1^N Y^{area}}{N}, \quad N = \text{number of iterations} \quad (2.7)$$

A sample of these two methods is given for *blade 3* at a Reynolds number of 60,000 in figure (2-10). The top plot shows the velocity residual versus time-step, and the bottom plot displays the area-average total pressure versus time-step.

The velocity residual abruptly changes as the magnitude of the time-step is increased. The sharp increase in the residual shown in the top of figure (2-10) at a time-step of 7500 corresponds to such an increase. This jump is not due to any physical phenomena, but is a product of the increased errors that occur when a bigger time-step is used. Even if an equal time step was used throughout, any variations in the flow field are hard to distinguish, as shown for the time-steps greater than 7500. No indication of changing flow dynamics is evident, leading one to believe that the flow had reached some sort of periodic convergence.

On the other hand, the area-averaged total pressure loss in the wake is a more useful quantity (bottom of figure 2-10). The early portion of the time trace shows the development and convection downstream of the starting vortex. Also, the area-average total pressure gives an accurate representation of the flow field, showing the oscillation of total pressure in the wake corresponding to the vortex street convected past the averaging plane.

Thus, this method provides a way to look at the wake development versus time, and the time at which one can begin to use the computed results to obtain the time-average flow quantities is more distinct. This was the method used for all the calculations, with a periodic flow usually obtained after 3 to 4 *ctu*'s. This time period is slightly longer than the time found using the simple arguments at the beginning of this section. A reason explaining this may be related to the lagging behind of the total pressure from other flow quantities

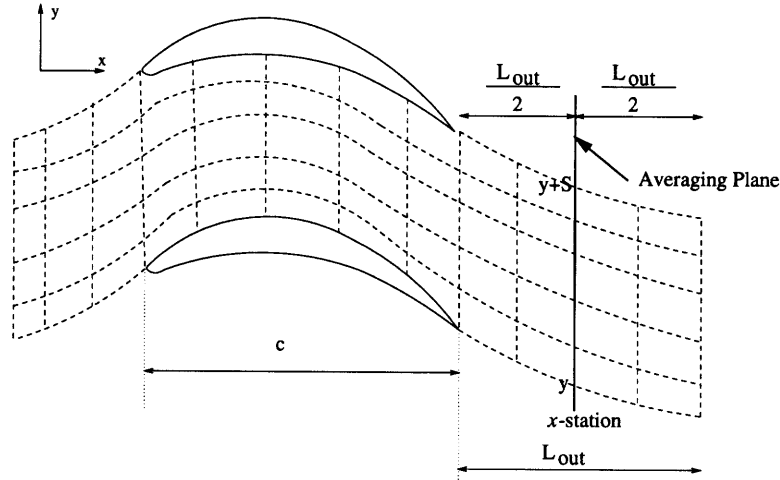


Figure 2-9: Area-averaging plane used to determine convergence

such as the velocity due to the time variations of the solution [13].

2.3.3 Time-Averages

Once the flow has reached a periodic state, a time-average of the primitive variables (u_x, u_y, p_t, ω_z) is initiated, for example :

$$\overline{u_x} = \frac{1}{T} \int_0^T u_x dt$$

The flow fields are typically averaged over 2 to 3 *ctu*'s covering 3 to 5 shedding cycles, depending upon the flow period. These averaged values can then be used to look at the gross features like pressure and skin friction along the blade surface for use in comparisons between the geometries as well as across the range of Reynolds numbers. However, when calculating non-linear quantities, such as mass-averaged total pressure, errors are introduced when the primitive average values are used.

Because of the size of the data sets generated for the primitive values alone, an average of all quantities of concern could not be made. Thus, the non-linear averages, such as the time-averaged total pressure flux at each point :

$$\overline{u_x p_t} = \frac{1}{T} \int_0^T u_x p_t dt$$

are generated using a series of "snapshots" of the flow fields. These pictures were also used to create movies that proved invaluable for the understanding of the unsteady flow phenomena, allowing one to link the graphical data to a series of pictures. The movies

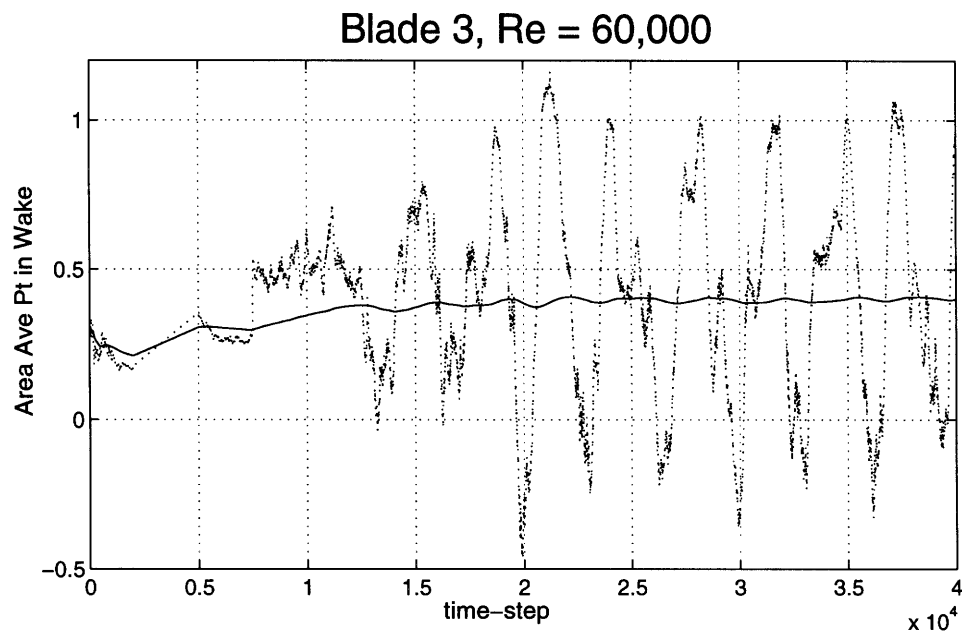
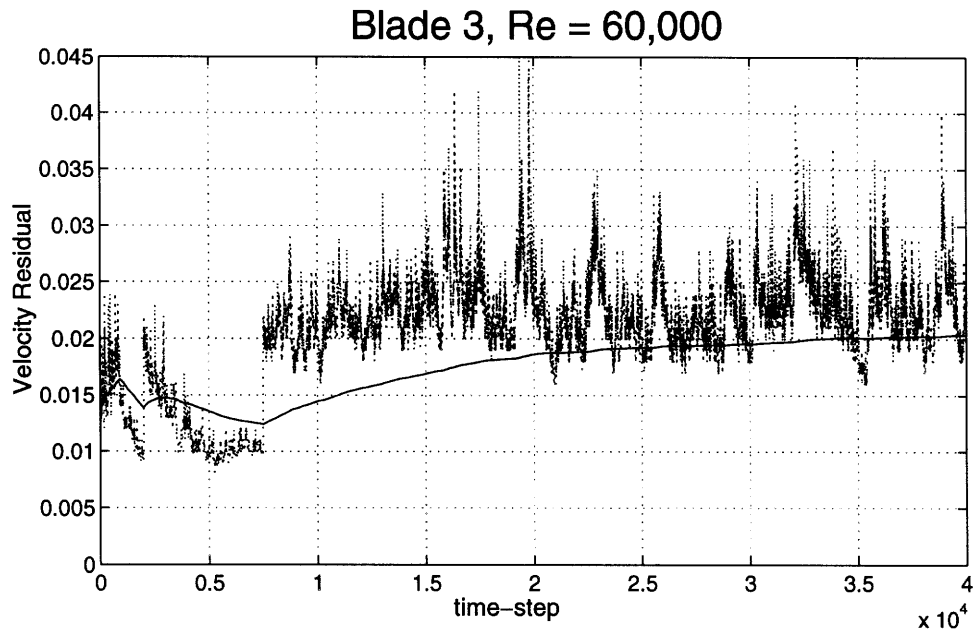


Figure 2-10: Top plot : velocity residual; Bottom plot : area-average versus convective time unit for a typical case, and the running average used for determination of convergence

enable insight into the similarities and differences between the geometries and Reynolds numbers that would not be possible if only a series of plots or graphs were used.

2.3.4 Total Pressure Loss Calculations

The following section details some of the problems associated with calculating a total pressure loss value for the unsteady flows associated with the operation of LPT blades at low Reynolds numbers. The recirculation associated with a separated region, and the noise produced by insufficient resolution are the major causes for concern when trying to extract a total pressure loss for the time-averaged flows. After the discussion of the problems encountered, some of the various methods used to circumvent the difficulties are explained.

Differences from Conventional Loss Calculations

For steady calculations, the determination of the total pressure loss for the stator cascade would pose little problem once the boundary layer profiles have been calculated. A mass-average of the total pressure at the trailing edge could be used to determine the profile loss, and a calculation of the mixed-out flow could be performed to determine a value for the loss far downstream of the blade row.

The mass-averaged total pressure, defined as,

$$\overline{p_t}^{mass} = \frac{\int_{inlet_y}^{y+S} u_x p_t dy - \int_x^{y+S} u_x p_t dy}{\int_y^{y+S} u_x dy} \quad (2.8)$$

is a satisfactory measure of the loss generated in a passage when the flow direction is uniform at a certain x -station. However, if back-flow occurs, as it does in flow separation, the flow direction can cause difficulties when performing a mass-average. This is due to the fact that the returning flow creates a change in the sign of the flux, $\mathbf{u} \cdot \mathbf{n}$, effectively adding total pressure to the flow average, thus skewing the loss measure. This cannot be simply reconciled by taking the absolute value of the flux, $|\mathbf{u} \cdot \mathbf{n}|$, as this would add to the mass flux.

A further complication specific to these calculations is the presence of noise in the vicinity of the pressure side trailing edge region. The abrupt pressure unloading on the pressure side

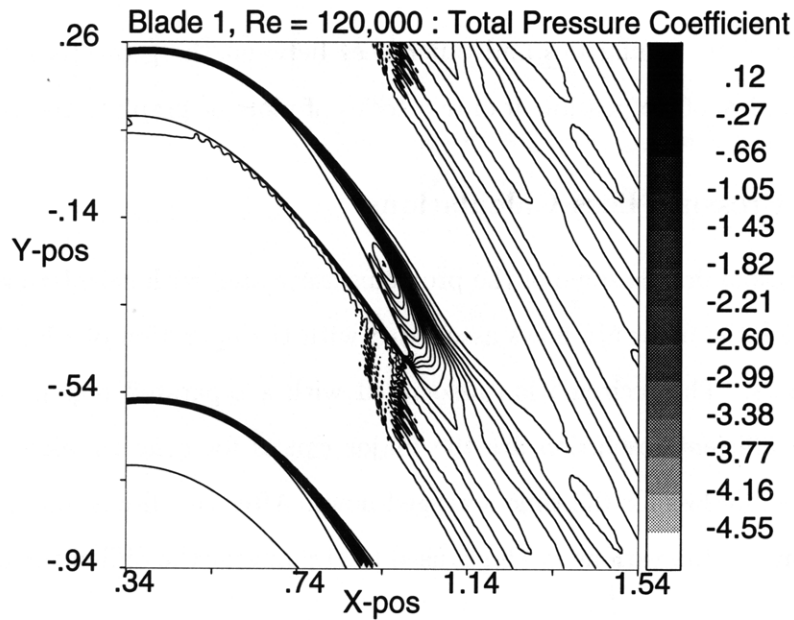


Figure 2-11: Effect of numerical noise on the total pressure coefficient, leading to the convection downstream of the total pressure deficit associated with the noise, Blade 1, Re = 120,000

creates strong gradients in the streamwise direction, amounting to a near discontinuity in the pressure distribution. Representation by a smooth, continuous basis function here inevitably leads to the development of saw-tooth oscillations, the well known Gibb's phenomenon. This noise is present in all calculations, and it creates a region where the total pressure is lower than it would be without the noise. In principle, this noise can be removed using selected cosmetic filtering, but this is not implemented here. Figure (2-11) displays the total pressure coefficient for *blade 1* at an exit Reynolds number of 120,000, indicating the presence of these oscillations. The vorticity, and hence the total pressure deficit associated with the noise convects downstream, complicating the performance calculations for a couple of reasons.

First, the noise produces a total pressure loss of the same magnitude as the loss associated with the pressure side boundary layer. Thus, when a mass-average is performed for x -stations located in this region, an incorrect loss value is obtained. Secondly, the noise convects downstream producing a wake which is wider than expected on the time-averaged basis, leading to problems when calculating the mixed-out total pressure loss.

Methods for Calculating Loss

Procedures to try and overcome the described difficulties had to be developed. One method consists of determining the boundary layer thickness based on the use of the vorticity as an

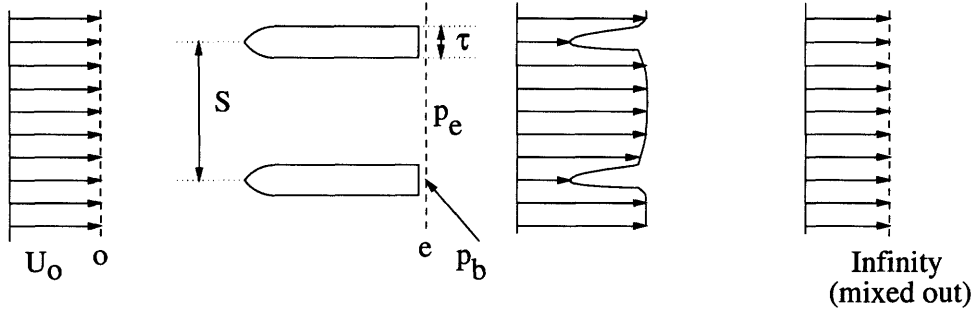


Figure 2-12: Nomenclature used for boundary layer parameters

identifier for the edge of the boundary layer. Then a mass-average is performed as before, only now the limits of integration are set by the boundary layer thickness. This has the advantage that, for the most part, the noise present in the solution is excluded. However, the problem associated with back-flow described earlier still exists.

Alternatively, one can appeal to the use of boundary layer parameters such as displacement thickness, momentum thickness, and energy thickness for calculating loss. It can be shown that the mass-average loss in a boundary layer and the mixed-out loss are related to these parameters by the following equations [6].

$$\frac{p_{t_o} - \overline{p_{t_e}}^{mass}}{\frac{1}{2}\rho U_o^2} = \frac{\delta_e^{**}}{S} \frac{1}{\left(1 - \frac{\tau}{S} - \frac{\delta_e^*}{S}\right)^3} \quad (2.9)$$

$$\frac{p_{t_o} - \overline{p_{t_\infty}}}{\frac{1}{2}\rho U_o^2} = \left[\frac{\frac{\tau}{S} + \frac{\delta_e^*}{S}}{1 - \frac{\tau}{S} - \frac{\delta_e^*}{S}} \right]^2 + \frac{2}{\left(1 - \frac{\tau}{S} - \frac{\delta_e^*}{S}\right)^2} \frac{\theta_e}{S} + \frac{\tau}{S} \frac{C_{p_b}}{\left(1 - \frac{\tau}{S} - \frac{\delta_e^*}{S}\right)^2} \quad (2.10)$$

where $C_{p_b} = \frac{p_e - p_b}{\frac{1}{2}\rho U_e^2}$, δ_e^* the displacement thickness, θ_e the momentum thickness, and δ_e^{**} the energy thickness (figure 2-12).

This also excludes noise, but back-flows again are an issue. Also, the calculation of time-averages for the non-linear quantities such as momentum and energy thicknesses is difficult because of the inability of a boundary layer height to be determined due to the dynamics that occur in the separated region. The momentum thickness and the energy thickness are non-linear, therefore, the two thicknesses must be calculated at every time step, and then time-averaged. But, if the boundary layer height can not be found, such as in the presence of a vortex, the momentum and energy thickness can not be calculated at every time step. All of the flows calculated in this investigation have separated regions dominated by vortices. This exposes the weakness of this method which was developed with

a uni-directional, steady boundary layer in mind.

A final procedure that was investigated was the use of the relation between the total pressure flux and the dissipation due to viscosity. The relation is obtained directly by taking the time-average of the equation describing the factors that influence the total pressure flux.

$$\nabla \cdot (\mathbf{u}p_t) = -\frac{\partial(\frac{1}{2}|\mathbf{u}|^2)}{\partial t} + \frac{1}{Re}\nabla \cdot (\mathbf{u} \times \boldsymbol{\omega}) - \frac{1}{Re}|\boldsymbol{\omega}|^2 \quad (2.11)$$

Assuming periodic flow, the time-average of the dynamic head is zero. Thus equation (2.11) becomes :

$$\nabla \cdot (\overline{\mathbf{u}p_t}) = \frac{1}{Re} \left(\nabla \cdot (\overline{\mathbf{u} \times \boldsymbol{\omega}}) - \overline{|\boldsymbol{\omega}|^2} \right) \quad (2.12)$$

where the overbar denotes a time-average : $\overline{A} = \frac{1}{T} \int_0^T A dt$

Using Gauss' theorem, equation (2.12) can be rewritten as follows.

$$\int_S (\overline{\mathbf{u}p_t}) \cdot \mathbf{n} dS = \frac{1}{Re} \left(\int_S (\overline{\mathbf{u} \times \boldsymbol{\omega}}) \cdot \mathbf{n} dS - \int_V \overline{|\boldsymbol{\omega}|^2} dV \right) \quad (2.13)$$

The second term on the right hand side of equation (2.13) involving $|\boldsymbol{\omega}|^2$, is termed *enstrophy*, and this integral is an order of magnitude larger than the integral involving the $\mathbf{u} \times \boldsymbol{\omega}$ term :

$$\left| \int_V \overline{|\boldsymbol{\omega}|^2} dV \right| \gg \left| \int_S (\overline{\mathbf{u} \times \boldsymbol{\omega}}) \cdot \mathbf{n} dS \right| \quad (2.14)$$

Using typical values found in these calculations, an order of magnitude analysis demonstrates that relation (2.14) holds. The following will show that the vorticity in the boundary layer is of the order of 100, whereas the freestream velocity is only of order 1.

The inlet dimensionalized velocity has a value of $V_{t_{inlet}} = 1.25$, and with a velocity ratio of 1.5 for the passage, the exit velocity, ideally, has a value of $V_{t_{exit}} = 1.88$. The order of magnitude for the vorticity can be found by simply looking at a typical value of $\frac{\Delta u}{\Delta y}$ across the boundary layer. The velocity changes from a value of $u|_{y=0} = 0$ at the wall to a value of, on average (using the mean of the total inlet and total exit velocities), $u|_{y=\delta} = 1.5$ at the boundary layer edge. Using an exit axial chord based Reynolds number of 60,000, a typical Reynolds number based on distance from the leading edge for a point at 1/2 chord, is about

30,000. Using the general relation that the boundary layer thickness varies as $1/\sqrt{Re_x}$, a value for Δy is approximately $\frac{1}{\sqrt{Re_x}} = 0.006$. This process leads to a crude estimation of the average vorticity in the boundary layer of $\frac{\Delta u}{\Delta y} = \frac{1.5}{0.006} = 250$, which is certainly $O(100)$.

Hence, the enstrophy term is of the order of 100^2 , and the convective term, $\mathbf{u} \times \boldsymbol{\omega}$, is of order $(1)(100)$. Thus, the term involving the enstrophy is approximately 100 times greater than the convective term. Therefore the total pressure flux is approximately equal to the volume integral of the enstrophy.

$$\int_S (\overline{\mathbf{u}p_t}) \cdot \mathbf{n} \, dS \approx -\frac{1}{Re} \int_V |\overline{\boldsymbol{\omega}}|^2 \, dV \quad (2.15)$$

Based upon the above analytical analysis, the enstrophy can be used as a method for calculating the total pressure flux over the domain. The advantage in using enstrophy is that since an absolute value of the vorticity is used, the calculation of the total pressure loss does not rely on the flow direction, only on the amount of dissipation. A discussion and comparison of the various performance calculations will be given in appendix (B).

2.3.5 Conventions

All velocities stated are dimensionalized by the inlet axial velocity. The static and total pressure coefficients, and the skin friction are dimensionalized by the total inlet dynamic head.

$$u = \frac{U}{u_{x_{inlet}}} ; v = \frac{V}{u_{x_{inlet}}} \quad (2.16)$$

$$C_p = \frac{p - p_{inlet}}{\frac{1}{2} V_{T_{inlet}}^2} \quad (2.17)$$

$$C_t = \frac{p_t - p_{t_{inlet}}}{\frac{1}{2} V_{T_{inlet}}^2} \quad (2.18)$$

$$C_f = \frac{\tau}{\frac{1}{2} V_{T_{inlet}}^2} \quad (2.19)$$

The total pressure loss (obtained from any of the means described in section 2.3.4) is dimensionalized using the *exit dynamic head*. Since the the exit average dynamic head will vary for the calculations because of the changing separation dynamics, the exit dynamic head will be held constant using the approximate gas angles given in section (2.2). This gives an exit total velocity of 1.5 times that of the incoming total velocity. Thus, for

example, if a mass-average loss is calculated, the ideal exit dynamic head will be used for non-dimensionalization in order to conform to the standard dimensionalization for a turbine.

$$\frac{\overline{p_{t_{in}}^{mass}} - \overline{p_{t_x}^{mass}}}{\frac{1}{2}V_{T_{exit}}^2} \quad (2.20)$$

Finally, all Reynolds numbers quoted are calculated using the axial chord and exit total velocity (*1.5 times the inlet total velocity*).

$$Re = \frac{V_{T_{exit}} c}{\nu} \quad (2.21)$$

Now that the basic tools and methods used for this research have been described, a presentation of the results obtained for the three geometries at the various Reynolds numbers is given in the next chapter. The sections are split into the lower Reynolds number solutions, followed by the higher Reynolds numbers, with both the time-average and unsteady features described.

Chapter 3

Presentation of Computed Results

3.1 Chapter Overview

The computed results to be presented in this chapter are categorized broadly into two groups :

1. the “low” Reynolds number solutions with exit Reynolds numbers of 20,000 and 30,000
2. the “high” Reynolds numbers solutions with exit Reynolds numbers of 60,000, 90,000, and 120,000

This categorization is based on the observed difference in the flow dynamics between the low and high Reynolds number solutions. The presentation for each Reynolds number case is subdivided further into two sections, one corresponding to the time-averaged flow fields, and the other to the unsteady flow dynamics.

The matrix of computed results for the three different geometries is given in table (3.1). The completion of the full proposed set of cases was not obtained due to time and resource limitations. Although the lower Reynolds number solutions are of little relevance to the regimes found in LPT operation, they were nevertheless useful for assessing the effects of Reynolds number on flow processes that determine separation and re-attachment. Emphasis was placed upon obtaining solutions for *blade 1* and *blade 3* because these two geometries have the largest difference in design.

Also, computations were performed to determine the influence of the inflow and outflow boundaries on the solutions. All of the cases shown in table (3.1) used an inflow boundary located 0.35 chords from the leading edge of the blade, and an outflow boundary at 0.7

Reynolds Number	20,000	30,000	60,000	90,000	120,000
Blade					
1	•	•	•	•	•
2	•	•			
3	•	•	•		•

Table 3.1: Matrix of solutions obtained for the three geometries for the range of exit Reynolds numbers from 20,000 to 120,000

chords downstream of the blade trailing edge. To assess the importance of the computational boundary placement on the solutions, a set of two configurations were investigated. The results of this investigation are given in appendix (A).

As the goal is to obtain an appreciation of those aspects of the flow field that set the LPT performance, the computed results are presented so as to elucidate the following :

1. the magnitude of the adverse pressure gradient, thus the blade geometry, plays a role in the shear layer roll-up process (associated with flow separation on the blade suction side)
2. the change in Reynolds number effects the location of shear layer instability

The time-average flow and blade performance are characterized in terms of :

- i. time-averaged total velocity and static pressure fields : these are used to assess the similarities and differences in the computed time-average flow structure, and to determine the extent to which the separated region influences the overall flow
- ii. time-averaged static pressure coefficient, C_p , and skin friction coefficient, C_f : these are examined to infer the impact the difference in loading for each blade has upon C_f and the implications the design parameters have upon the profile loss
- iii. total pressure losses : this is used as a figure of merit to rank the blades in terms of the amount of blade profile and mixed-out loss

Following the time-averaged results, the unsteady features associated with each solution will be presented to show :

- i. the temporal variation of area-averaged total pressure loss in the wake in terms of the frequency and amplitude content

- ii. shear layer roll-up position
- iii. the envelopes bounding the temporal variation in the blade surface static pressure
- iv. the relative amplitude of laminar and time-average Reynolds stress dissipation coefficients

These variables give a measure of the extent the flow unsteadiness influences the blade performance metrics, i.e., the load transferred to the blades and the associated total pressure loss generated by the blade boundary layers.

An appreciation of these unsteady features could potentially enable us to understand time-averaged flow behavior, as well as allowing one to predict the development of the separated shear layer as Reynolds number changes and as blade geometry changes for identical gas flow angles.

The implications of the computed results, such as trends that can be related to blade design, loss variation as a function of separation dynamics, and the effects of unsteadiness on the suction side boundary layer will be discussed in chapter (4).

3.1.1 Postprocessing of Results

Any attempt to establish a link between the time-average flow and the flow unsteadiness requires the examination of the unsteady flow features. For this reason, emphasis was placed upon acquiring a set of “snapshots” detailing the essence of the unsteady character of the solutions.

Each time-averaged flow was computed from the unsteady flow over a time interval of at least $2\ ctu$ (the lowest shedding frequencies encountered for these sets of solutions was about $1.5\ ctu^{-1}$, which translates into an averaging time covering about 3 flow periods). The time-averaging was accomplished using the flow field at every 5 time-steps (with the time-step size being $0.0002\ ctu$), so as to incorporate any flow unsteadiness that may influence the time-average.

The previously described “snapshots” were simply a saving of the flow variables (velocity, pressure, and vorticity) at a sampling frequency corresponding to $0.03\ ctu$. Again this was done to insure that the important unsteady features are duly accounted for. An important use of these unsteady flow variables was the creation of a series of movies for each solution. A movie was made for the static pressure coefficient, the total velocity, and the vorticity;

each movie consisted of about 25 “snapshots”, thus covering about 0.75 *ctu* (at least one flow period). These movies proved invaluable for obtaining an appreciation of the unsteady flow features that impact the blade performance.

3.2 Low Reynolds Number Solutions

The results given in this section correspond to the solutions obtained at exit Reynolds numbers of 20,000 and 30,000 for all three blade geometries. Although these solutions are for Reynolds numbers that are low compared to those in the normal operation of a LPT, the results are useful for assessing/quantifying the change in the flow separation with Reynolds number, as well as for investigating the effects of Reynolds number on the performance characteristics of the various designs. These low Reynolds number cases also serve as a test bed for the spectral code. The ability for the code to discriminate/differentiate changes in flow structure associated with nominal changes in blade profile would be of value to the blade designer. Therefore to demonstrate that the code would be useful at LPT operating Reynolds numbers, it must first be shown that this code can capture the changes in flow processes associated with changing blade design, at these low Reynolds numbers in the very least.

3.2.1 Time-Average Solutions at $Re = 20,000$

Presentation of computed results at $Re = 20,000$ will serve to set up the overall framework for the analysis of these complex flow fields. Such a framework will be used to postprocess and present results at all other Reynolds numbers for these three blade geometries.

3.2.2 Total Velocity and Static Pressure Contours at $Re = 20,000$

The time-averaged total velocity and static pressure coefficient contours of the three geometries at an exit Reynolds number of 20,000 are given in figure (3-1). These contour plots are useful for the overall comparison between the three geometries; any major difference in the unsteady nature of the flow (of engineering interest) should be reflected in the time-averaged quantities. The static pressure contours provide a more transparent interpretation of the flow field behavior than the total velocity, but the velocity contours are given as well so an appreciation for the overall flow features can be had.

All the blades exhibit a pressure side separation bubble as well as a separation of the suction side boundary layer. The boundary layer leaves the blade nearly tangential to the surface, with the pressure side shear layer re-attaching. However, the suction side shear layer remains separated for the entire length downstream of the separation point for all three blades.

One of the differences between the geometries is seen by looking at the pressure contours found in the separated regions of the blades. The portions of the blades with flow separation are characterized by a nearly constant pressure region extending from the blade surface through the shear layer. Any variations of the static pressure in the separated region are an indication of a difference in the unsteady flow processes.

Thus, an inference can be made from the pressure contours for *blade 1* in the trailing edge region that there must exist a dynamical structure causing a localized gradient in the pressure.

The cause for the pressure gradient is a vortex located very close to the trailing edge on the time-averaged basis (figure 3-2), with a low pressure region in the vortex core and an increase of pressure as one moves outward from the vortex center. *Blade 2* also shows the same type of localized pressure gradients near the trailing edge, but it is not as organized as for *blade 1*. Finally, *blade 3* shows signs of a vortex in the separated region (figure 3-3), but it has even less of an effect on the pressure distribution in the trailing edge region than the vortex present for *blade 2*.

As alluded to in the above, *blade 1* has the largest inviscid adverse pressure gradient, with *blade 3* having the smallest. Thus, a plausible explanation for the difference in the time-averaged static pressure contours can be linked to the magnitude of the pressure gradient in the aft portion of the blade. The explanation of these observations are directly linked to the unsteady shedding process, and will be described in detail in section (3.2.6).

A second difference seen from the pressure contours relates to the extent of effective flow blockage associated with each separated region in the trailing edge plane. At the $x/c = 1.0$ plane, the separated flow constitutes a substantial fraction of the exit area for all cases; this would result in higher core flow velocities. An estimate of the fraction of the suction side separated region can be obtained from the time-averaged vorticity contours (see figure 3-4). The computed vorticity distribution and the viewing of the set of total velocity movies made at this Reynolds number for all three blades give the indication that the flow separation for

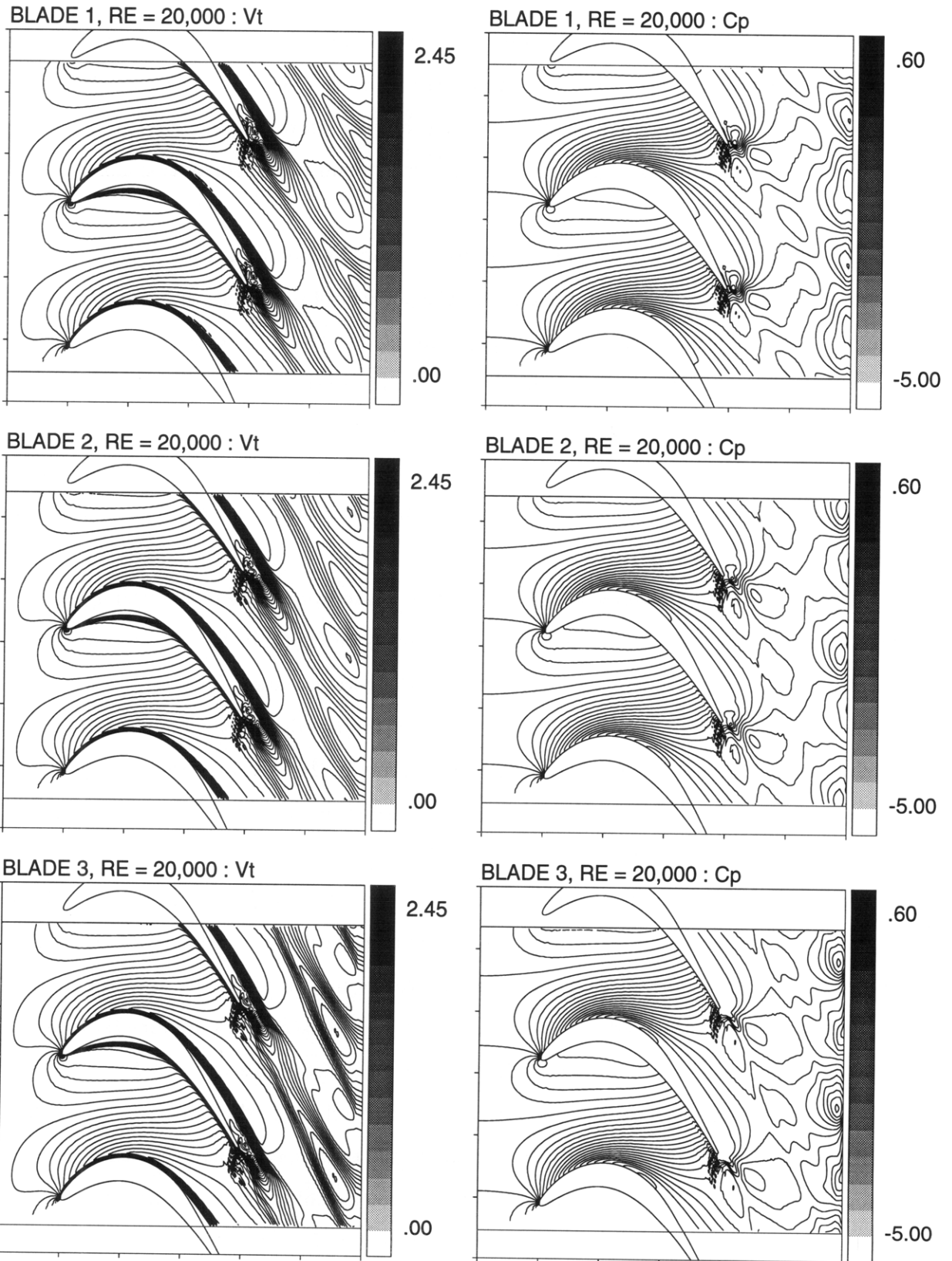


Figure 3-1: Time-averaged total velocity and static pressure coefficient contours for all blades at $Re = 20,000$, illustrating suction side flow separation and a separation bubble on pressure side

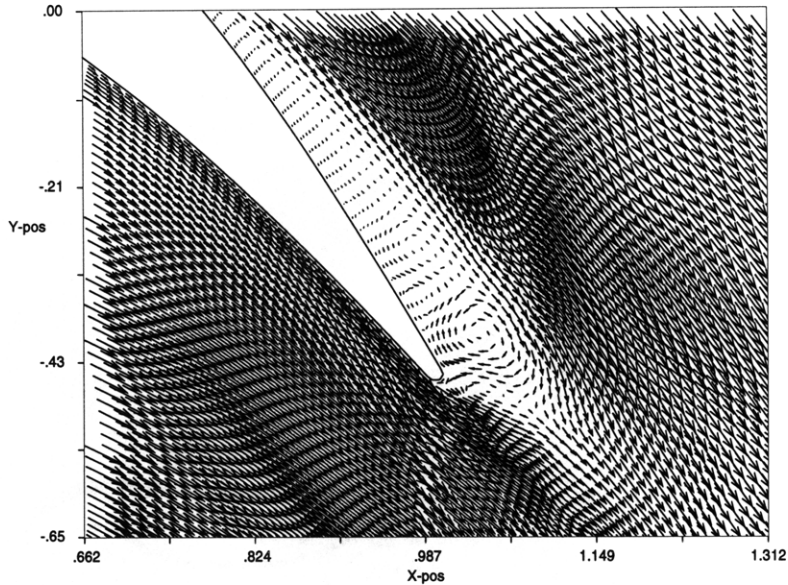


Figure 3-2: *Blade 1*, $Re = 20,000$, time-averaged velocity vectors indicating presence of a vortex at the trailing edge region

blade 1 constitutes a larger fraction of the exit flow area than that for *blade 3*.

The stronger inviscid pressure gradient in the aft region of *blade 1* over that for *blade 3* could plausibly explain the higher value of blockage at the trailing edge plane for *blade 1*.

3.2.3 Surface Static Pressure Coefficient and Skin Friction at $Re = 20,000$

The surface pressure distribution is of interest as this sets the loading distribution on the blade. More importantly the surface pressure reflects the state of the blade surface boundary layer, with regions of separation being identified by nearly zero pressure gradient.

The time-average static pressure coefficient over the blades is given in figure (3-5), with the lower curve representing the suction side pressure and the upper the pressure side. These plots show the presence of the separated region on the trailing portion of all blades, as indicated by the nearly constant pressure region at these locations. The pressure side has nearly zero pressure gradient for x/c from 0.1 to about 0.6; this is a result of the separation bubble extending from $x/c = 0.1$ to $x/c = 0.6$. Likewise, the static pressure remains essentially constant on the suction side downstream of the separation point.

The skin friction also reflects the behavior of the blade surface boundary layer. It assumes a value of zero at the separation points and becomes negative when areas of recir-

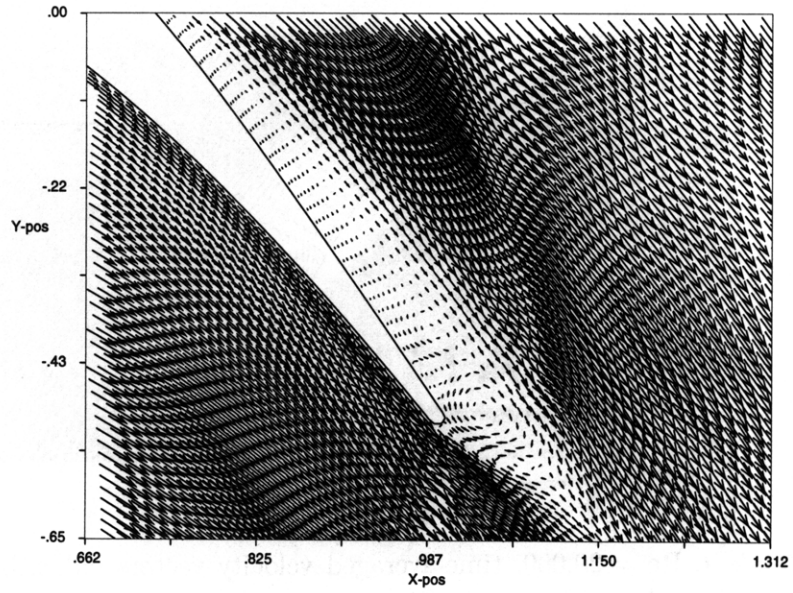


Figure 3-3: *Blade 3*, $Re = 20,000$, time-averaged velocity vectors indicating presence of a vortex at the trailing edge region

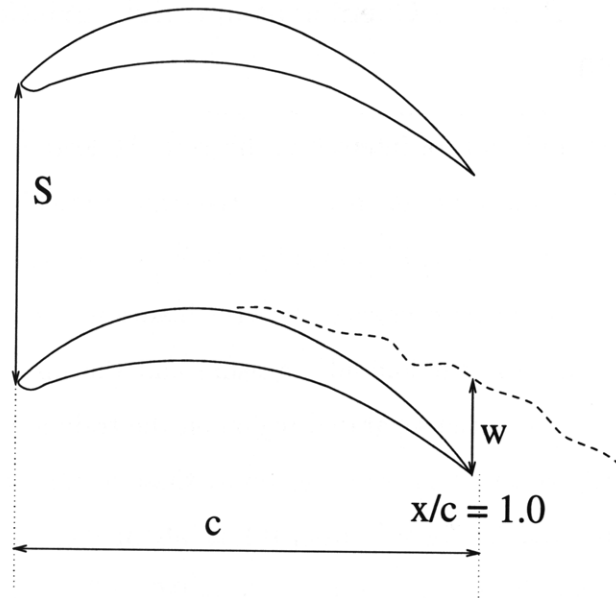


Figure 3-4: Nomenclature for separated region used in calculating the percentage of blockage, w/S

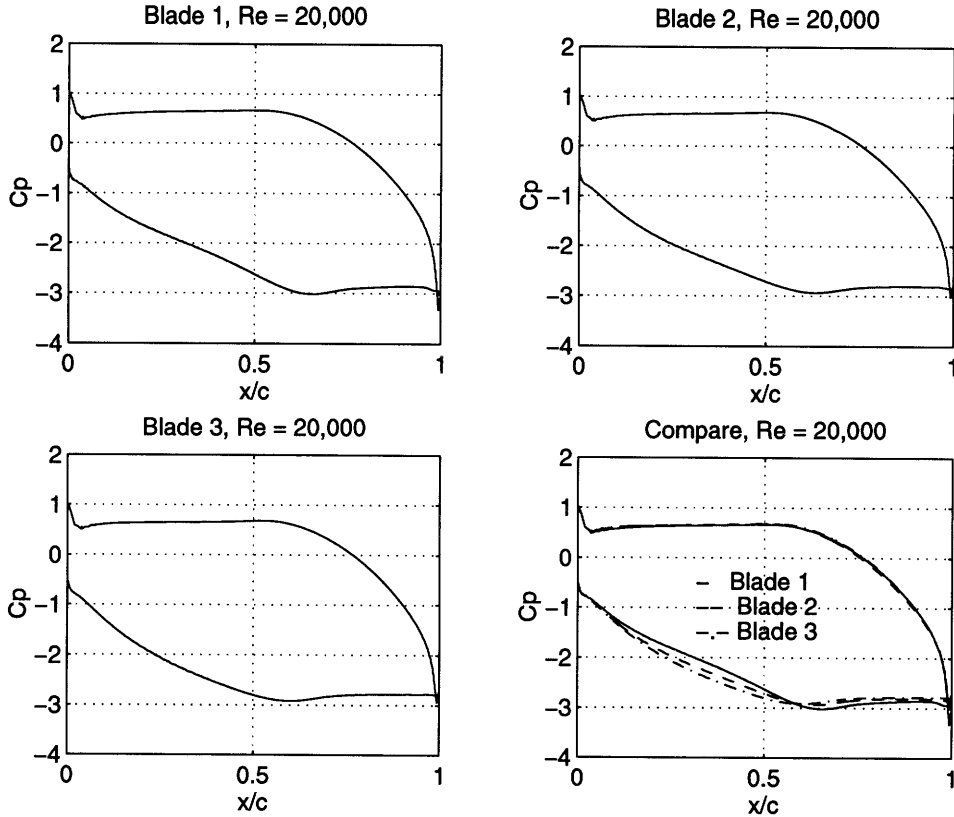


Figure 3-5: Time-averaged static pressure on the blade surface for $Re = 20,000$

ulation are present.

Skin friction serves as a measure of entropy production, i.e.

$$\dot{S} = \int_0^\delta \frac{1}{T} \tau_{xy} dV_x \quad (3.1)$$

Higher skin friction corresponds to larger shear, which is directly related to higher rates of entropy production.

The blade surface skin friction distribution is shown in figure (3-6); a composite plot is also presented for purpose of contrasting among the 3 blade designs. The skin friction comparison shows that *blade 3* has a larger pressure side separation bubble; this is most likely a result of the relatively smaller radius of curvature found for *blade 3* (figure 3-7) as compared to *blade 1*. Thus, this smaller radius of curvature translates into a stronger adverse pressure gradient for the pressure side leading edge for *blade 3*, leading to an earlier separation of the pressure side boundary layer for *blade 3*.

Blade 3 also separates on the suction side earlier. This could be inferred through the

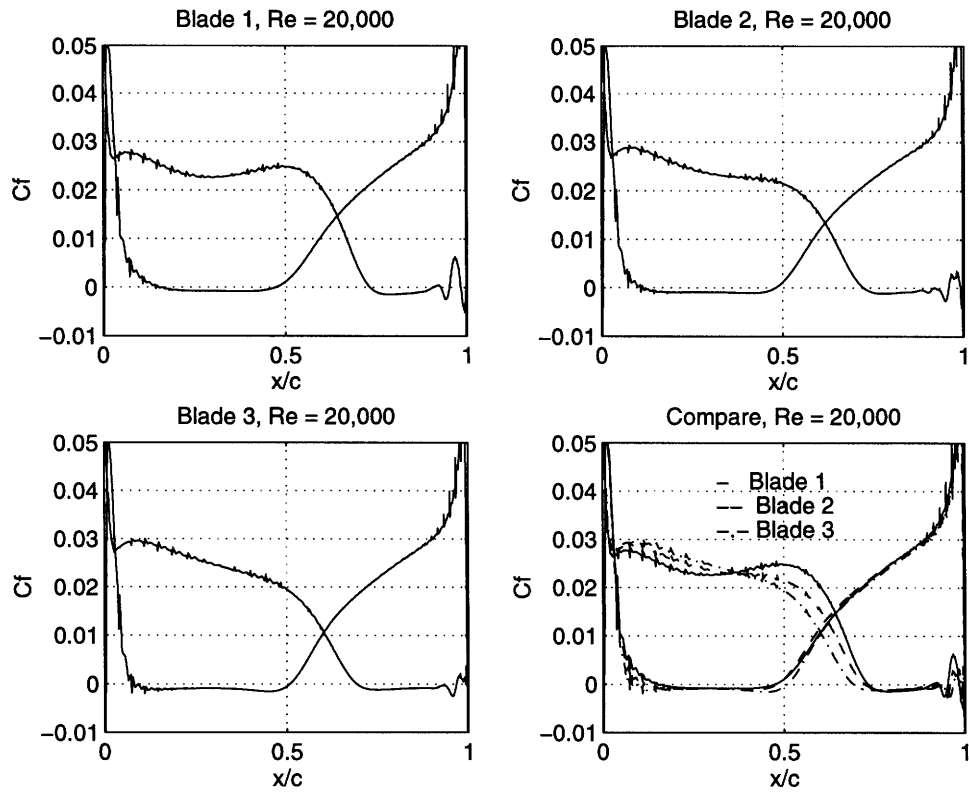


Figure 3-6: Time-averaged skin friction on blade surface for $Re = 20,000$

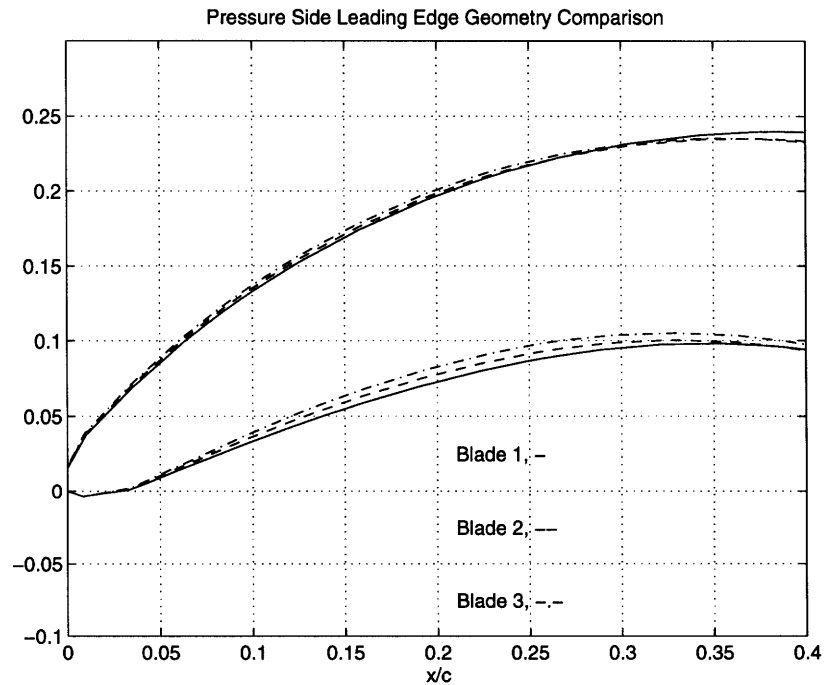


Figure 3-7: Comparison of leading edge geometry for the pressure side, showing the smaller radius of curvature for *blade 3* than for *blade 1*

inviscid surface pressure distribution in figure (2-5), where *blade 3* has its minimum pressure point furthest upstream. Using the point where the skin friction becomes zero as a point of separation/re-attachment, figure (3-6) shows that *blade 3* separates on suction side earlier than *blade 1* and *blade 2*.

This subsection has demonstrated the use of the surface static pressure as a tool in the determination of the extent of boundary layer separation. The static pressure can also be used to determine the loading on each blade, and thus can serve as a tool for comparison between the three geometries.

The skin friction was shown to produce much of the same information relating to the length of separated regions as the C_p plots did. In addition, the time-averaged C_f can be used to determine the point of time-average separation, as well as to serve as a link between the state of the boundary layer and entropy production.

3.2.4 Total Pressure Loss at $Re = 20,000$

This subsection presents the determination of loss for each design. To start with, we will examine the variation in the dissipation coefficient with Reynolds number, and its impact on entropy production. This will be followed by an assessment of loss levels for the various designs and an establishment of the link between the observed loss level and computed flow features. Finally, a discussion on the magnitude of the mixed-out loss compared to the profile loss for these low Reynolds number solutions will be given.

Thus, the determination of the total pressure loss incurred in the passage can be computed from any one of the following :

- i. mass-averaging the time-averaged total pressure at the trailing edge plane; or
- ii. entropy; or
- iii. mixing-out of the flow at the blade trailing edge at a constant area

Dissipation Coefficient

The utility of using the dissipation coefficient and its variation with momentum thickness Reynolds number is given in this subsection. This coefficient is of use for both the time-averaged flows as well as a way to determine the effect of flow unsteadiness on the dissipation.

The skin friction comparison between the three blades (figure 3-6) indicates larger values of C_f in the forward region of the blade on the suction side for *blade 3* than *blade 1*, with a switch in this trend at an axial distance of about $x/c = 0.4$. This indicates that *blade 3* has larger velocities on the suction side in the first four tenths of the blade, which can thus be related to a larger rate of entropy production as will be shown next.

The rate of entropy production as a function of the freestream velocity can be investigated by looking at a “dissipation coefficient”, C_d . This coefficient can be defined using the rate of entropy production per unit surface area, \dot{S} [4].

$$\dot{S} = \int_0^\delta \frac{1}{T} \tau_{xy} dV_x \quad (3.2)$$

The dissipation coefficient is then given as

$$C_d = \frac{T\dot{S}}{\rho U_e^3} \quad (3.3)$$

Denton [4] explains how the dissipation coefficient is fairly insensitive to changes in the state of the boundary layer at Reynolds numbers based on momentum thickness, Re_θ , greater than 500. He references Schlichting [12] on the correlation of experimental data leading to the following variation of C_d with Re_θ .

$$C_{d_{t,u,v}} = 0.0056 Re_\theta^{-1/6} \quad (3.4)$$

$$C_{d_{laminar}} = \beta Re_\theta^{-1} \quad (3.5)$$

The value of β varies minimally with the state of the boundary layer, i.e. with the shape factor, and it has a typical magnitude of about 0.17. The form of the dissipation curves versus Re_θ is given in figure (3-8), with the value of β taken as 0.173 (an analytical result found for a boundary layer without a pressure gradient [4]). It should be noted that above $Re_\theta \approx 200$, C_d varies little for either turbulent or laminar boundary layers.

Thus, a small variation of the dissipation coefficient at momentum thickness Reynolds numbers above about 200 implies that the rate of entropy generation per unit surface area is largely dependent upon the magnitude of the freestream velocity. Using equation (3.3), the entropy production is shown to be proportional to the cube of the velocity when C_d is

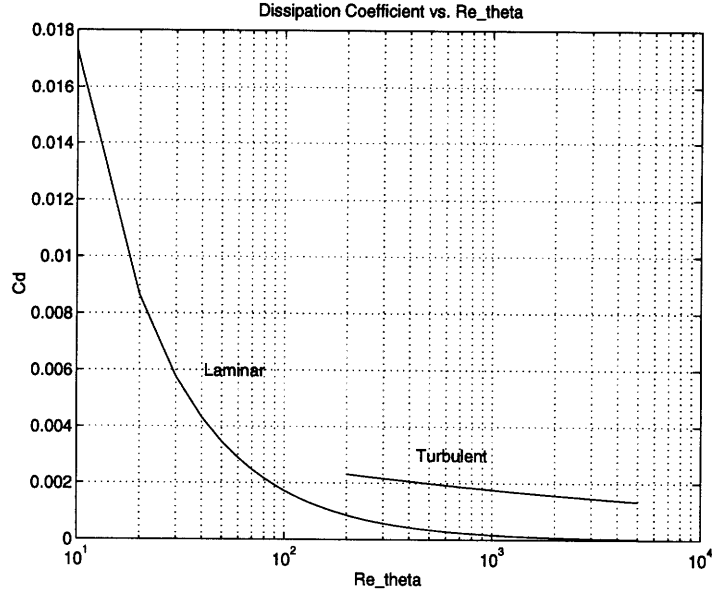


Figure 3-8: Variation of the dissipation coefficient with momentum thickness Reynolds number, laminar and turbulent, after [4]

nearly constant, i.e.

$$\dot{S} = \frac{C_d \rho U_e^3}{T} \quad (3.6)$$

This is the basis for the statement that the larger suction side velocities over the forward portion of *blade 3* as compared to *blade 1* should lead to higher entropy production.

The freestream velocity, U_e , for the suction and pressure surfaces is compared for the three blades in figure (3-9) at Reynolds number of 20,000. This demonstrates that *blade 3* has higher freestream velocities in the forward portion of the blade. The lower pressure over the forward portion of *blade 3* (compared to *blade 1*) results in a correspondingly higher velocity. Likewise, the skin friction for *blade 3* is the largest in magnitude.

The above arguments show that the rate of entropy production should be higher for *blade 3* than for *blade 1*. It can be shown for low speed flows, where incompressibility can be assumed, that the flux of entropy is proportional to the flux of total pressure.

$$\nabla \cdot (\mathbf{u}s) = -\frac{R}{p_t} \nabla \cdot (\mathbf{u}p_t) \quad (3.7)$$

Therefore, the increased rate of entropy production for higher flow velocities should translate into larger losses of total pressure for *blade 3* over *blade 1*. This is indeed the case as shown

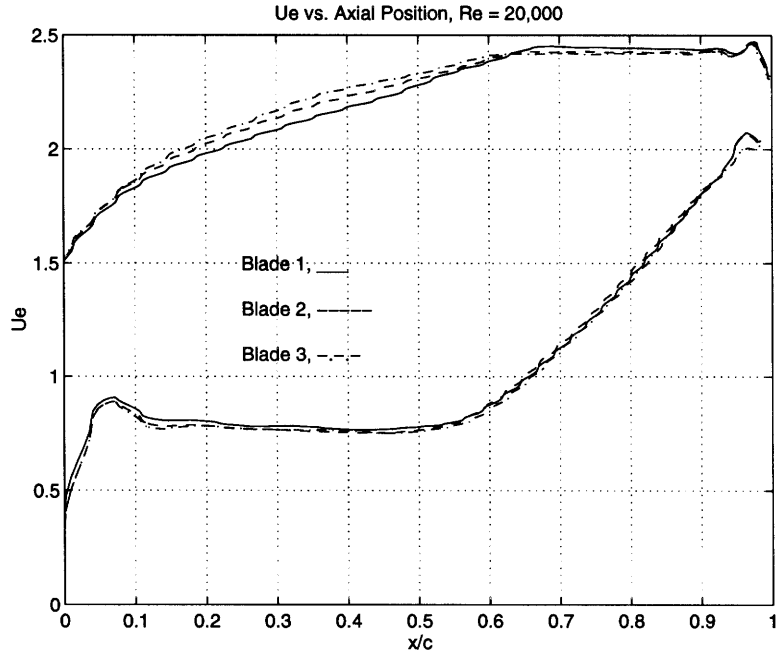


Figure 3-9: Freestream velocity versus axial position, comparison for the three geometries at exit Reynolds number of 20,000

in figure (3-10), where the mass-averaged total pressure loss on the suction and pressure sides of the blade is plotted for all three geometries. Relatively smaller loss is generated on the pressure side until the trailing edge region where the velocity increases rapidly. The suction side is the major source of loss in the passage. Figure (3-10) displays the fact that *blade 3* has a higher profile loss over most of blade as compared to the other geometries. In the trailing edge region, the trends switch slightly, with *blade 2* ending with the highest value of loss. As explained in chapter (2), the calculation of a mass-averaged quantity is hampered when regions of back-flow exist, as occurs for these solutions. Therefore, the value of loss obtained in the trailing edge region must be viewed with skepticism.

Loss Calculated Using Enstrophy

Another method, which was shown in chapter (2) to be approximately equivalent, at least analytically, to the total pressure loss, involves the integration over the control volume of the dissipation occurring in the passage.

$$\int_S (\overline{\mathbf{u} p_t}) \cdot \mathbf{n} dS \approx -\mu \int_V \overline{|\boldsymbol{\omega}|^2} dV \quad (3.8)$$

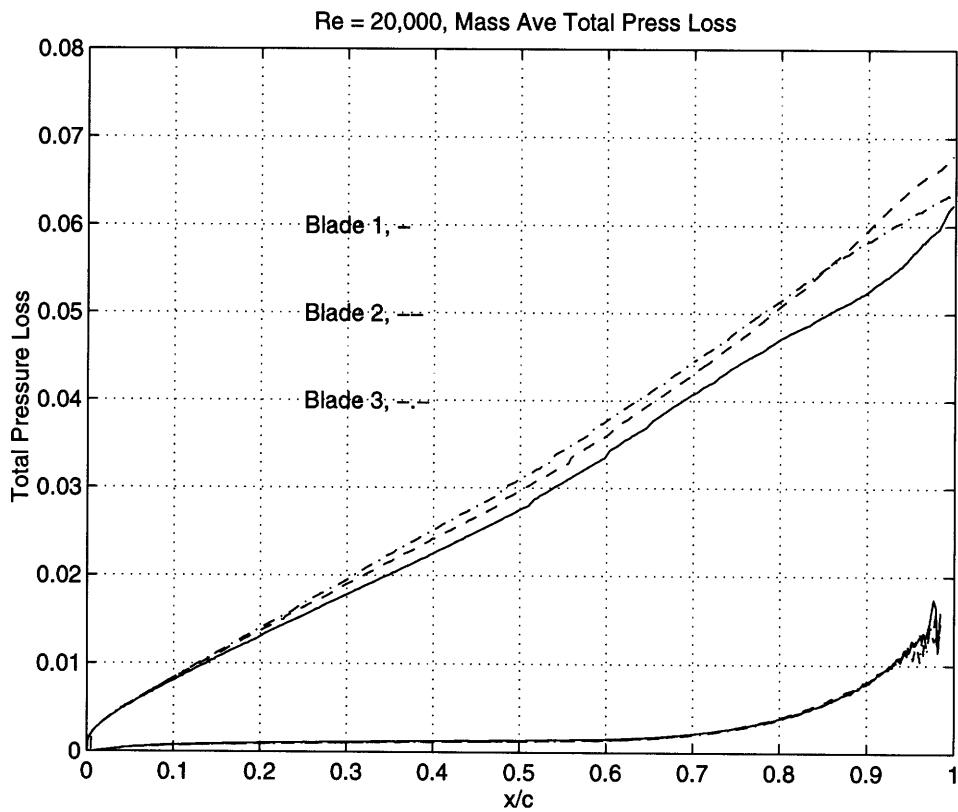


Figure 3-10: Mass-averaged total pressure loss, dimensionalized by exit dynamic head, for the suction and pressure sides at a Reynolds number of 20,000; majority of the loss occurs on the suction side, and *blade 3* has a higher loss value just until the trailing edge region

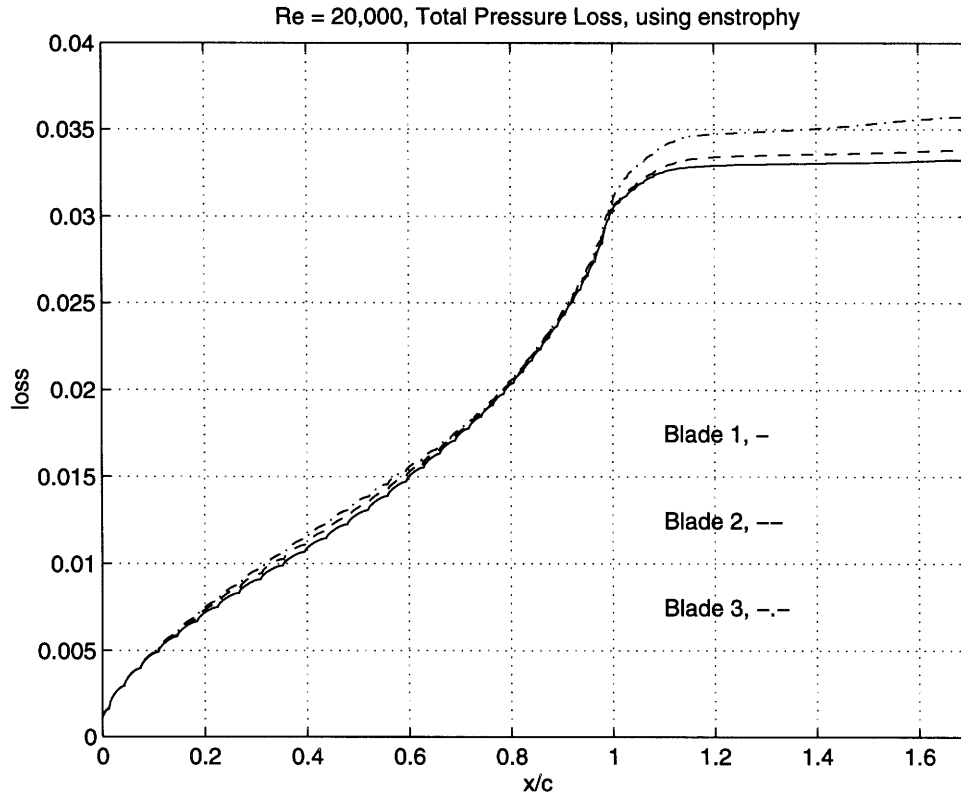


Figure 3-11: Loss for all three geometries, calculated using enstrophy at $Re = 20,000$

When the right hand side of the above equation is divided by the mass flux, a mass-averaged total pressure loss is obtained. The quantity on the left hand side, termed enstrophy, is plotted in figure (3-11) for the three geometries.

The loss calculated using enstrophy shown in figure (3-11) again conveys that *blade 3* has higher loss than *blade 2* or *blade 1*. The use of enstrophy bypasses the problems encountered in the mass-averaging technique when recirculation occurs.

A concern is that the loss calculation using the enstrophy gives values of total pressure loss that are approximately 1/2 of those predicted using mass-averaging (for this $Re = 20,000$ case), although the trend of *blade 3* having the highest amount of loss remains the same. This topic is further discussed in appendix (B).

Importance of Mixed Out Loss

As of yet, nothing has been said of the magnitude of loss resulting from the suction side separation. Denton [4] points out that a large amount of additional loss is generated by the mixing downstream of a separated blade. He reasons that if the base pressure coefficient,

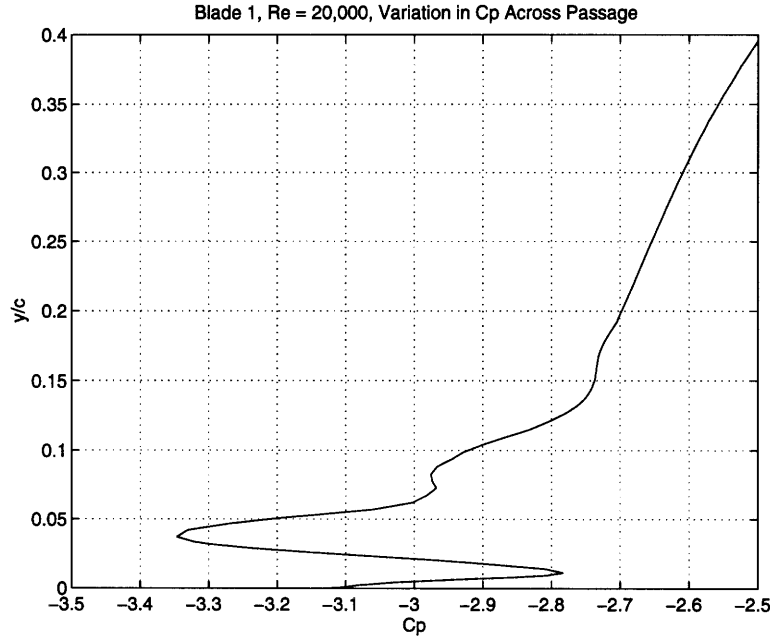


Figure 3-12: Variation in the static pressure across the blade passage at the trailing edge plane for blade 1, $Re = 20,000$, showing that the pressure is not constant within the separated region

$C_{pb} = \frac{p_e - p_b}{\frac{1}{2}\rho U_e^2}$ (reference figure 2-12), is assumed to be zero, the extra loss added because of the separated region is given by :

$$\left(\frac{p_{t_o} - \overline{p_{t_e}^{mass}}}{\frac{1}{2}\rho U_o^2} \right)_{separation} = \left(\frac{\delta_e^{*2} + 2\tau\delta_e^*}{S^2} \right) \quad (3.9)$$

The assumption that the static pressure is the same in the separated region as it is in the freestream, i.e. $C_{pb} = 0$, is not very good, especially when looking at the time-average pressure across the blade passage (given in figure 3-12). The time-average vortex located in the trailing edge region is the cause for the pressure variation seen across the separated region, and thus hampers the mixing calculation.

For example, Denton shows that a separation resulting in 10% blockage only adds 1% to the total pressure loss when equation (3.9) is used, which does not correspond to the high values of loss seen for a separated boundary layer. Therefore, to account for the higher loss, Denton acknowledges the fact that the base pressure is most likely non-zero, and that it should be included in the loss calculation to make up the additional loss seen in test data.

Equation (3.9) does indicate that the greater the blockage, the greater the additional

mixed-out loss due to the separation will be. As alluded to in the above, *blade 1* has a slightly higher value for the blockage, w/S , than *blade 3*, and thus one can assume the mixed out loss will be greater for *blade 1*. Therefore, it is entirely possible that *blade 1* has a larger value of total loss, even though it has a smaller value of profile loss relative to *blade 3*.

Taking a typical value of displacement thickness for the three blades of $\delta_e^* = 0.1$ (found using the time-averaged velocity profile at the trailing edge), a trailing edge thickness, τ , of 0.01 *chords*, and a value for S of 0.42 (reference figure 3-13), results in a loss due to mixing of 0.068.

Comparing this to the value of profile loss found for the blades (figure 3-10) which was on the order of 0.065, the mixing out of the separated region produces a loss that is nearly equal to that produced within the passage, and this is without including the base pressure term in the mixing calculation. The inclusion of the base pressure term is not done because it is unclear as to what pressure to use for the separated region, especially considering that the mixing of the wake is actually the mixing out of individual vortices, and not the mixing of a simple velocity defect.

Therefore, a true evaluation of the performance for these geometries, especially for the highly separated cases found at the lower Reynolds numbers, can not be made unless an accurate measure of the total mixed-out loss is used.

The magnitude of the aft adverse *inviscid* pressure gradient appears to set the blade performance. The more adverse the gradient, the thicker the separated region, and thus, as crudely demonstrated in this section, the larger the total mixed-out loss. Therefore, although the aft loaded blade (*blade 1*) incurs a lower total pressure loss in the forward portion of the blade due to lower freestream velocities, the more severe inviscid pressure gradient (as compared to *blade 3*) may very well cause the mixed-out loss to be greater for *blade 1*.

3.2.5 Summary of Time-Averaged Results at $Re = 20,000$

This subsection has looked at how the performance of the three blades may vary, on the time-averaged basis. The focus has been on the magnitude of the aft adverse pressure gradient, and thus the comparison between aft and forward loading of the LPT blade.

The static pressure contours reveal differing dynamics between the blades; the flow

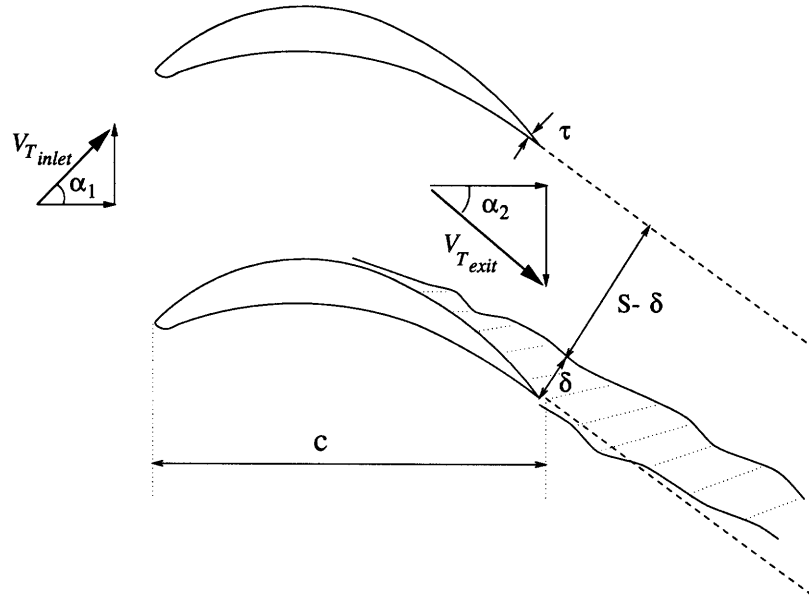


Figure 3-13: Nomenclature used for an approximate calculation of the mixing loss due to a separated boundary layer

blockage due to the blade surface boundary layer is larger for *blade 1* than that for *blade 3*. The higher velocities found over the forward section of *blade 3*, due to the forward loading, as compared to *blade 1*, translates into higher values of profile loss. Finally, the uncertainty for the magnitude of the mixed-out loss clouds the determination of which blade design is superior.

3.2.6 Unsteady Flow Features at $Re = 20,000$

A motivation behind these calculations was to assess the sensitivity of the unsteady flow processes to changes in geometry and Reynolds number. To accomplish this, we use the following methods to serve as a measure, or a figure of merit, of the significance of the unsteady flow features.

The first quantity used to display the unsteadiness associated with these low Reynolds number solutions is the area-averaged total pressure loss at an $x - station$ downstream of the blade trailing edge. This was used previously for the determination of when the flow becomes periodic (section 2.3.2). This is useful because it displays the wake characteristics in terms of the vortex shedding frequency and amplitude.

Next, “snapshots” of the solutions are used to provide insight into the flow features. The main goal of this exercise is to determine the point where the shear layer becomes unstable,

and thus, the point where a vortex is formed by the roll-up of the separated boundary layer. Connections between the shedding frequency and the boundary layer characteristics at the point of separation are examined to determine any relationships that can be found, closely following the work done by Pauley [11].

The static pressure and skin friction fluctuations on the blade surface indicate the level of unsteadiness in the separated region; they also indicate where on the aft region of the blade the shear layer roll up takes place. It will be shown that the magnitude of the pressure gradient in the aft portion of the blade plays a major roll in this process.

The velocity fluctuations associated with the flow unsteadiness lead to “Reynolds stress” effects, resulting in an added dissipation. Laminar and “Reynolds stress” dissipation coefficients will be determined for quantitatively assessing the relative importance of the unsteadiness on blade performance characteristics.

3.2.7 Total Pressure Variation in the Wake at $Re = 20,000$

Shown in figure (3-14) is the variation in area-averaged total pressure at a point in the wake versus time for all three blades at a Reynolds number of 20,000. The quantity plotted for these time traces is the difference between the area-averaged total pressure at the inflow plane and that at the $x - station$ half way between the blade trailing edge and the outflow plane (figure 2-9), made non-dimensional by the area-averaged inlet total pressure, i.e.

$$Y^{area} = \frac{(\overline{p_t^{area}})_{inlet} - (\overline{p_t^{area}})_{x-station}}{(\overline{p_t^{area}})_{inlet}} \quad (3.10)$$

The variations of the total pressure in the wake are due to the convection downstream of a vortex street, with each vortex constituting a region of low total pressure. As a vortex moves through the averaging plane, a lower average total pressure is monitored.

It should be noted that for *blade 1* and *blade 2*, there are actually instances where the area-averaged loss passes the zero point and becomes negative. This would indicate that $(\overline{p_t^{area}})_{x-station} > (\overline{p_t^{area}})_{inlet}$, which at first glance does not make sense because additional energy has not been added to flow. This is clarified by looking at the equation of motion

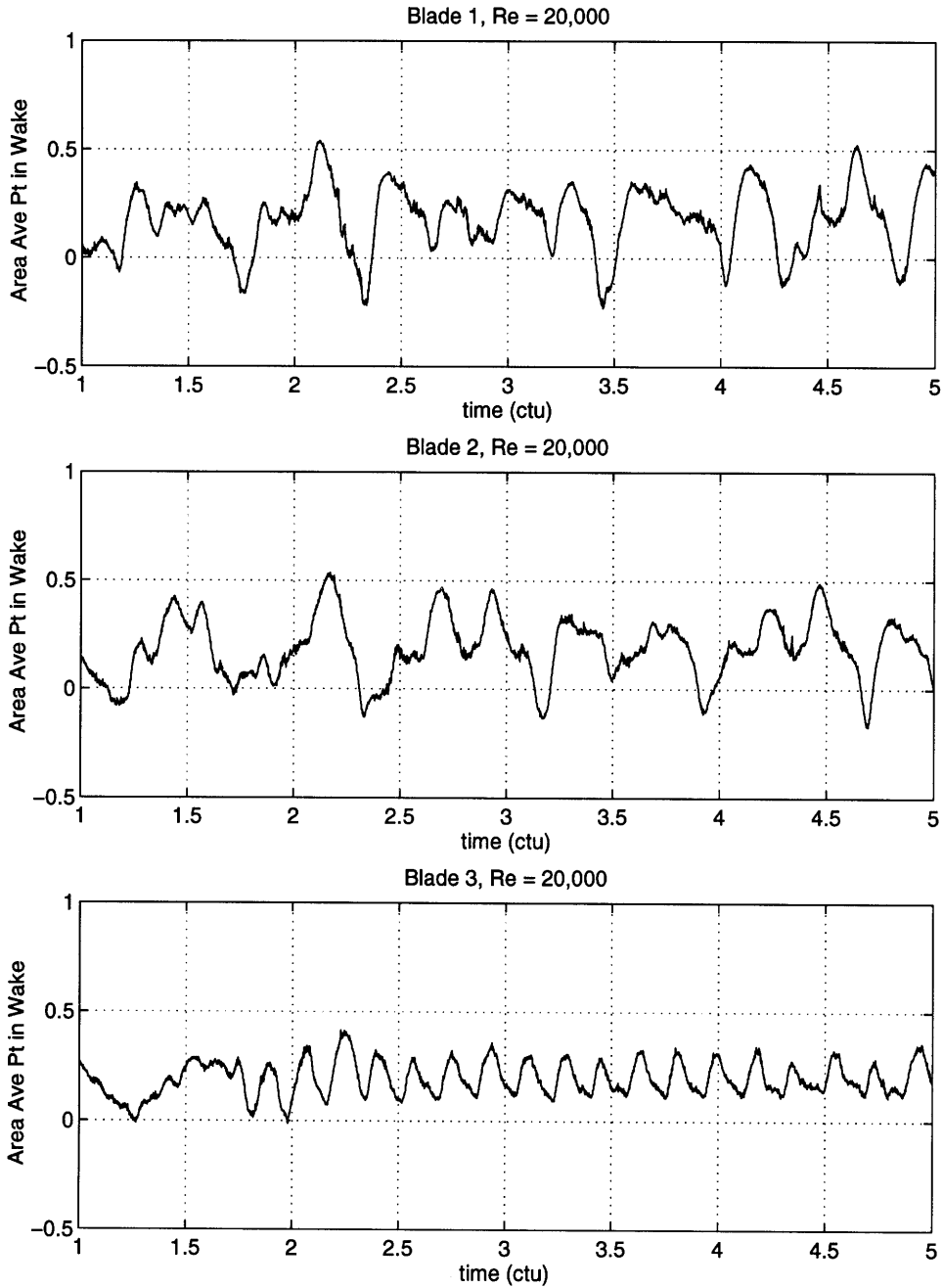


Figure 3-14: Variation of area-averaged total pressure in the wake as a function of time showing the differences in the wake structure for each blade, $Re = 20,000$

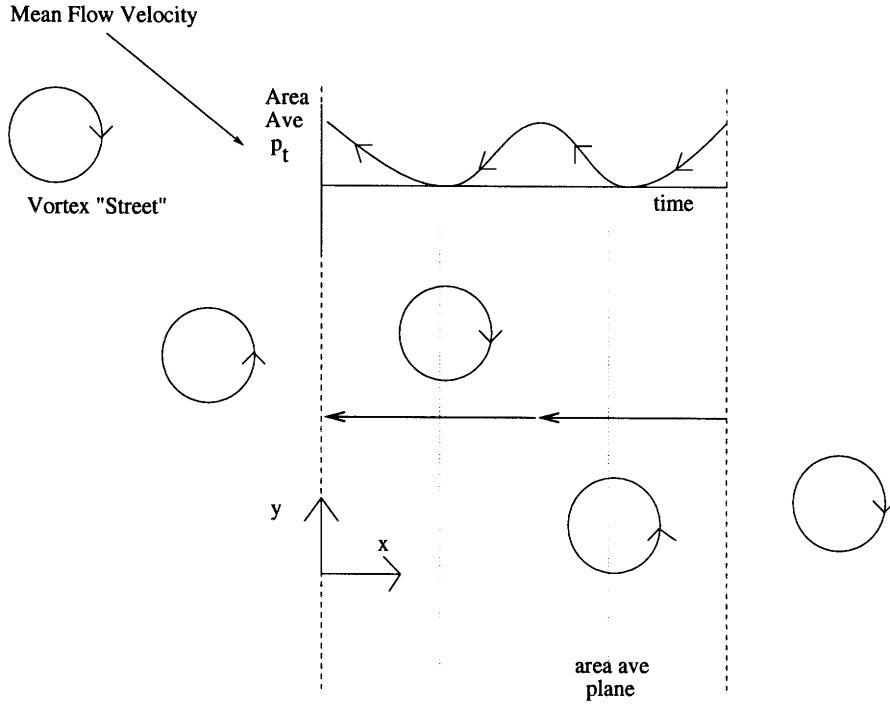


Figure 3-15: Variation in total pressure with time for an averaging plane moving through a line of vortices

for the flow :

$$\nabla p_t = \mathbf{u} \times \boldsymbol{\omega} + \frac{1}{Re} \nabla^2 \mathbf{u} - \frac{\partial \mathbf{u}}{\partial t} \quad (3.11)$$

This demonstrates that the total pressure can be changed via three means.

1. the convection of fluid past a region of vorticity
2. the dissipation associated with viscosity
3. the unsteadiness of the velocity field

Both items 1 and 2 can only decrease the total pressure, but the unsteady term can either decrease or increase the total pressure, depending on the sign of $\frac{\partial \mathbf{u}}{\partial t}$.

As a vortex moves past a stationary point in the wake, the total pressure decreases as the vortex moves over the point, and then increases again as one moves out of the vortex (figure 3-15). This is the cause of the total pressure variations shown in figure (3-14) for the three blades, with the occasional excursion of the area-averaged loss below zero related to the unsteady velocity field convected past the area-averaging plane.

Both *blade 1* and *blade 2* show considerable variation in the area-averaged loss. This is due to differences in the size and strength of the vortices produced during the shedding process. *Blade 3* has a wake consisting of vortices of nearly equal strength and shed at a single dominant frequency. Thus, the vortices shed for *blade 3* are smaller but more closely spaced as compared to those for *blade 1* or *blade 2*.

Figure (3-16) displays the power spectral density (PSD) of the time traces in figure (3-14). These plots allow one to determine the shedding frequency accurately, as well as the amount of power associated with each frequency. *Blade 3* has most of the shedding concentrated at one frequency which is on the order of 1.5 to 2.0 times the shedding frequency of the other two blades.

Any difference seen in the shedding frequency is an indication of a variance in the dynamics leading to the shedding of vortices. By investigating the time-average total pressure loss in the wake, one can determine that there must be different dynamics occurring for *blade 3* as compared to *blade 2* or *blade 1*. A look at these differences is made in the next section.

3.2.8 Shear Layer Behavior at $Re = 20,000$

The indications of differing wake structure for the blades shown in figure (3-14), can also be seen using instantaneous snapshots of the flow field. Specifically, the vorticity field is used because of the clarity in which the wake structure is brought out using this quantity.

Representative snapshots of the instantaneous vorticity fields for *blade 1* and *blade 3* at a Reynolds number of 20,000 are given in figures (3-17) and (3-18). Notice the smaller vortex sizes, in terms of radii, for *blade 3* than *blade 1* and that the vortex spacing in the wake is correspondingly smaller for *blade 3*. This confirms the observations made earlier in this section when looking at the area-averaged total pressure loss in the wake versus time (figure 3-14). Thus, the wake for *blade 3* has smaller amplitude fluctuations in total pressure, but at a higher frequency.

The higher frequency shedding suggests that the extent of the separation for *blade 3* is smaller than that for *blade 1*. This statement is made because, if the Strouhal number is considered to be constant for the two blades, an increase in frequency must correspond to a decrease in separation thickness.

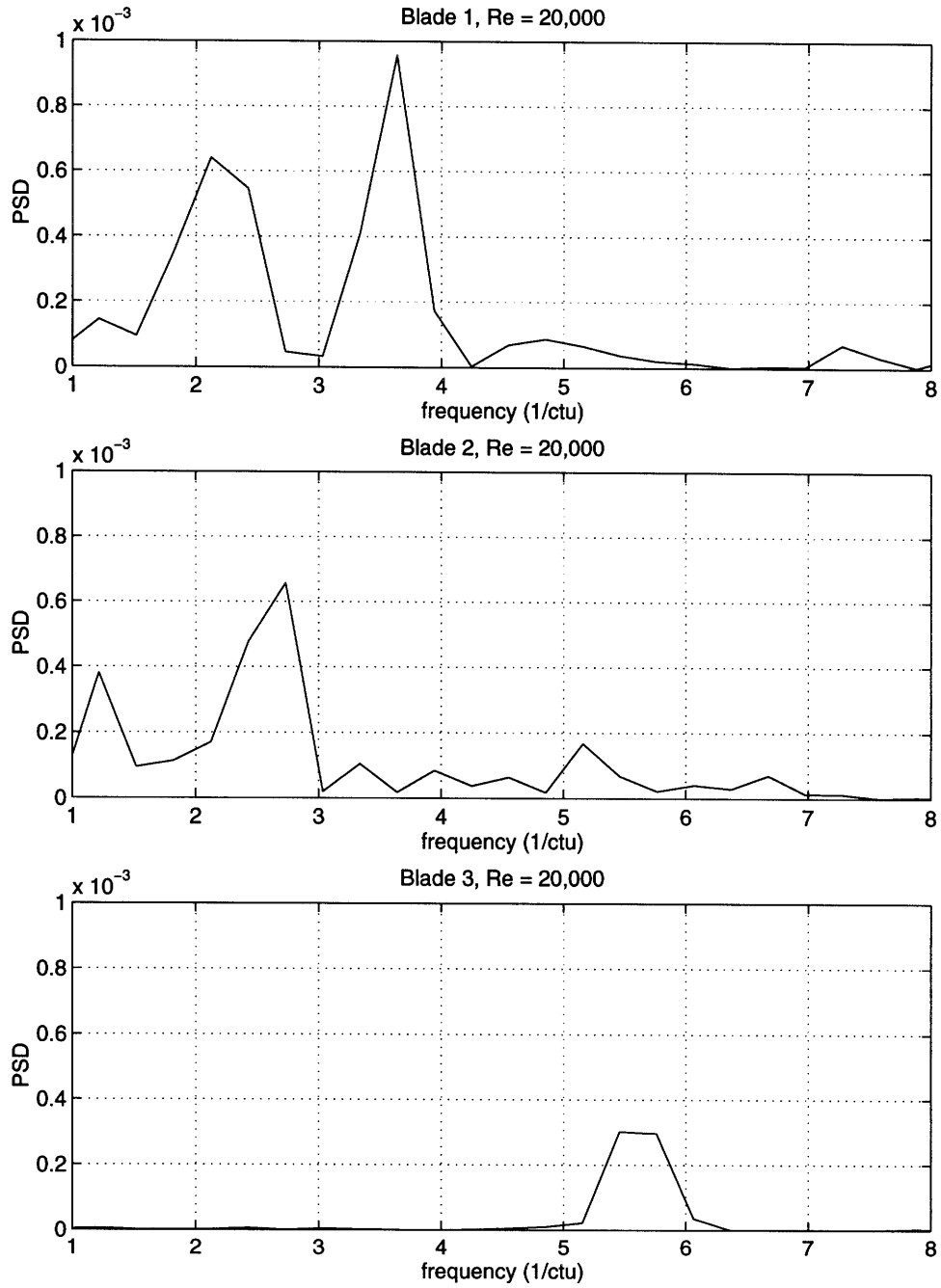


Figure 3-16: Power spectral density of time traces given in figure (3-14), variation in shedding frequencies for the three blades, $Re = 20,000$

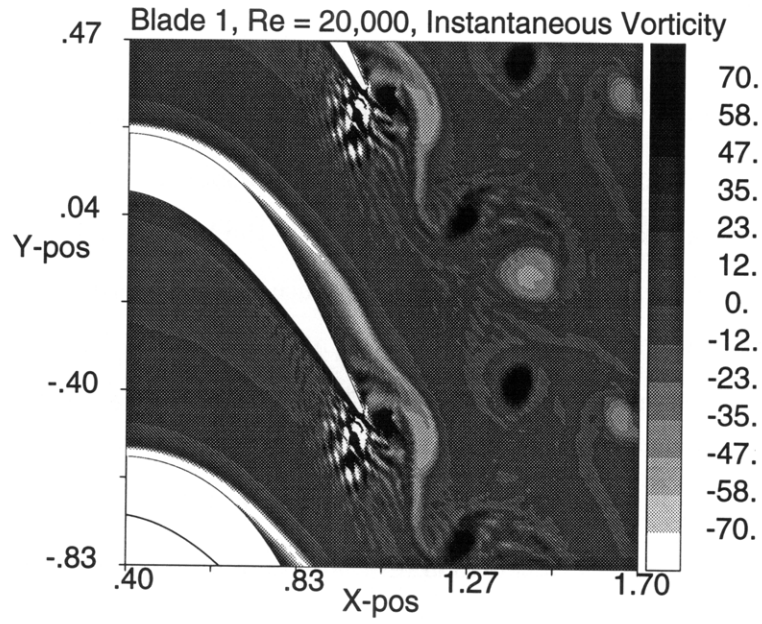


Figure 3-17: Instantaneous vorticity field for *blade 1* , Re = 20,000

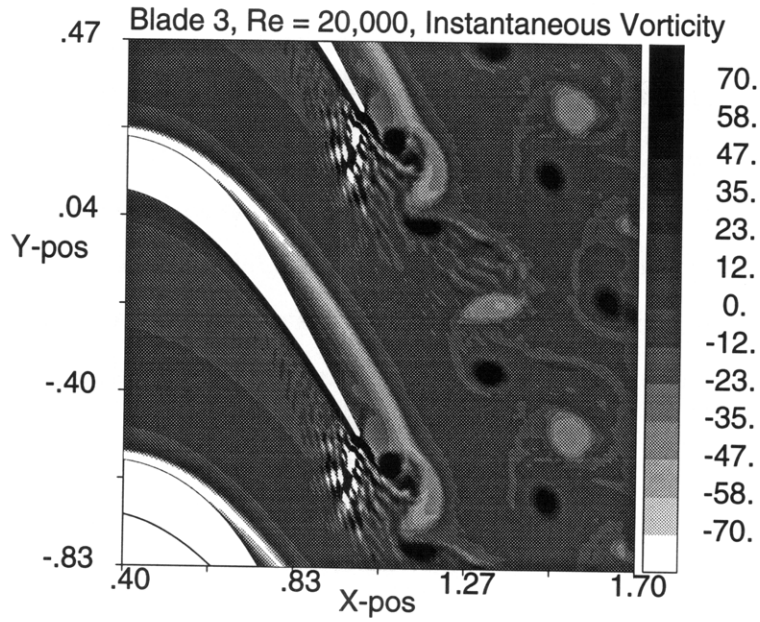


Figure 3-18: Instantaneous vorticity field for *blade 3* , Re = 20,000

The Strouhal number is defined here as,

$$S_t = \frac{f_{shed} d}{U_{ete}} \quad (3.12)$$

where f_{shed} is the shedding frequency, d the trailing edge thickness plus separation width, and U_{ete} the freestream velocity just above the separated region at the trailing edge.

Using the time-averaged vorticity fields to determine the boundary layer thickness (see figure 3-13), the separated shear layer lies at a distance of 0.14 chords above the trailing edge for *blade 1*, whereas the layer for *blade 3* lies at a distance of 0.11 chords; this is in accord with the statement made previously that the extent of separation for *blade 3* must be smaller than *blade 1*.

A rough calculation of the Strouhal number for *blade 1*, using a freestream velocity of 2.4 (obtained using figure 3-9), a thickness of 0.14, and an approximate shedding frequency of 3.5 (found using figure 3-16), the Strouhal number turns out to be 0.20. Doing the same for *blade 3*, using a velocity of 2.4, a thickness of 0.11, and a frequency of 5.5, results in a Strouhal number of 0.25. The Strouhal number corresponding to the shedding from a circular cylinder has a value of about 0.21 [2], therefore the approximate Strouhal number calculations for *blade 1* and *blade 3* are in agreement with the value for a cylinder.

The location for which the properties of the shear layer lead to vortex formation can be compared to the predicted location given by inviscid linear stability theory. As mentioned in chapter (1), the numerical experiment performed by Pauley [11] found that the point of vortex formation is set by the value of the non-dimensional frequency associated with the most amplified frequency, determined from inviscid linear stability analysis [9]. This non-dimensional frequency is defined based on the maximum value of the vorticity in the shear layer, and the velocities of the two streams of fluid on the boundary of the shear layer. Following [11], the non-dimensional frequency is given as :

$$\omega^* = \frac{(2\pi f)\delta_{\omega_z}}{4\bar{u}} \quad (3.13)$$

where, δ_{ω_z} is a “vorticity” thickness defined as :

$$\delta_{\omega_z} = \frac{\Delta u}{\left(\frac{\partial u}{\partial y}\right)_{max}} \quad (3.14)$$

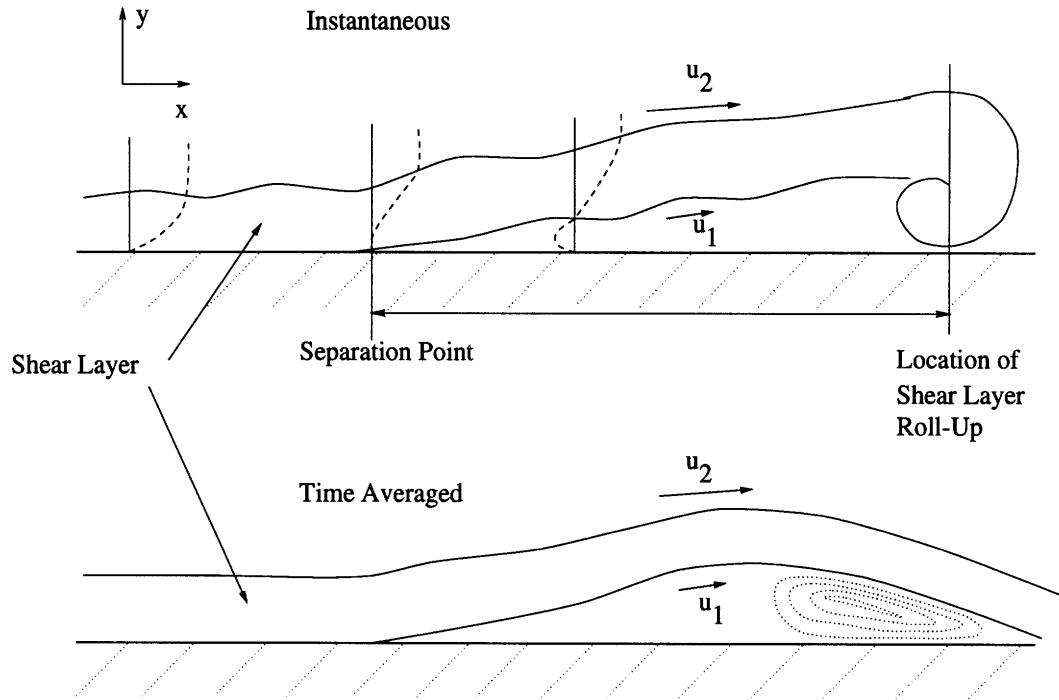


Figure 3-19: Shear layer roll-up and the time-averaged flow corresponding for this situation

Blade	u_2	u_1	$\left(\frac{\partial u}{\partial y}\right)_{max}$	f	ω^*
1	2.43	-0.43	46	2.85	0.28
2	2.38	0.14	39	2.7	0.19
3	2.30	0.04	38	2.75	0.22

Table 3.2: Values used for calculation of ω^* , $Re = 20,000$

with $\Delta u = u_2 - u_1$, and $\bar{u} = \frac{1}{2}(u_2 + u_1)$. The situation and nomenclature is displayed in figure (3-19). Michalke [9] showed that the most amplified frequency is $\omega^* = 0.21$.

Thus, to assess if this result holds for these more complicated flows (compared to the channel flow used by Pauley), the shedding frequency observed for the flows will be non-dimensionalized by the velocities, u_2 and u_1 , using the method given by equation (3.13). The velocities and the maximum vorticity in the shear layer are found at a location corresponding to the approximate center of the time-averaged vortex, depicted in figure (3-19).

Table (3.2) gives the velocities and vorticity values used for the non-dimensionalization, along with the observed vortex shedding frequency determined through flow observation and the power spectral density plots (figure 3-16).

The numbers used to calculate ω^* can only be approximated, as the position of vortex

roll-up is not steady. Also, a determination of the vortex shedding frequency from the suction side shear layer is not at all exact. For example, the power spectrum plot (figure 3-16) for *blade 1* has peaks at two frequencies, thus for that case, an average of the two was taken. Also, the frequency used for *blade 3* was taken as 1/2 of the frequency shown in figure (3-16), because an observation of the flow reveals that each peak in the area-averaged loss (figure 3-14) for *blade 3* corresponds to a pair of alternating vortices; one shed from the pressure side, one from the suction side. Thus, to obtain the frequency of shedding from the suction side shear layer alone, the dominant frequency needs to be divided by two.

Despite these inaccuracies, the computed non-dimensionalized frequencies closely approximate the most amplified frequency of $\omega^* = 0.21$ determined from linear instability analysis. Therefore, if one can assume that the shear layer will become unstable at $\omega^* = 0.21$, the two velocity values and a maximum vorticity in the boundary layer can be used to determine the frequency at which vortices are shed.

3.2.9 Location of Separation Point in Steady versus Unsteady Flow

Section (3.2.3) displayed the use of the time-averaged skin friction as a method for determining the point separation. The separation/re-attachment point was found by looking for points where the C_f reached a value of zero. This is valid for a time-averaged flow, but not so for an unsteady flow.

This can be seen from the results for an example shown in figure (3-20), which displays an instantaneous plot of the skin friction over the suction surface and the corresponding total velocity contours. If the point of zero C_f were used to determine the separation point, one would conclude that separation does not occur until around $x/c = 0.85$; however the computed velocity contour plot shows that the flow separates upstream of $x/c = 0.85$.

The explanation of this observation can be deduced from an examination of the equation of motion in the vicinity of the wall, where the convective acceleration can be neglected compared to the pressure gradient and viscous forces. For steady flow, the result obtained is the usual balance between the pressure gradient and the viscous force, thus :

$$\frac{\partial p}{\partial x} = \mu \frac{\partial^2 u}{\partial y^2} \quad (3.15)$$

A favorable pressure gradient, $\frac{\partial p}{\partial x} > 0$, implies that $\frac{\partial^2 u}{\partial y^2} > 0$, and for an adverse pressure

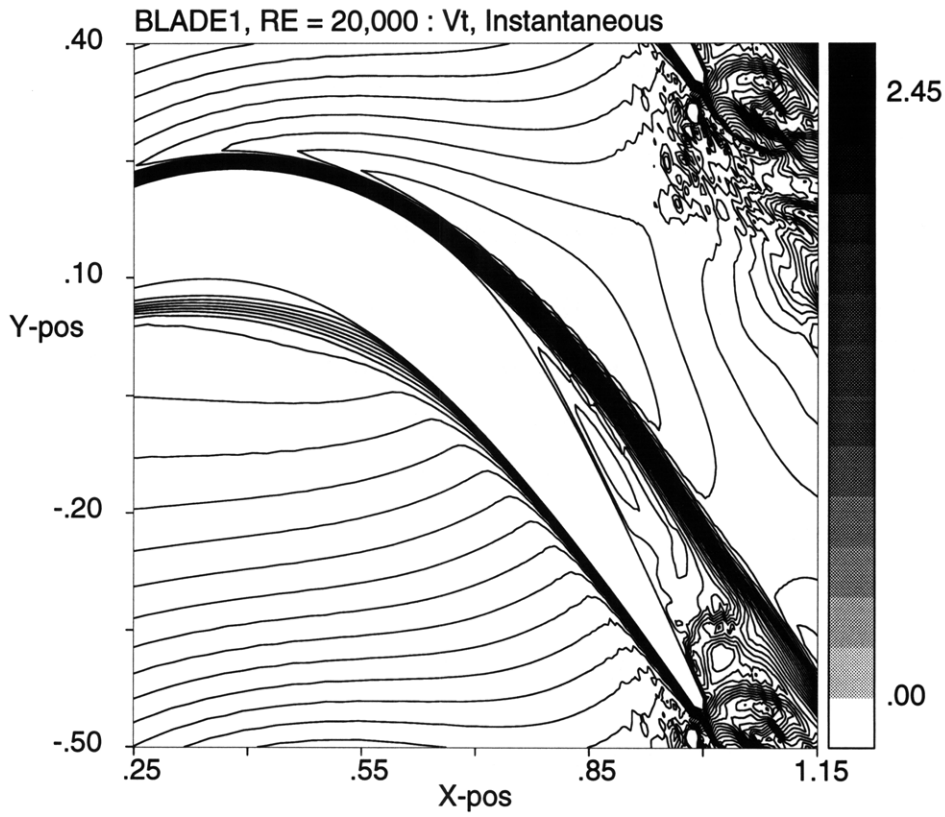
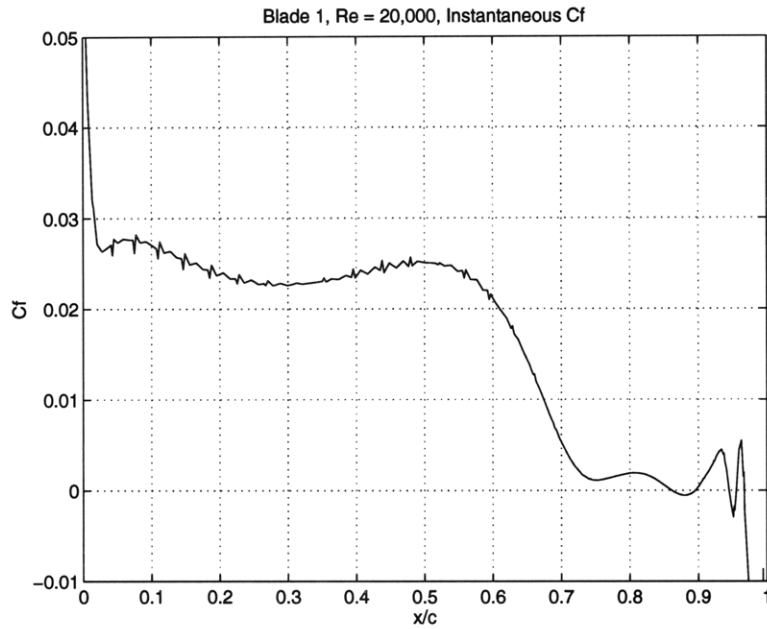


Figure 3-20: Instantaneous skin friction on suction surface, and instantaneous total velocity contours for the same time, *blade 1*, $Re = 20,000$, showing that the point of zero skin friction does not correspond to the point of separation in unsteady flow

gradient, $\frac{\partial p}{\partial x} < 0$, the possibility of a reverse flow occurs, with $\frac{\partial^2 u}{\partial y^2} < 0$. The point where, $\frac{\partial p}{\partial x} = 0$, indicates that the velocity profile will have an inflection point, and thus as usual for steady flow, the point of separation is taken as the point where the shear stress tends to zero, $\frac{du}{dy} = 0$, at $y = 0$ [5].

However, this same line of reasoning does not hold for unsteady flow because of the additional term that must be included in the balance of forces in the near wall region :

$$\frac{\partial u}{\partial t} + \frac{\partial p}{\partial x} = \mu \frac{\partial^2 u}{\partial y^2} \quad (3.16)$$

The balance of forces is not only between the pressure and viscous terms, but the unsteadiness of the velocity field must be taken into account. For a time-averaged case with flow *periodicity*, the $\frac{\partial u}{\partial t}$ term will no longer play a role, and thus, the method of using the point of zero skin friction as the point of separation is valid in the time-averaged flow fields.

The determination of the point of separation in an unsteady flow using the location of zero skin friction is not correct. One should use the flow streamlines or the change in velocity through the boundary layer at various axial locations to determine the point at which the flow at the wall reverses direction.

3.2.10 Static Pressure Deviations Due to Unsteadiness at $Re = 20,000$

The effects of the separation dynamics on the static pressure distribution can be investigated by looking at the static pressure fluctuations over the blade surface. Figure (3-21) displays the static pressure variations over the blade and the standard deviation of these variations as a function of axial distance through the passage. The standard deviation of the pressure from the mean is defined as :

$$\sigma = \sqrt{\frac{1}{N-1} \sum_{j=1}^N (p_j - \bar{p})^2} \quad (3.17)$$

where N is the number of time samples, and the mean is defined as :

$$\bar{p} = \frac{1}{N} \sum_{j=1}^N (p_j) \quad (3.18)$$

The solid curves on the static pressure plots are a mean surface pressure for the blade.

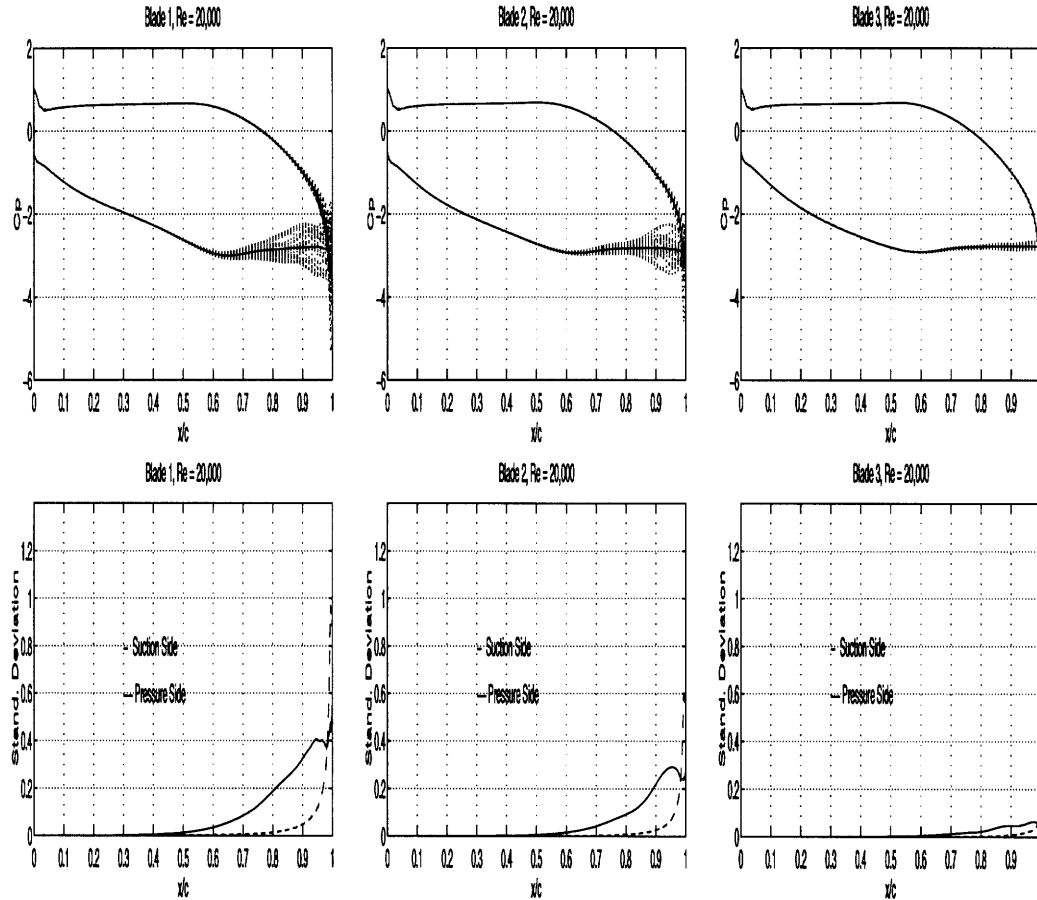


Figure 3-21: Static pressure envelopes over the blade surface and standard deviation of the fluctuations for blades 1, 2, 3, at $Re = 20,000$

The magnitude of the pressure deviation from the mean allows one to determine the level of “unsteadiness” in the pressure at a certain location. This allows a statement to be made on how important the time variations are at a certain point in the flow field.

The standard deviation plots show that *blade 1* undergoes the largest pressure fluctuations in magnitude and in terms of influence upstream, with variations occurring as far up as $x/c = 0.5$, whereas *blade 2* has pressure fluctuations that extend from the trailing edge to $x/c = 0.6$ and *blade 3* to $x/c = 0.7$. The pressure surface has minimal pressure fluctuations except near the trailing edge. The time-average results of section (3.2.1) for the $Re = 20,000$ solutions show that *blade 1* has a distinct vortex in the trailing edge region, while that for *blade 3* indicates the presence of a weak vortex. These observations thus correlate with the magnitude of the pressure deviations in the trailing edge region.

As indicated by the greater deviation in pressure for *blade 1* and *blade 2*, the dynamics associated with the vortex shedding occur closer to the trailing edge than they do for *blade*

3 . The suction side shear layer upstream of the trailing edge for *blade 1* is under a large influence from the unsteady pressure generated by the vortex shedding. *Blade 3* has little variation in the pressure from the average static pressure in the aft portion of the blade, and the separated shear layer is only slightly influenced.

3.2.11 Dissipation Coefficient at $Re = 20,000$

A last look at the unsteady features for the $Re = 20,000$ solutions focuses upon the net dissipation coefficient, being a sum of the laminar dissipation and that due to time-averaged flow unsteadiness. This coefficient was defined in section (3.2.4). Substituting equation (3.2) into (3.3) results in the following expression for C_d , where U_e is the freestream velocity directly above the boundary layer, V_t the total velocity in the flow field, and τ_{xy} the shear stress, i.e. :

$$C_d = \frac{1}{\rho U_e^3} \int_0^\delta \tau_{xy} dV_t \quad (3.19)$$

Using the Boussinesq approximation, the shear stress can be written as a combination of a laminar term and a turbulent term, with ε being a “turbulent viscosity”.

$$\tau_{xy} = (\nu + \varepsilon) \frac{\partial V_t}{\partial y} \quad (3.20)$$

The turbulent shear stress term is an approximation for the effective turbulent shear stress, $-\overline{\rho u'v'}$, resulting from a Reynolds averaging of the Navier-Stokes equations. Replacing the shear stress in (3.19) with the expression in (3.20), results in the breaking up of the dissipation coefficient into two terms, one due to laminar shear, and the other to deviations of the velocities from a time-averaged velocity.

$$C_d = (C_d)_{lam} + (C_d)_{u'v'} = \frac{1}{U_e^3} \int_0^\delta \frac{\partial V_t}{\partial y} dV_t + \frac{1}{U_e^3} \int_0^\delta (-\overline{u'v'}) dV_t \quad (3.21)$$

Even though the calculations performed for this investigation used no turbulence modeling, the velocity fluctuations still contribute a momentum transfer, and thus a stress, to the flow in the separated region. Therefore, a measure of this added contribution to the net dissipation is made by calculating the $\overline{u'v'}$ term. This is accomplished using the time-averaged flow field, and the computed unsteady flow. The $\overline{u'v'}$ terms that are calculated

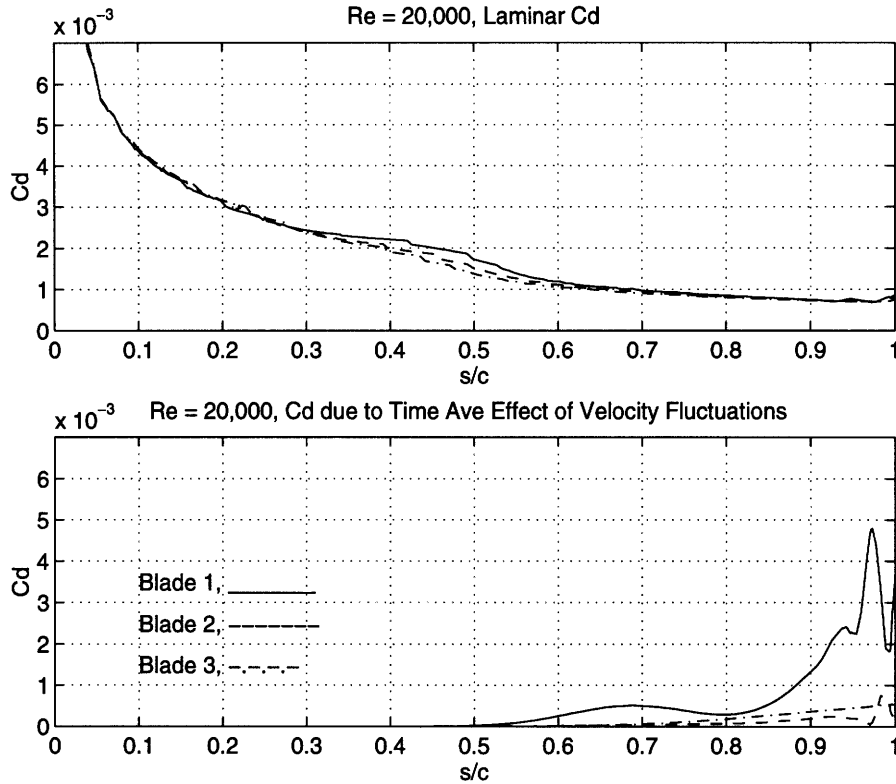


Figure 3-22: Laminar and unsteady dissipation coefficients on the suction side for all three geometries at $Re = 20,000$, plotted along the blade surface

give an order of magnitude assessment for the dissipation due to the velocity fluctuations.

The laminar and unsteady dissipation coefficients for the suction side at a Reynolds number of 20,000 are shown in figure (3-22), while the ratio of the unsteady fluctuation to the laminar dissipation is given in figure (3-23). The $(C_d)_{u'v'}$ for *blade 1* becomes on the order of 6 to 7 times $(C_d)_{lam}$ in the trailing edge region, thus a large part of the dissipation can be attributed to the fluctuating velocity. The dissipation due to the fluctuations for *blade 2* and *blade 3* have much less of an impact upon the total C_d .

To summarize, the flow unsteadiness associated with separation/roll-up effectively increases the value of C_d by a value ranging from 1 to 6, depending on the blade design.

3.2.12 Summary of Observed Unsteady Features at $Re = 20,000$

The computed flow field at $Re = 20,000$ for the 3 blade designs indicate a suction side separation, which is not surprising considering the extremely low Reynolds number. Even at this Reynolds number, a difference is seen in the unsteady flow features between the designs.

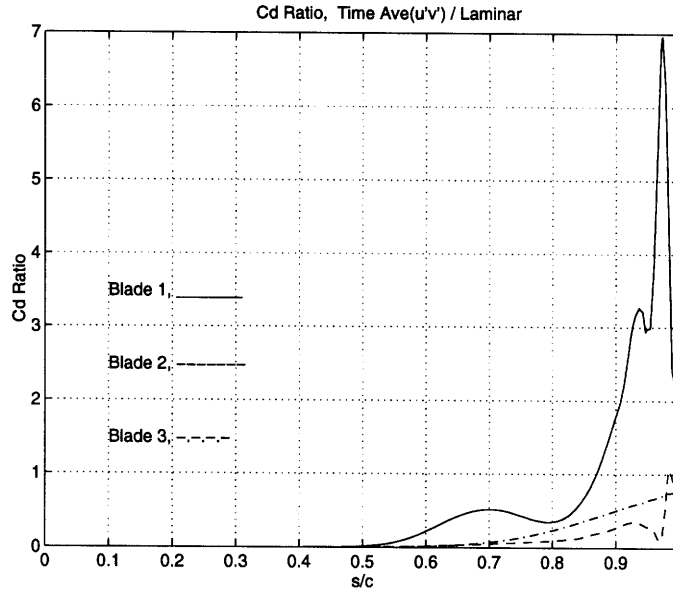


Figure 3-23: Ratio of the unsteady to laminar dissipation coefficients on the suction side, $Re = 20,000$, plotted along the blade surface

The stronger *inviscid* pressure gradient for *blade 1* leads to a decrease in the shear layer stability as compared to *blade 3*. *Blade 2* lies in between *blade 1* and *blade 3* in terms of the magnitude of the *inviscid* pressure gradient. This change in shear layer stability over the geometries results in variations in the shedding process, vortex shedding frequencies, and the effective dissipation, thus leading to differences in the time-averaged flow fields.

3.2.13 Time-Average Solutions at $Re = 30,000$

The format used for the $Re = 20,000$ solutions will be followed again in this section. The only difference is that the explanations for the use of certain quantities as tools toward the understanding of the flows have already described, allowing the remaining sections to focus on the presentation of the results.

3.2.14 Total Velocity and Static Pressure Contours at $Re = 30,000$

The pressure and velocity contours for all three blades are given in figure (3-24). The time-average pressure contours in the trailing edge region for the three blades allow the inference to be made that different dynamics are occurring that causes the pressure in the trailing edge region to vary between the geometries.

Specifically, *blade 1* has an elongated region of low pressure extending over the last

two-tenths of chord, whereas *blade 2* and *blade 3* show an area of low pressure that is concentrated in the trailing edge region. The pressure contours for *blade 2* and *blade 3* look similar to those for *blade 1* at a Reynolds number of 20,000 (figure 3-1), allowing one to infer that the unsteady flow dynamics for *blade 2* and *blade 3* at $Re = 30,000$ may resemble those for *blade 1* at $Re = 20,000$.

The velocity contours demonstrate that the pressure side bubble remains, with no indications of any differences from the 20,000 case. The suction side shear layer again remains separated downstream of the trailing edge for all three geometries. As in the $Re = 20,000$ case, the velocity vectors near the trailing edge indicate the presence of a vortex on the time-average basis (figure 3-25, and 3-26). The vector plot for *blade 3* (figure 3-26) has the same features in terms of vortex position as that for *blade 1* at $Re = 20,000$ (figure 3-2). One could thus infer from this that the unsteady flows are similar for *blade 3* at 30,000 as that for *blade 1* at 20,000.

The elongation of the time-average vortex for *blade 1* leads one to argue that a change in the dynamical structure of the suction side separation has occurred. Explanations for this difference are related to the increase in the flow unsteadiness in this region.

3.2.15 Surface Static Pressure Coefficient and Skin Friction at $Re = 30,000$

The time-average difference in the three designs can be inferred by the blade surface pressure distribution shown in (figure 3-27). The surface pressure for *blade 1* indicates the presence of the time-average vortex on the suction side. It is characterized by a drop in pressure associated with the vortex, whereas this same feature is not present for the other two geometries.

The time-average skin friction (figure 3-28) indicates the changing nature of the flow over the suction side for *blade 1*. Using the value where C_f reaches zero as the criterion for separation, *blade 3* separates earlier than *blade 1* as it did for the $Re = 20,000$ solution. The skin friction is larger in magnitude over the first 0.4 chords for *blade 3* as compared to the other blades, again due to the forward loading. The only significant change between the blade comparisons in figure (3-28), as compared to those for $Re = 20,000$, is the change in the trailing edge region for *blade 1*. This dip in C_f towards large negative values for *blade 1* is associated with the recirculation found within the time-average vortex.

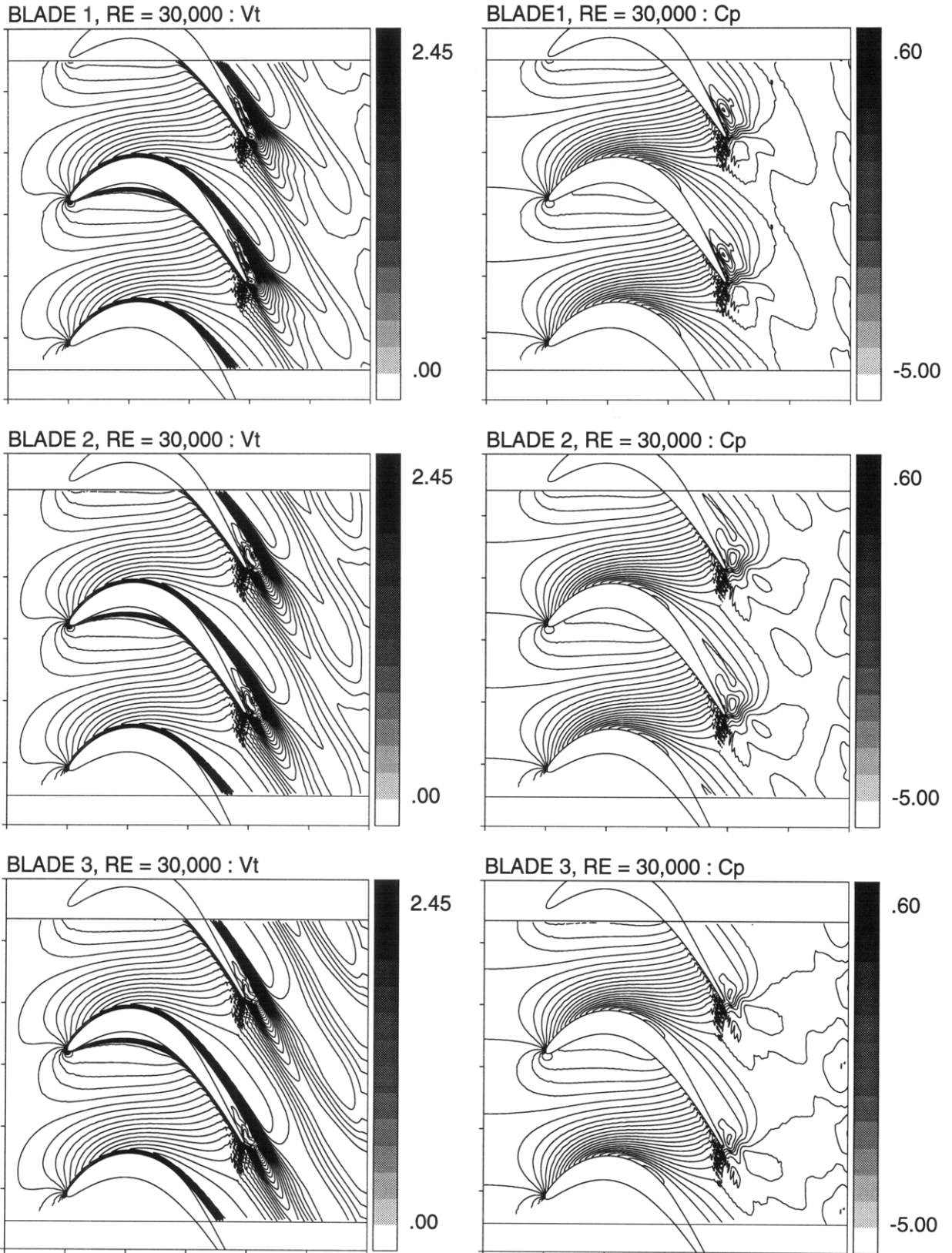


Figure 3-24: Time-averaged total velocity and static pressure coefficient contours, blades 1, 2, 3, $Re = 30,000$

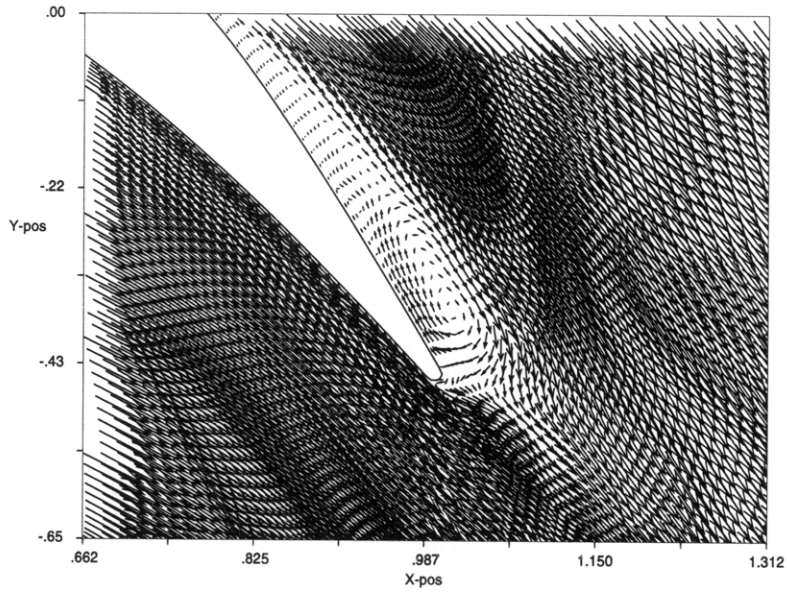


Figure 3-25: *Blade 1*, $Re = 30,000$, time-averaged velocity vectors indicating presence of a vortex at the trailing edge region

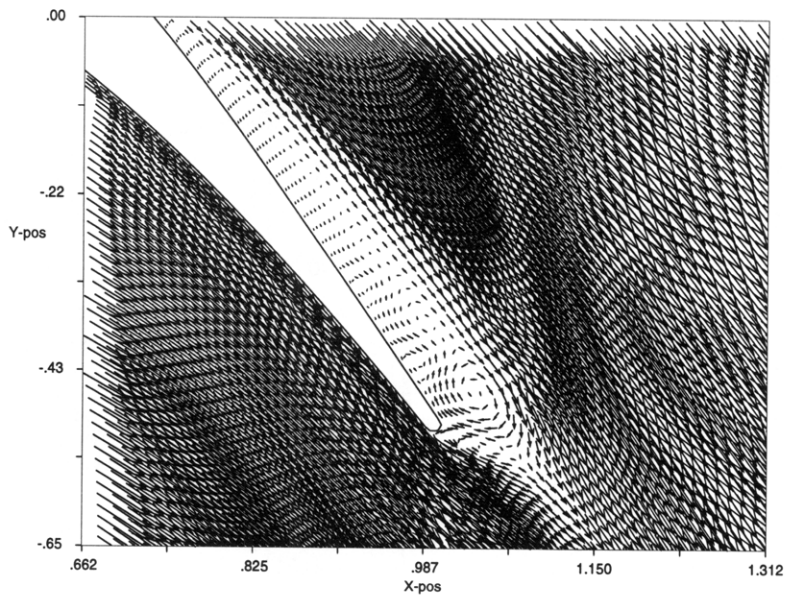


Figure 3-26: *Blade 3*, $Re = 30,000$, time-averaged velocity vectors indicating presence of a vortex at the trailing edge region

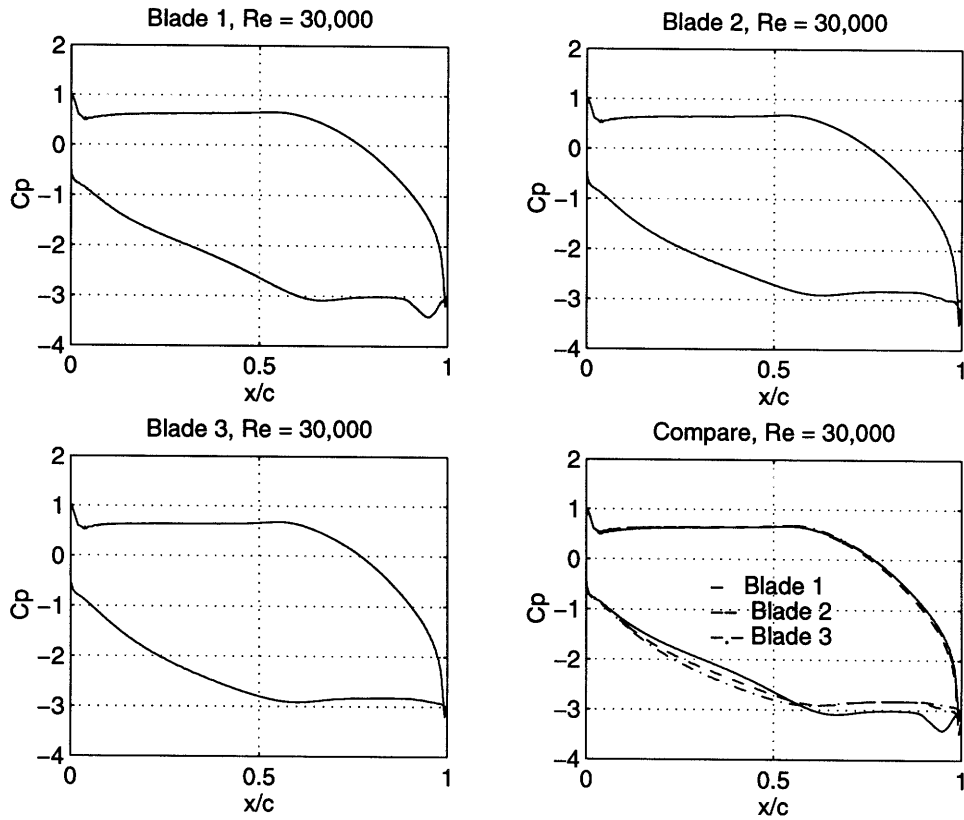


Figure 3-27: Time-averaged static pressure on the blade surface for $Re = 30,000$

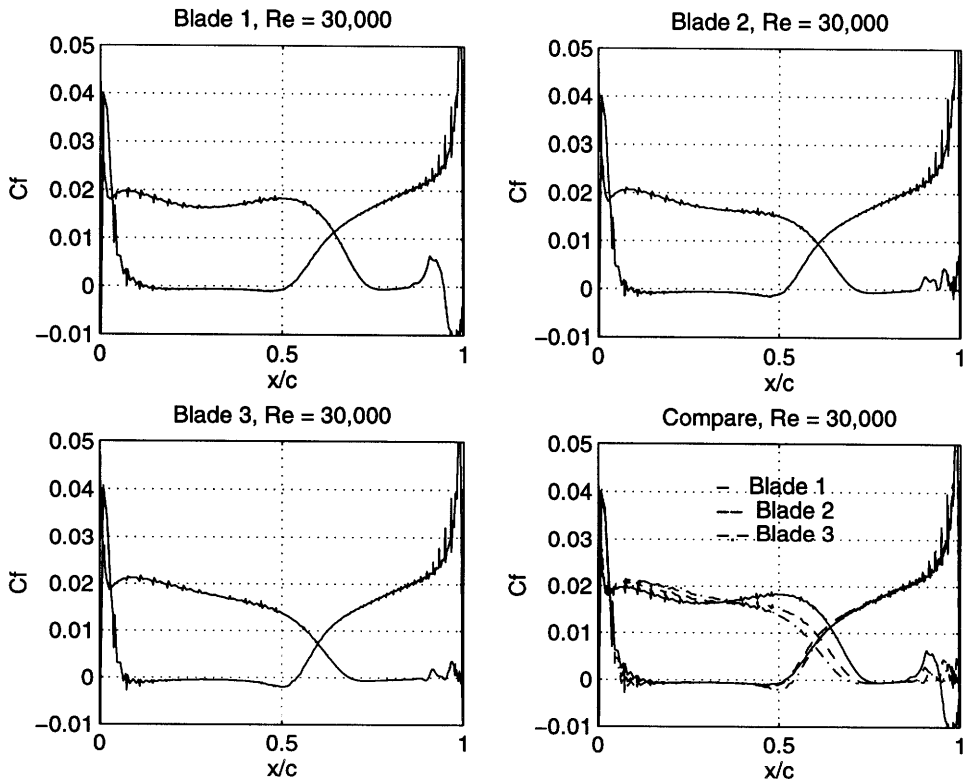


Figure 3-28: Time-averaged skin friction on blade surface for $Re = 30,000$

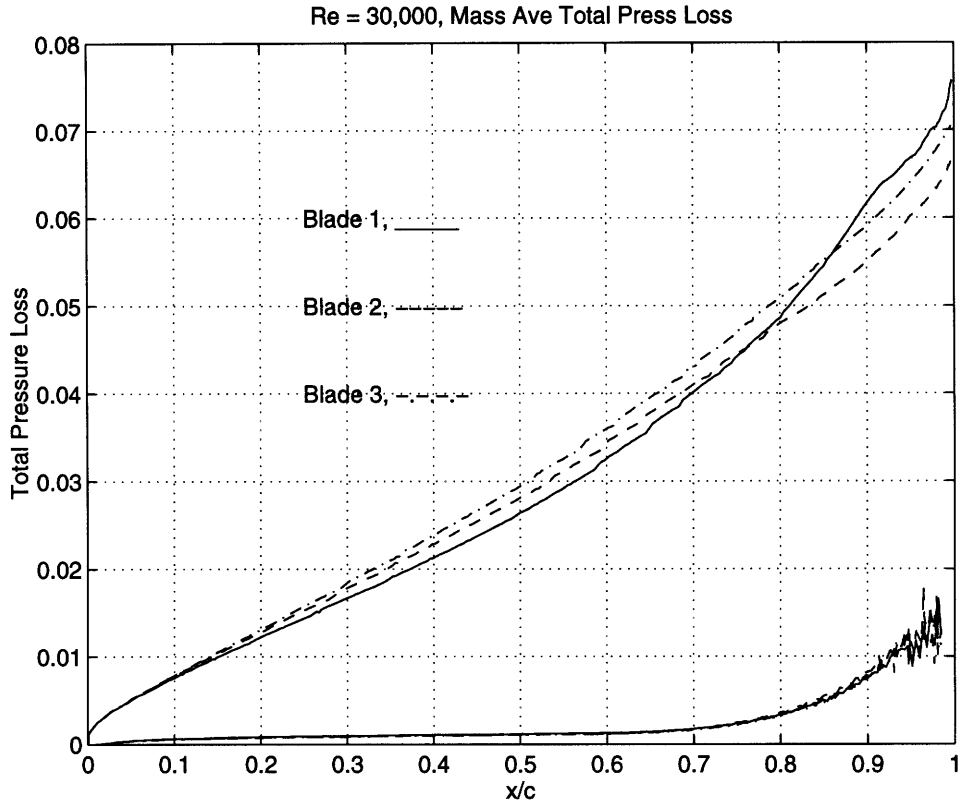


Figure 3-29: Mass-averaged total pressure loss, made non-dimensional by exit dynamic head, for the suction and pressure sides at a Reynolds number of 30,000

3.2.16 Total Pressure Loss at Re = 30,000

The mass-averaged total pressure loss for the three blades at Re = 30,000 is given in figure (3-29). As shown for the Re = 20,000 case (figure 3-10), *blade 3* continues to have higher profile loss, with *blade 1* having the lowest, and *blade 2* in between.

The sharp increase of mass-averaged loss for *blade 1* at $x/c = 0.8$ is due to the movement of the time-average vortex (shown in figure 3-25) upstream.

The loss calculated using enstrophy, is shown in figure (3-30). *Blade 3* has larger loss, with *blade 1* showing the smallest loss. The sharp increase in loss level for *blade 1* associated with the vortex on the suction side seen in the mass-average total pressure loss plot is not apparent for the loss curve determined using enstrophy.

An assessment of loss levels is not complete without examining the order of magnitude for the loss associated with the mixing out of the wake. Using equation (3.9), with $\tau = 0.01$, $S = 0.42$, and $\delta_e^* = 0.10$ (with δ_e^* being a typical value for the three blades at Re = 30,000 at the trailing edge), the added loss due to mixing (without including the base pressure

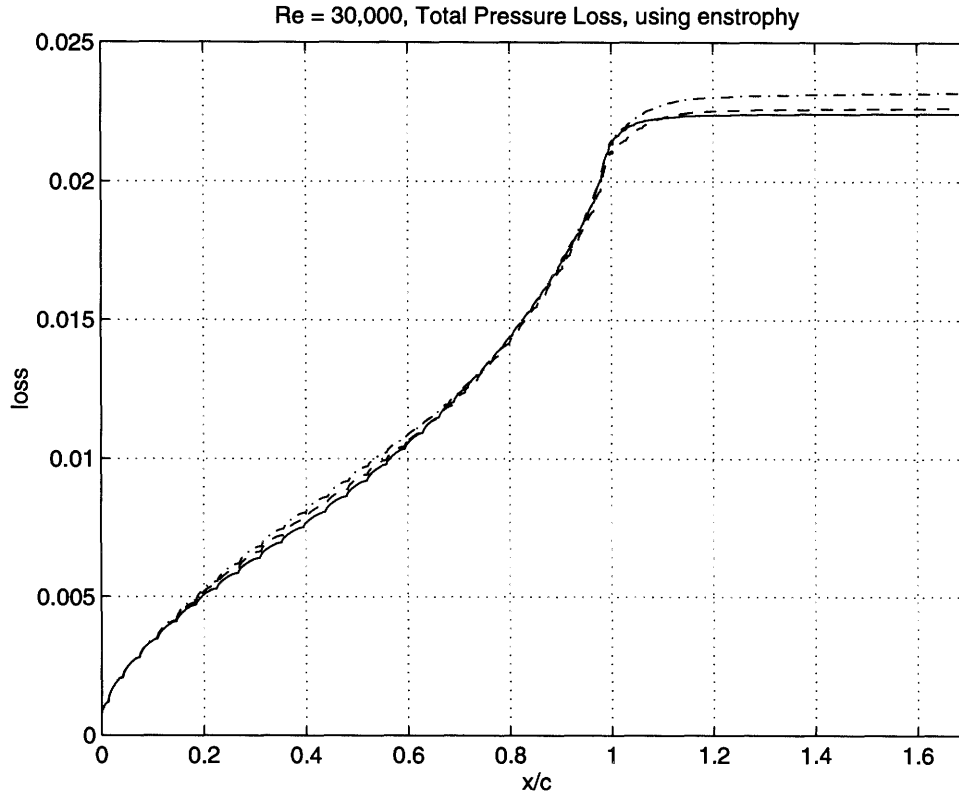


Figure 3-30: Loss for all three geometries, calculated using enstrophy at $Re = 30,000$

effects) is again 0.068, as it was for the $Re = 20,000$ case.

3.2.17 Summary of Time-Averaged Results at $Re = 30,000$

The increase in Reynolds number from 20,000 to 30,000 has two effects upon the computed flow fields. One, the time-average pressure for *blade 1* in the aft region on the suction side indicates a low pressure region in the last 0.2 axial chords of the blade. This region was shown to be attributed to the presence of a vortex under the separated shear layer. Second, the increase in Reynolds number has the effect of amplifying the recirculation at the trailing edge for *blade 3* as compared to the 20,000 case. The time-average vortex for *blade 3* moves upstream as compared to its position downstream of the blade trailing edge in the 20,000 case. A comparison of the velocity vector plots (3-26) and (3-3) demonstrates this point.

The changes described in the time-average flows are a product of the unsteady flow in the separated region. A comparison of these unsteady features between the blades and explanations for the observed change in dynamics between the Reynolds numbers of 20,000 and 30,000 will be presented next.

3.2.18 Unsteady Features at $Re = 30,000$

Two unsteady features will be focused on in this section : (i) the dynamics that lead to the changing time-average flow field in the shear layer for *blade 1* will be investigated; (ii) and, the movement upstream of the time-average vortex in the trailing edge region for *blade 3* is explained.

The differing dynamics observed in the solutions attest to the ability of the spectral code to differentiate between small blade design changes.

3.2.19 Total Pressure Variation in the Wake at Re of 30,000

Increasing the Reynolds number to 30,000 has the most effect on *blade 1* and *blade 3*. Figure (3-31) displays the time trace of the area-averaged total pressure loss in the wake. When comparing these traces with the time traces for $Re = 20,000$ (figure 3-14), it is observed that the variations for *blade 1* become more regular, i.e., one frequency is more dominant than the others. The solution for *blade 1* at $Re = 20,000$ indicates that two dominant frequencies are present. This can be seen by comparing the power spectral density plots in figures (3-16) and (3-32).

Blade 3 has a large change in its shedding dynamics. The high frequency shedding present in the $Re = 20,000$ solution, which was on the order of 2 times the shedding frequency for the other geometries, decreases to a lower frequency at $Re = 30,000$, comparable to the that for *blade 1* and *blade 2* at $Re = 20,000$. The shedding for *blade 3* at $Re = 30,000$ has no dominant frequency, and resembles the total pressure traces for *blade 1* and *blade 2* at $Re = 20,000$.

3.2.20 Shear Layer Behavior at $Re = 30,000$

The observed changes in the shedding frequency for *blade 3*, and the development of a more regular shedding for *blade 1* are attributed to changes in the suction side separation dynamics. The increase in Reynolds number causes the shear layer to become unstable earlier, effecting the overall unsteady nature of the flow.

The roll up of the suction side shear layer for *blade 1* begins upstream of the trailing edge. This was not the case for $Re = 20,000$, where the shear layer formed into vortices downstream of the trailing edge. Figures (3-33) through (3-40) provide a look at the shedding process

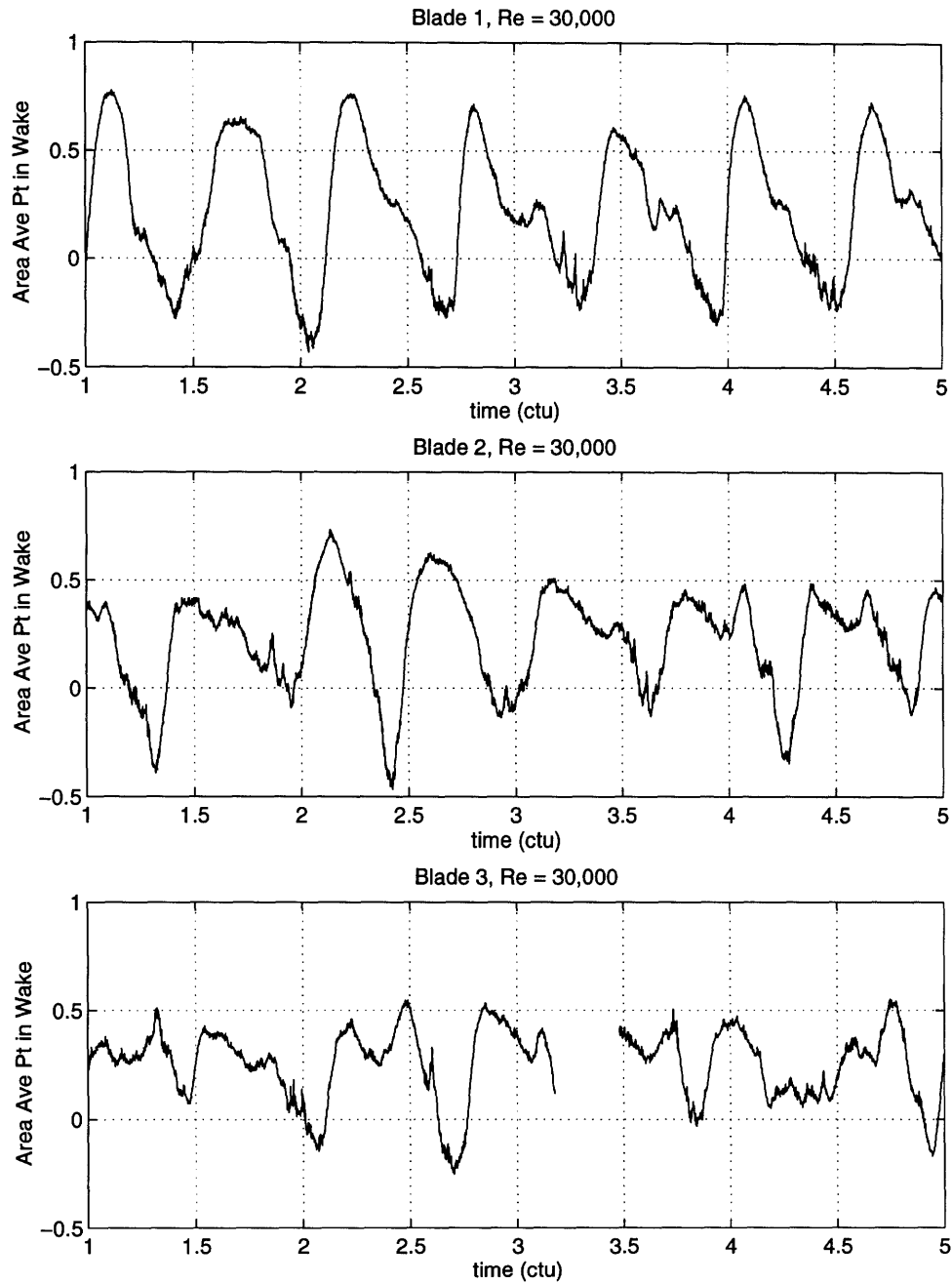


Figure 3-31: Variation of area-averaged total pressure in the wake as a function of time showing the differences in the wake structure for each blade, $Re = 30,000$ (the break in the curve for *blade 3* is due to a loss of data)

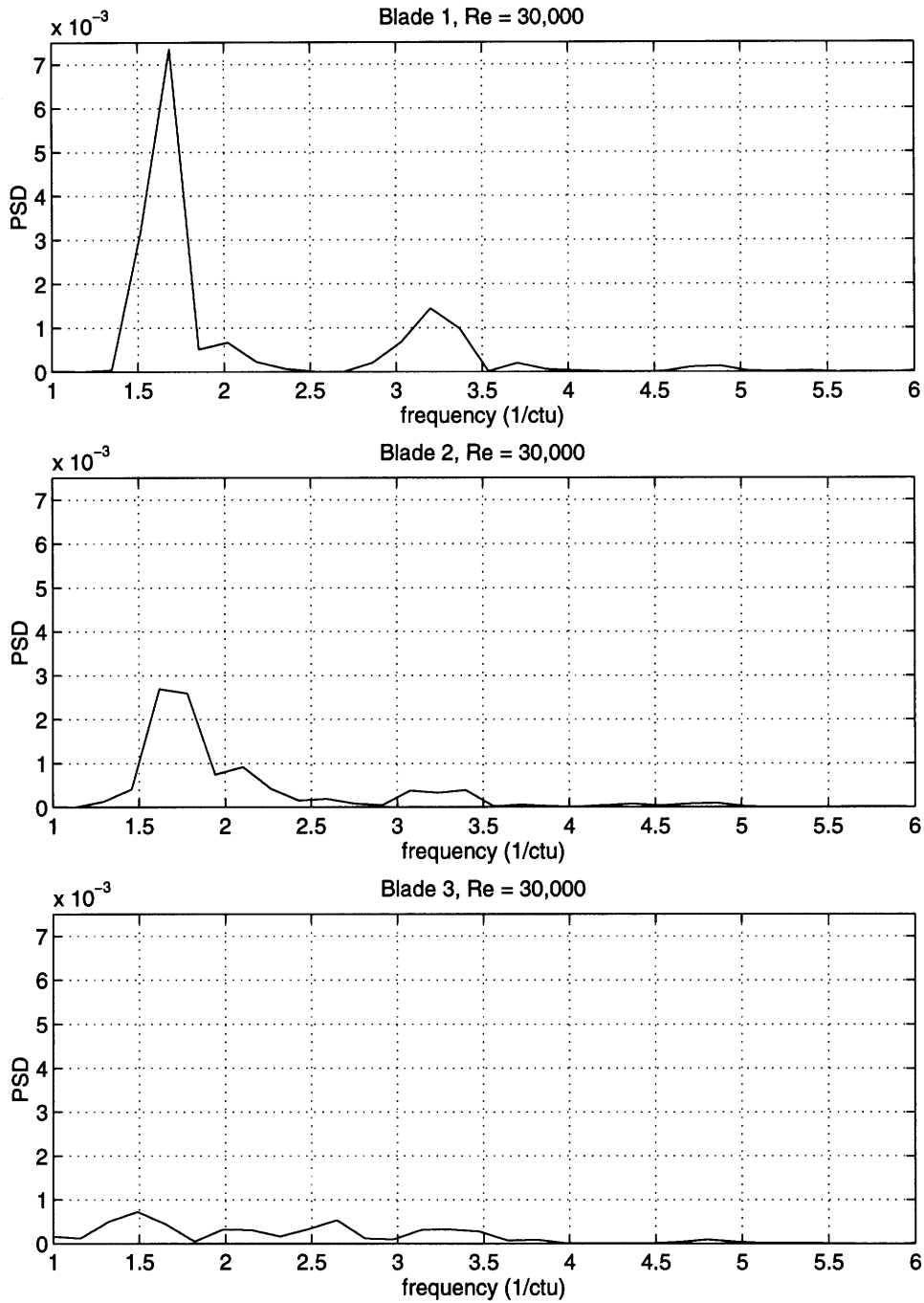


Figure 3-32: Power spectral density of time traces given in figure 3-31, variation in shedding frequencies for the three blades, $Re = 30,000$

for *blade 1* at $Re = 30,000$. The eight frames (with a time of 0.09 ctu between frames) detail the shedding cycle for *blade 1*.

This cycle consists of the shedding of a large vortex from the suction side, followed by a vortex from the pressure side. As the next large suction side vortex is formed, additional vorticity is produced and is shed from the blade suction side. This results in the shedding of two pair of vortices; two from the suction side boundary layer, and two from the pressure side.

Frame 1 (figure 3-33) depicts the point in the process immediately prior to the shedding of the large suction side vortex. Frames 2 and 3 show the breakoff of the suction side vortex, as well as the beginning of the roll-up of the pressure side shear layer. By frame 4, the large pressure side vortex is formed (black region directly downstream of the trailing edge), and the pressure field caused by this flow feature stagnates the fluid over the suction side. It is during this time period that the buildup of suction side vortical fluid occurs. At frame 7, the first small vortex from the suction side has been shed, and the formation of the pressure side vortex is taking place. Finally, frame 8 returns back to the point shown in frame 1, with the last small pressure side vortex forming, and release of the large suction side vortex imminent.

The upstream movement of the time-averaged vortex in the trailing edge region for *blade 3* is due to the earlier roll-up of the shear layer as the Reynolds number is increased from 20,000 to 30,000. Figure (3-41) is an instantaneous plot of the vorticity at a point where the suction side shear layer is forming into a vortex. Comparing this picture to that found in figure (3-18), one observes that the location of the vortex formation indeed has moved upstream. These plots also show the increase in vortex size and spacing associated with the change in Reynolds number, as compared with the high frequency shedding, and small vortices found for *blade 3* at $Re = 30,000$.

Following the same procedure as given in the preceding section, the non-dimensional frequency is calculated using equation (3.13). The determination of the vortex shedding frequency from the suction side shear layer is easier for *blade 1* and *blade 2* as compared to the 20,000 case because of the single dominant frequency in the wake (figure 3-32). This dominant frequency found for *blade 1* and *blade 2* corresponds to frequency at which the suction side shear layer forms into a vortex. An observation of the movies made for *blade 1* and *blade 2* confirm that this procedure is correct.

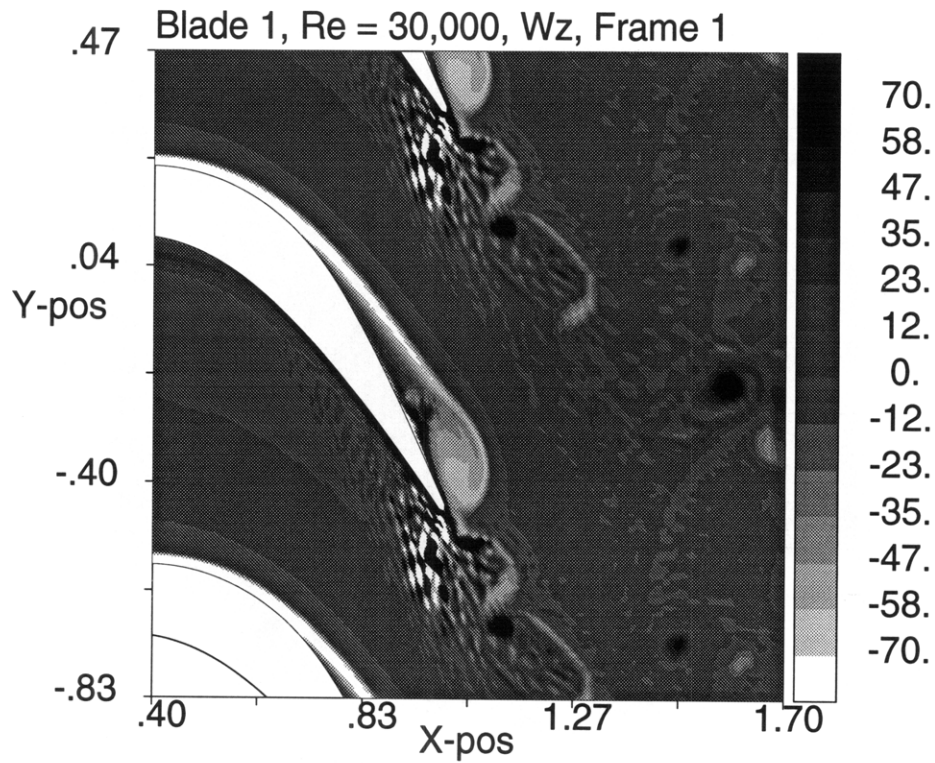


Figure 3-33: Instantaneous vorticity field for *blade 1*, Re = 30,000, T = 0.00 ctu

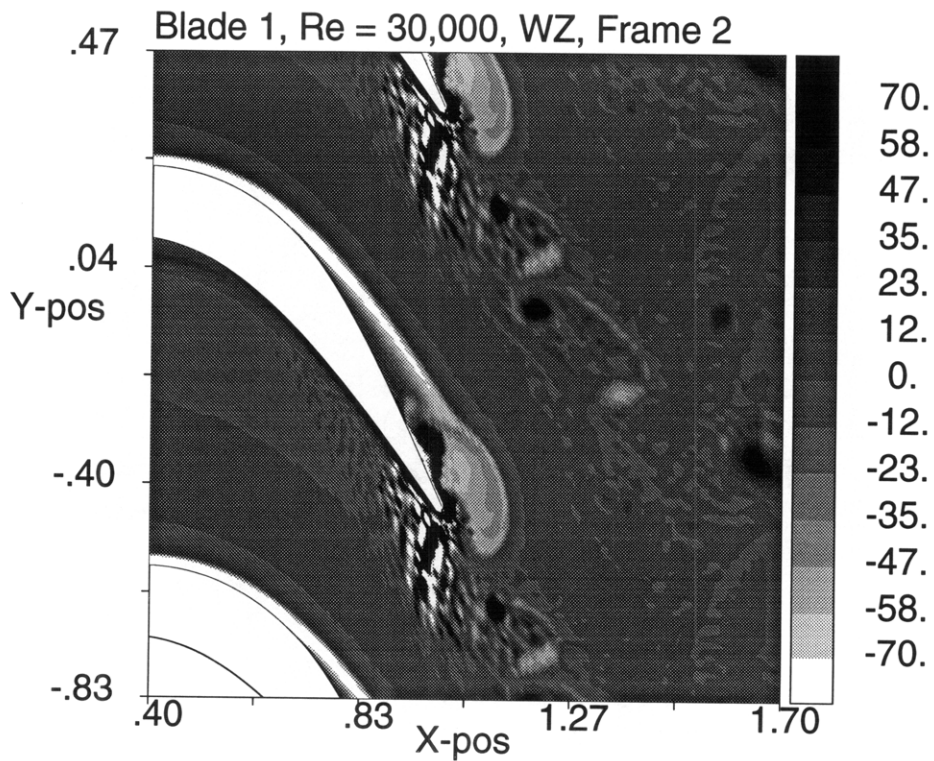


Figure 3-34: Instantaneous vorticity field for *blade 1*, Re = 30,000, T = 0.09 ctu

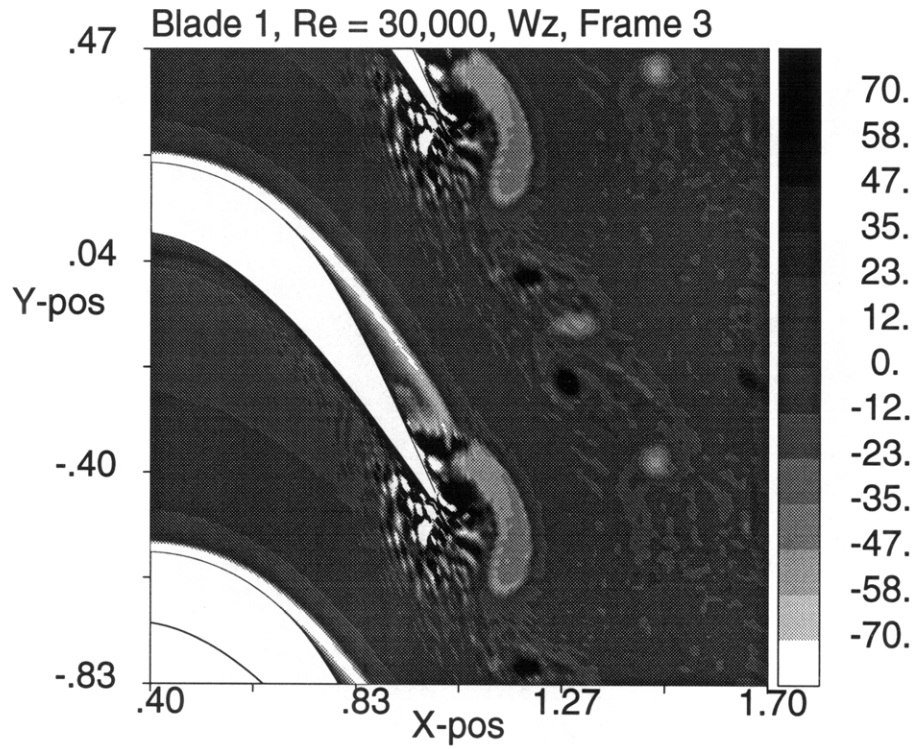


Figure 3-35: Instantaneous vorticity field for *blade 1*, Re = 30,000, T = 0.18 ctu

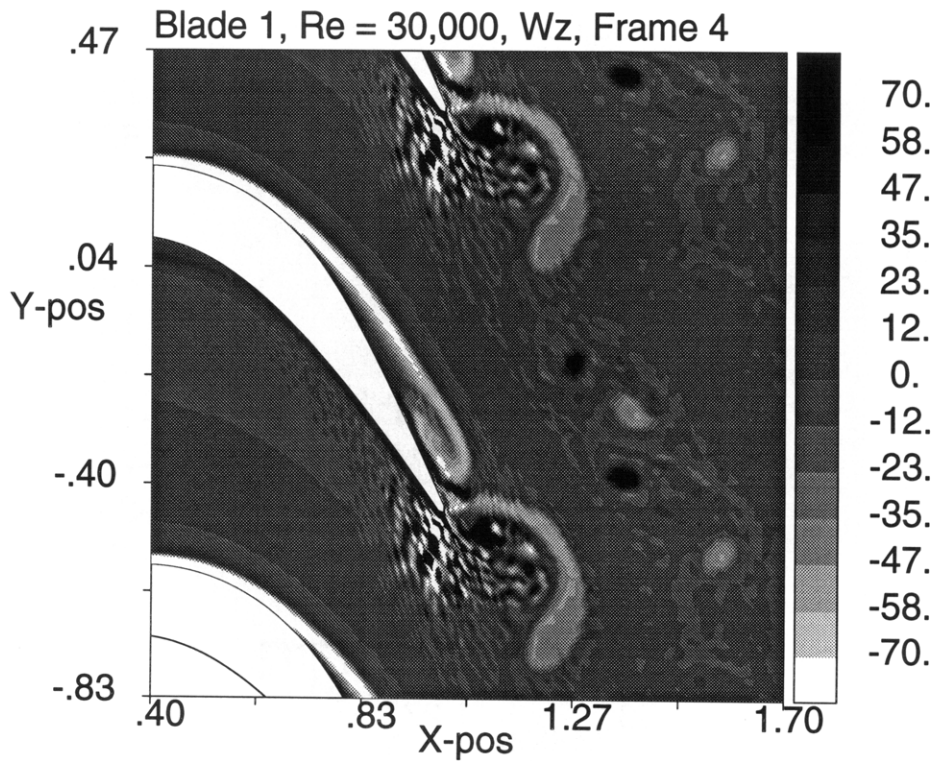


Figure 3-36: Instantaneous vorticity field for *blade 1*, Re = 30,000, T = 0.27 ctu

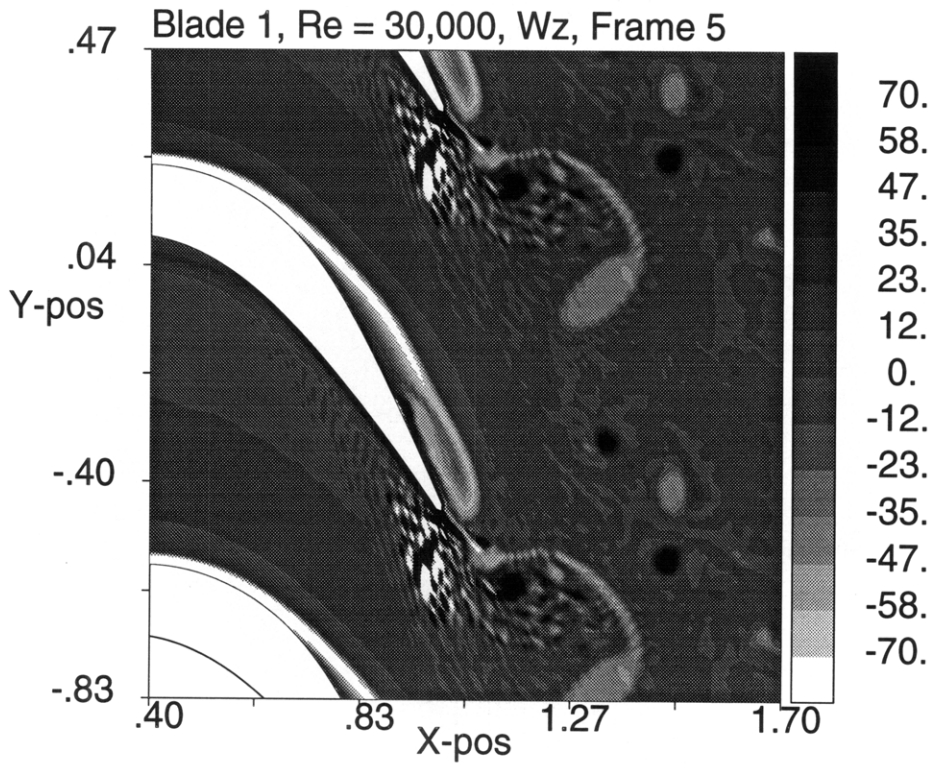


Figure 3-37: Instantaneous vorticity field for *blade 1*, Re = 30,000, T = 0.36 ctu

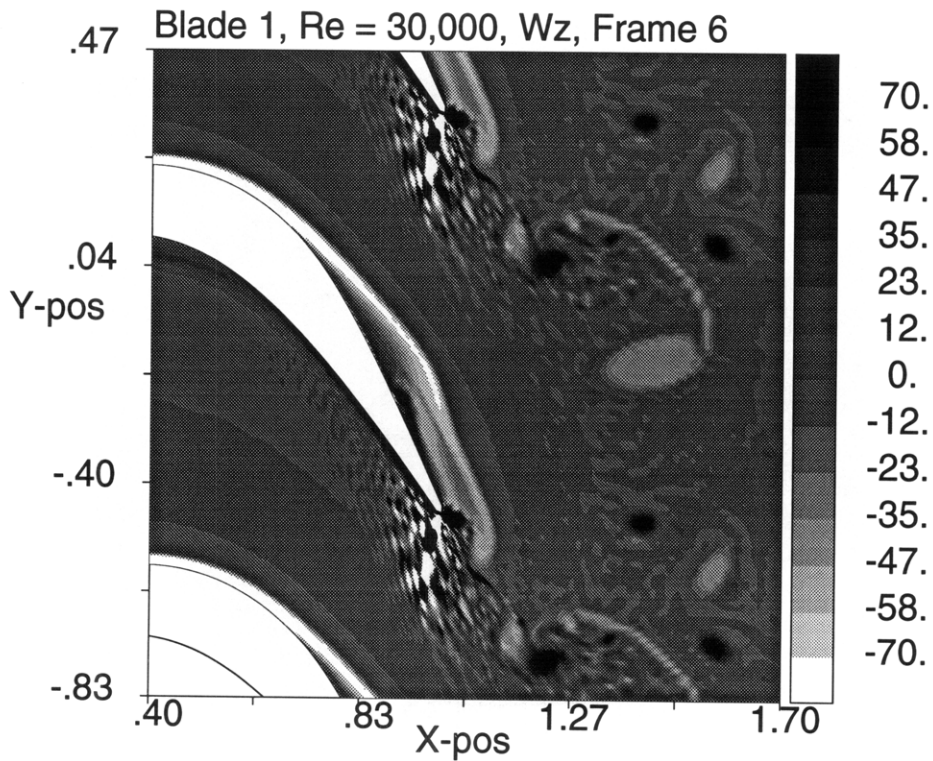


Figure 3-38: Instantaneous vorticity field for *blade 1*, Re = 30,000, T = 0.45 ctu

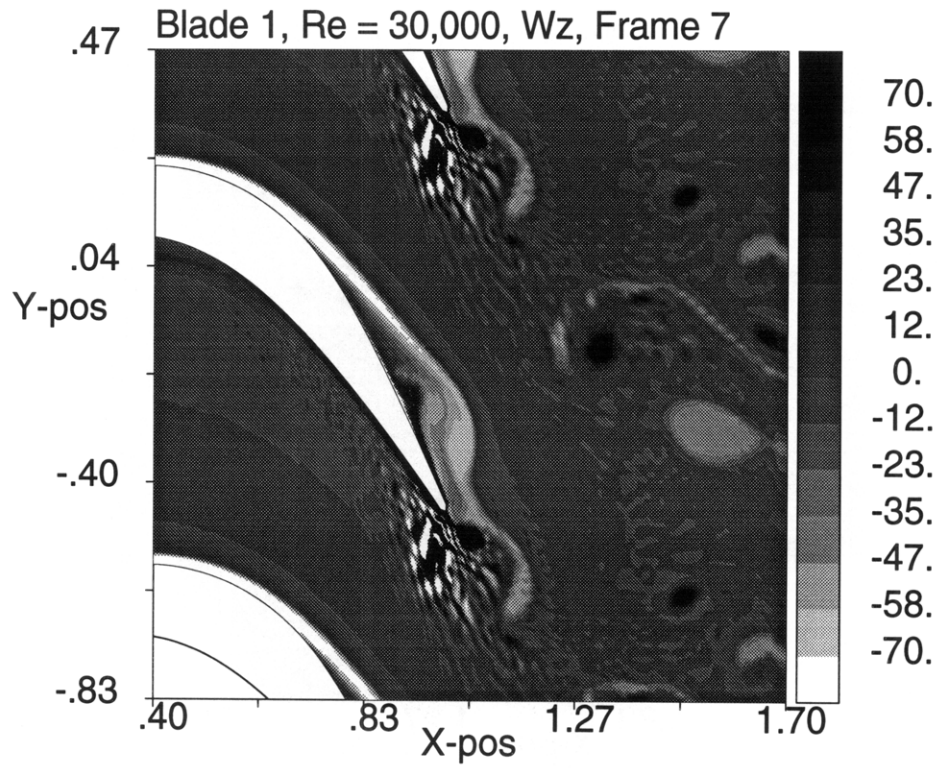


Figure 3-39: Instantaneous vorticity field for *blade 1*, Re = 30,000, T = 0.54 ctu

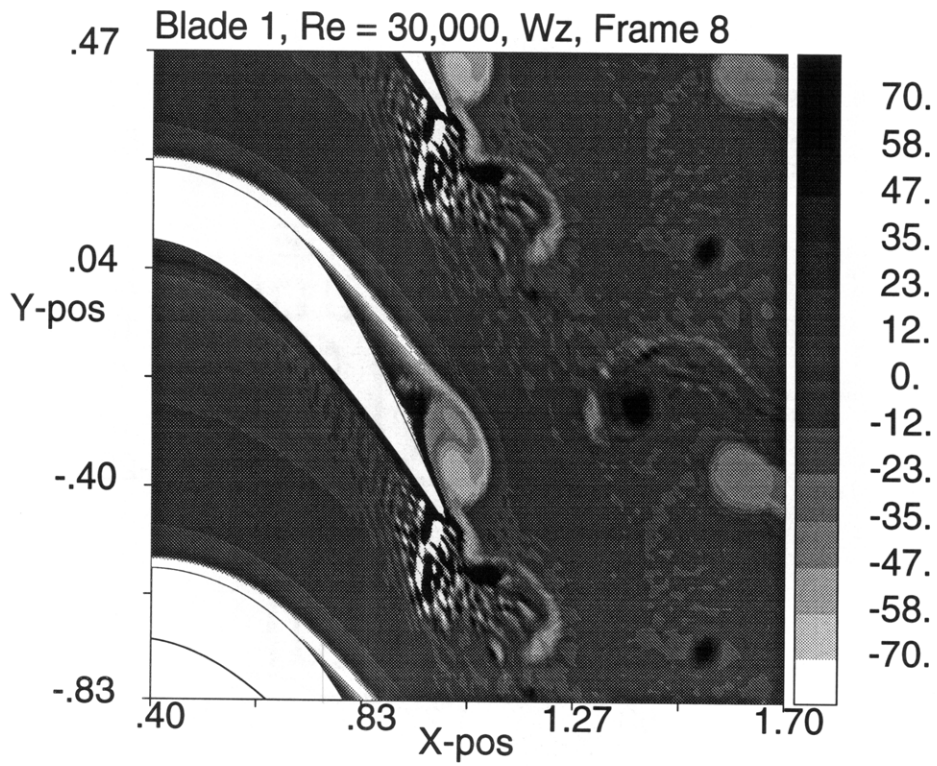


Figure 3-40: Instantaneous vorticity field for *blade 1*, Re = 30,000, T = 0.63 ctu

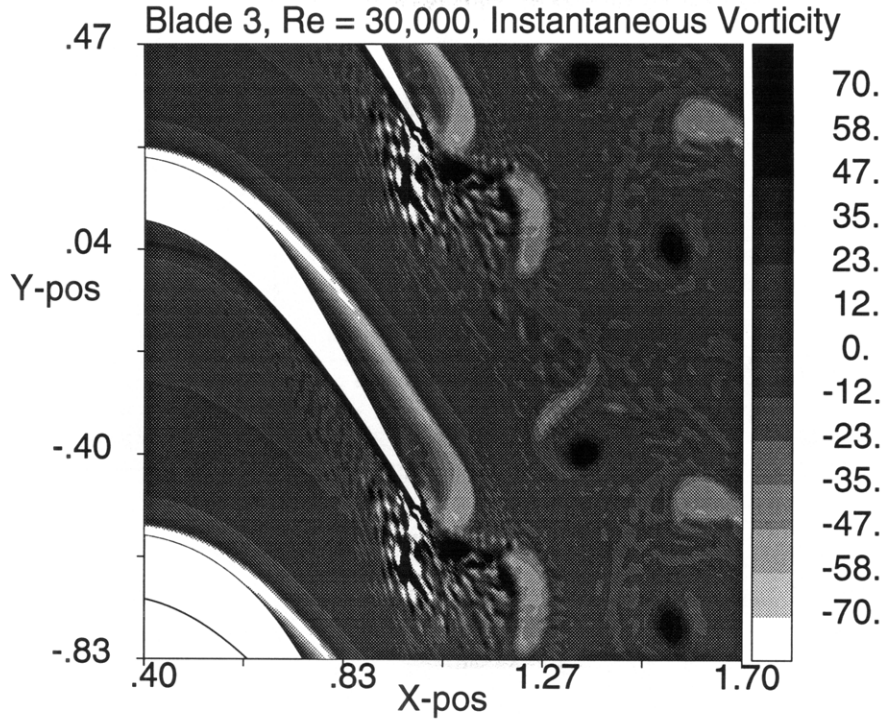


Figure 3-41: Instantaneous vorticity field for *blade 3*, Re = 30,000

Blade	u_2	u_1	$\left(\frac{\partial u}{\partial y}\right)_{max}$	f	ω^*
1	2.48	-0.60	43	1.7	0.20
2	2.39	0.32	25	1.7	0.16
3	2.42	0.08	35	2.7	0.23

Table 3.3: Values used for calculation of ω^* , Re = 30,000

The determination of a suction side vortex shedding frequency for *blade 3* is less exact. The shedding cycle is very much like that for *blade 1* and *blade 2* at the Reynolds number of 20,000. Therefore, for simplicity, the frequency chosen for *blade 3* in table (3.3) corresponds to the shedding frequency used for *blade 2* in table (3.2). As for the Re = 20,000 case, these non-dimensional shear layer shedding frequencies at Re = 30,000 are within the range of the most amplified frequency of $\omega^* = 0.21$.

3.2.21 Static Pressure Deviations Due to Unsteadiness at Re = 30,000

Another result of the increase of Reynolds number from 20,000 to 30,000 is given by the change in the unsteadiness of the blade surface pressure (figure 3-42). *Blade 1* shows a marked increase in the pressure deviation over that for Re = 20,000 on the suction side.

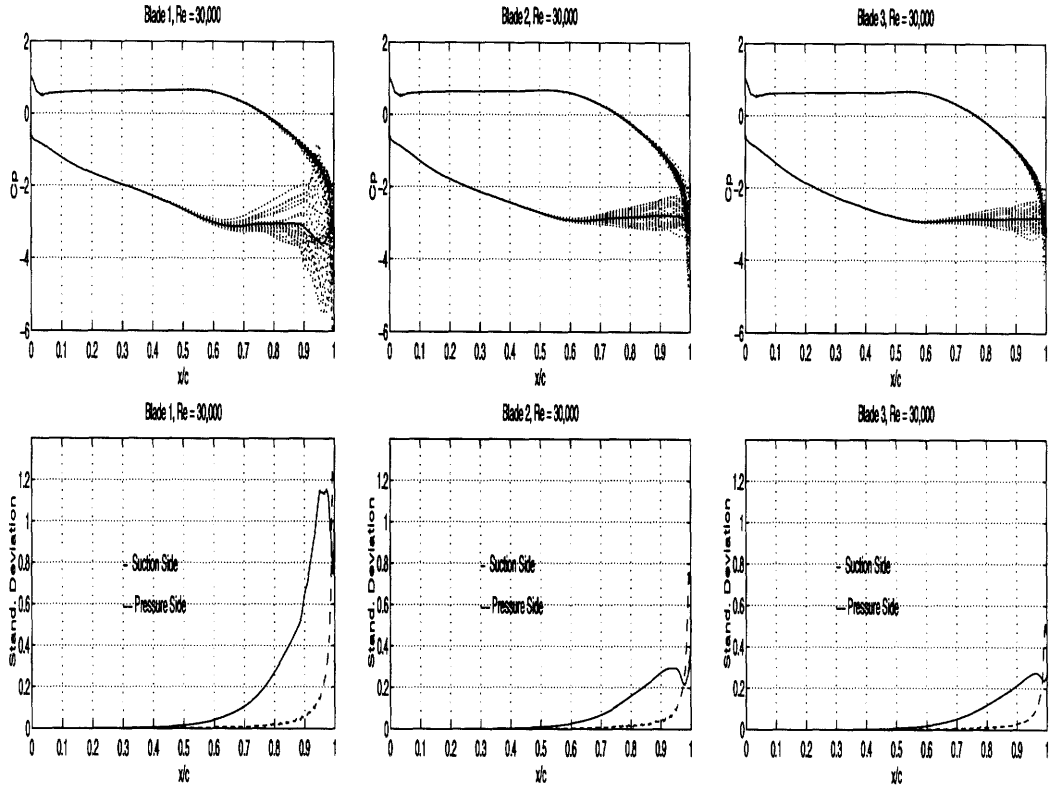


Figure 3-42: Static pressure envelopes over the blade surface and standard 3 deviation of the fluctuations for blades 1, 2, 3, at $Re = 30,000$

Notice the rapid increase of the pressure deviation in the last 9/10 of chord. Also, the unsteadiness for *blade 3* at $Re = 30,000$ increases when compared to the situation at $Re = 20,000$ (figure 3-21).

As described in the previous sections, the location of the shear layer roll-up on the suction side for *blade 1* moves upstream of the roll-up location occurring for $Re = 20,000$. This causes the pressure to have large amplitude fluctuations in the region within the last 0.1 axial chords of the blade.

Little change in the pressure deviations is observed for *blade 2* when comparing figures (3-21) and (3-42). This corresponds to the observations made by looking at the movies made for the two Reynolds numbers. The shedding moves upstream slightly, but there is no big change in the dynamics as is found for *blade 1* or *blade 3*.

The pressure fluctuations for *blade 3* increases from the 20,000 case, and the pressure “envelope” formed is similar to the one for *blade 2* at this Reynolds number.

Thus, one can infer from these findings that *blade 1* is further along in the re-attachment process than the other two blades, with *blade 3* being the geometry furthest from re-

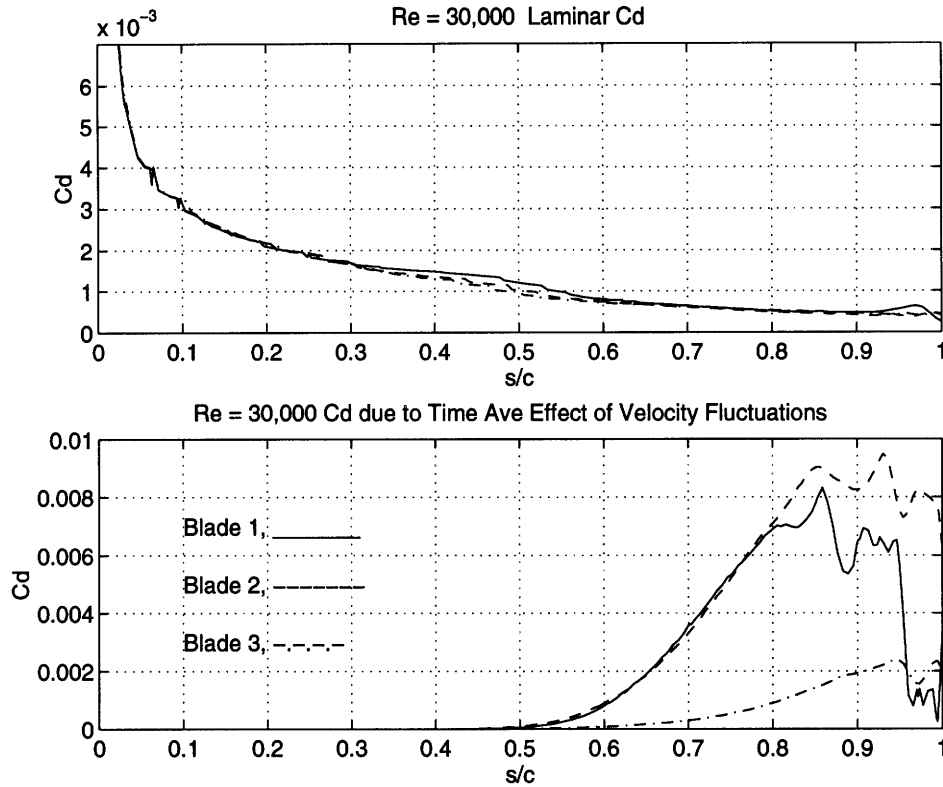


Figure 3-43: Laminar dissipation coefficient and dissipation coefficient associated with unsteadiness on the suction side for all three geometries at $Re = 30,000$, plotted along the blade surface

attachment. These results are linked to the blade geometry, with the aft loading for *blade 1* promoting an earlier roll-up.

3.2.22 Dissipation Coefficient at $Re = 30,000$

A final look at the solutions for all three geometries at $Re = 30,000$ is made using the dissipation coefficient. Figure (3-43) details the laminar dissipation coefficient and the dissipation coefficient associated with flow unsteadiness. The ratio of these two coefficients is given in figure (3-44).

The laminar dissipation is nearly identical for the three geometries, whereas the unsteady dissipation is greatly increased for *blade 1* and *blade 2* as compared to that for *blade 3*. Also, $(C_d)_{u'v'}$ for *blade 1* and *blade 2* is larger than the corresponding values at $Re = 20,000$ (figure 3-22). The ratio $(C_d)_{u'v'}/(C_d)_{lam}$ approaches a value of 15 to 20 in the last 0.2 chords. Thus, the process of the shear layer roll-up on the suction side increases the effective dissipation in this region.

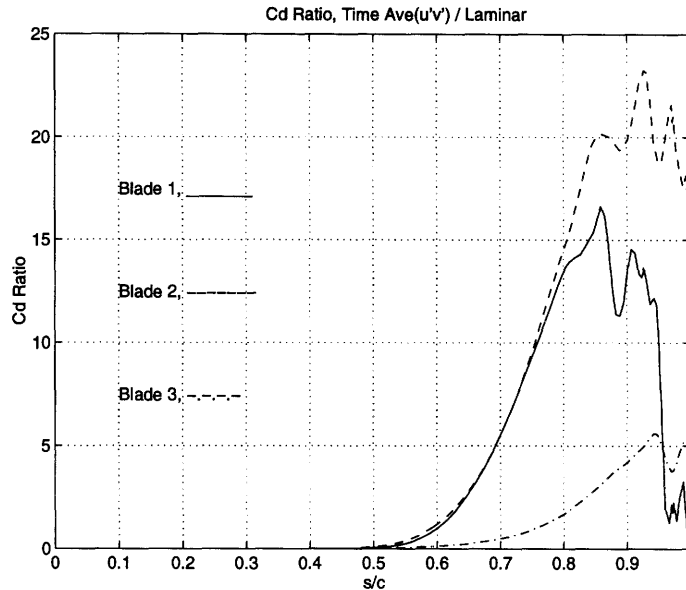


Figure 3-44: Ratio of the unsteady to laminar dissipation coefficients on the suction side, $Re = 30,000$, plotted along the blade surface

3.2.23 Summary of Observed Unsteady Features at $Re = 30,000$

The change of Reynolds number from 20,000 to 30,000 produces two major changes for the set of solutions. The roll-up location of the suction side shear layer moves over the blade surface for *blade 1*. This change coincides with an increase in amplitude of the pressure deviations as well as the effective dissipation.

The other change is related to the shedding dynamics observed for *blade 3*. The $Re = 20,000$ solution for *blade 3* features the shedding of small vortices, at a high frequency. The increase in the Reynolds number to 30,000 causes this process to shift so that the shear layer roll-up occurs closer to the blade trailing edge, with an increase in the size of the vortex shed and a decrease in the shedding frequency.

These differences observed in the flow features for the three geometries is an indication that the spectral code is able to detect flow field changes due to small variances in the design. This renders a measure of confidence that solutions for higher Reynolds numbers can likewise be accomplished, and that they could be of utility to discern dynamical differences between the three blades.

3.3 High Reynolds Number Solutions

The categorization of the solutions into “low” Reynolds number cases and “high” Reynolds number cases was made for two reasons.

One, the lower Reynolds numbers are characterized by a roll-up process of the suction side shear layer that occurs downstream of the blade trailing edge. The only solution that showed a suction side shear layer roll-up occurring upstream of the trailing edge was *blade 1* at $Re = 30,000$.

The higher Reynolds number cases all show a similar process, with the formation of the suction side vortex taking place upstream of the trailing edge. Thus, the unsteady dynamics are different when compared to the majority of the low Reynolds number solutions.

Second, the distinction between the solutions is made because of the drop in loss level seen. A periodic re-attachment process occurs on the suction side, corresponding to a drop in the loss. This is especially evident for the 90,000 and 120,000 cases. Also, the Reynolds numbers used for these high Reynolds number cases is more on par with those found in LPT operation.

3.3.1 Time-Average Solutions at $Re = 60,000$

As demonstrated in table (3.1), computations were made at a Reynolds number of 60,00 for *blade 1* and *blade 3* only. This was done because of time limitations, and since the trends for the blades follow a certain pattern (as found by observing the low Reynolds number solutions), it was determined that calculations for *blade 1* and *blade 3* were sufficient.

Computed results will be presented to highlight :

1. the similarity in the flow field for *blade 3* at $Re = 60,000$ to that for *blade 1* at 30,000
2. the change in the shedding process for *blade 1* at $Re = 60,000$ compared to the process found for *blade 1* at 30,000

3.3.2 Total Velocity and Static Pressure Contours at $Re = 60,000$

Computations at an exit Reynolds number of 60,000 were made for *blade 1* and *blade 3* with the time-averaged static pressure and total velocity contours given in figure (3-45). A low pressure region still remains over the suction surface for *blade 1* as was seen at the lower

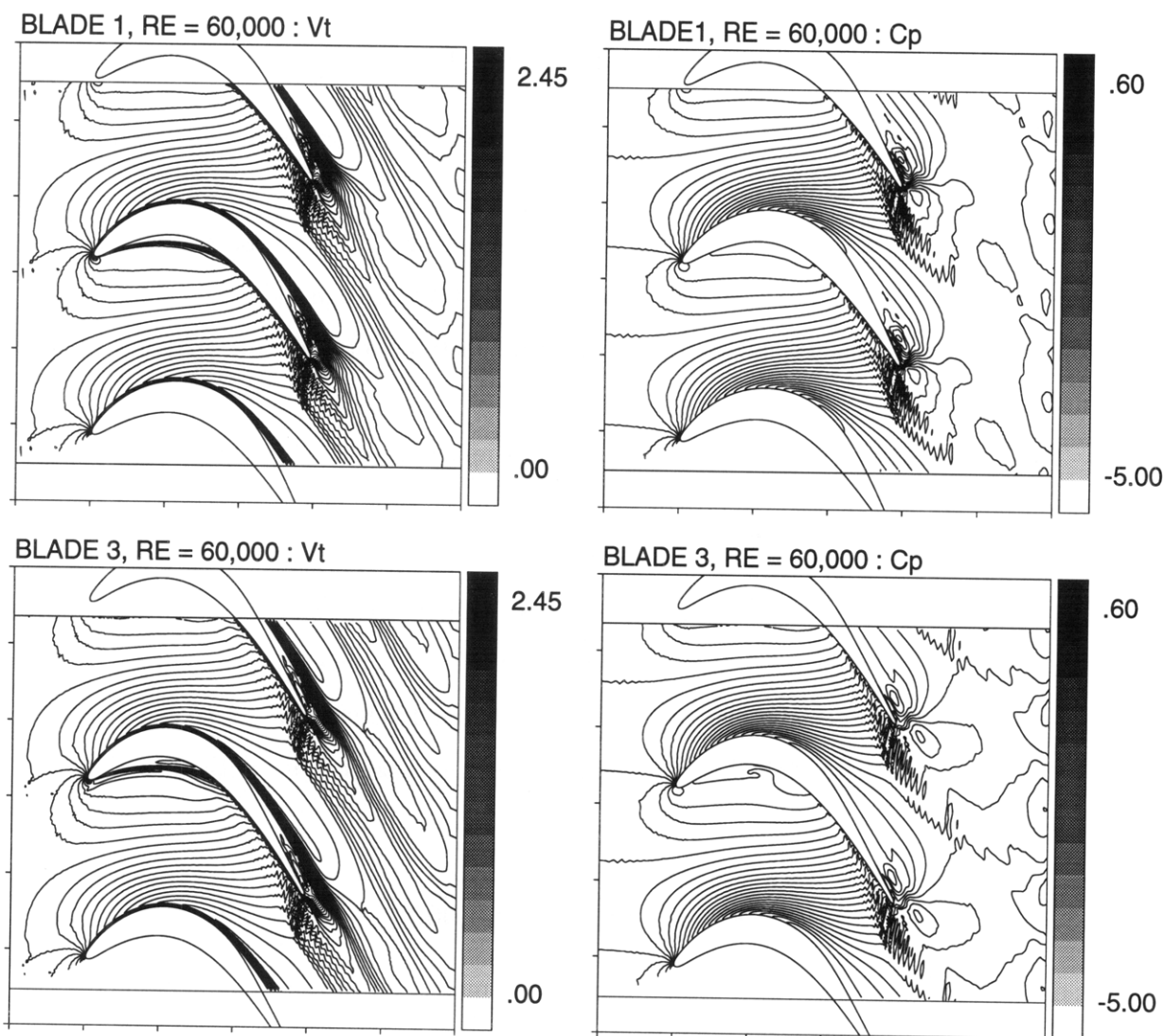


Figure 3-45: Time-averaged total velocity and static pressure coefficient contours, blades 1, 3, $Re = 60,000$

Reynolds numbers, but the separated region is observed to be reduced in size upon closer examination of time-averages and the movies of the computed unsteady flow fields. The solution for *blade 3* indicates a low pressure region on the suction side, as well as a change in the structure of the pressure side separation bubble.

The shear layer in the concave portion of the pressure side for *blade 1* remains steady, with no observable difference seen in the time-average between the 30,000 case and this 60,000 case. However, a change is noticed for the shear layer for *blade 3* on the pressure side.

As will be shown in section (3.3.6), this change in the time-average pressure side shear

layer for *blade 3* is due to unsteady shedding of vortices. The pressure side geometry for *blade 3* is compared to *blade 1* in figure (3-7). This indicates that *blade 3* has a smaller radius of curvature on the pressure side as compared to *blade 1*. This may be the reason for the differing time-average pressure side separation bubbles between the blades.

Once again, it is seen that the blade geometry is a factor in determining the Reynolds number the shear layer will become unstable. The aft loaded blade (*blade 1*) has been shown to have an earlier point of shear layer roll-up compared to the forward loaded blade (*blade 3*).

This same principle applies to the pressure side. The smaller radius of curvature for *blade 3* in the concave region causes the inviscid pressure gradient to be greater in magnitude than that found for *blade 1*. Thus, the shear layer for *blade 3* tends to become unstable earlier than that for *blade 1*.

3.3.3 Surface Static Pressure Coefficient and Skin Friction at $Re = 60,000$

The surface pressure and skin friction (figure 3-46) demonstrate the same features as shown in the contour plots. *Blade 3* has developed a low pressure region at the trailing edge, similar to that for *blade 1* at this Reynolds number. From the dynamics observed for the low Reynolds number solutions, this low pressure region on the suction side is a direct result of the unsteady flow features that develop in the aft region of the blade.

The time-averaged C_f plots indicate the changing dynamics on both the suction sides, and for *blade 3*, the beginning of the breakup of the pressure side bubble.

3.3.4 Total Pressure Loss at $Re = 60,000$

The mass-averaged total pressure loss for *blade 1* and *blade 3* is shown in figure (3-47). The trend found at lower Reynolds numbers continues at $Re = 60,000$, with *blade 3* generating more profile loss than *blade 1*. The jump in loss in the last 0.1 chords for both blades is due to the presence of a time-average vortex associated with the shear layer. This time-average flow feature constitutes a region of low momentum fluid in the trailing edge region, causing the time-average loss to rise.

The loss due to enstrophy is not of the same magnitude as the loss found using the mass-averaged total pressure, with the enstrophy loss being about 3 times smaller in magnitude

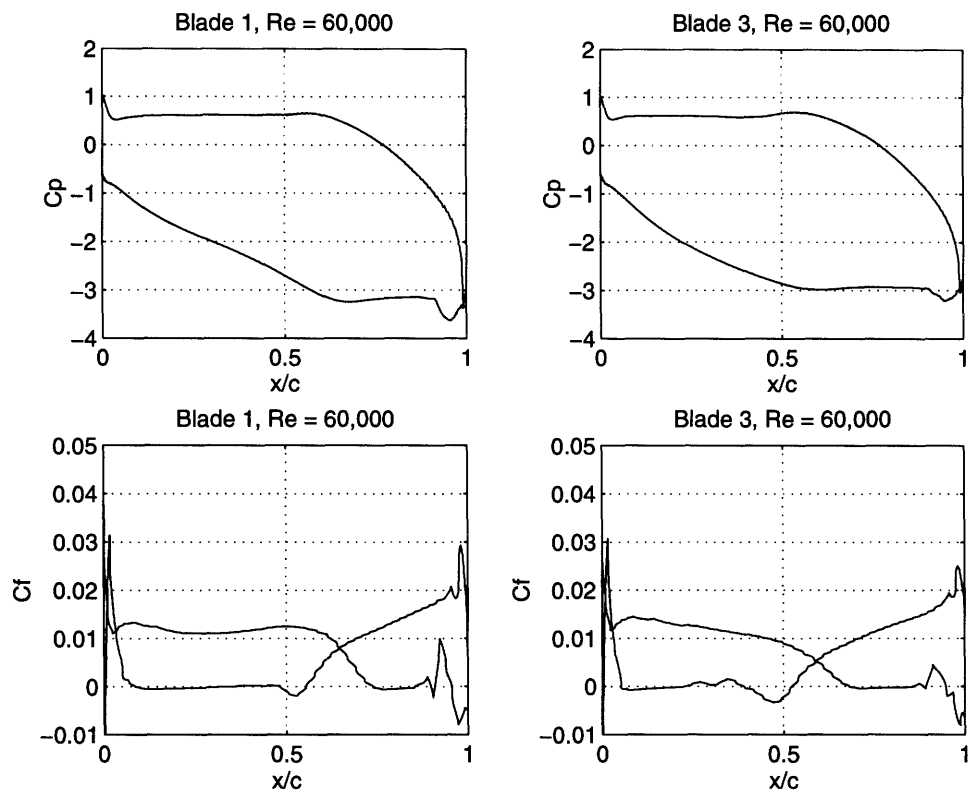


Figure 3-46: Time-averaged static pressure and skin friction on blade surface for $Re = 60,000$, blades 1 and 3

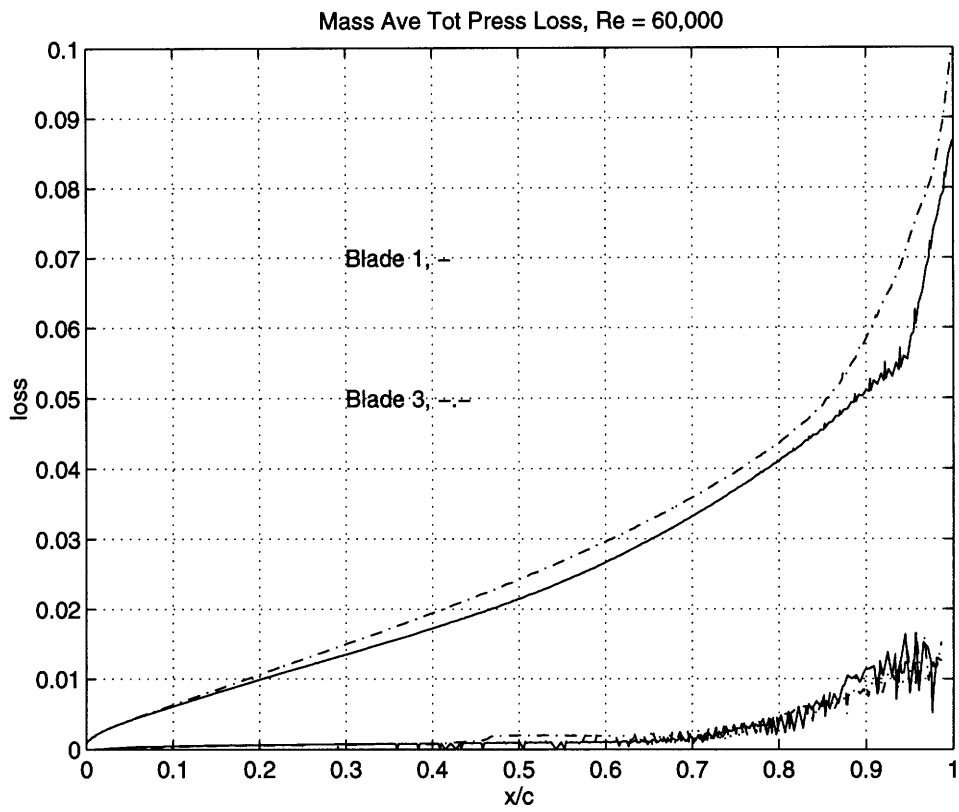


Figure 3-47: Mass-averaged total pressure loss, dimensionalized by exit dynamic head, for the suction and pressure sides at a Reynolds number of 60,000

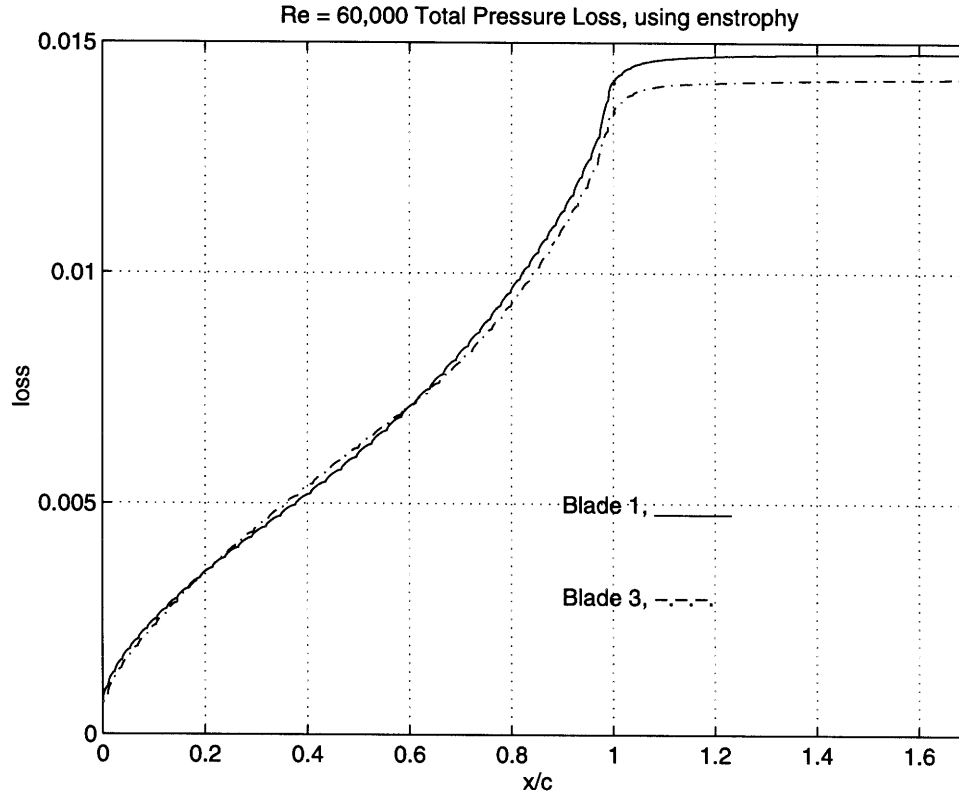


Figure 3-48: Loss calculated using enstrophy, $Re = 60,000$

for this 60,000 case.

Use of enstrophy translates into a smaller loss for *blade 3* at the trailing edge as compared to *blade 1*. For the lower Reynolds numbers (20,000 and 30,000) *blade 3* had higher loss than *blade 1*. Care must be taken when viewing these results because of the disagreement between the mass-averaged loss and enstrophy loss.

Performing a rough calculation for the mixing loss using equation (3.9), with a displacement thickness of $\delta_e^* = 0.076$ (found using the properties at the trailing edge for *blade 1*) results in an added loss due to mixing of 0.040. This is a decrease over the value found at $Re = 30,000$ ($loss_{mix} = 0.068$) by a factor of 1.7.

3.3.5 Summary of Time-Averaged Results at $Re = 60,000$

The time-average results at $Re = 60,000$ show that the time-average flow for *blade 3* is similar to that for *blade 1* at $Re = 30,000$ and 60,000. Specifically, a low pressure region develops upstream of the trailing edge for *blade 3*.

Another characteristic of the solution for *blade 3* is the beginning of the breakup of the

pressure side separation bubble. This effect is seen at lower Reynolds numbers for *blade 3* than for *blade 1* because of the smaller radius of curvature for *blade 3* on the concave portion of the pressure side.

The instability leading to the breakup of the pressure side bubble for *blade 3* can be related to the shear layer instability found on the suction side. In both cases, the greater the magnitude of the adverse pressure gradient, the earlier the instability occurs. Thus, for *blade 3*, the smaller radius of curvature leads to a greater *inviscid* pressure gradient, and a development of shear layer instability before *blade 1*. The *inviscid* adverse pressure gradient for *blade 1* is largest on the suction side, and the separated shear layer tends to roll-up sooner for this blade as compared to *blade 3*.

3.3.6 Unsteady Features at $Re = 60,000$

This section focuses on the observed similarity of the calculated unsteady flow for *blade 3* at $Re = 60,000$ with that of *blade 1* at $Re = 30,000$. Examinations of the flow field movies lead to the conclusion that the shedding dynamics for the two calculations are nearly identical.

Also, the unsteady features found for *blade 1* at $Re = 60,000$ are similar to those for *blade 1* at $30,000$, with one slight difference. This is found when comparing the pressure deviations and the magnitude of the unsteady dissipation coefficients as compared to the $30,000$ solution for *blade 1*.

3.3.7 Total Pressure Variation in the Wake at $Re = 60,000$

The total pressure time traces in the wake and the power spectral density of the signal for both *blade 1* and *blade 3* at $Re = 60,000$ are given in figures (3-49) and (3-50). The time traces are similar between the two blades, with the same dominant frequency (between 1.6 and $1.7 \text{ } ctu^{-1}$). This result indicates that the shedding process for the two blades resemble each other.

The dominant frequency at $1.6 \text{ } ctu^{-1}$ for *blade 3* is analogous to that observed in the power spectral density plot for *blade 1* at $Re = 30,000$ (figure 3-32). This dominant shedding frequency for *blade 1* at $30,000$ corresponds to the frequency at which vortices are shed from the suction side, leading one to infer that the same dynamics are causing the dominant frequency for *blade 3* at $Re = 60,000$. The observations made from the movies confirm this, with the two unsteady flows being nearly indistinguishable from one another.

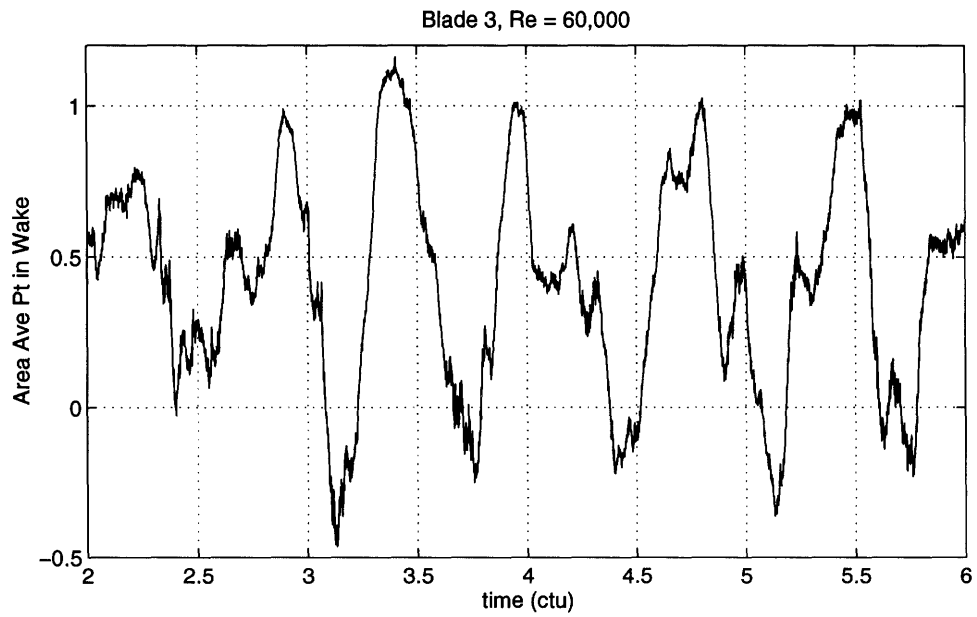
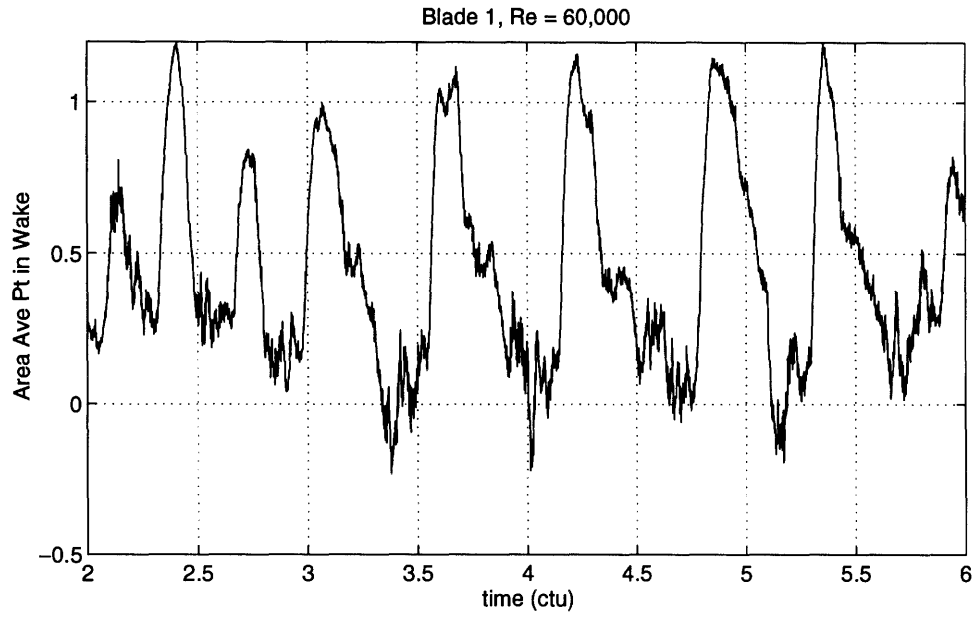


Figure 3-49: Variation of area-averaged total pressure in the wake as a function of time showing the differences in the wake structure for each blade, Re = 60,000

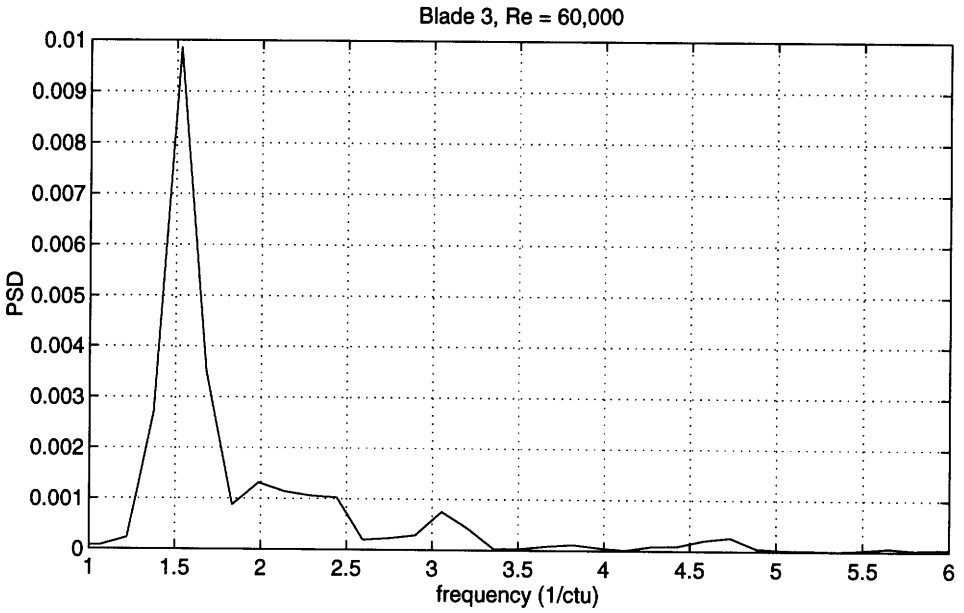
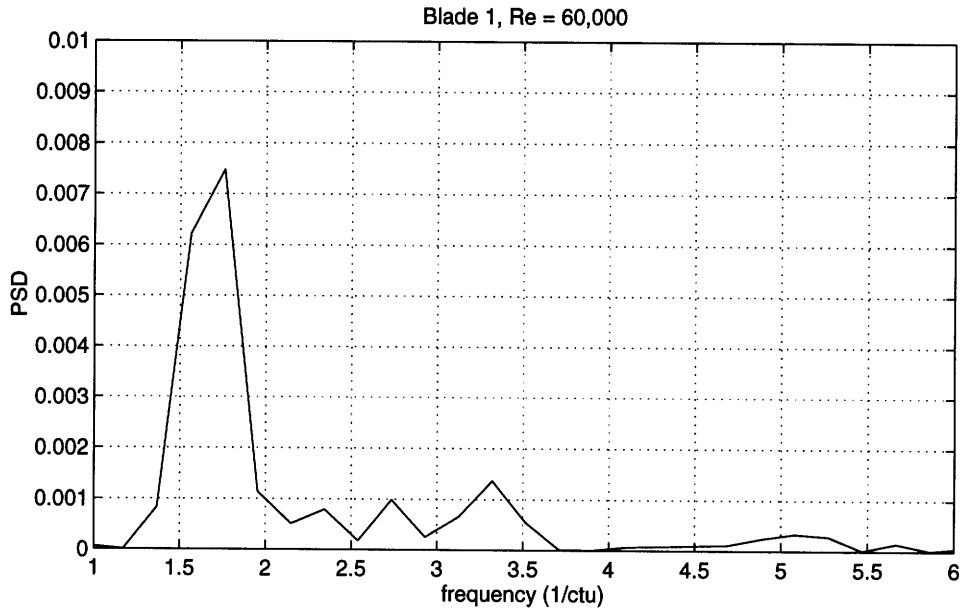


Figure 3-50: Power spectral density of time traces given in figure 3-49, variation in shedding frequencies for the three blades, Re = 60,000

3.3.8 Shear Layer Behavior at $Re = 60,000$

One of the noticeable differences for *blade 1* at this 60,000 case from the 30,000 case is the instability that develops for the pressure side separation bubble. Although the breakup of the pressure side shear layer into distinct vortices does not occur, an oscillation in the shear layer is present. This has little effect upon the surface pressure in this region, but it is noted for this case because it is the first sign of an impending breakup of the pressure side bubble for *blade 1*.

A larger change in the pressure side separation bubble is evident for *blade 3* than for *blade 1* at this Reynolds number. Distinct vortices are shed from the pressure side shear layer for *blade 3*, whereas *blade 1* only shows oscillations in the shear layer position.

The vortices shed from the pressure side for *blade 3* are organized, and travel down the pressure side. The region between $x/c = 0.4$ and 0.6 is the region where the disturbances have the most impact, and downstream of this, the favorable pressure gradient on the pressure side tends to reduce the non-uniformity associated with the vortices. Figures (3-51) and (3-52) display a snapshot of the dynamics on the pressure sides of *blade 1* and *blade 3*.

Blade 3 has the widest variation in its unsteady flow features for the three Reynolds numbers of 20,000, 30,000, and 60,000. The shedding process evolves from high frequency vortices in the wake for the 20,000 calculation, to a lower frequency shedding at 30,000. The trend towards an earlier shear layer roll-up remains the same at 60,000. The vortex shedding from the suction side closely resembles the dynamical process evident in the *blade 1*, $Re = 30,000$ case, i.e, a pair of large vortices shed, with two pair of small vortices shed in between the lower frequency process (refer to the frame of pictures 3-33 to 3-40). Thus, it would appear that the same sequence of events is occurring for *blade 3* as the Reynolds number changes, with the difference being that the dynamics for *blade 3* are lagging behind the developments seen for *blade 1*.

A check of the non-dimensional frequency is made for the suction side shear layer, to see if it corresponds with the linear stability theory. This is done for the suction side for *blade 1* and *blade 3*, as well as for the pressure side of *blade 3*, where vortex shedding is observed.

As in all the other calculations (tables 3.2 and 3.3), the point of shear layer roll-up falls

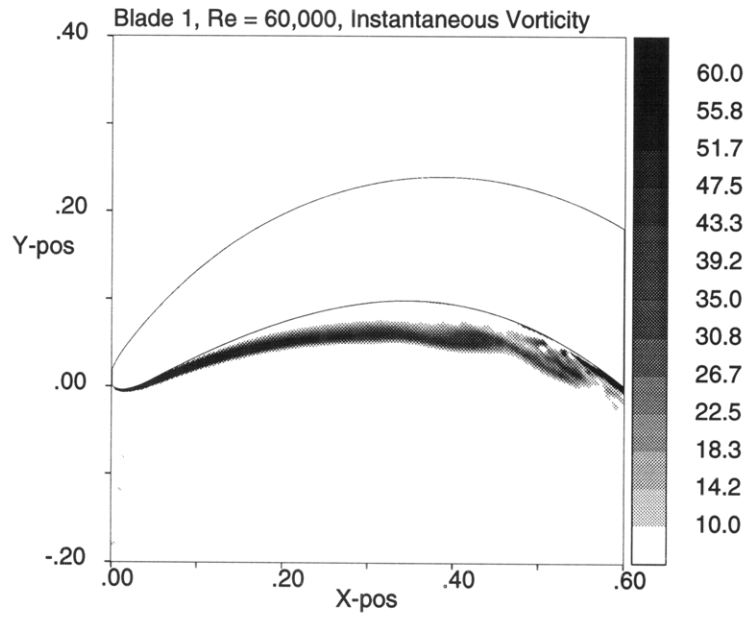


Figure 3-51: Instantaneous vorticity field for *blade 1*, Re = 60,000

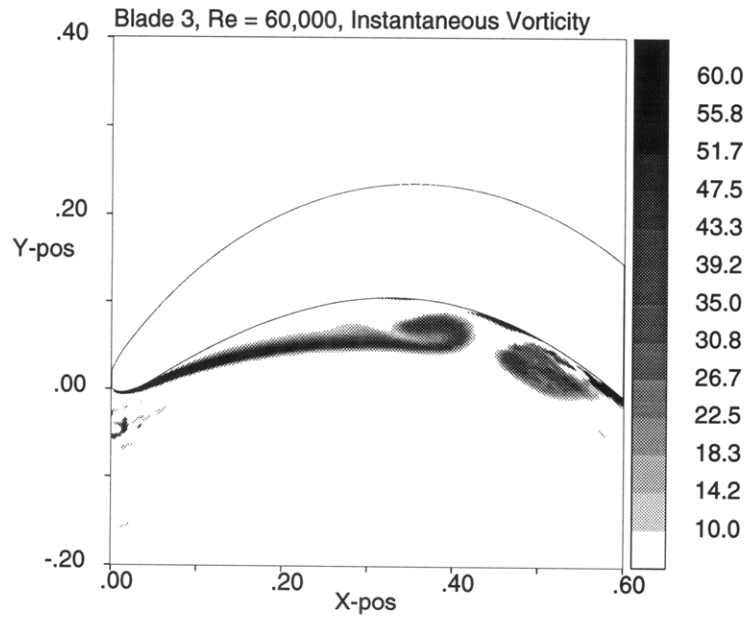


Figure 3-52: Instantaneous vorticity field for *blade 3*, Re = 60,000

Blade, side	u_2	u_1	$\left(\frac{\partial u}{\partial y}\right)_{max}$	f	ω^*
1, suction	2.53	-0.70	53	1.6	0.17
3, suction	2.47	-0.51	43	1.6	0.18
3, pressure	0.74	-0.13	27	1.2	0.20

Table 3.4: Values used for calculation of ω^* , $Re = 60,000$

within the range of $\omega^* = 0.21$.

3.3.9 Static Pressure Deviations Due to Unsteadiness at $Re = 60,000$

As expected, the movement upstream of the suction side shear layer roll-up for *blade 3* has an effect on the unsteadiness seen in the static pressure in the aft portion of the blade (figure 3-53). The standard deviation from the mean static pressure reaches a magnitude of 1, which is of the same order as the fluctuations seen for *blade 1*.

There are two interesting features seen on the standard deviation plots. First, the pressure fluctuations on the pressure side for all previous calculations have been nearly zero. The pressure deviation plot for *blade 3* (3-53) indicates that significant pressure fluctuations occur on the pressure side, between $x/c = 0.4$ and $x/c = 0.6$. These fluctuations are attributed to the vortex shedding from the pressure side shear layer. No such pressure deviations are seen for the *blade 1* calculation.

The other feature to point out from these plots is the “hump” seen for the suction side pressure deviation for *blade 1* at $Re = 60,000$. The deviation rises from a location of $x/c = 0.5$ to $x/c = 0.8$ where the deviations remain nearly constant, and even decrease slightly till the point $x/c = 0.9$. At this point there is a sharp rise in the pressure deviation. A correlation of this plot with observations made from the series of movies lead to the result that the majority of the unsteadiness associated with the vortex shedding on the suction side is localized within the last 0.1 axial chords of the blade.

Comparing the deviation plot for *blade 1* at 60,000 with that for *blade 1* at 30,000 (figure 3-42), the previous statements could not be made for the 30,000 calculation. The unsteadiness in the pressure rose rapidly from $x/c = 0.7$ to the trailing edge. Thus, the shedding process occurring for *blade 1* at 30,000 has a greater impact upon the overall flow field as compared to the localized shedding found for the 60,000 case.

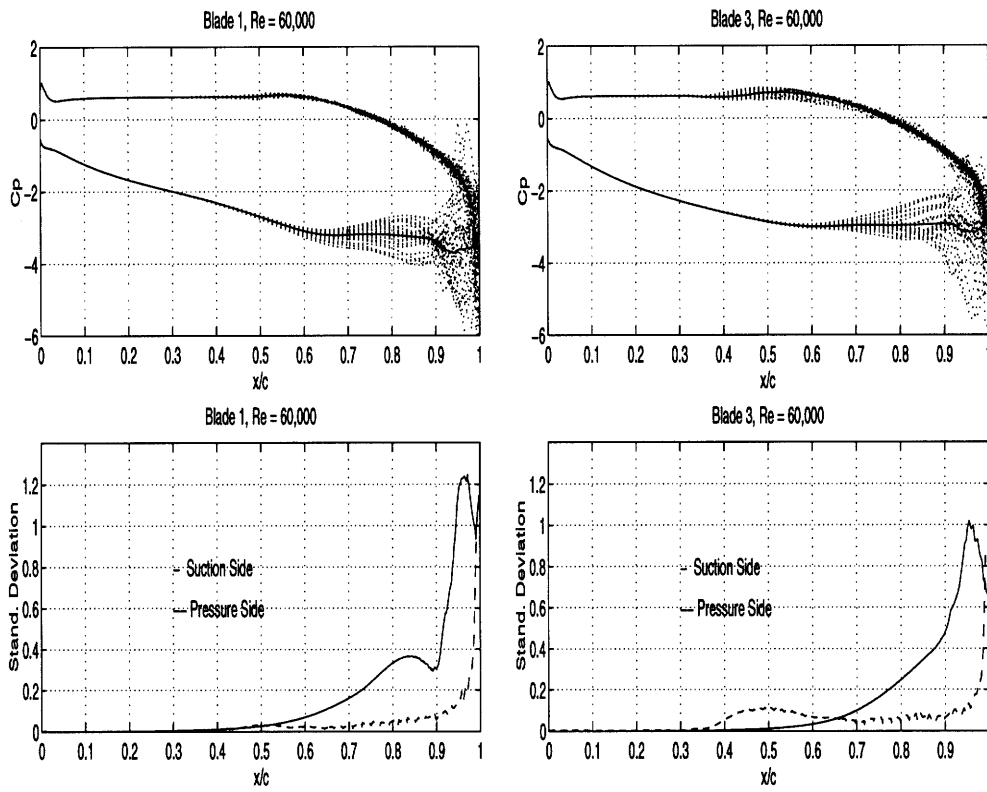


Figure 3-53: Static pressure envelopes over the blade surface and standard deviation of the fluctuations for blades 1, 3, at $Re = 60,000$

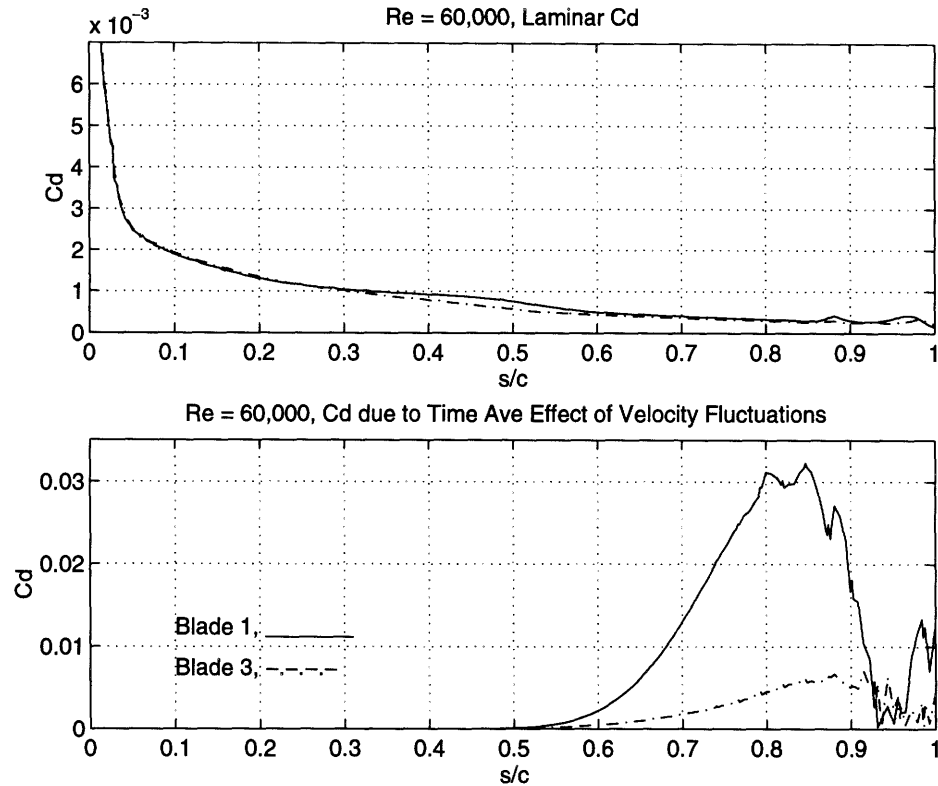


Figure 3-54: Laminar and unsteady dissipation coefficients on the suction side for all three geometries at $Re = 60,000$, plotted along the blade surface

3.3.10 Dissipation Coefficients at $Re = 60,000$

The laminar and unsteady dissipation coefficients are given in figure (3-54), with the ratio $(C_d)_{u'v'}/(C_d)_{lam}$ plotted in figure (3-55).

These figures reiterate the main points discussed in this section; the calculation for *blade 3* at 60,000 resembles that for *blade 1* at 30,000, and although the flow features are nearly the same for *blade 1* at 30,000 and 60,000, there is a change in the amount of unsteadiness.

The ratio of the unsteady to laminar dissipation coefficient for *blade 3* is on the order of 20 in the region just upstream of the trailing edge. This value is comparable to that found for *blade 1* and *blade 2* at $Re = 30,000$.

The increase in the unsteadiness for *blade 1* at 60,000 over that at 30,000 can be quantified by the ratio $(C_d)_{u'v'}/(C_d)_{lam}$. This reaches a magnitude of 100 in the aft region of the blade, as compared to values of 20 for a Reynolds number of 30,000. This increase in the dissipation could be considered a factor in the boundary layer re-attachment process.

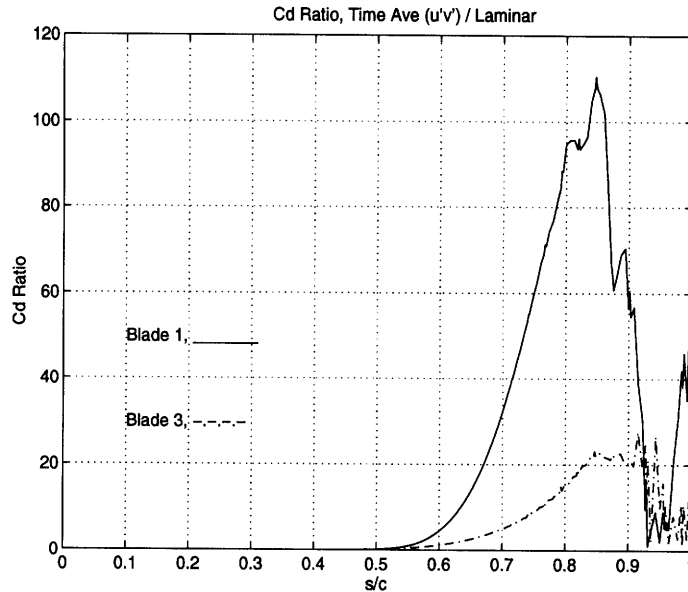


Figure 3-55: Ratio of the unsteady to laminar dissipation coefficients on the suction side, $Re = 60,000$, plotted along the blade surface

3.3.11 Summary of Observed Unsteady Features at $Re = 60,000$

The two main points discussed in this section were the similarity of *blade 1* at 30,000 to *blade 3* at 60,000, and the change in the unsteady character of *blade 1* from 30,000 to 60,000. These demonstrate the fact that *blade 3* lags behind *blade 1* in terms of the suction side shear layer development, with *blade 1* being closer to re-attachment. Therefore, if the time at which re-attachment occurs as a function of Reynolds number is used as a figure of merit, *blade 1* would have an advantage over *blade 3*.

3.3.12 Time-Average Solutions at $Re = 90,000$ and 120,000

The solutions for the Reynolds numbers of 90,000 and 120,000 are presented in the same section because of the observed similarity in the unsteady flow dynamics, as well as the comparable loss levels. A calculation was performed only for *blade 1* at 90,000, whereas solutions were calculated for both *blade 1* and *blade 3* at 120,000.

3.3.13 Total Velocity and Static Pressure Contours at $Re = 90,000$ and 120,000

The time-averaged flow contours for these solutions are given in figure (3-56). The suction side separation has decreased substantially compared to that for the $Re = 60,000$ solutions.

The low pressure region resulting from the time-average vortex on the suction side (figures 3-57, 3-58, and 3-59) has moved upstream from the trailing edge.

An elongation of the time-average vortex is a result of the shedding process, with vortices being formed well upstream of the trailing edge for *blade 1* at $Re = 120,000$. The convection downstream of these vortices results in a relatively large region of re-circulation found in the last two-tenths of axial chord for *blade 1*.

3.3.14 Surface Static Pressure Coefficient and Skin Friction at $Re = 90,000$ and $120,000$

The surface C_p and C_f for *blade 1* at 90,000 and 120,000 are shown in figure (3-60), and a comparison of C_p and C_f at $Re = 120,000$ for *blade 1* and *blade 3* is given in figure (3-61). As in previous cases, the time-average shows the indication of the low pressure region associated with the trailing edge vortex for *blade 1*. The fluctuations in C_f on the pressure side indicate the break-up of the pressure side separation bubble.

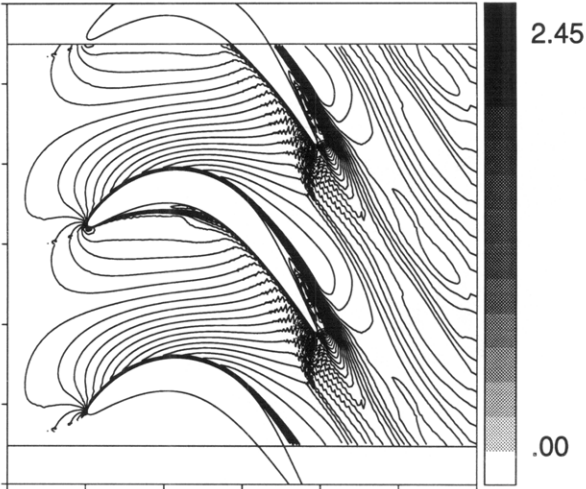
The region of low pressure found in the last two-tenths of chord from the trailing edge is an indication of the re-attachment of the suction side boundary layer, with a large adverse pressure gradient following the low pressure region. This is a result of the transport of fluid by the vortex from the freestream back towards the blade surface. Similar results have been found experimentally and in other detailed computations; the observed time-averaged separation bubble re-attachment correlates with a large pressure gradient at the point where the freestream fluid is being convected towards the surface [11].

3.3.15 Total Pressure Loss at $Re = 90,000$ and $120,000$

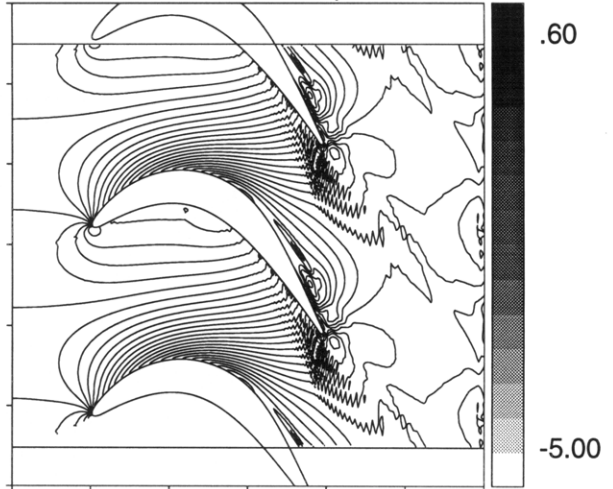
The loss calculated using the mass-averaged total pressure for *blade 1* at $Re = 90,000$ and $120,000$ is shown in figure (3-62). A comparison of the loss for *blade 1* and *blade 3* is made in (3-63). The loss found using enstrophy is given in figures (3-64) and (3-65). The loss is lower, as expected, for the 120,000 case over that found in 90,000. The rapid rise in loss in the last two-tenths of chord is associated with the time-averaged vortex present in this region. Once again, *blade 3* generates slightly more profile loss as compared to *blade 1*.

The time-average displacement thickness at the trailing edge for *blade 1* at 90,000 is $\delta_e^* = 0.068$, and for 120,000 $\delta_e^* = 0.058$. The displacement thickness for *blade 3* at 120,000 is $\delta_e^* = 0.048$.

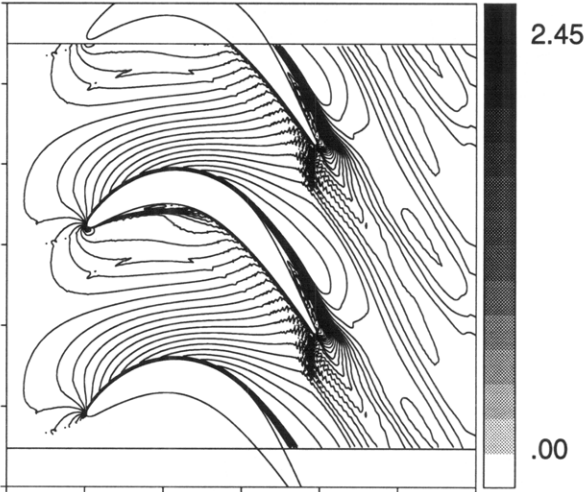
BLADE 1, RE = 90,000 : Vt



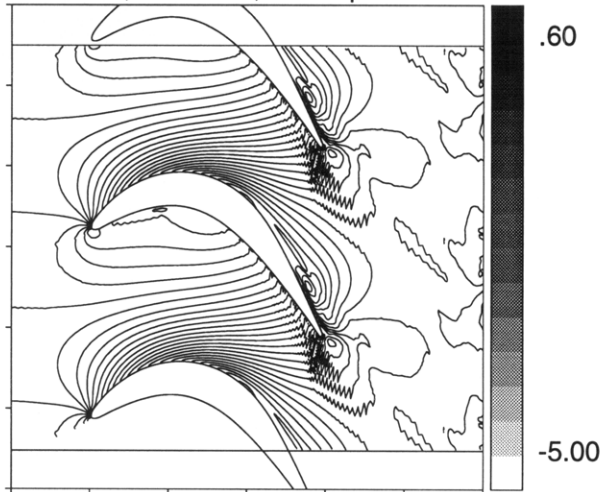
BLADE 1, RE = 90,000 : Cp



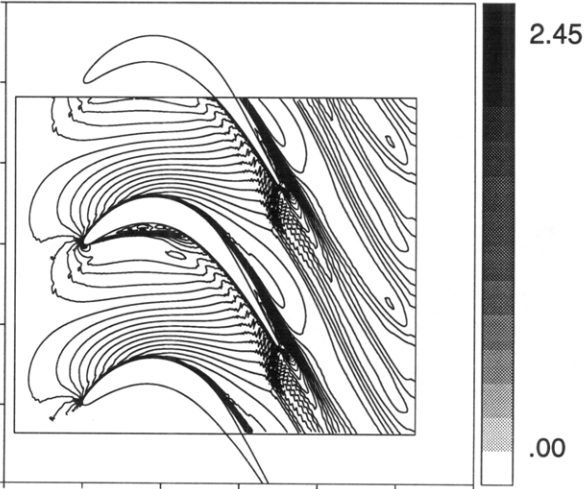
BLADE 1, RE = 120,000 : Vt



BLADE 1, RE = 120,000 : Cp



BLADE 3, RE = 120,000 : Vt



BLADE 3, RE = 120,000 : Cp

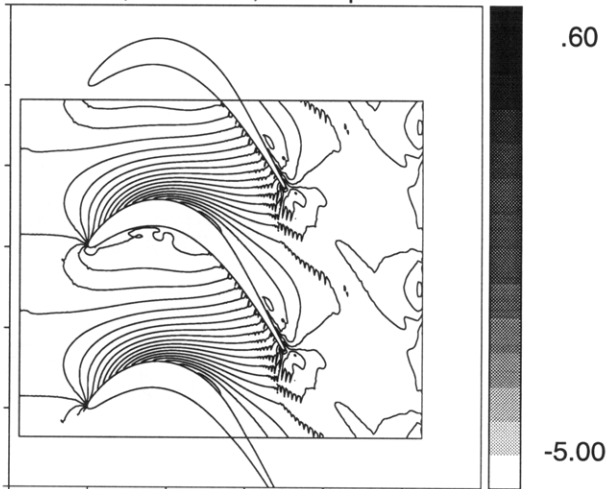


Figure 3-56: Time-averaged total velocity and static pressure coefficient contours, Re = 90,000 blade 1, Re = 120,000 blades 1 and 3

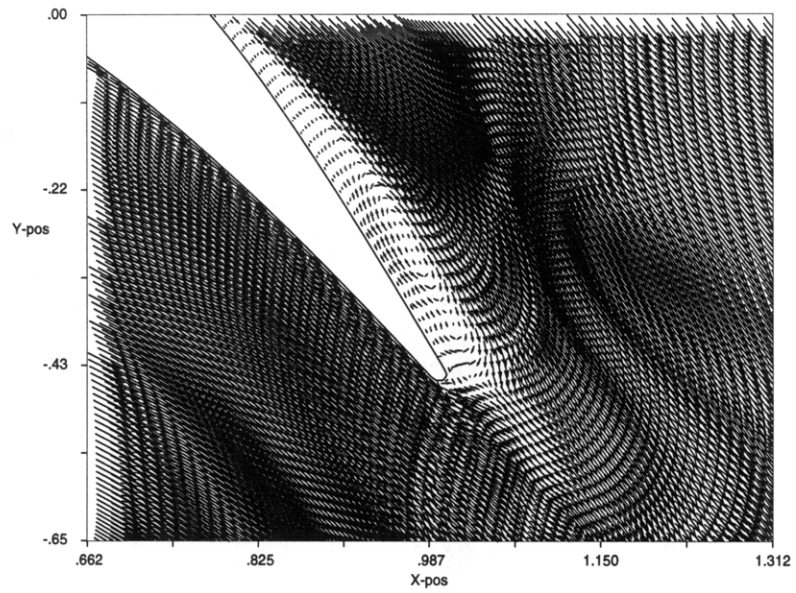


Figure 3-57: *Blade 1*, $Re = 90,000$, time-averaged velocity vectors indicating presence of a vortex at the trailing edge region

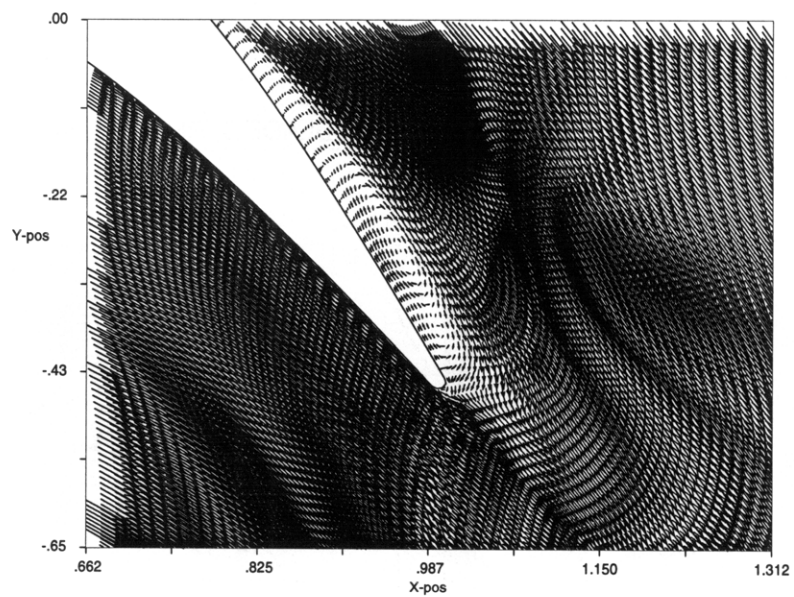


Figure 3-58: *Blade 1*, $Re = 120,000$, time-averaged velocity vectors indicating presence of a vortex at the trailing edge region

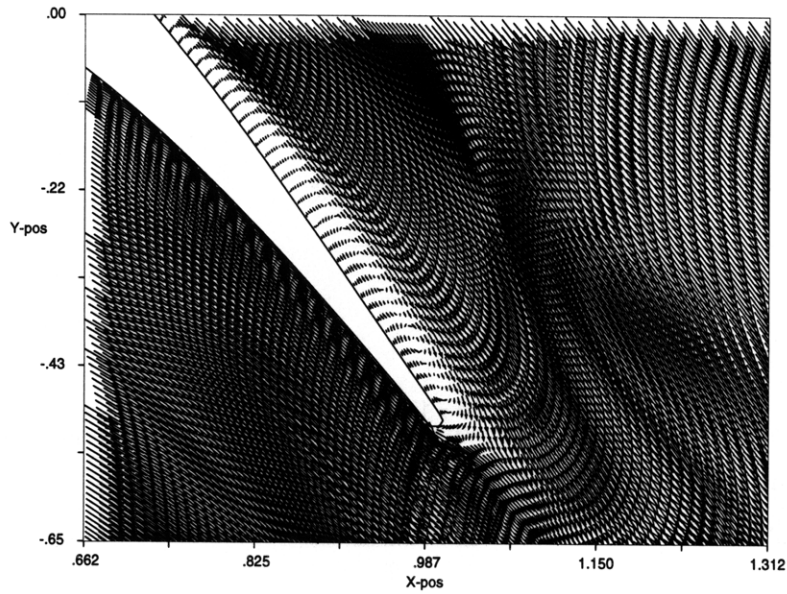


Figure 3-59: *Blade 3*, $Re = 120,000$, time-averaged velocity vectors indicating presence of a vortex at the trailing edge region

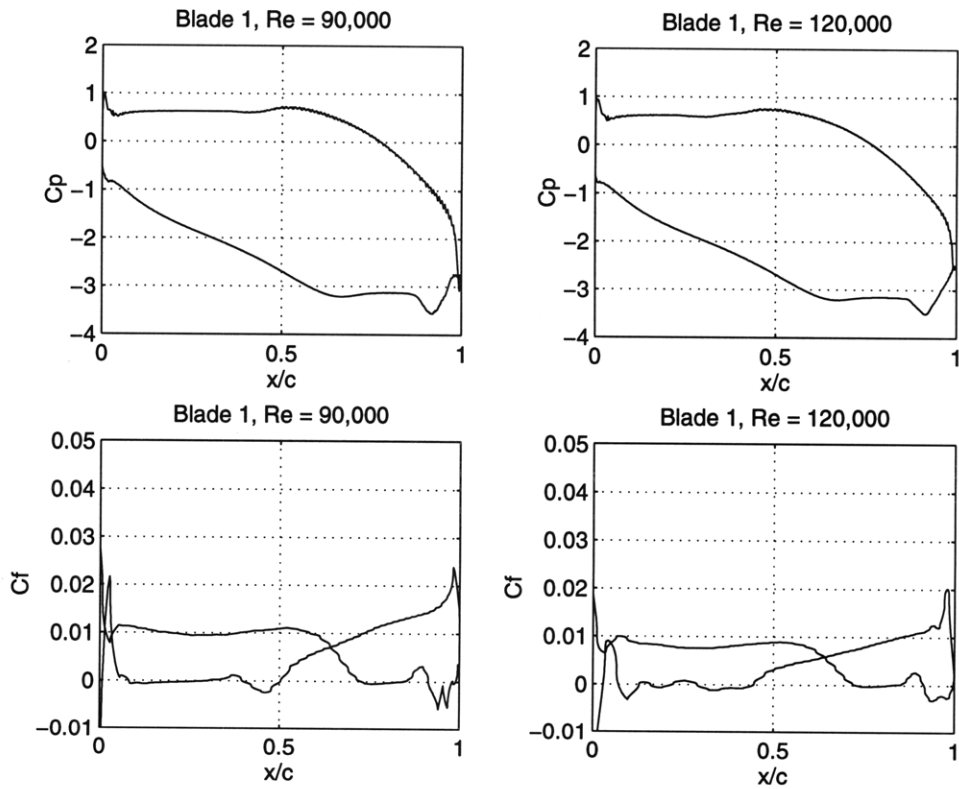


Figure 3-60: Time-averaged static pressure and skin friction on blade surface for *blade 1* at $Re = 90,000, 120,000$

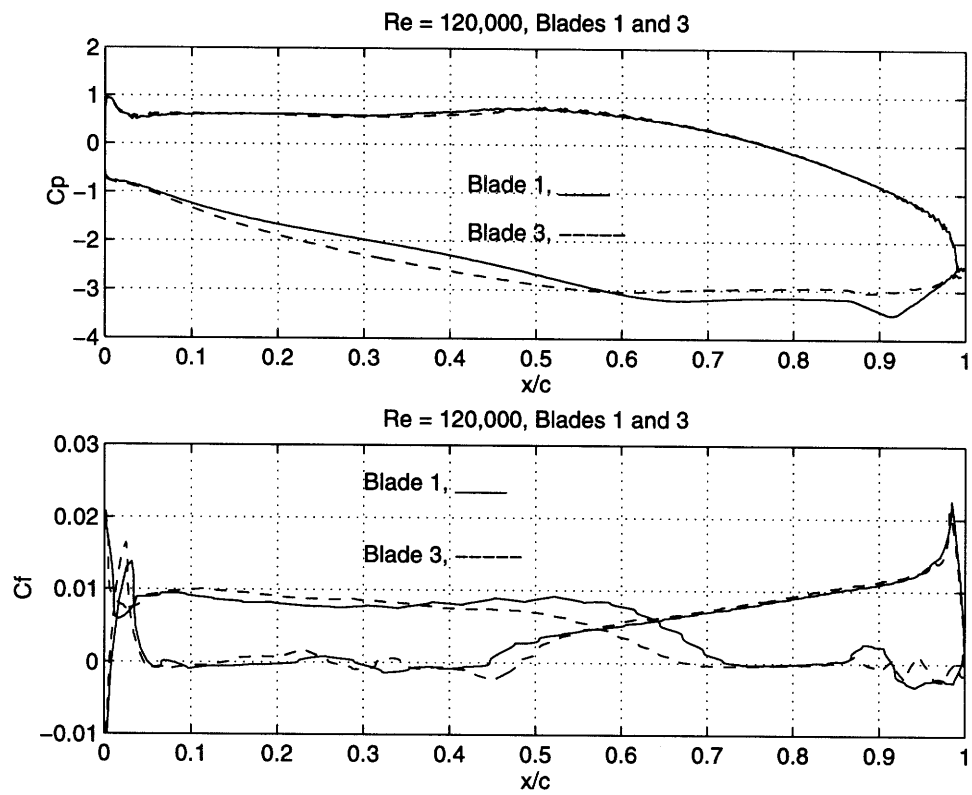


Figure 3-61: Time-averaged static pressure and skin friction on blade surface for $Re = 120,000$, blades 1 and 3

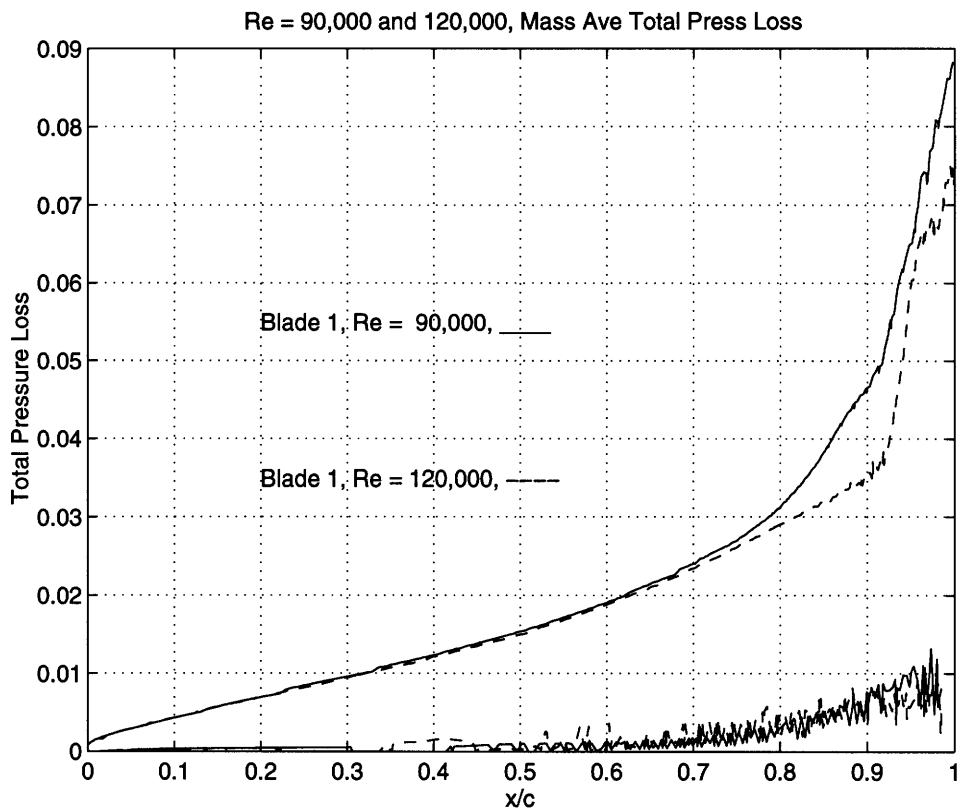


Figure 3-62: Mass-averaged total pressure loss, dimensionalized by exit dynamic head, for the suction and pressure sides at a Reynolds number of 90,000 and 120,000

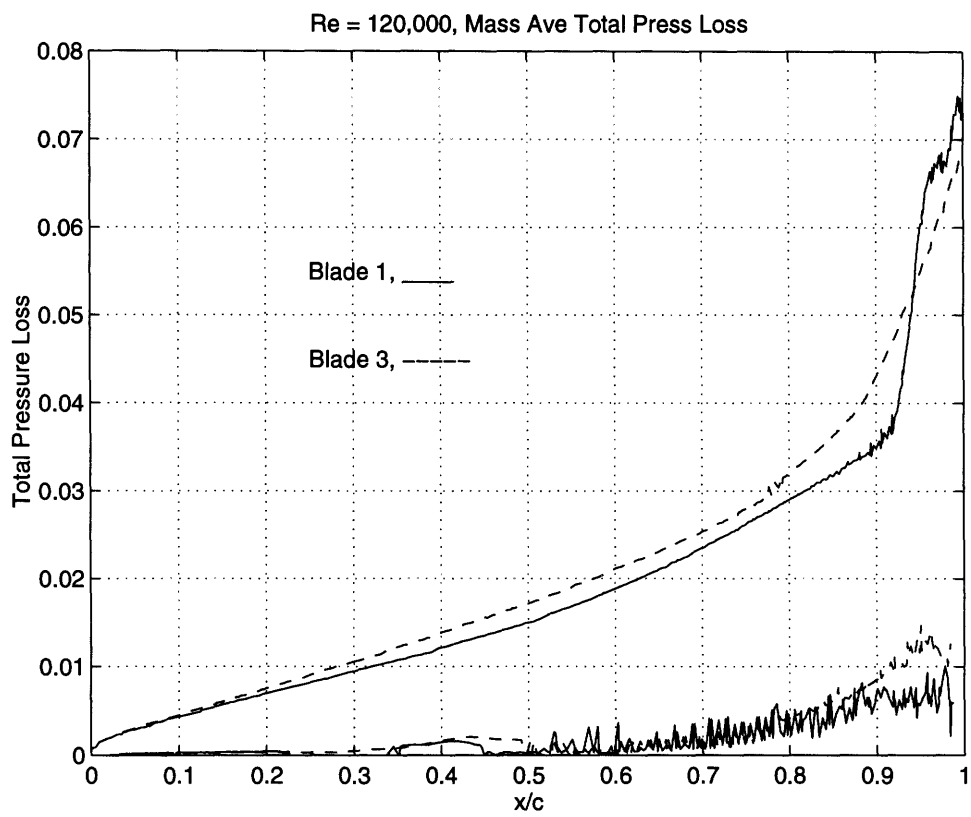


Figure 3-63: Mass-averaged total pressure loss, dimensionalized by exit dynamic head, for the suction and pressure sides at a Reynolds number of 120,000 for *blade 1* and *blade 3*

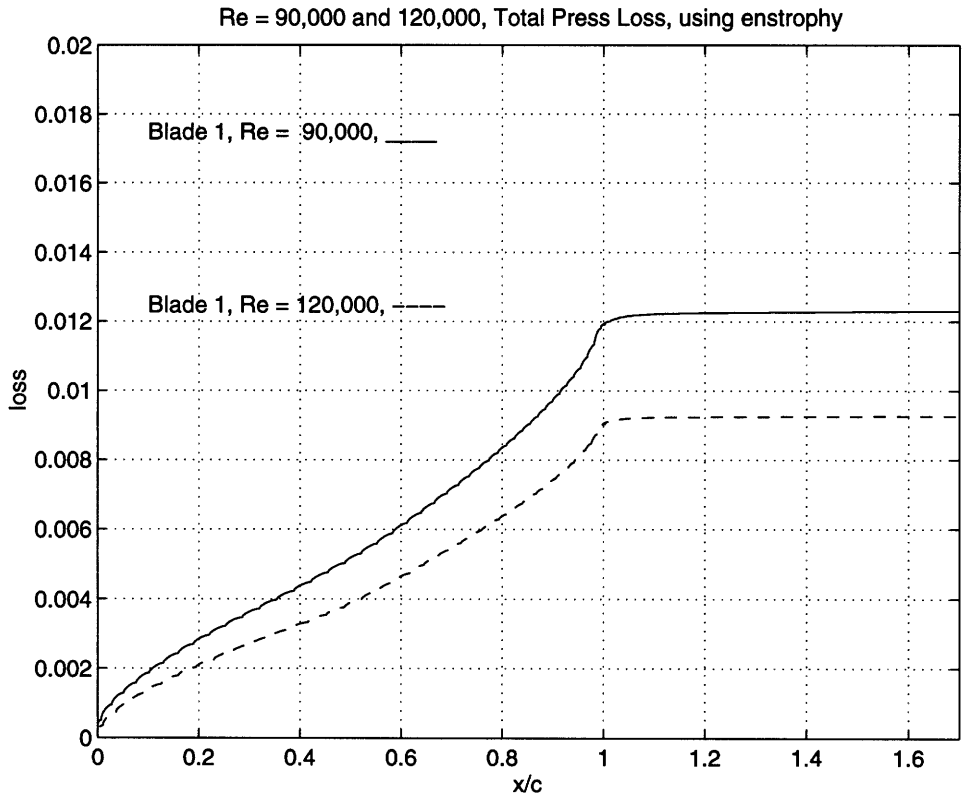


Figure 3-64: Loss calculated using enstrophy, Re = 90,000 and 120,000

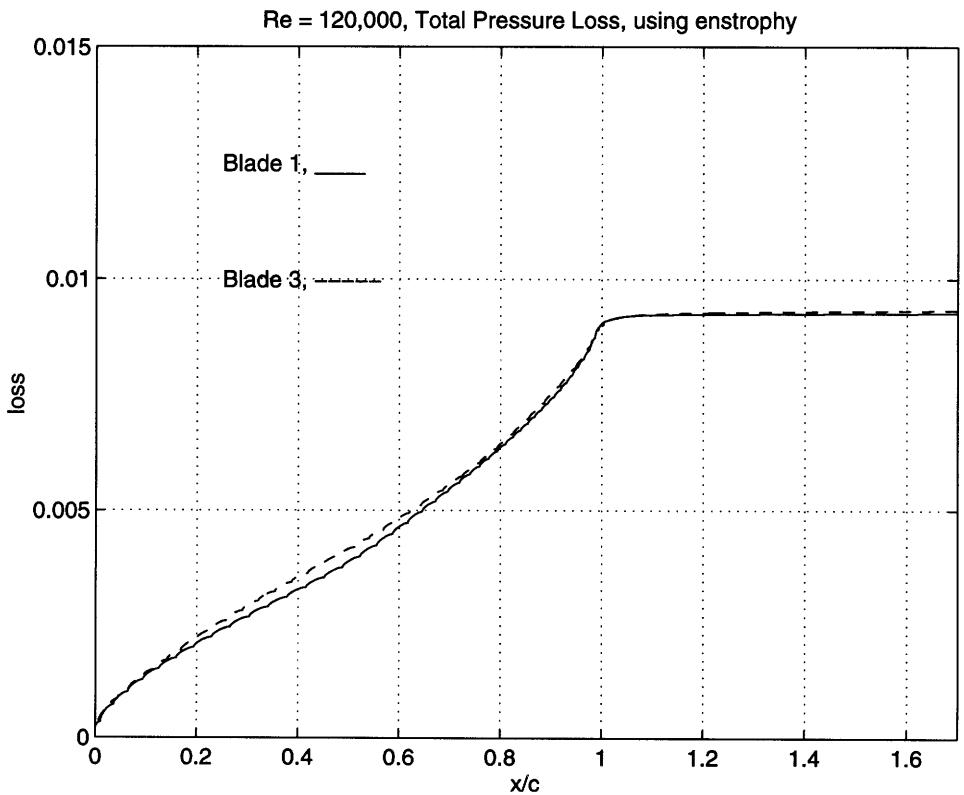


Figure 3-65: Loss calculated using enstrophy, Re = 120,000, blade 1 and blade 3

These displacement thicknesses translate into an additional mixed-out loss due to separation of 0.034 for the 90,000 case, 0.025 for the *blade 1*, 120,000 case, and 0.019 for the *blade 3*, 120,000 case. A comparison of this approximate calculation for the mixed out loss with that found for *blade 1* at 60,000 ($loss_{mix} = 0.04$) demonstrates that the mixing loss drops by a factor of 1.5 as one moves from a Reynolds number of 60,000 to 120,000.

3.3.16 Summary of Time-Averaged Results at $Re = 90,000$ and $120,000$

The same trend in the time-average flow features appear for these calculations as shown in low Reynolds number cases. Namely, the location of the time-average vortex moves upstream, away from the trailing edge as the Reynolds number increases. This corresponds with the earlier onset of instability found for the separated shear layer as Reynolds number increases.

An interesting development for the 120,000 case is the difference in the time-average displacement thickness at the trailing edge between *blade 1* and *blade 3*. The smaller displacement thickness for *blade 3* translates into less mixed-out loss compared to *blade 1*.

3.3.17 Unsteady Features at $Re = 90,000$ and $120,000$

After reviewing the movies made using the calculated solutions for *blade 1* at 90,000 and 120,000, it is observed that the shedding process for the two Reynolds numbers are similar. The roll-up of the suction side shear layer occurs upstream of the trailing edge ($x/c = 0.85$). The vortex that is formed transports the shear layer toward the blade surface, causing a periodic re-attachment of the flow.

However, a noticeable difference is found when comparing the solutions for *blade 1* and *blade 3* at 120,000. The shedding process is quite different, with suction side vortex formation for *blade 3* occurring at the trailing edge, with less of an effect on the overall flow field.

3.3.18 Total Pressure Variation in the Wake at $Re = 90,000$ and $120,000$

The total pressure variation in the wake for these calculations, and the frequency content of this variation are given in figures (3-66), through (3-70). Both calculations for *blade 1* at 90,000 and *blade 3* at 120,000 have at least two dominant frequencies present, whereas the

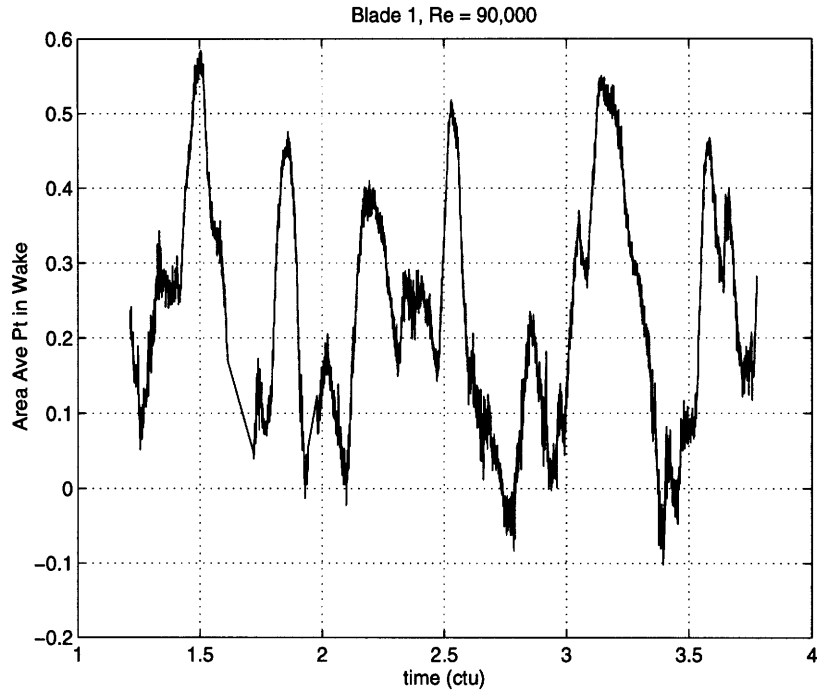


Figure 3-66: Variation of area-averaged total pressure in the wake as a function of time showing the wake structure for *blade 1* , $Re = 90,000$

calculation for *blade 1* at 120,000 shows only one dominant peak (around 2.5 ctu^{-1}). This corresponds with the difference in the shedding processes observed between the cases.

3.3.19 Shear Layer Behavior at $Re = 90,000$ and 120,000

A series of instantaneous vorticity pictures are presented in figures (3-72) through (3-75). These detail the shedding process for *blade 1* at $Re = 90,000$, displaying the periodic re-attachment that occurs on the suction side.

Frame 1 is at a point where a suction side vortex is shed and the shear layer has re-attached. The next frame (figure 3-73), shows the movement downstream of the vortex associated with the shear layer re-attachment. This process continues, with the shedding of the suction side shear layer, and the periodic re-attachment occurring at a point of $x/c = 0.9$. The same sequence occurs for *blade 1* at $Re = 120,000$, with the only difference being that the shear layer rolls-up slightly earlier as compared to the 90,000 case.

A review of the instantaneous flow fields for *blade 3* at 120,000 indicates that the roll-up process is very different compared to *blade 1* at 120,000. The shedding is confined to the trailing edge region for *blade 3* , with less blockage observed for *blade 3* over the *blade 1*

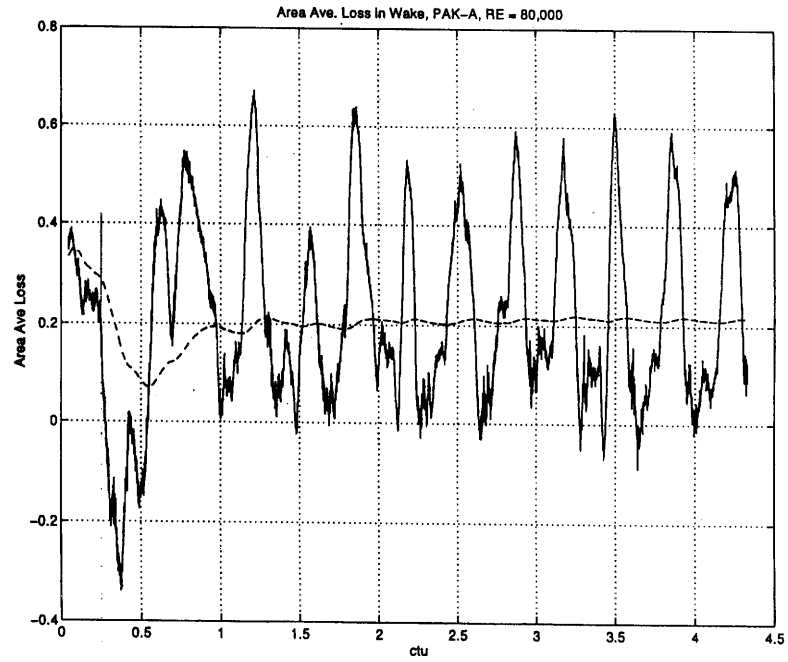


Figure 3-67: Variation of area-averaged total pressure in the wake as a function of time showing the wake structure for *blade 1* , $Re = 120,000$

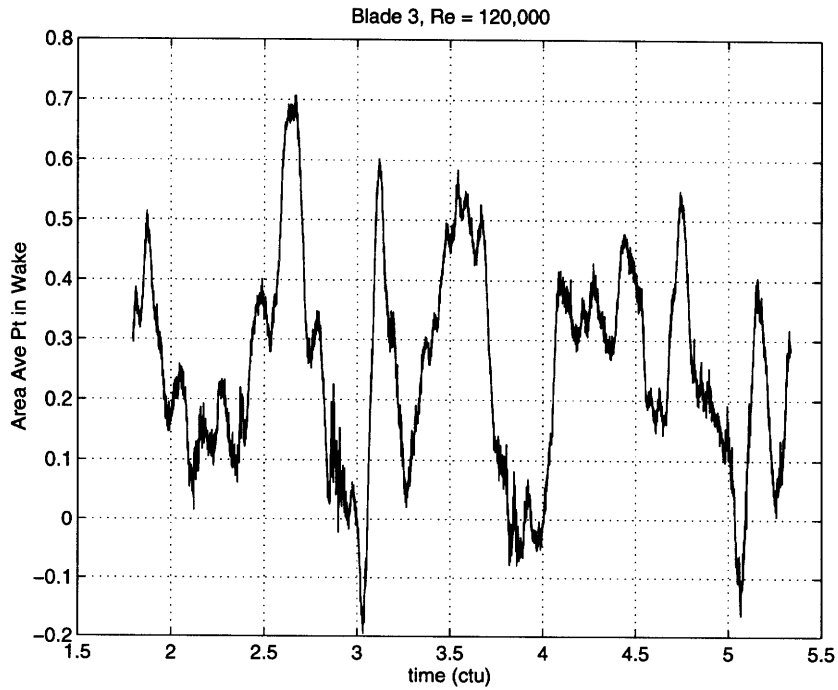


Figure 3-68: Variation of area-averaged total pressure in the wake as a function of time showing the wake structure for *blade 3* , $Re = 120,000$

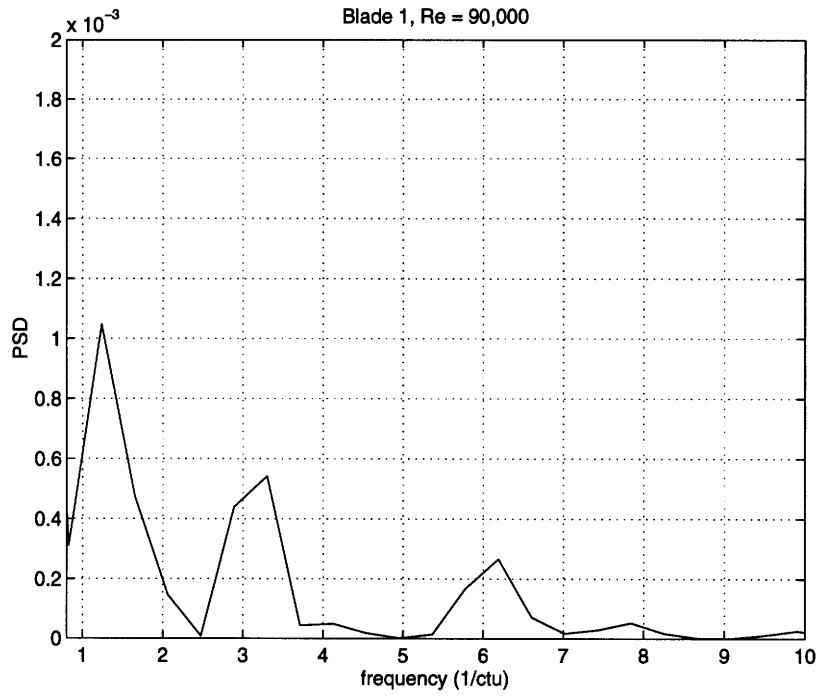


Figure 3-69: Power spectral density of time trace given in figure (3-66), *blade 1* , Re = 90,000

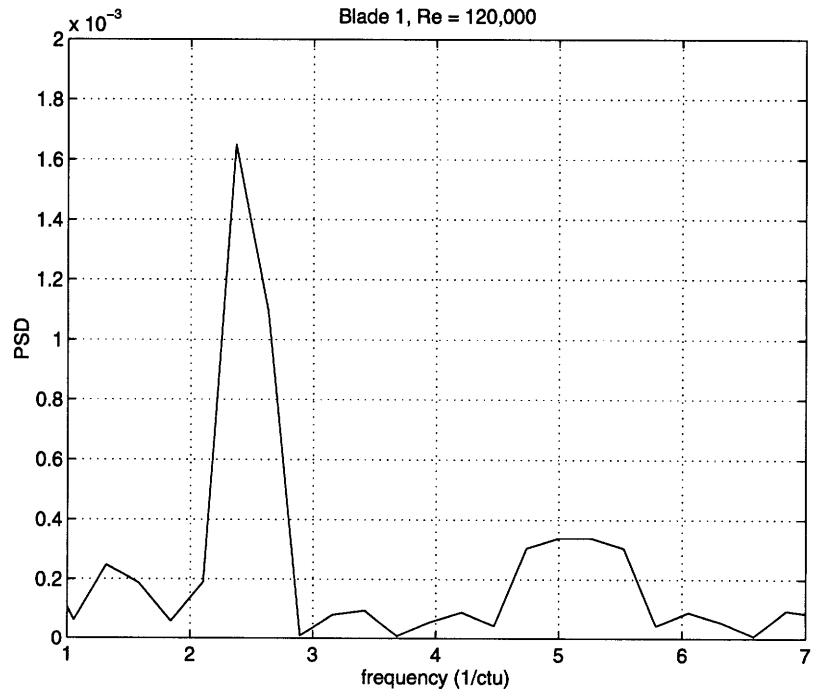


Figure 3-70: Power spectral density of time trace given in figure (3-67), *blade 1* , Re = 120,000

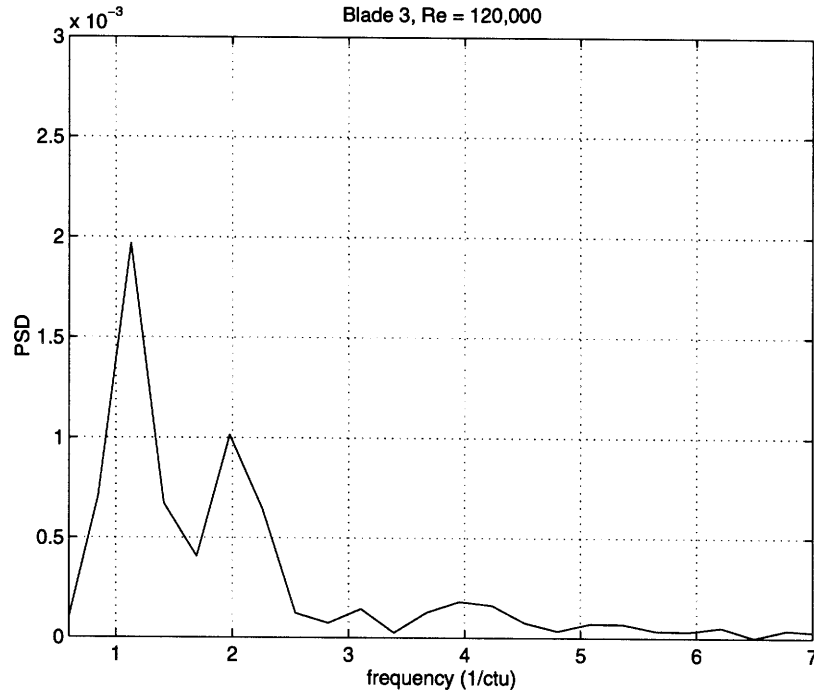


Figure 3-71: Power spectral density of time trace given in figure (3-68), *blade 3* , $Re = 120,000$

case at 120,000.

3.3.20 Static Pressure Deviations Due to Unsteadiness at $Re = 90,000$ and 120,000

The main feature observed from an examination of the pressure deviations from the mean (figure 3-76), is the localized nature of the shedding process for the $Re = 120,000$ case. The shedding that takes place for the $Re = 90,000$ case has a greater effect on the upstream pressure, whereas the break-off of the suction side vortex for the 120,000 calculation is a more localized feature. The same “hump” in the pressure deviation seen in the region between $x/c = 0.8$ and $x/c = 0.9$ for the *blade 1* 120,000 case was also seen for the calculation at 60,000 for *blade 1* (figure 3-53).

Also, the shedding of vortices from the pressure side shear layer is evidenced by the non-zero pressure deviations found on the pressure side. This is especially evident for *blade 3* at $Re = 120,000$.

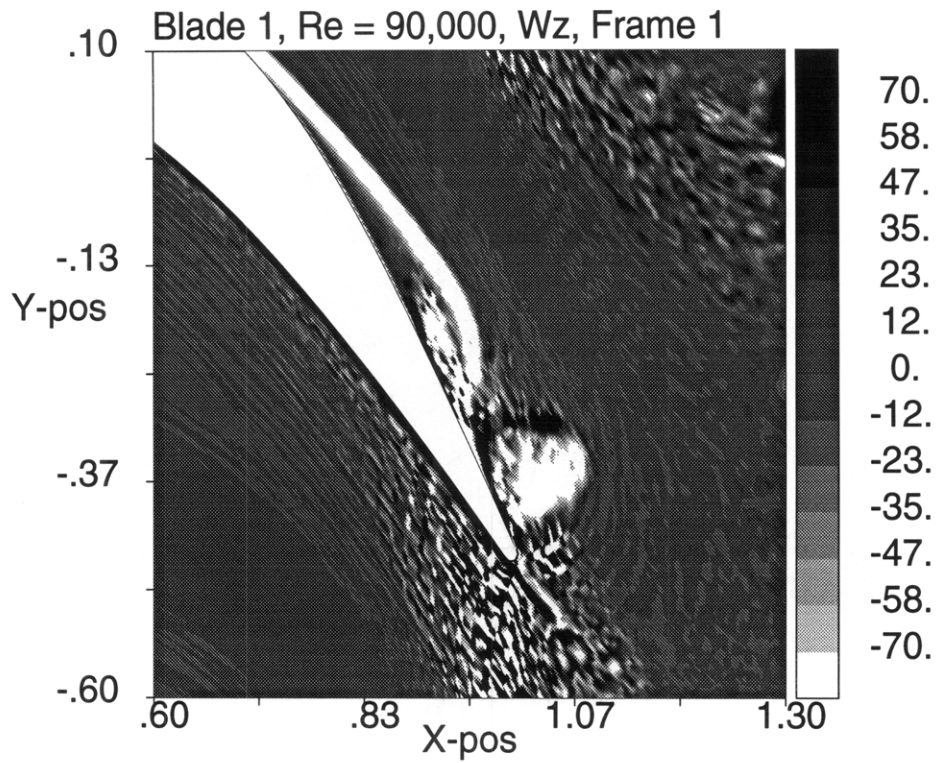


Figure 3-72: Instantaneous vorticity field for *blade 1* , Re = 90,000, T = 0.00 ctu

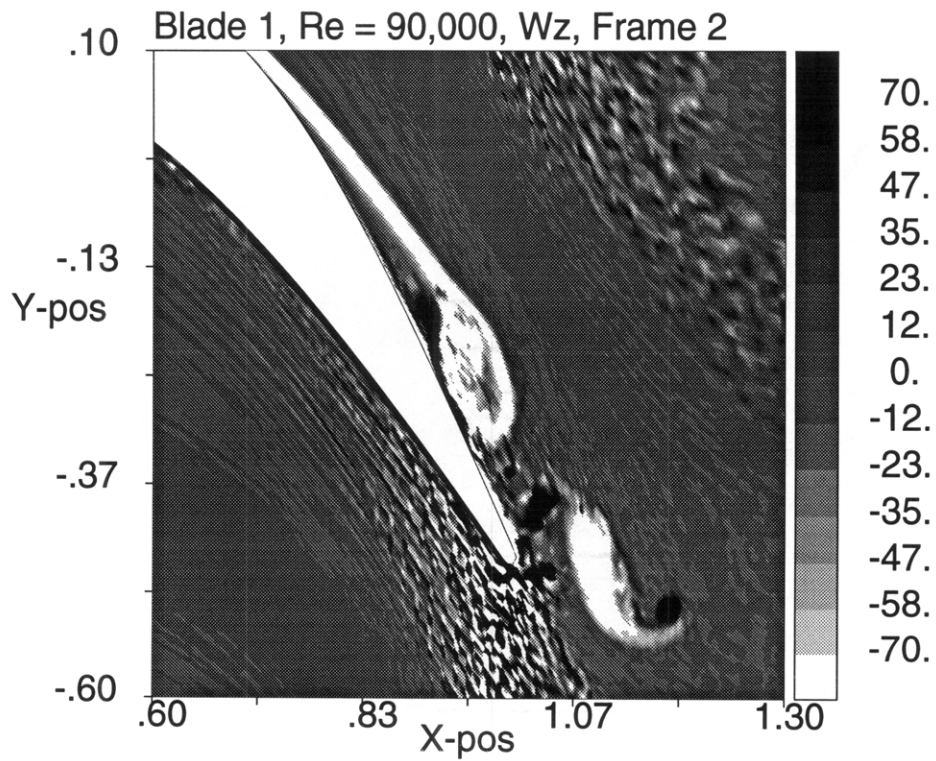


Figure 3-73: Instantaneous vorticity field for *blade 1* , Re = 90,000, T = 0.09 ctu

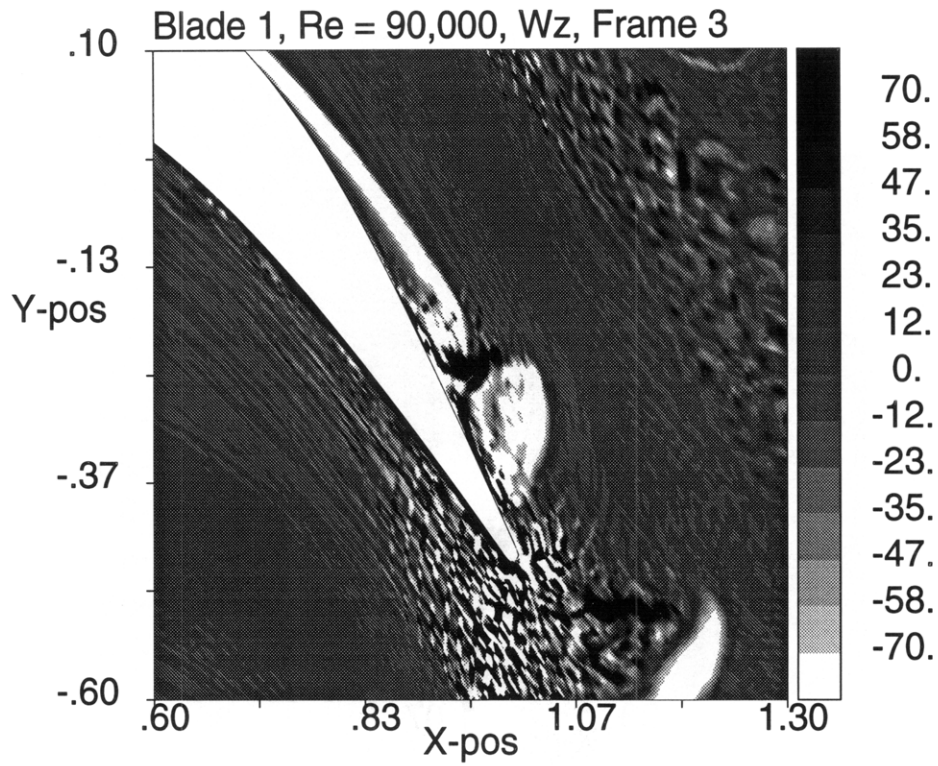


Figure 3-74: Instantaneous vorticity field for *blade 1*, Re = 90,000, T = 0.18 ctu

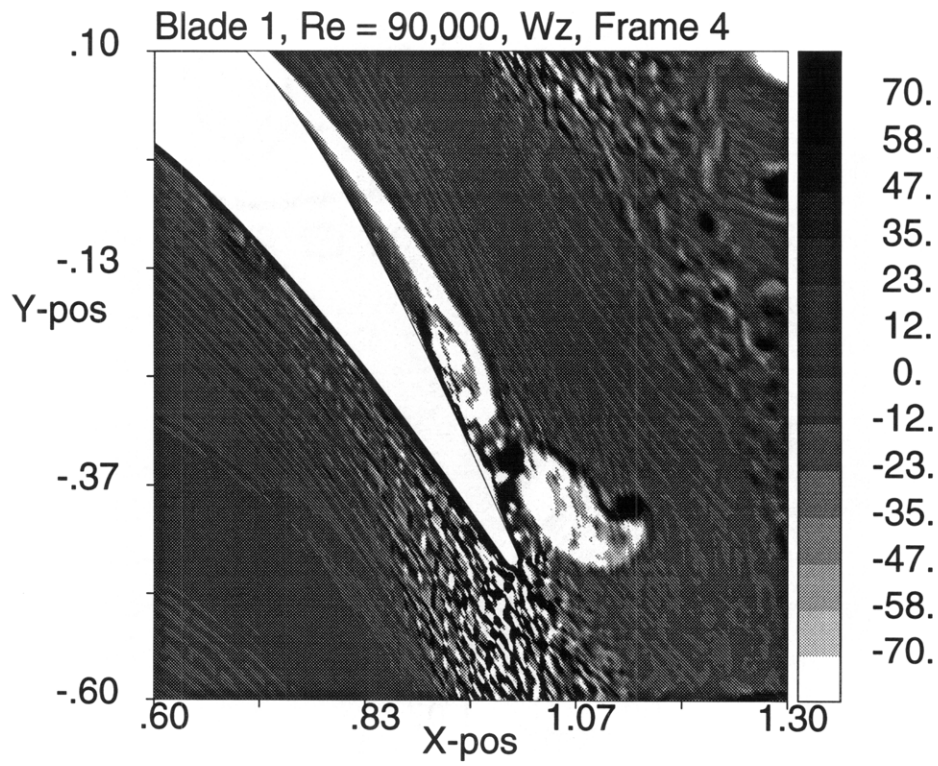


Figure 3-75: Instantaneous vorticity field for *blade 1*, Re = 90,000, T = 0.27 ctu

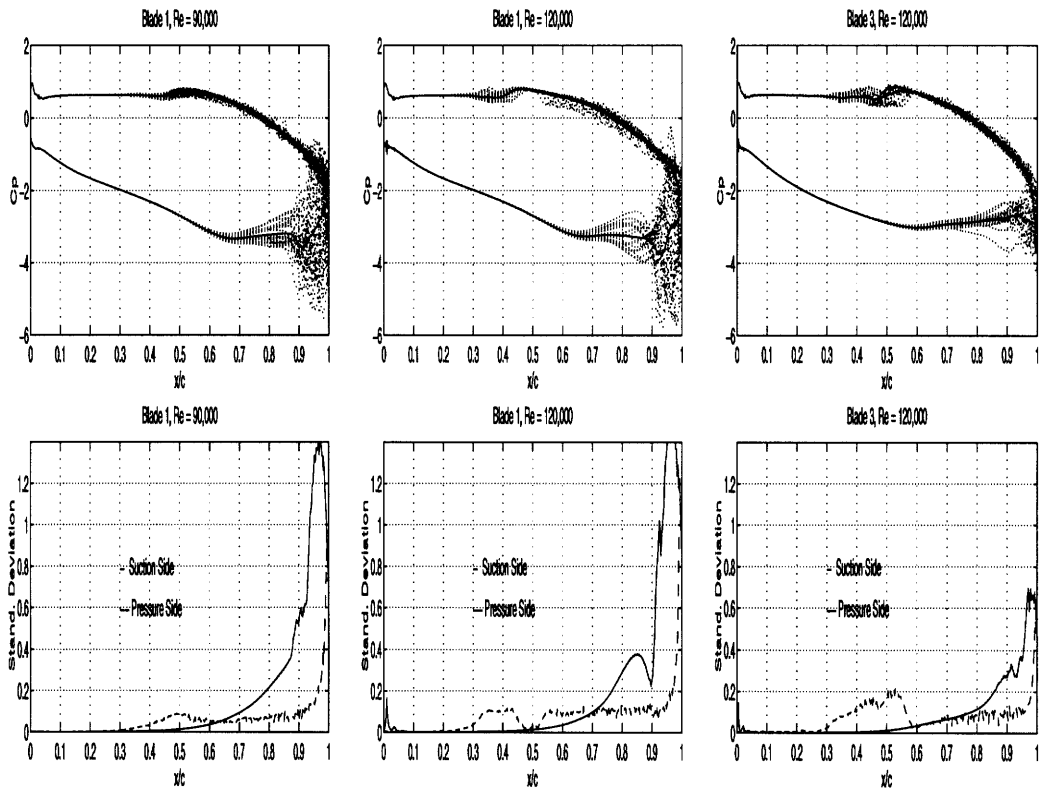


Figure 3-76: Static pressure envelopes over the blade surface and standard deviation of the fluctuations for blade 1, at Re = 90,000 and 120,000

3.3.21 Dissipation Coefficients at $Re = 90,000$ and $120,000$

The laminar and unsteady dissipation coefficients for *blade 1* at 90,000 and 120,000 are displayed in figure (3-77), with the ratio of two values given in figure (3-78). The results for *blade 3* at 120,000 are given in (3-79) and (3-80). The shedding causes the unsteady dissipation to be on the order of 100 times greater than the laminar dissipation for *blade 1* at 90,000 and 120,000.

An interesting feature to note is the decrease in the unsteady C_d for the 120,000 case. This corresponds to a decrease in the magnitude of the pressure deviation (figure 3-76) found between the two Reynolds numbers. The explanation for this result is that the shedding for the 120,000 case is more localized to the last two-tenths of axial chord, and has less influence upon the flow than the shedding seen for 90,000.

The ratio of the dissipations for *blade 3* at 120,000 is smaller, being on the order of 50 in the aft region of the blade. This smaller dissipation due to the velocity fluctuations is due to the difference in the shedding process for this case compared to that for *blade 1* at $Re = 120,000$.

3.3.22 Summary of Observed Unsteady Features at $Re = 90,000$ and $120,000$

The calculations for *blade 1* at 90,000, and *blade 1* and *blade 3* at 120,000 display a large drop in the loss level, with the mixed out loss being about 1.5 times less than that found for the 60,000 case. This has to do with the occurrence of a periodic re-attachment of the suction side boundary layer. The dynamical features for *blade 1* at 90,000 and 120,000 are similar, with the shedding for the 120,000 case having less of an influence upon the overall flow field upstream of the trailing edge. The vortex formation on the suction surface for *blade 3* at 120,000 has even smaller influence on the upstream flow, as shown by the smaller dissipation due to unsteady velocity fluctuations.

3.3.23 Summary of Key Results Presented

These calculations demonstrate that minor changes in blade profile (maintaining the same gas flow angles) play an important role in determining the shedding process for a given Reynolds number. It was shown that *blade 3* lags behind *blade 1* in terms of the suction

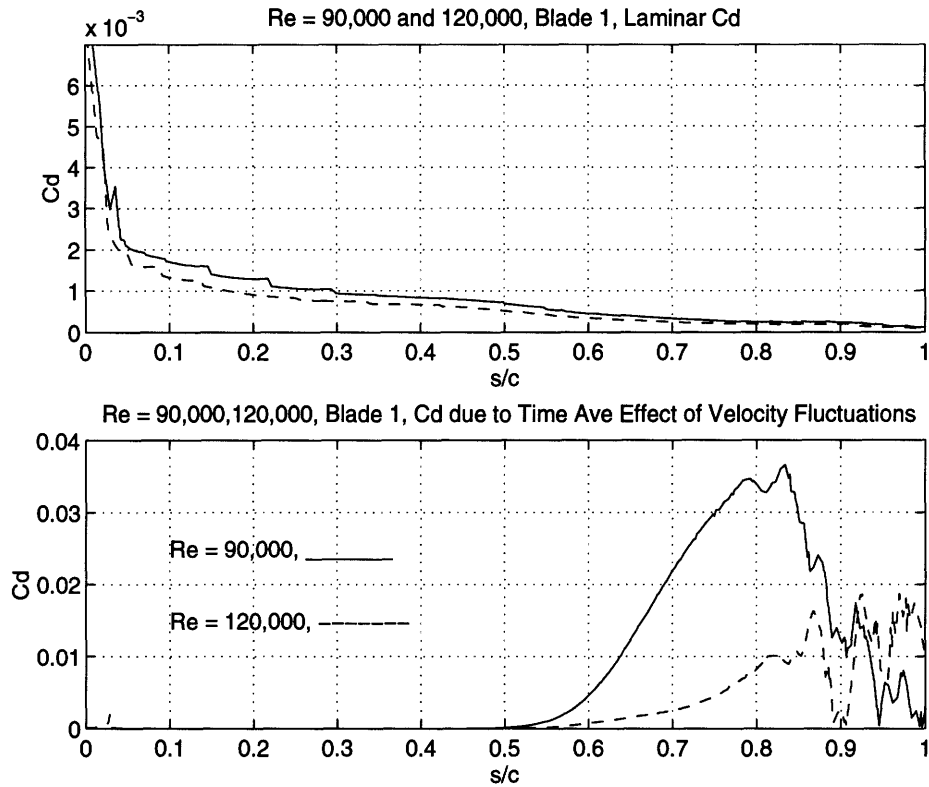


Figure 3-77: Laminar and unsteady dissipation coefficients on the suction side for *blade 1* at $Re = 90,000$ and $120,000$, plotted along the blade surface

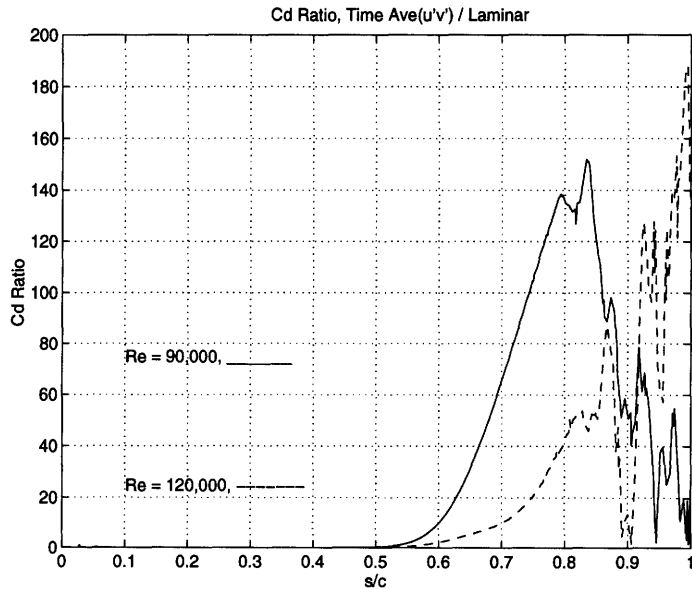


Figure 3-78: Ratio of the unsteady to laminar dissipation coefficients on the suction side, $Re = 90,000$ and $120,000$, plotted along the blade surface

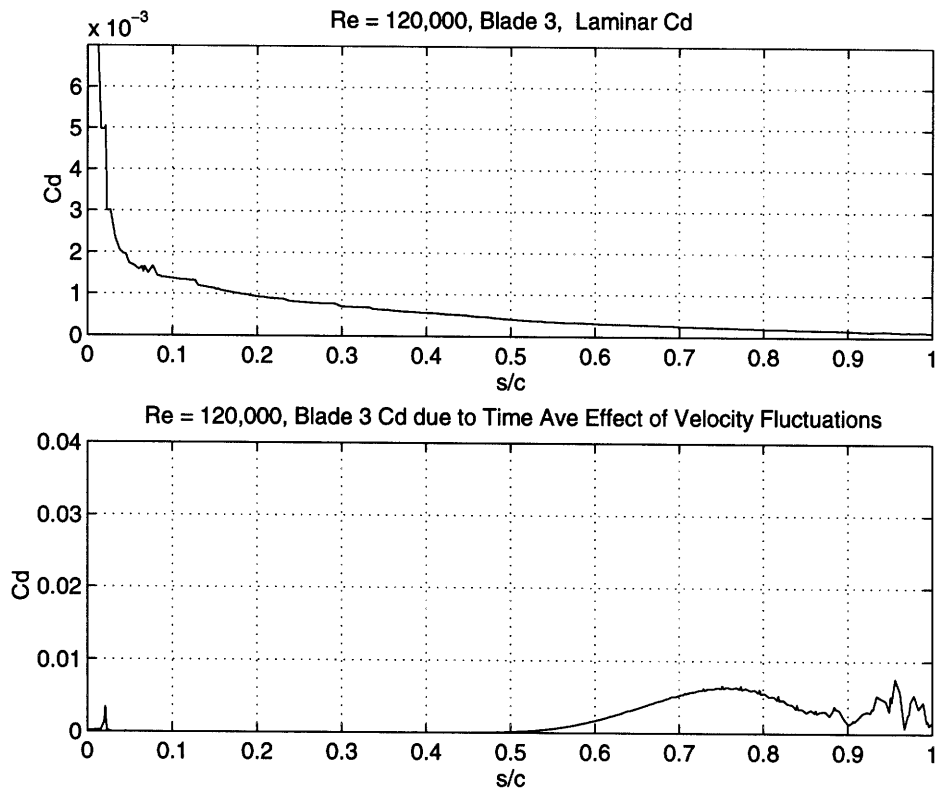


Figure 3-79: Laminar and unsteady dissipation coefficients on the suction side for *blade 3* at $Re = 120,000$, plotted along the blade surface

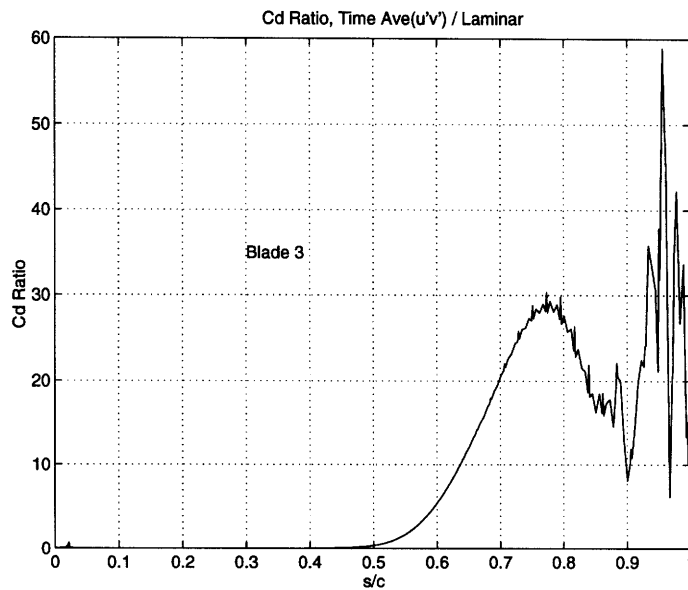


Figure 3-80: Ratio of the unsteady to laminar dissipation coefficients on the suction side for *blade 1* at $Re = 120,000$, plotted along the blade surface

side shear layer development. The vortex formation on the suction side for *blade 3* occurs downstream of that for *blade 1* at all the Reynolds numbers.

The profile loss for *blade 3* was shown to be the largest due to the increased velocities in the front half of the passage compared to *blade 1* , however, the observation was made that the extent of trailing edge flow blockage produced by the suction side shear layer was smaller for *blade 3* compared to *blade 1* . This corresponds to a smaller mixed-out total pressure loss, and thus, could more than make up the difference in profile loss between the designs.

Chapter 4

Implications on LPT Design and Issues of Fluid Dynamical Interest

The results presented in chapter 3 will now be synthesized to deduce the implications on how changes in LPT performance can be linked to flow behavior changes with design and Reynolds number. Comparisons of the blade profiles over the Reynolds number range used will be made, along with a discussion on the tradeoffs between the different geometries used.

We will first examine the implications these results have upon blade design. A statement will be made as to which blade has better performance, at least for the range of Reynolds numbers investigated.

This is then followed by a section on the implications these results have on an understanding of fluid dynamical processes. Many of the points to be presented in this section have been described in chapter 3, thus this section constitutes a synthesis of the ideas previously set forth. The focus will specifically be on :

1. the determination of a vortex shedding frequency from a separated shear layer
2. the use of the frequency determination in estimating the location of vortex formation and re-attachment points at higher Reynolds numbers
3. the variation in profile and mixed-out loss with Reynolds number with a focus on the relation between the performance and the changing unsteady flow features as the Reynolds number increases
4. the choice in blade loading, aft or forward, showing the effects on shear layer devel-

opment, and the implications the magnitude of the pressure gradient at the point of separation has upon the angle at which the shear layer leaves the wall

5. the tradeoff between aft and forward loading, with the implications on profile and mixed-out loss

4.1 Implications on LPT Blade Design

The design of a LPT blade is performed with the goal of achieving the lowest total pressure loss, i.e. the best performance, throughout the engine operating range.

During the course of LPT operation, the LPT blade will encounter situations where a laminar separation of the suction side boundary layer may occur, resulting in a sharp increase in the total pressure loss. Thus, a criterion that can be used to distinguish between two blade designs is the value of Reynolds number for which suction side boundary layer re-attachment occurs. The lower the Reynolds number at which the boundary layer re-attaches the better.

Using this as a criterion, the trends presented in chapter 3 indicate that *blade 1* is a better design. This statement is made because the suction side separation for *blade 1* appears to be closer to the conditions for re-attachment at all the Reynolds numbers investigated. The determination of which blade is closer to re-attachment is made by observing where the roll-up of the shear layer takes place. The closer to the separation point this instability occurs, the better. The earlier point of instability observed for *blade 1* is used as a sign that the shear layer for *blade 1* will re-attach at a lower Reynolds number.

Another mechanism causing a reduction in performance, besides boundary layer separation, is the amount of profile loss produced by the attached boundary layer (over the forward surfaces of the blade). It was shown that the profile loss is a strong function of the freestream velocity for large enough momentum thickness Reynolds numbers, Re_{θ} . Therefore, using the amount of profile loss produced as a criterion, *blade 1* would again be chosen as the better blade, over *blade 3*. The forward loading of *blade 3* causes larger freestream velocities in the forward section of the passage, thus higher rates of entropy production.

Uncertainties in design assessment stem from the fact that the amount of mixing loss associated with each blade can only be approximated. Observations of the solutions indicate that *blade 3* has a smaller region of blockage at the trailing edge plane. This would lead

to lower mixed out loss, but no statement can be made as to whether this benefit would outweigh the increased profile loss seen for *blade 3* over *blade 1* .

Also, this smaller region of blockage translates into a smaller distance between the shear layer and the blade surface. Even though the vortex shedding for *blade 1* occurs further upstream of the trailing edge, the closer proximity of the shear layer to the blade surface for *blade 3* may play a role in determining the re-attachment Reynolds number. This is a topic that can only be investigated by performing calculations at even higher Reynolds numbers.

A last uncertainty is due to effect of inlet conditions upon the observed suction side dynamics. The solution comparisons between the “normal” cases (i.e. where the inflow boundary is 0.35 chords from the blade leading edge) and calculations performed with the inflow and outflow boundaries moved further from the blade is presented in appendix (A). The results of this comparison show that inlet conditions play an important role in the development of the suction side shear layer. Thus, one could infer that situations encountered in an actual engine, such as wake transport would also be a major factor in determining the performance of a LPT blade.

4.2 Implications on Fluid Dynamic Issues

4.2.1 Determination of Shedding Frequency

This section demonstrates that the Strouhal number based upon momentum thickness and freestream velocity at the point of separation can be used to determine the frequency at which the shear layer will form into vortices. First, the Strouhal number will be calculated for all of the solutions shown in table (3.1). A comparison will be made with another computational experiment performed by Pauley [11], and the implications this has upon the prediction of the unsteady nature of these flows will be discussed.

Table (4.1) displays the time-averaged momentum thickness, and freestream velocity at the point of separation, $(\frac{s}{c})_{sep}$, on the suction side for all the calculations performed. The point of separation is determined using the location where the time-average C_f reaches a value of zero on the suction side. Also shown is the observed vortex shedding frequency for the suction side shear layer. The Strouhal number is calculated according to :

$$St_{\theta} = \frac{\theta f_{shedding}}{u_e} \quad (4.1)$$

Blade	Reynolds Number	$\left(\frac{s}{c}\right)_{sep}$	θ	u_e	$f_{shedding}$	St_θ
1	20,000	0.61	0.0060	2.44	2.85	0.007
2	20,000	0.61	0.0067	2.43	2.7	0.007
3	20,000	0.58	0.0068	2.41	2.75	0.008
1	30,000	0.62	0.0060	2.47	1.7	0.004
2	30,000	0.60	0.0064	2.43	1.7	0.005
3	30,000	0.58	0.0062	2.43	2.7	0.007
1	60,000	0.61	0.0044	2.54	1.7	0.003
3	60,000	0.57	0.0049	2.46	1.6	0.003
1	90,000	0.60	0.0033	2.53	3.0	0.004
1	120,000	0.60	0.0031	2.53	3.0	0.004
3	120,000	0.55	0.0032	2.46	1.7	0.002

Table 4.1: Values used for determination of Strouhal number at point of separation

The computational experiment performed by Pauley [11] determined a Strouhal number based upon conditions at separation for three Reynolds numbers. The computations involved the flow through a straight channel, with suction applied at the top surface of the channel to create an adverse pressure gradient. This investigation found that for the three Reynolds used in the numerical study ($Re_x = 59,629, 120,544, \text{ and } 238,515$), the Strouhal number was nearly constant at :

$$St_\theta = 0.00686 \pm 0.6\%$$

This study found that the shedding frequency was independent of suction strength, therefore of the magnitude of the pressure gradient; also, the shedding frequency was found to increase as the Reynolds number was increased. The current investigation, using the three LPT geometries, produces a range of St_θ from 0.002 to 0.008, which are of the same order of magnitude as that found in reference [11]. There seems to be a tendency for larger St_θ at the lower Reynolds numbers.

In summary :

1. as the Reynolds number increases, the location of vortex formation moves upstream of the trailing edge; this corresponds to a shift from a regular vortex shedding process to a relatively less regular shedding, with various vortex sizes present
2. above a critical Reynolds number, after the roll-up position moves upstream of the trailing edge, the shedding translates from an irregular shedding process which involves

Blade, Re	u_2	u_1	$\left(\frac{\partial u}{\partial y}\right)_{max}$	f	ω^*
1 20,000	2.43	-0.43	46	2.85	0.28
2 20,000	2.38	0.14	39	2.7	0.19
3, 20,000	2.30	0.04	38	2.75	0.22
1, 30,000	2.48	-0.60	43	1.7	0.20
2, 30,000	2.39	0.32	25	1.7	0.16
3, 30,000	2.42	0.08	35	2.7	0.23
1, 60,000	2.53	-0.70	53	1.6	0.17
3, 60,000	2.47	-0.51	43	1.6	0.18
1, 90,000	2.57	-0.56	75	3.0	0.20
1, 120,000	2.53	-0.37	78	3.0	0.16

Table 4.2: Values used for calculation of ω^*

non-uniform vortex sizes, back to a shedding consisting of identical sized vortices, but with the vortex formation occurring upstream of the trailing edge

Therefore, for vortex formation that occurs upstream of the trailing edge, the shedding frequency increases with Reynolds number, as seen in Pauley [11]. This effect can be explained as follows: The increase in Re corresponds to a decrease in momentum thickness so that for a constant Strouhal number (based upon the momentum thickness) the shedding frequency must increase.

4.2.2 Estimation of Point of Vortex Formation

In this section, we will examine how the position of vortex formation, and thus the point of periodic re-attachment can be calculated approximately. The relation between the non-dimensional frequency (ω^*) and the point of vortex formation will be used to develop the line of reasoning.

The computed results indicate that the increase in Re correlates with a decrease in the length between the point of separation and the point of shear layer instability.

For the convenience of presenting the arguments that follows below, we reproduce tables (3.2, 3.3, 3.4) as table (4.2).

The increase in Re corresponds to a decrease in momentum thickness, and thus for a constant St_θ , the shedding frequency increases. Using the definition for the non-dimensional

frequency (equation 3.13), ω^* can be rewritten as :

$$\omega^* = \frac{\pi f_{shedding}(u_2 - u_1)}{\left(\frac{\partial u}{\partial y}\right)_{max} (u_2 + u_1)} \quad (4.2)$$

If $f_{shedding}$ increases, a term on the right hand side of equation (4.2) must vary in order for ω^* to remain constant. The velocities u_2 and u_1 do not vary significantly, therefore the term that balances the increase in $f_{shedding}$ must be the maximum vorticity in the shear layer, $\left(\frac{\partial u}{\partial y}\right)_{max}$.

This trend is seen in table (4.2), specifically for *blade 1* . The maximum vorticity in the shear layer (at the point of maximum instability) increases as Reynolds number increases.

If the growth of the shear layer is known (i.e. $\delta = f(x/c)$) the point of instability can be estimated, assuming that the magnitudes of the velocities on either side of the shear layer remain approximately constant, i.e. :

$$\left(\frac{\partial u}{\partial y}\right)_{max} \approx \frac{u_2 - u_1}{\delta} \quad (4.3)$$

Thus, this simple argument can be used to obtain the point of instability over the blade using the following method :

1. Assuming St_θ is constant, and knowing θ and u_e at separation, $f_{shedding}$ can be found from :

$$f_{shedding} = \frac{St_\theta u_e}{\theta} \quad (4.4)$$

2. Next, the shedding frequency is used with the assumption that the point of shear layer roll-up corresponds to $\omega^* = 0.21$; this gives the maximum vorticity as :

$$\left(\frac{\partial u}{\partial y}\right)_{max} = \frac{\pi f_{shedding}(u_2 - u_1)}{\omega^*(u_2 + u_1)} \quad (4.5)$$

3. Using a known function for the growth of the shear layer, the point at which roll-up occurs could be approximated using :

$$\delta(x/c) \approx \frac{u_2 - u_1}{\left(\frac{\partial u}{\partial y}\right)_{max}} \quad (4.6)$$

4.2.3 Variation in Profile and Mixed-Out Losses with Reynolds Number

An assessment of the relation of profile and mixed-out loss to Reynolds number as well as the observed unsteady flow features will be made in this section.

Figures (4-1) through (4-5) illustrate the variation of mass-averaged loss with Reynolds number for the three blade profiles. A display of the variation of the profile loss versus exit Reynolds number, using a mass-average in one case (taking the value of loss at a point $x/c = 0.6$), and enstrophy in the other (taking the value found at $x/c = 1.2$) is given in (4-6 and 4-7). The loss value is taken at $x/c = 0.6$ for the mass-averaged case in order to obtain a ranking of the blade profile loss occurring in the forward portion of the passage, without having to worry about the problems associated with the flow re-circulation in the last 4/10 of the blade. The enstrophy loss values are taken at $x/c = 1.2$ because $|\omega_z|^2$ is unaffected by the reversed flow in the separated region, and therefore is a measure of the total dissipation in the passage boundary layers.

All of these graphs indicate the trend of decreasing profile loss with increasing Reynolds number. The profile loss is slightly greater for *blade 3* than *blade 1* at Reynolds numbers of 20,000, 30,000, and 60,000 when comparing the mass-averaged loss at a point $x/c = 0.6$.

The variation of loss using mass-averaging indicates a sharp drop between the Reynolds numbers of 60,000 and 90,000, with very little difference in the loss between 90,000 and 120,000. Using enstrophy, the variation in loss is much more gradual between 60,000 and 90,000.

This sharp drop in the mass-average loss may be associated with the difference in vortex shedding dynamics observed. At a Reynolds number of 60,000, the suction side shear layer for *blade 1* still exhibits a shedding of a large vortex, at a low frequency, as compared to higher Reynolds numbers, where a higher frequency shedding is observed.

A brief assessment of the mixing loss is now made, making use of the displacement thickness at the trailing edge. Table (4.3) displays the displacement thickness, δ^* , at the trailing edge, and the corresponding estimate for the added loss due to mixing. This calculation

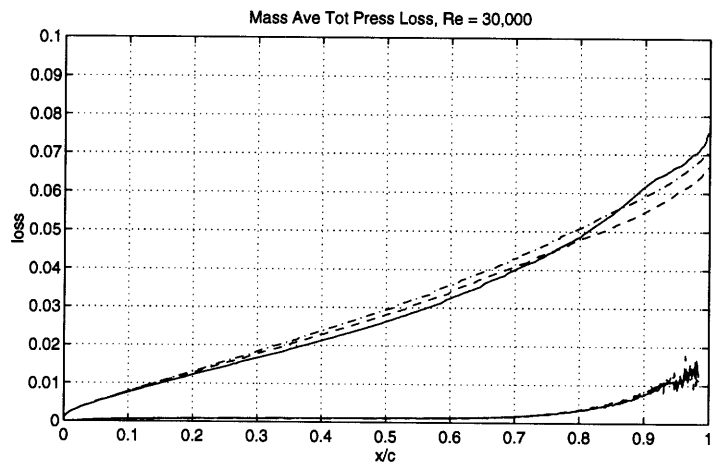
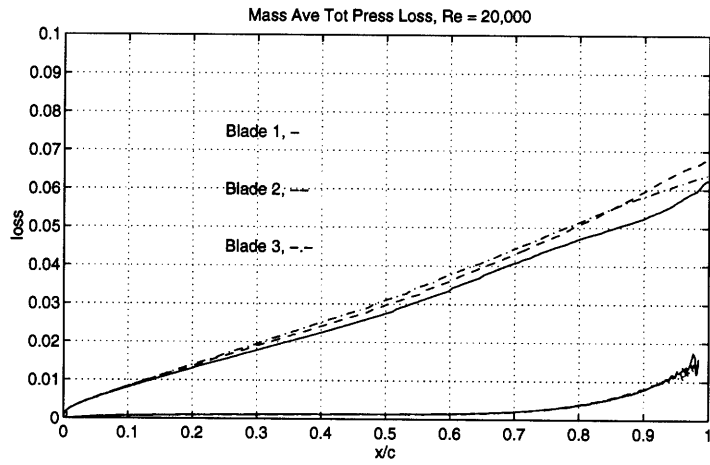


Figure 4-1: Mass-averaged total pressure loss for the three geometries at Re = 20,000 and 30,000

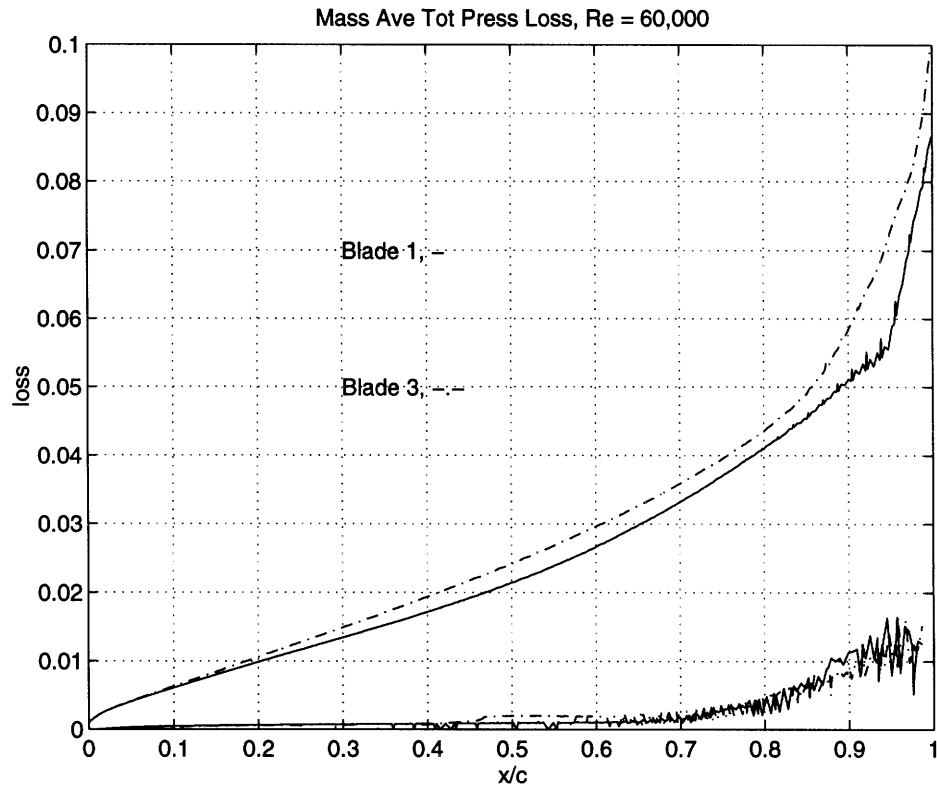


Figure 4-2: Mass-averaged total pressure loss for *blade 1* and *blade 3* at $Re = 60,000$

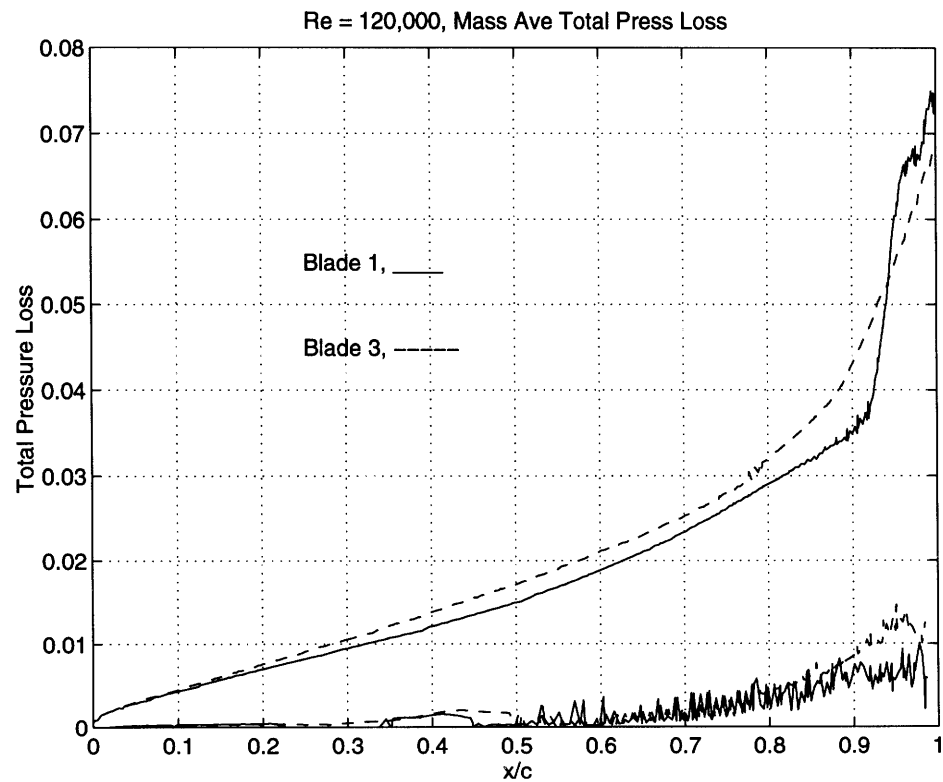


Figure 4-3: Mass-averaged total pressure loss for *blade 1* and *blade 3* at $Re = 120,000$

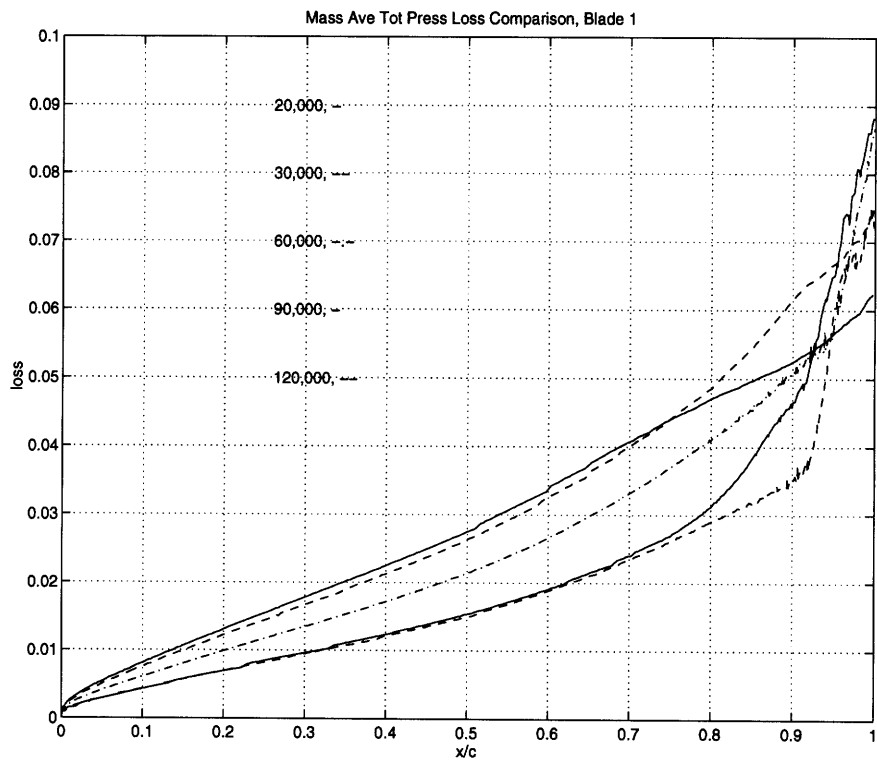


Figure 4-4: Mass-averaged total pressure loss for *blade 1* , at all Reynolds numbers used in the investigation

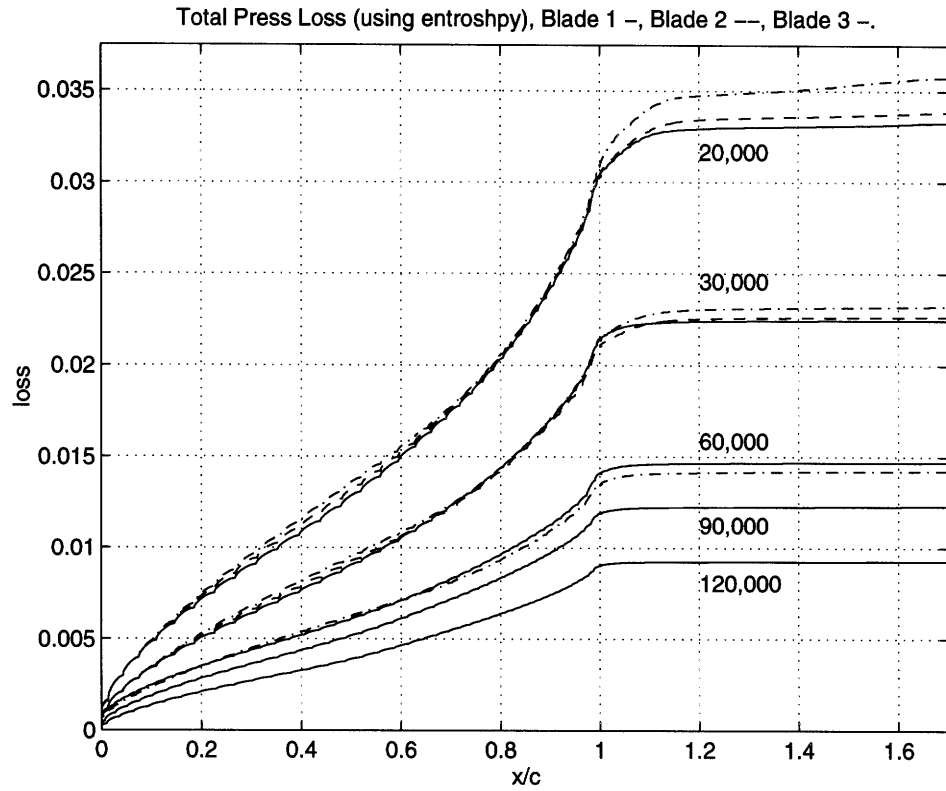


Figure 4-5: Total pressure loss calculated using enstrophy for calculations

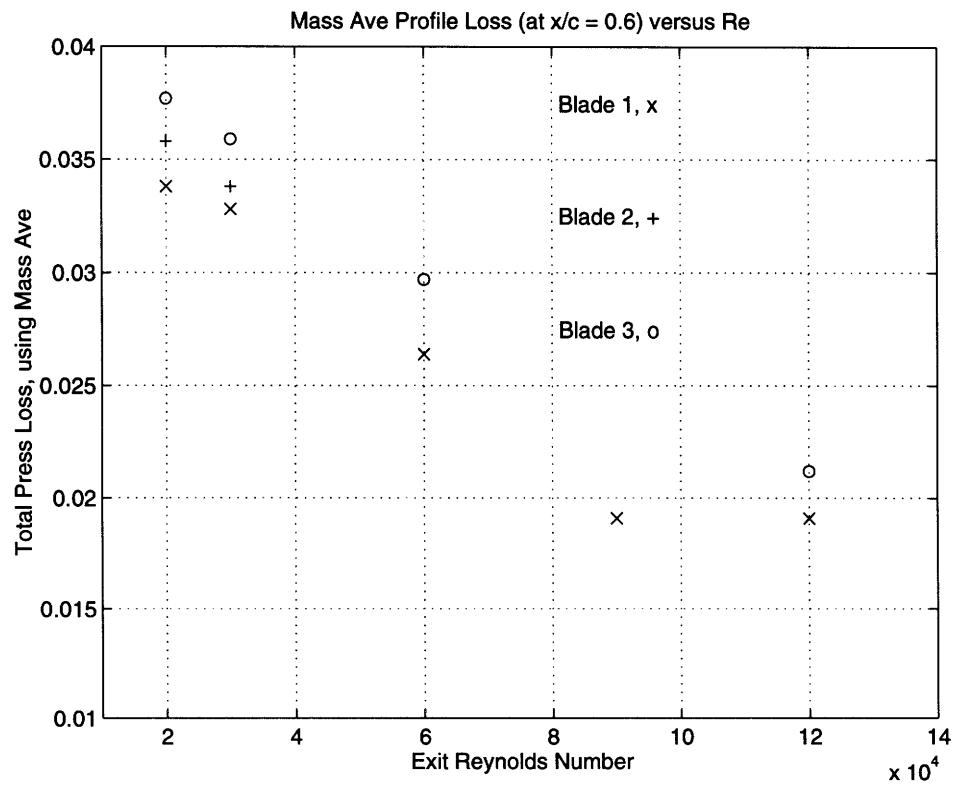


Figure 4-6: Loss vs. Reynolds number, using mass-average

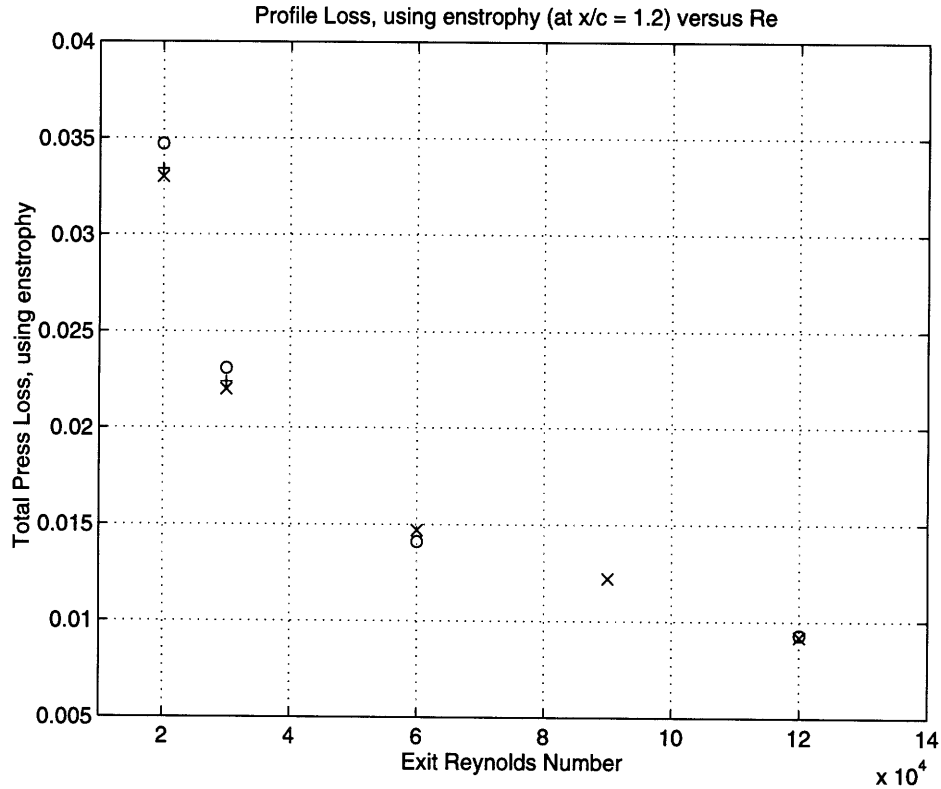


Figure 4-7: Loss vs. Reynolds number, using enstrophy

assumes the base pressure term, C_{p_b} , is zero, and that the trailing edge thickness, τ , is 0.01 chords. The exit flow area is taken as that normal to the flow direction, and for an exit angle of 58 degrees, the area is, $S = 0.42$. The approximation used to determine the added loss is equation (3.9).

These results highlight the need for a better determination of the mixing loss if any true ranking of the geometries is to be made. This simple calculation shows that the mixing loss due to the separated shear layer is on order of 1/2 of the total loss, especially when the separated region takes up more than 10% of the exit flow area.

4.2.4 Effects of Blade Loading on Shear Layer Development

The second focus of this investigation was to determine the impact the blade geometry has on the unsteady flow features. We begin by examining the differences observed in shear layer development associated with a variation in the type of blade loading used.

The effect of blade design can be deduced from an examination of the computed flows for the three geometries at any given Reynolds number. For instance, at $Re = 30,000$, the

Blade, Re	δ^*	Added Loss due to Mixing
1 20,000	0.11	.08
2 20,000	0.11	.08
3, 20,000	0.09	.06
1, 30,000	0.10	.07
2, 30,000	0.12	.09
3, 30,000	0.10	.07
1, 60,000	0.07	.04
3, 60,000	0.07	.04
1, 90,000	0.06	.03
1, 120,000	0.06	.03
3, 120,000	0.05	.02

Table 4.3: Values used for calculation of ω^*

shear layer roll-up for *blade 1* takes place upstream of the trailing edge, while the instability does not arise in *blade 3* until after the trailing edge.

Thus, the influence of blade geometry, as seen in these solutions, is found in terms of the point at which the shear layer becomes unstable. It is a well known result that an adverse pressure gradient destabilizes a flow, whereas a favorable pressure gradient can have stabilizing effects on the flow [2].

The more adverse the pressure gradient, the earlier transition to a turbulent boundary layer will occur. The analogy can then be made for the inviscid instability for a separated shear layer. The more adverse the pressure gradient, the sooner the roll-up into a discrete vortex will take place. This explains the “lagging” behind in the re-attachment process seen for *blade 3*. The forward loading associated with *blade 3* has a correspondingly less severe *inviscid* adverse pressure gradient.

These calculations lead one to infer that earlier re-attachment will occur for an aft loaded blade. Not only does the shear layer tend to become inviscidly unstable sooner, leading to shorter distances between the separation point and the point of vortex development, but the shear layer will also tend to transition earlier; the increased momentum transfer associated with the turbulent shear layer will cause it to have a larger growth rate, and thus intersect the blade surface before a laminar shear layer would.

Another interesting effect of the pressure gradient, especially in the region of separation, is the determination of the angle the separated shear layer will make with the wall (figure

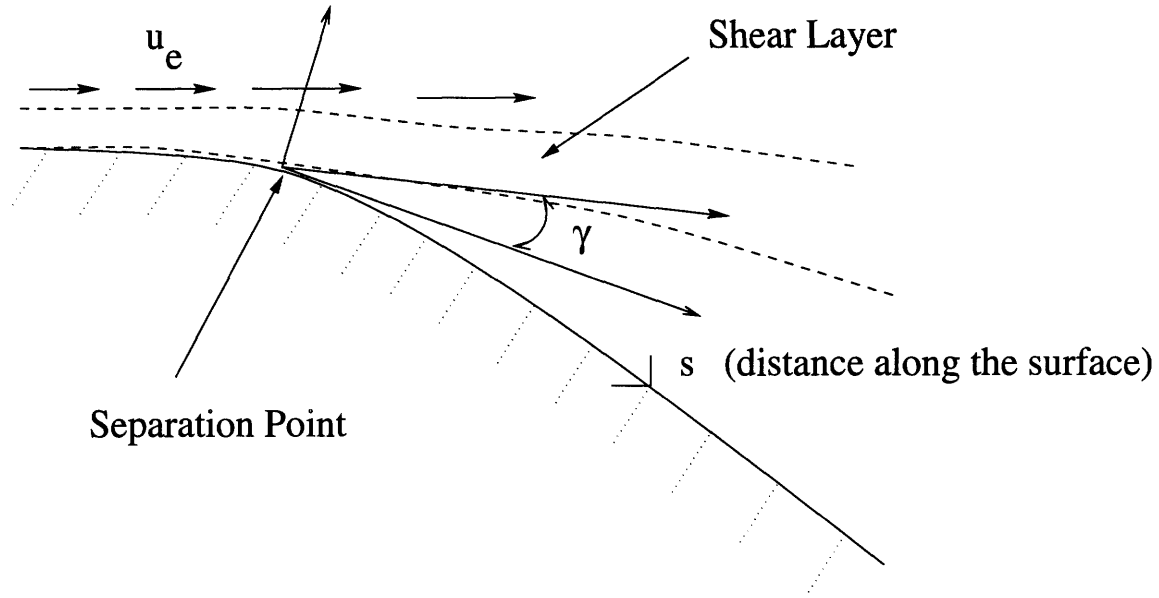


Figure 4-8: Nomenclature for determining the angle the shear layer makes with the wall at the separation point

4-8). The angle at separation can be determined using the ratio of the time-averaged pressure gradient at separation and the gradient in the shear stress [3] :

$$\gamma = \text{atan} \left(-3 \frac{d\tau/ds}{dp/ds} \right) \quad (4.7)$$

Table (4.4) determines the value of the constant using the following formula :

$$\kappa = -\tan(\gamma) \frac{dC_p/ds}{dC_f/ds} \quad (4.8)$$

with, $C_p = \frac{p-p_{inlet}}{\frac{1}{2}V_{T_i;nlet}^2}$, and $C_f = \frac{\tau}{\frac{1}{2}V_{T_i;nlet}^2}$. The values for the constant, κ , are in the general range of 2.0 to 4.0, thus confirming the analytical result of

$$\tan(\gamma) \frac{dC_p/ds}{dC_f/ds} = -3 \quad (4.9)$$

4.2.5 Profile and Mixing Loss Tradeoffs Associated with Choice of Blade Geometry

This final section focuses upon the tradeoffs associated with the choice of blade loading. This will be based on the generated profile and mixed-out losses, as well as the implications these geometry variations have upon the development of the separated shear layer.

Blade, Re	dC_p/ds	dC_f/ds	γ , observed	κ
1, 20,000	1.03	-0.071	8.5	-2.2
2, 20,000	0.94	-0.050	10.0	-3.3
3, 20,000	0.82	-0.054	8.0	-2.1
1, 30,000	0.50	-0.034	9.0	-2.3
2, 30,000	0.47	-0.036	7.5	-1.7
3, 30,000	0.57	-0.035	9.0	-2.6
1, 60,000	0.90	-0.034	8.0	-3.7
3, 60,000	0.61	-0.024	9.0	-4.0
1, 90,000	0.71	-0.040	5.5	-1.7
1, 120,000	0.56	-0.022	6.0	-2.7

Table 4.4: Calculation of angle shear layer makes with solid surface at point of separation

The results that have been presented show that the aft loaded blade (*blade 1*) develops less profile loss than the forward loaded blade (*blade 3*). This has to do with the higher freestream velocities found for the forward loaded design.

Another observation relating to the blade geometry, is that after an investigation of the movies, the forward loaded blade tends to have its suction side separation closer to the blade surface at the trailing edge plane. This can be reasoned to be so by the magnitudes of the inviscid adverse pressure gradients occurring in the aft region of the blades. The aft loaded blade has the greater inviscid pressure gradient, thus the flow is retarded more and would tend to have a larger region of separation at the trailing edge plane. On the other hand, the forward loaded blade separates earlier, but because of the gentle aft inviscid gradient, the shear layer remains closer to the wall than for the aft loaded blade.

Since the displacement thickness at the trailing edge is a main cause of the added loss due to separation, A method that would tend to keep δ^* small at the trailing edge would be advantageous. Therefore, it is found that there are tradeoffs between a forward loaded blade, which has higher profile loss, but smaller loss due to separation, as compared to an aft loaded blade with the opposite features.

Chapter 5

Summary and Conclusions

5.1 Summary and Conclusion

A first-of-a kind calculation of the two-dimensional, incompressible flow through a LPT passage has been implemented for three LPT blade designs with identical gas angles for a range of exit Reynolds numbers from 20,000 up to 120,000; the first chapter presented the motivation for this investigation as well as the technical objectives of the work. The second chapter describes the method used for performing the calculations, and some of the postprocessing procedures. Computed results and explanations for the observed flow features are presented in chapter (3). Finally, the fourth chapter discussed the implications these results have upon distinguishing between seemingly similar blade designs, as well as aspects of fluid dynamics that set the flow field.

The time-averaged flows indicate that *blade 1* has better performance for the range of Reynolds numbers investigated. The two criteria used to reach this conclusion are the position of a time-average vortex on the suction side, indicating the aft region of a separation bubble, and the magnitude of the profile loss generated.

The process leading to re-attachment is directly linked to the observed unsteady flow features. The dynamics associated with the vortex shedding were shown to be a function both of Reynolds number and of the type of loading used in a blade design. The earlier suction side shear layer instability seen for *blade 1* as compared to *blade 3* or *blade 2*, leads to a smaller length between the separation point and the time-average location of the vortex associated with the shear layer re-attachment.

This work has also shown that it is possible to use higher order numerical schemes (such

as the spectral method) to compute two-dimensional, unsteady flow at Reynolds numbers above 100,000. More importantly, such a method demonstrates the ability to detect changes in flow behavior due to slight changes in blade design, but with identical gas flow angles.

5.2 Future Work

The natural continuation of this work would be to implement simulations at Reynolds numbers for which a steady re-attachment of separated flow occurs on the blade suction side. Following this, the response of LPT flow fields to upstream moving wakes could be assessed in terms of the time-average as well as the temporal flow behavior.

The extension of the incompressible spectral code to a compressible code would also be useful. A comparison between solutions at the same Reynolds number would allow one to make inferences on how important compressibility is on the dynamical processes associated with a separated shear layer. The accomplishment of a compressible spectral code would leave only the requirement of two-dimensionality as an assumption for a direct simulation.

A difference was seen between the value of loss calculated using a mass averaged total pressure and the value of loss found using enstrophy. Further work should examine why this disparity is observed.

Last, a comparison of these direct solutions using experimental data would help one judge the effectiveness of the spectral code in capturing the flow features that drive the LPT blade performance. A goal is to determine if a high performing two-dimensional profile, designed using a numerical scheme with the resolution of the spectral code, translates into a well designed three-dimensional LPT blade. An answer to such a question can only be found through a comparison of calculations and experimental data.

Appendix A

Effects of Inflow and Outflow Boundary Placement on Solution

Several cases were run to determine the influence of boundary placement on the computed solutions. Normal boundary placement consisted of using an inflow boundary 0.35 chords from the leading edge and an outflow boundary 0.7 chords from the trailing edge. A display of this boundary placement is given in figure (A-1). These smaller grids were used in order to compute solutions at the higher Reynolds numbers (90,000 and 120,000), due to the amount of computational resources required for a solution as Reynolds number increases. Therefore, to have consistency between the solutions, the same boundary placement was used at the lower Reynolds numbers, even though it would have been possible to use more elements.

To determine the effect of the proximity of the inflow and outflow boundaries on the solutions, a case was run for both *blade 1* and *blade 3* at $Re = 30,000$ with the inflow boundary moved to 1.0 chord from the leading edge, and the outflow boundary moved to 1.7 chords from the trailing edge. The grid used for *blade 1* is shown in figure (A-2).

A final calculation was performed for *blade 1* only to determine if the inflow or the outflow boundary had the most effect on the solution. The inflow boundary was moved back to the original position of 0.35 chords from the leading edge, with the outflow boundary kept as for the “large” grid case at 1.7 chords from the trailing edge. This grid is displayed in figure (A-3). The results from this solution were conclusive in determining which boundary had the most effect.

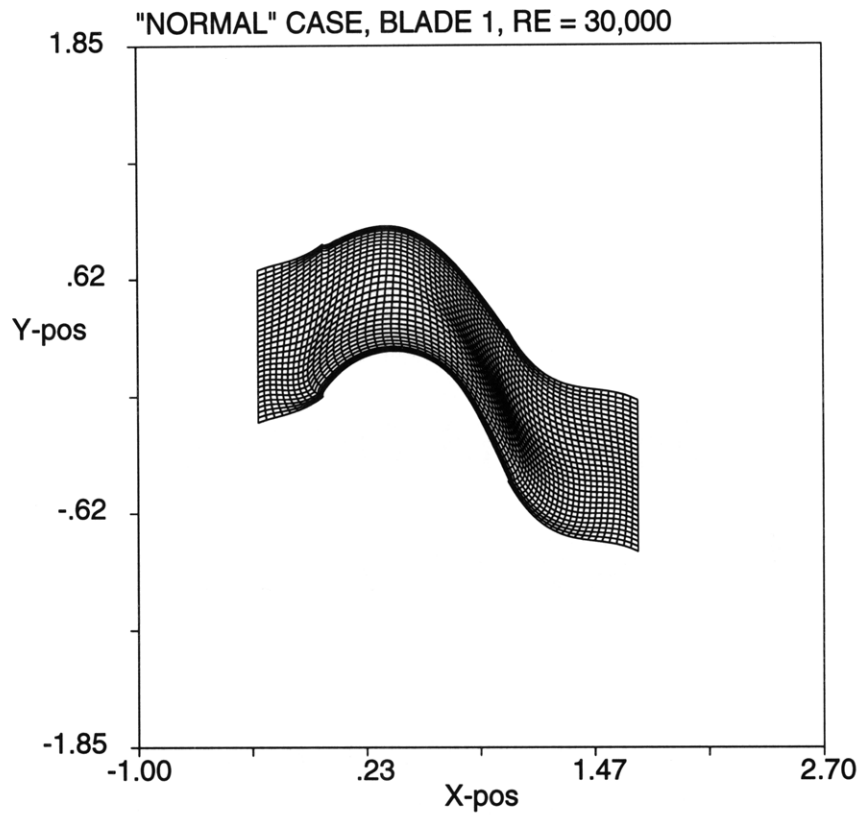


Figure A-1: Grid used for the cases shown in table (3.1), "normal" grid

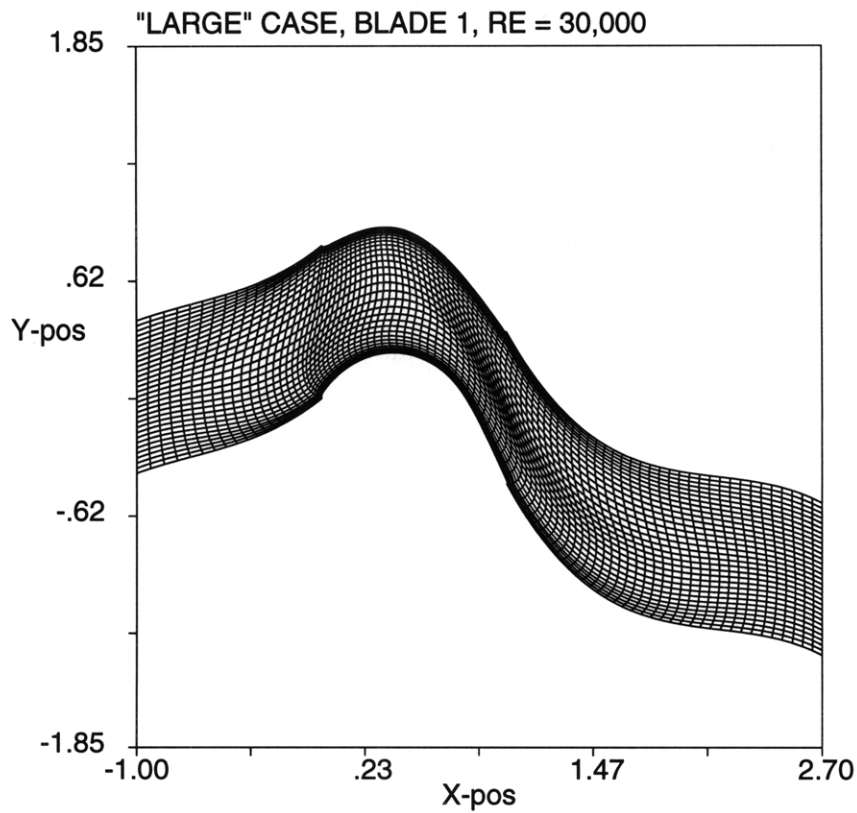


Figure A-2: Grid used the "large" grid cases

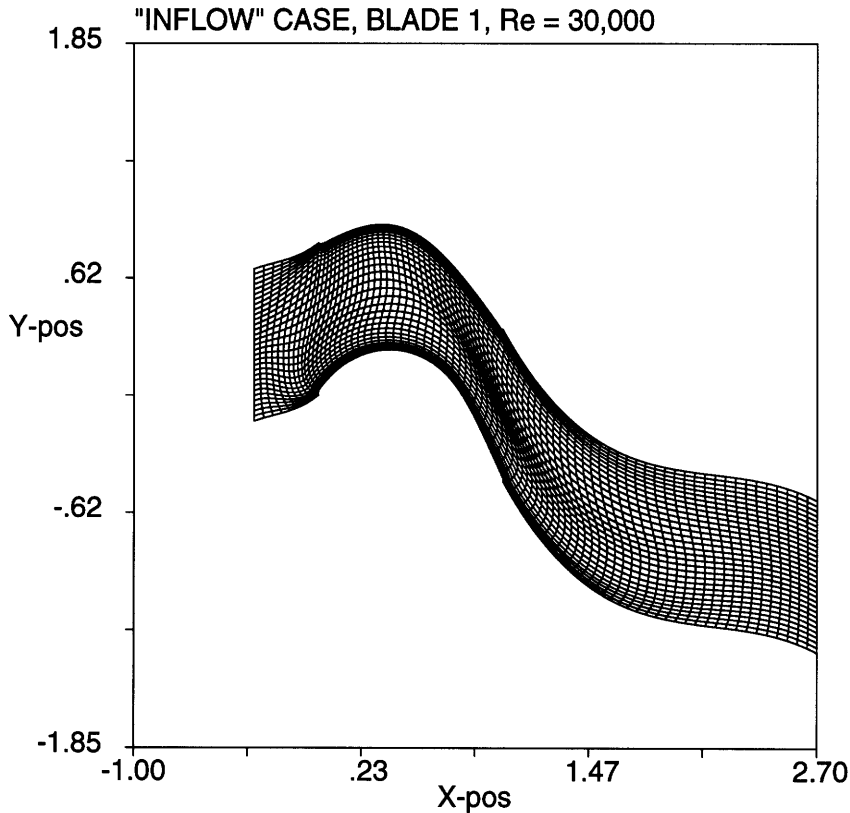


Figure A-3: Grid used the “inflow” grid cases

A.1 Results

Moving the boundaries further away from the blade, as for the “large” grid case, had an effect on the solution. Observations of the flow movies demonstrate that the change in boundary placement from the “normal” to the “large” grid had differing effects on *blade 1* as compared to *blade 3*.

The location of vortex generation associated with the suction side shear layer for *blade 1* moved downstream, nearly past the trailing edge for the “large” case, whereas the shear layer roll-up for *blade 1* for the “normal” case occurred upstream of the trailing edge. A demonstration of this can be seen in a static pressure comparison over the blade between the two cases shown figure (A-4). Any sign of a low pressure region associated with a time-average vortex in the separated region is nearly gone for the “large” grid solution, indicating that the vortex roll-up occurs downstream of the trailing edge. Because of this, a change in the amount of unsteadiness is seen between the two cases, with the “normal” case showing larger variations in the static pressure on the suction side (compare figures A-5 and A-6)

Performing the same process for *blade 3*, using a “normal” grid and a “large” grid, also

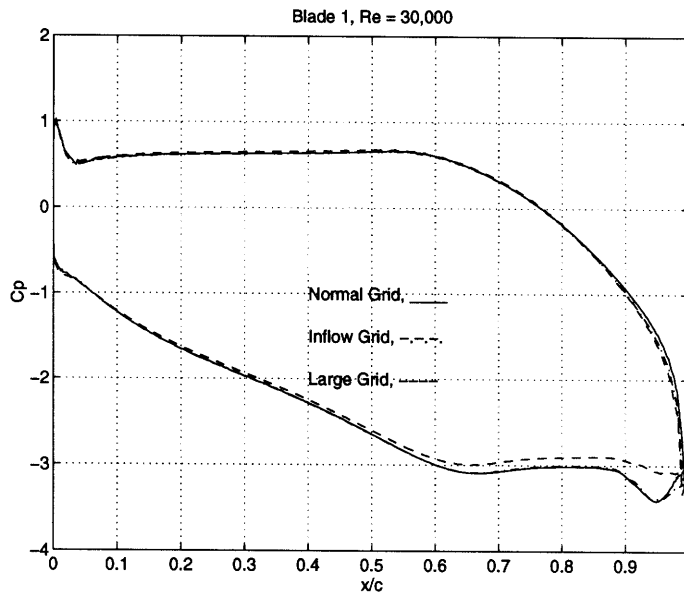


Figure A-4: Static pressure comparison for *blade 1* at $Re = 30,000$ between the three different boundary placements used, “normal”, “large”, and the “inflow” cases

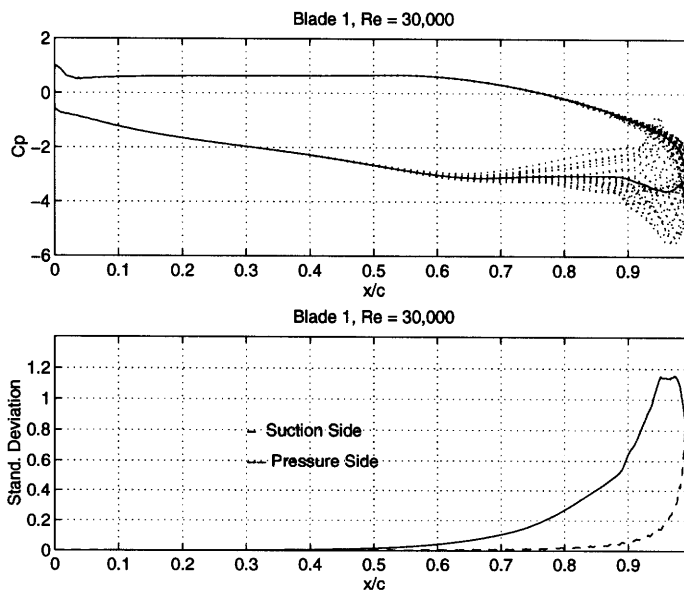


Figure A-5: Static pressure envelope and standard deviation of the pressure from the mean for *blade 1* at $Re = 30,000$, “normal” case

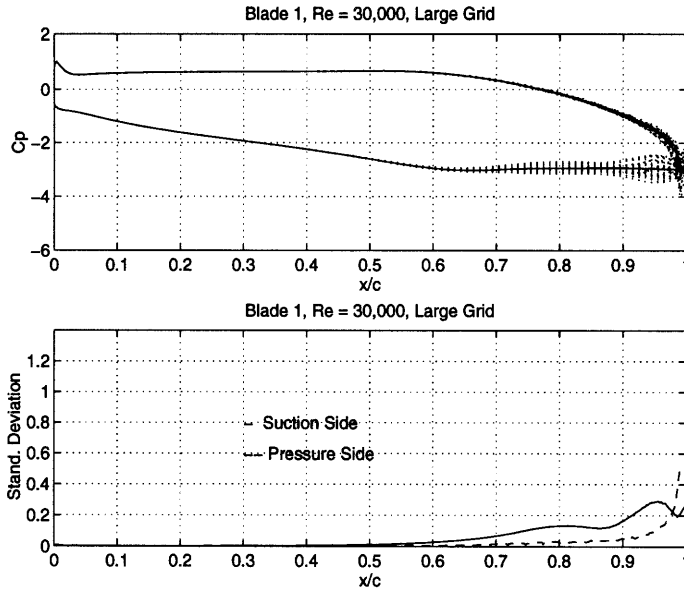


Figure A-6: Static pressure envelope and standard deviation of the pressure from the mean for *blade 1* at $Re = 30,000$, “large” case

showed differences in the solutions. But, unlike the solution change for *blade 1*, the static pressure over the blade was less effected, with the only difference being the presence of a time-averaged vortex on the suction surface right at the trailing edge (figure A-7). The movement of the boundaries outwards thus changed the solution for *blade 3* by moving the location of shear layer roll-up upstream for the “large” grid case, with an associated increase in the static pressure unsteadiness observed (compare figures A-8 and A-9).

To investigate which boundary had the most effect upon the solution, the inflow boundary was moved back to the position of 0.35 chords from the leading edge, as found for the “normal” grids, but the outflow boundary was kept 1.7 chords away. This grid is termed the “inflow” grid.

A calculation was performed for *blade 1* at $Re = 30,000$. The static pressure over the blade is shown in figure (A-4). The static pressure matches almost exactly with that for the “normal” grid case. Also, a comparison of the static pressure deviations (compare figures A-5 and A-10) show that the two cases have equivalent magnitudes of pressure deviations on the suction side. Observations of the movies for the two cases reveal that the shedding dynamics are nearly identical.

Therefore, it was concluded that the *inflow* boundary has the most effect on the solution. Because of time, and computational constraints, further computations using an “inflow” grid

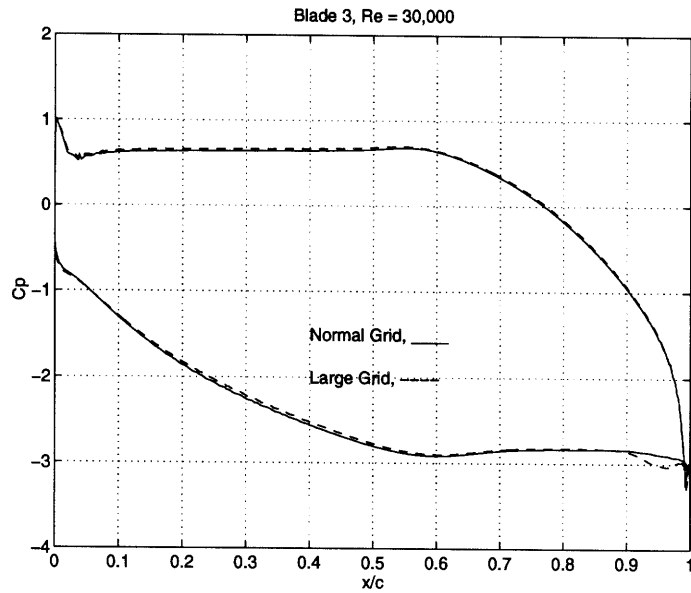


Figure A-7: Static pressure comparison for *blade 3* at $Re = 30,000$ between the two different boundary placements used, “normal”, “large” cases

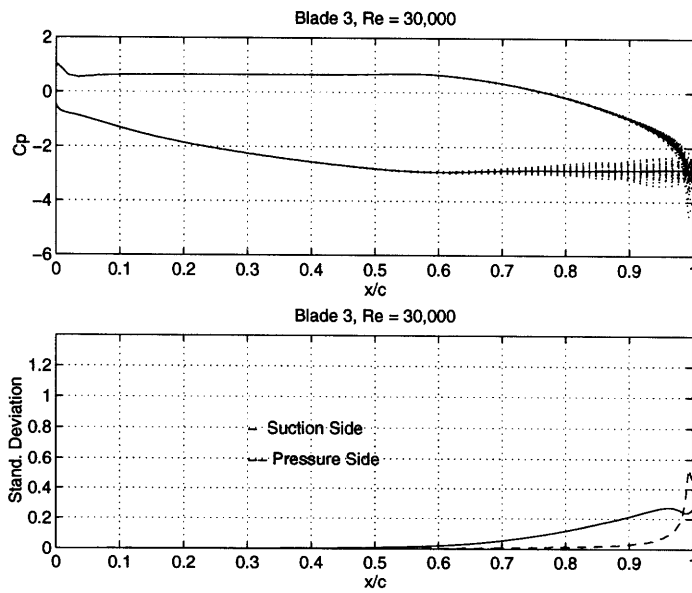


Figure A-8: Static pressure envelope and standard deviation of the pressure from the mean for *blade 3* at $Re = 30,000$, “normal” case

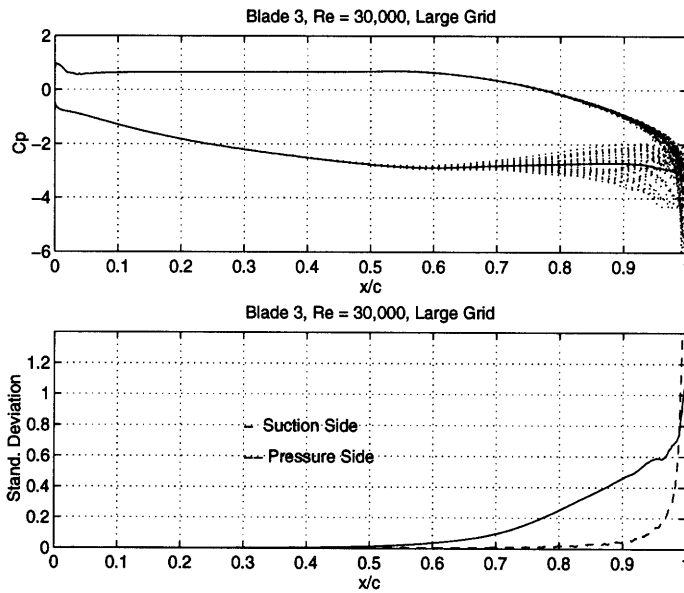


Figure A-9: Static pressure envelope and standard deviation of the pressure from the mean for *blade 3* at $Re = 30,000$, “large” case

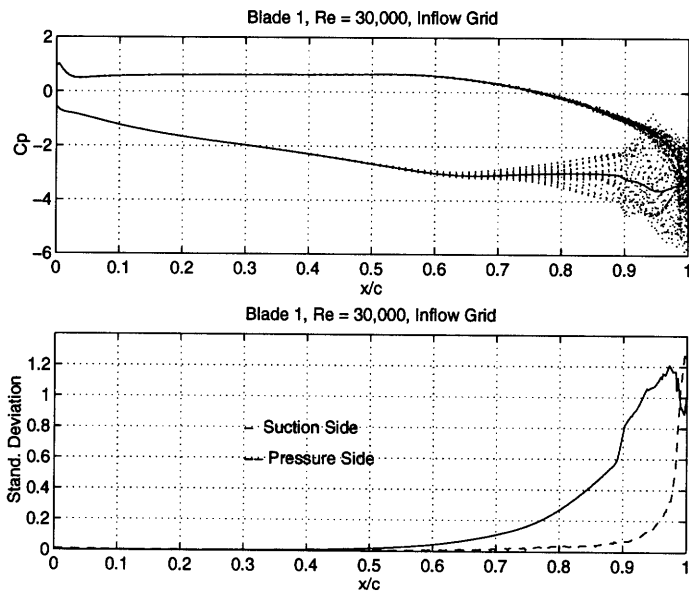


Figure A-10: Static pressure envelope and standard deviation of the pressure from the mean for *blade 1* at $Re = 30,000$, “inflow” case

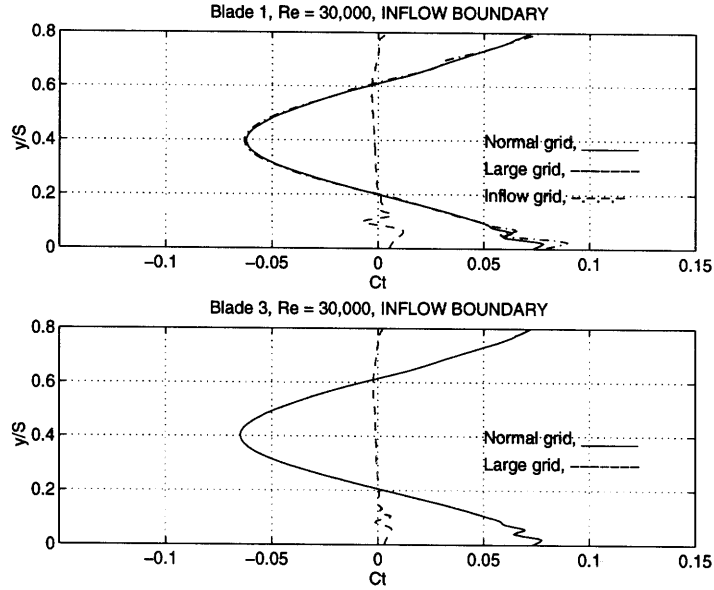


Figure A-11: Total pressure variation at the inflow plane for *blade 1* and *blade 3* for the three various boundary placements

for *blade 3* were not performed.

A.2 Explanation of Results

The reason for the changes seen in the solutions is attributed to the effect the inflow boundary proximity to the leading edge has upon the incoming total pressure profile across the span. Figure (A-11) shows the total pressure variation across the blade span at the inflow boundary plane. The “normal” and “inflow” cases indicate a variation in the total pressure, whereas the “large” case shows no such deviation from a constant span-wise total pressure profile.

The condition prescribed at the inflow boundary is the angle and magnitude of the incoming flow velocity. Therefore, the pressure is allowed to vary at the inflow boundary. The closeness of the boundary to the blade leading edge for the “normal” and “inflow” cases leads to a static pressure variation due to the potential field produced by the blade. The “large” case has an inflow boundary far enough from the blade leading edge for this variation in the static pressure not to cause any deviations of the total pressure.

This total pressure profile convects from the inflow boundary to the blade passage, with the total pressure profile at the inlet to the passage for the cases shown in figure (A-12). Figure (A-13) shows the profile at a plane $x/c = 0.75$, again showing the variation in the

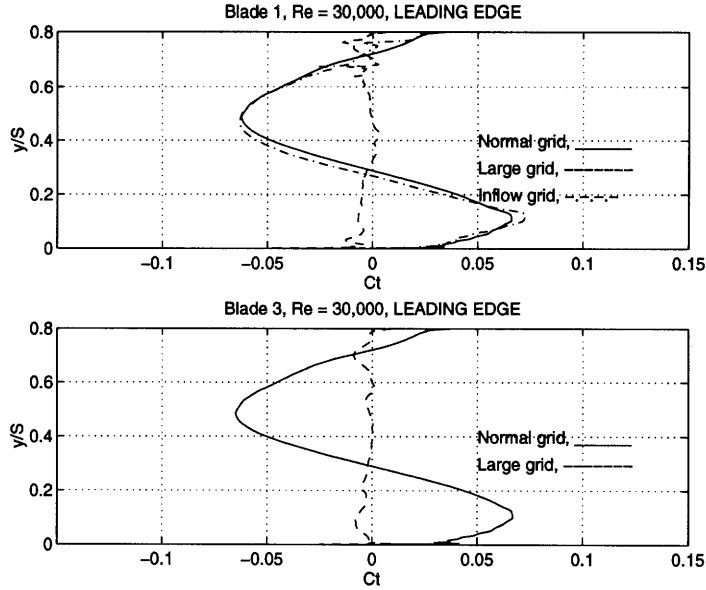


Figure A-12: Total pressure variation at the leading edge plane, $x/c = 0$, for *blade 1* and *blade 3* for the three various boundary placements

total pressure across the passage for the cases where the boundary was located close to blades.

A.3 Implications

These results thus show that the incoming total pressure profile can impact the time-average as well as the unsteady flow dynamics. The exact process in which the interaction occurs is unclear, with the shear layer roll-up moving downstream for *blade 1* as the inflow boundary was moved away from the leading edge, and the roll-up for *blade 3* moving upstream. For the time-averaged flow, a variation in the total pressure profile at the inflow plane implies an accompanying vorticity profile.

$$\nabla \cdot (\overline{\mathbf{u}p_t}) = \frac{1}{Re} \left(\nabla \cdot (\overline{\mathbf{u} \times \boldsymbol{\omega}}) - \overline{|\boldsymbol{\omega}|^2} \right) \quad (\text{A.1})$$

Since the velocity at the inflow plane is constant, the variation in p_t must have an associated variation in $\boldsymbol{\omega}$. This vorticity also convects through the passage, and could lead to clues as to why the unsteady flow dynamics are changed.

The fact that the incoming total pressure profile causes variations in the observed dynamics could be a cause of concern when trying to compare the solutions at all the Reynolds

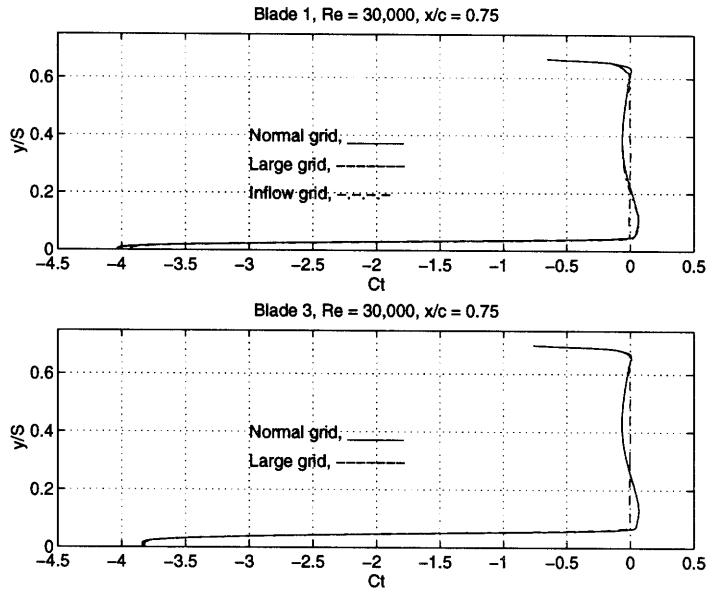


Figure A-13: Total pressure variation at a plane $x/c = 0.75$ for *blade 1* and *blade 3* for the three various boundary placements

numbers. But as can be seen in figure (A-14), the same total pressure variation is present for all the calculated solutions. Thus this consistency allows us to confidently compare the observed flow fields found using the “normal” grids.

This changing in dynamics with the incoming total pressure profile should serve as notice that the flow fields found for actual engine operating conditions, with the downstream convection of wakes from previous blade rows, may be significantly different from those found for an isolated cascade.

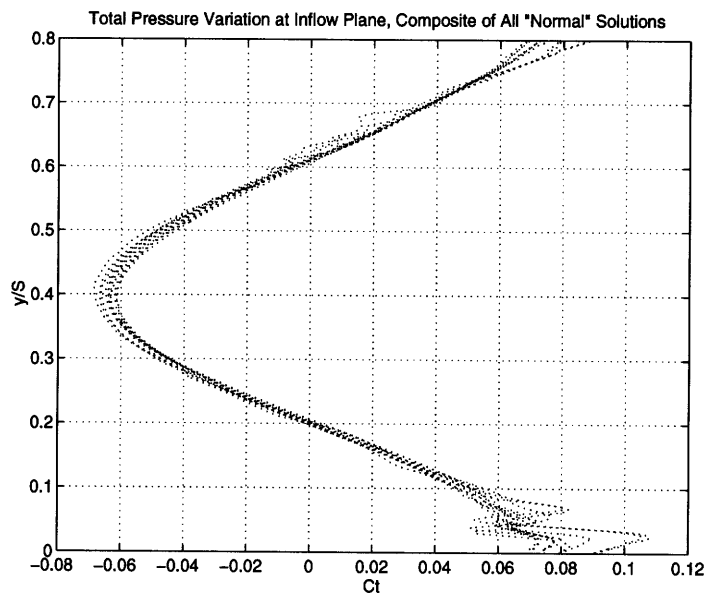


Figure A-14: Total pressure variation at the inflow plane for all the “normal” grid solutions

Appendix B

Loss Calculation Procedures

B.1 Loss Calculations

The mass-averaged total pressure loss presented in chapter (3) is calculated using the following method :

1. For each “snapshot” of the flow field (created for making the movies), the value of $(\mathbf{u}C_t)$ is calculated at every point in the flow field.
2. A time-average of this value is calculated using the 20 to 30 “snapshot” flow fields, providing the non-linear time-average, $\overline{(\mathbf{u}C_t)}$.
3. A determination of the boundary layer thickness on pressure and suction sides is made by finding the point where the vorticity reaches zero, or where the change in vorticity across the passage reaches a value of zero, $\partial\omega_z/\partial y = 0$, with appropriate measures taken to eliminate errors due to regions of flow recirculation (see figure B-1).
4. The mass-averaged total pressure loss is calculated using the non-linear time-averaged values, with the integration performed only through the boundary layers (this assumes that the total pressure coefficient, $\overline{C_t}$, is zero outside of the boundary layers). The integration is performed in the boundary layers only because we are trying to avoid the total pressure loss generated by the noise found on pressure side in the trailing edge region :

$$(\overline{C_t})_{mass} = \frac{\int_0^\delta \overline{(u_x C_t)} dy}{\int_0^S u_x dy} \quad (\text{B.1})$$

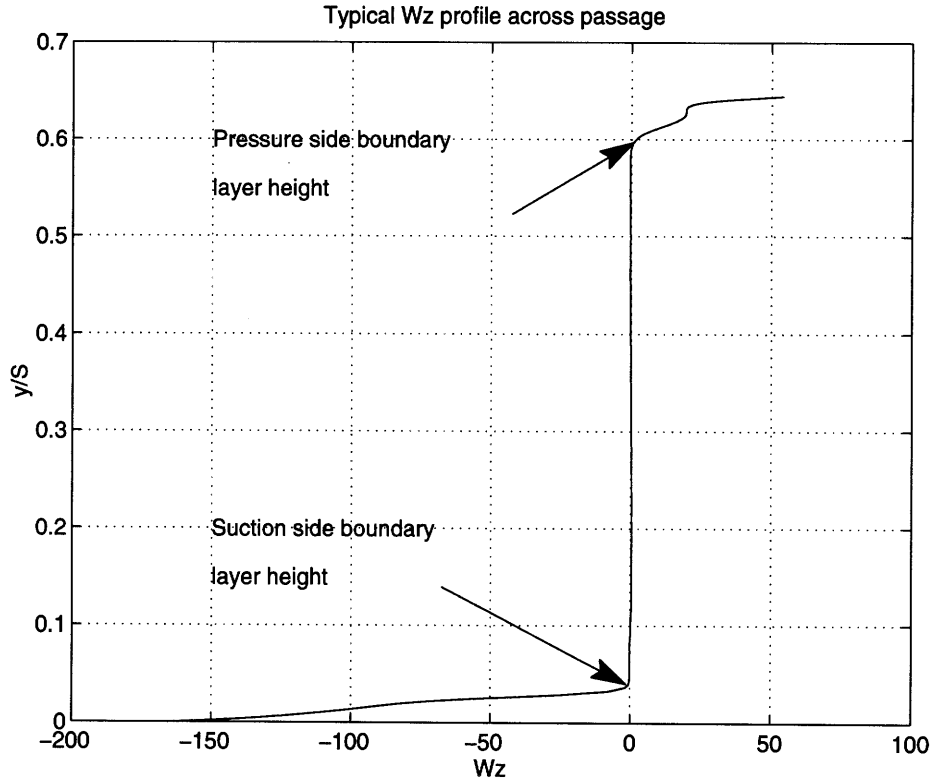


Figure B-1: Typical vorticity profile across the passage, used for the determination of boundary layer thicknesses

5. This procedure is followed for both the suction and pressure sides, and $(\overline{C_t})^{mass}$ is the quantity plotted for all of the total pressure loss plots presented in chapters (3) and (4).

The calculation of loss using enstrophy, $|\omega|^2$, was performed using the volume integral of $|\omega|^2$ for the whole computational domain.

$$Total\ Pressure\ Loss \approx \frac{-2}{Re} \int \int |\overline{\omega}|^2 dx dy \quad (B.2)$$

This integral is *not* restricted to the boundary layers because of the nature of the noise on the pressure side. This noise has fluctuations of both positive and negative vorticity, and thus on the time-average, the noise tends to cancel itself out. This is not true for the total pressure because, even though the vorticity could have positive or negative values, a total pressure loss is generated independent upon the sign of the vorticity.

As stated previously in chapter (2), the calculation of the loss by either method should be approximately equivalent :

$$\int_S (\overline{u p_t}) \cdot \mathbf{n} \, dS \approx -\frac{1}{Re} \int_V \overline{|\boldsymbol{\omega}|^2} \, dV \quad (\text{B.3})$$

One of the questions not answered as of yet is why the loss calculated on the left hand side of equation (B.3) is not equivalent to that found using the right hand side. This is seen by a comparison of the loss magnitudes given for the various cases in chapter (3).

B.2 Loss Calculation for a Blasius Profile

To investigate the equivalence of the mass-averaged total pressure loss and the volume integral of the enstrophy, the calculation of the loss using both methods is performed on a Blasius boundary layer profile. The similarity solution existing for the velocity profile is used in order to calculate the total pressure flux and the vorticity field.

Following standard procedure for non-dimensionalizing the y-coordinate and the velocity for a Blasius similarity solution [1] :

$$y = \eta \left[\sqrt{\frac{\nu x}{u_e}} \right] \quad (\text{B.4})$$

$$u(\eta) = u_e f' \quad (\text{B.5})$$

$$f = f(\eta) \quad (\text{B.6})$$

$$f' = \frac{df}{d\eta} \quad (\text{B.7})$$

The values of f' and f'' are tabulated, and can be used to calculate the velocity at any point in the boundary layer at any x-position. Figure (B-2) shows the nomenclature to be used.

Using the velocity field, the total pressure flux and the volume integral of the enstrophy

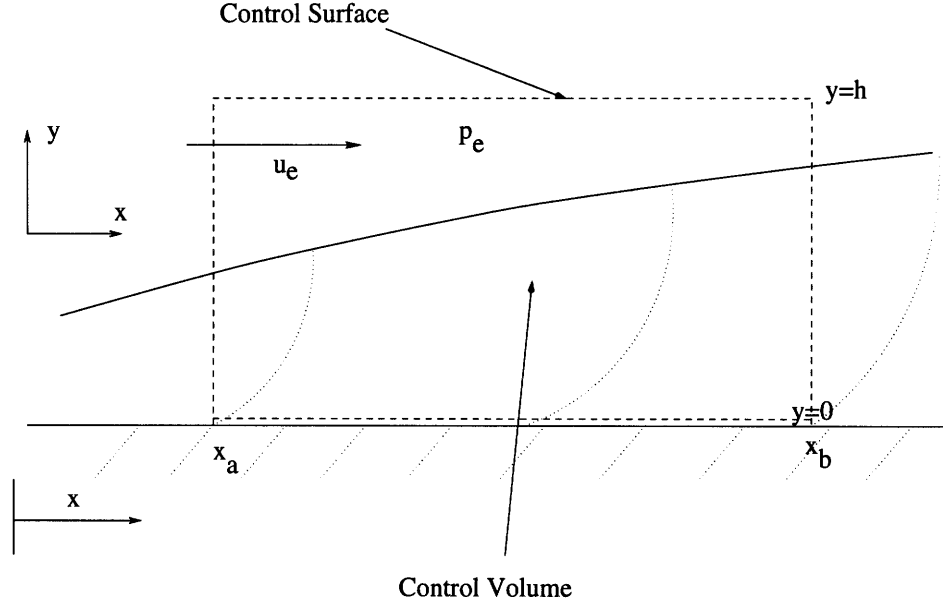


Figure B-2: Nomenclature to be used for calculating the loss associated with a Blasius boundary layer

can be found as functions of the non-dimensional height, η .

$$p_t(\eta) = p_e + \frac{1}{2}\rho u^2 \quad (\text{B.8})$$

$$up_t = u_e p_e f' + \frac{1}{2}\rho u_e^3 (f')^3 \quad (\text{B.9})$$

$$(\omega_z)^2 = \left(\frac{du}{dy}\right)^2 = \frac{u_e^3}{\nu x} (f'')^2 \quad (\text{B.10})$$

These quantities can then be integrated using the control volume shown in figure (B-2),
i.e. :

$$Y_1 = \left(\int_0^h up_t dy\right)_B - \left(\int_0^h up_t dy\right)_A \quad (\text{B.11})$$

$$Y_2 = -\mu \int_0^h \int_{x_A}^{x_B} \left(\frac{du}{dy}\right)^2 dx dy \quad (\text{B.12})$$

The assumptions made in this approach are that the velocity normal to the wall, v , and its derivative with respect to x , dv/dx , are small compared to the streamwise velocity, u , and du/dy . It was shown earlier that :

$$Y_1 \approx Y_2$$

h	Y_1	Y_2	Y_3
.030	-0.0086	-0.0077	-1.7e-7
.025	-0.0082	-0.0076	-1.8e-7
.020	-0.0069	-0.0073	-1.9e-7
.015	-0.0047	-0.0064	-1.9e-7

Table B.1: Comparison of mass-averaged total pressure loss and loss calculated using entstrophy for a Blasius boundary layer

With the approximation being for the Blasius profile that the term,

$$Y_3 = \mu \int_S (\overline{\mathbf{u} \times \boldsymbol{\omega}}) \cdot \mathbf{n} \, dS \quad (\text{B.13})$$

is small compared to the entstrophy volume integral, Y_2 . The $\mathbf{u} \times \boldsymbol{\omega}$ term for the two-dimensional flow found in this situation becomes the vector :

$$\mathbf{u} \times \boldsymbol{\omega} = (v\omega_z)i + (-u\omega_z)j \quad (\text{B.14})$$

Thus, the flux through the vertical faces only involves the term, $v\omega_z$.

Finally, reaching the point of this exercise, the total pressure flux can be shown to be of comparable magnitude to the volume integral of the entstrophy. Table (B.1) compares the values for Y_1 , Y_2 , and Y_3 for various control volume sizes. The values used in the calculation are :

$$u_e = 1.0, p_{t_e} = 1.0, \rho = 1.0, \mu = \frac{1}{20000}$$

thus giving, $p_e = 0.5$, and $\nu = \mu/\rho = 1/20000$.

The integral is taken between the x values of $x_A = 0.2$ and $x_B = 1.0$. The various values shown are for different control volume heights, h , and a plot of the boundary layer profiles is given in figure (B-3).

Thus, table (B.1) shows that the entstrophy term, Y_2 , and the total pressure flux, Y_1 , are not exactly equal, even for this simplified case for flow over a flat plate. The difference is not due to the neglected term, Y_3 , because as shown, it is of several orders of magnitude smaller than the value of Y_2 .

The only explanation left to account for the difference is numerical problems, but several cases were run for the same conditions shown in table (B.1) but with 100 times more points

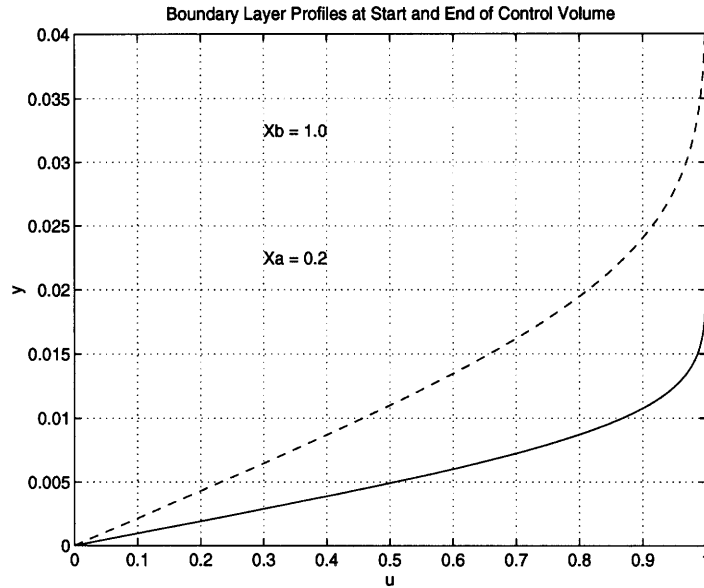


Figure B-3: Boundary layer profiles at edges of control volume, for $\mu = 1/20000$

used in the grid, and the result was only 1% off of the values shown.

Therefore, the conclusion is that although the enstrophy is valuable for determining the amount of dissipation due to the boundary layers and giving a way to compare various solutions, care must be taken when trying to relate the loss calculated by this method to a mass-averaged total pressure loss.

Appendix C

Grid Effects and Computational Effort

C.1 Effect of Gridding on Solution Stability

Two general lessons were learned from the set of calculations used in this investigation regarding the effect of gridding schemes. One, a grid that works well for one calculation may not work so well for another, and two, there are some general guidelines that can be followed to increase the success in obtaining a periodically converged solution. Because no strict analytical guideline can be derived regarding spatial discretization and time-step for this spectral scheme, much of the work involved in these calculations dealt with finding grids and time-steps that were stable.

During the process of obtaining the solutions found in table (3.1), nearly the same number of calculations were performed which became unstable as ones that were usable. The main cause of the instability stems from the skewed spectral elements located in the center of the passage in the trailing edge region (figure C-1).

The instability generated in these skewed elements can be triggered via three observed means. These are the ratio of elements between sections of the grid, the interaction of the suction side boundary layer, and the propagation of noise from the pressure side.

The grid generator creates an H-grid, with three separate sections. The inflow region, passage region, and the outflow region. The spectral elements can be clustered differently in these various regions, i.e., near the leading and trailing edge, as well as in the boundary

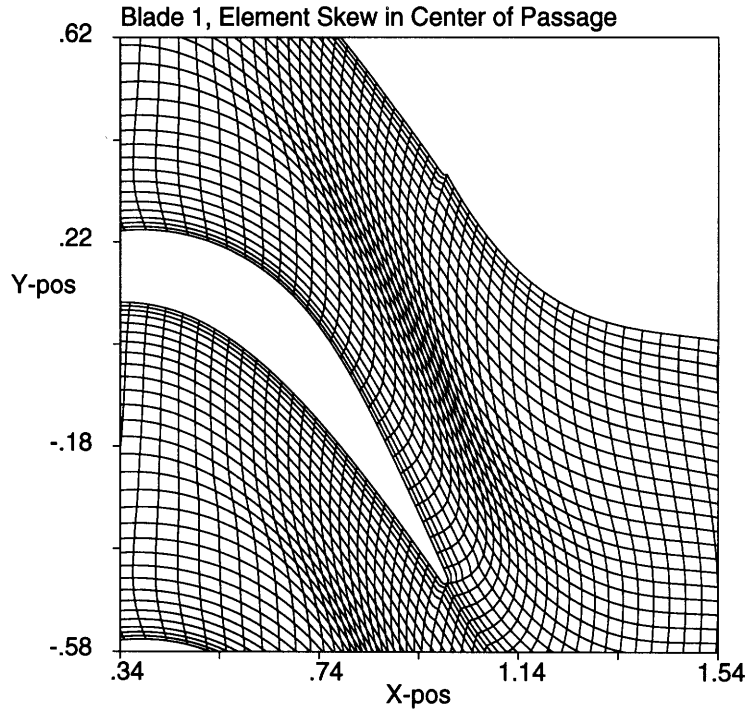


Figure C-1: Typical skewing of spectral elements in center of the passage, trailing edge region

layers. Although not true for all cases, in general it is best to cluster the elements such that the elements on either side of the inflow-passage boundary, or the passage-outflow boundary are nearly the same size (figure C-2), i.e. : $\frac{L_1}{L_2} \approx 1.0$

Another method for avoiding the development of an instability is to reduce the amount of skew in the elements as much as possible. Keeping the number of badly skewed elements as far from the suction side boundary layer is advantageous. Many solutions became unstable when the shedding process of the suction side shear layer reached the skewed elements, seemingly triggering an instability. This was observed in the flow movies, where no noise was present in the center of the passage, and as soon as the suction side shear layer reached the skewed elements, noise appears and propagates upstream.

Therefore, to avoid large areas of skewed elements (which is inherent with this grid generation scheme when using large blade turning from the inflow to outflow), the elements can be clustered near the leading edge region, and towards the blade surfaces. However, moving elements towards the inflow region has the effect of creating more noise for the elements in the trailing edge region on the pressure side due to a large stream-wise pressure gradient. This noise produced by lack of resolution of flow gradients can also create a instability in the solution.

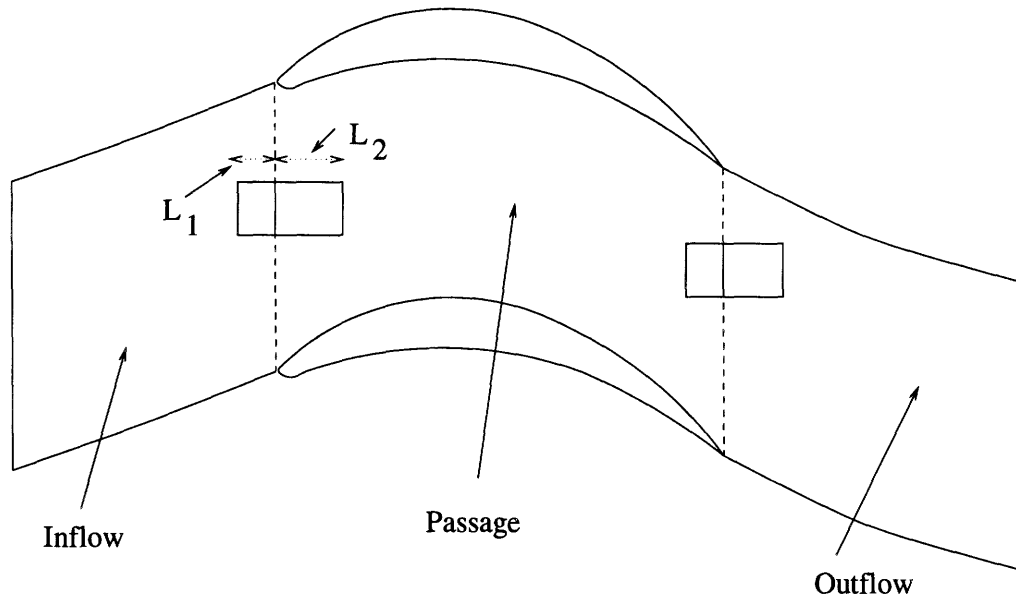


Figure C-2: Important to have nearly equal element widths on either side of the grid sections

Thus, the lessons learned are that it is best to have nearly equal elements sizes across the three gridding areas, and to rearrange the elements as to best relieve the skewness found around the trailing edge plane. There is a tradeoff between moving the elements away from the trailing edge region to avoid skewness and the resolution of the flow gradients present in aft region of the passage.

Reynolds Number	Number of Elements	Solver Size (MB)	Typical Time-Step
20,000, 30,000	2100	144	0.0003
60,000, 90,000	4050	229	0.0002
120,000	4386	251	0.0001

Table C.1: Typical solver sizes and time-steps for the various grids used

C.2 Computational Effort

The computations involved for this investigation were intensive from the standpoint of both the computer memory required as well as the amount of CPU time needed.

A typical case using 4000 spectral elements (as used for the $Re = 60,000$ and $90,000$ cases), requires on the order of 230 MB of memory. Using an IBM RS/6000 590, about 10 CPU hours is require for 1000 time-steps. With the total number of time-steps needed to complete a solution being on the order of 40,000, the solution time can reach on the order of 15 to 20 days. The use of faster machines (such as DEC Alphas) greatly decreased the solution time needed, but the resources needed to complete the full proposed matrix of solutions in the time allotted was never obtained.

Table (C.1) gives a look at the solver sizes required for the various grids used. The typical time-steps shown are at about the maximum allowable for stability for a given grid and Reynolds numbers.

Bibliography

- [1] Chuen-Yen Chow. *An Introduction to Computational Fluid Mechanics*. Seminole Publishing Company, 1983.
- [2] Chuen-Yen Chow and Arnold M. Kuethe. *Foundations of Aerodynamics, Bases of Aerodynamic Design, 4th ed.* Wiley, 1986.
- [3] Dr. Eugene Covert. Personal communication. M.I.T., May 1997.
- [4] J. D. Denton. Loss mechanisms in turbomachines. *Journal of Turbomachinery Journal*, 115, October 1993.
- [5] Robert A. Granger. *Fluid Mechanics*. Dover, 1995.
- [6] E. M. Greitzer. Class notes, internal flows in turbomachinery. 1996.
- [7] H.P. Horton. *Laminar Separation Bubbles in Two- and Three-Dimensional Incompressible Flow*. PhD thesis, University of London, 1968.
- [8] Robert E. Mayle. Fundamental aspects of boundary layers and transition in turbomachines. In *Von Karman Institute for Fluid Dynamics, Lecture Series 1991-06*, pages 1–60, 1991.
- [9] A. Michalke. On the inviscid instability of the hyperbolic-tangent velocity profile. *Journal of Fluid Mechanics Journal*, pages 543–556, 1964.
- [10] S. A. Orszag and L. Kells. Transition in plane poiseuille and plane couette flow. *Journal of Fluid Mechanics Journal*, 1980.
- [11] Laura L. Pauley, Parviz Moin, and William C. Reynolds. The instability of two-dimensional laminar separation. In *Conference on Low Reynolds Number Airfoil Aerodynamics, Univ. of Notre Dame*, June 1989.

- [12] H. Schlichting. *Boundary Layer Theory, 7th ed.* McGraw-Hill, New York, 1978.
- [13] Brent Staubach. Personal communication. Pratt and Whitney, August 1996.
- [14] I. Tani. Low-speed flows involving bubble separations. *Prog. Aero. Sciences Journal*, 5:70–103, 1964.
- [15] Theodore V. Valkov. *The Effect of Upstream Rotor Vortical Disturbances on the Time-Average Performance of Axial Compressor Stators.* PhD thesis, Massachusetts Institute of Technology, 1996.
- [16] Harold H. Youngren. Analysis and design of transonic cascades with splitter vanes. Master's thesis, Massachusetts Institute of Technology, 1991.